IECO

Volume 8 No 1 Year 2025

■ Volume 8

■ No 1

■ Year 2025

University of Sistan and Baluchestan

Iranian Association of Electrical and Electronics Engineers

International Journal Of

Industrial Electronics Control and Optimization

In This Issue:

Research Articles:

IECO

International Journal Of
Industrial Electronics Control and Optimization

About Journal

The University of Sistan and Baluchestan entered into strategic partnership with Iranian Association of Electrical and Electronic Engineers (IAEEE) to publish the **International Journal of Industrial Electronics Control and Optimization (IECO)**. The IECO is a refereed international journal which presents to the international scientific community important results of work in these fields, whether in the form of modeling simulation, analysis, fundamental research, development, application, design or real-time implementation. The scope of IECO is broad, encompassing all aspects of Industrial Electronics, Control and Optimization.

Note: International Journal of Industrial Electronics, Control and Optimization (IECO) has qualified to **ACADEMIC RESEARCH JOURNAL (ELMI-PAJOHESHI)** status certified by the ministry of Science, Research and Technology of Iran (No. 231566/3/18 dated 1396/10/09), and is published by the University of Sistan and Baluchestan through a formal partnership (No. 952/2/1500 dated 1395/11/04) with Iranian Association of Electrical and electronic Engineers (IAEEE) in order to develop scientific and research cooperation.

Aims and Scope

International Journal of Industrial Electronics, Control and Optimization (IECO) is a Peer reviewed journal of advanced and state-of-the-art in the science and engineering of Industrial Electronics, Control and Optimization. Its Scope encompasses the applications of Industrial Electronics, power systems, control, optimization and computational intelligence for the enhancement of industrial and manufacturing system and processes. The scope of the journal include the following:

I. Industrial Electronics

- Low and high-power converters
- Renewable energy
- Drive control techniques
- Techniques for advanced power semiconductor devices
- Power quality and utility applications
- Communications
- Flexible AC Transmission Systems (FACTS)
- Control in power electronics
- Electromagnetic and thermal performance of electronic power converters
- Motion control, robotics, sensors and actuators
- Fault detection and diagnosis
- Power systems
- Factory automation, communication, and computer networks

II. Control

- Adaptive control
- Control of process systems
- Control theory
- Data processing
- Design of control systems
- Hybrid systems
- Identification and observation
- Intelligent systems
- Model-predictive control
- Optimal control
- Robust control
- Fractional order systems

III. Optimization

- Ant Colony
- Chaos Theory
- Evolutionary Computing
- Fuzzy Computing
- Hybrid Methods
- Immunological Computing
- Neuro Computing
- Particle Swarm
- Probabilistic Computing
- Rough Sets
- Wavelet

International Journal Of
Industrial Electronics Control and Optimization
Print ISSN: 3517-2645
Online ISSN: 3568-2645
Homepage: https://ieco.usb.ac.ir/

The Stochastic P2P Energy Management Scheme for Integrated Energy Microgrid Considering P2G and Electricity Network Fee

Meysam Feili[1] | Mohammad Taghi Ameli[2*]

Department of Electrical Engineering, University of Shahid Beheshti, Tehran, Iran [1,2]
Corresponding author's email: m_ameli@sbu.ac.ir

Article Info

Article type:
Research Article

Article history:
Received: 13-June-2024
Received in revised form: 18-August-2024
Accepted: 20-August-2024
Published online: 21-March-2025

Keywords:
Integrated energy systems,
Microgrids,
Stochastic optimization,
AC power flow,
Peer-to-peer energy market.

ABSTRACT

The prominent role of natural gas networks in mitigating the intermittency of renewable energy resources has highlighted the importance of integrated operation between electricity and gas grids. Additionally, energy storage systems, such as batteries and hydrogen, play a crucial role in power balancing and energy management. Previous research on the synergy between electricity and natural gas systems has primarily focused on the operational constraints of each grid. Only a few studies have explored market-driven models, such as peer-to-peer (P2P) energy trading, for the integrated operation of these networks. Furthermore, the limited studies that have implemented the peer-to-peer (P2P) market model for the integrated operation of power and natural gas grids have been conducted in two distinct phases: scheduling and trading. This paper introduces a stochastic P2P market-based optimization model for the coupled operation of natural gas and electricity grids, considering smart grid technologies such as power-to-gas (P2G) storage, batteries, and demand response (DR). Also, the presented framework incorporates alternating current (AC) power flow, natural gas steady-state model, and the power grid usage fee through the electrical distance model. The simulation results indicate that the proposed method significantly decreases total operating costs, reduces power losses, improves network component synergy, and enhances the performance of both networks.

	Indices	S^{fit}	Feed − in tariff price ($/kWh)
i, j	Index of network's node	S^{gas}	Natural gas tariff ($/kWh)
s	Index of scenarios	P^{dem}	Power demand (MW.)
n	Index of reduced scenarios	$\phi^{flex,MAX}$	Max demand flexibility(%)
t	Index of time (hour)	$\phi^{flex,MIN}$	Min demand flexibility(%)
N_{ng}	Nanogrid node	η_{dec}	The efficiency of battery discharging (%)
N_{gt}	Gas turbine node	η_{ch}	The efficiency of battery charging (%)
N_e	Power grid node	SOC(0)	Initial SOC level of battery (MWh)
N_g	Natural gas node	SOC^{min}	Min SOC level
N_{p2g}	P2G node	SOC^{max}	Max SOC level
N_{gc}	Gas compressor node	$PR.^{min}$	Gas pressure minimum level (psi)
	Constants	$PR.^{max}$	Gas pressure maximum level (psi)
S^{rit}	Electricity price ($/kWh)	G	The real part of the admittance matrix
S^{cur}	Power shedding penalty ($/kWh)	B	The imaginary part of the admittance matrix
$\mathbb{C}\phi_{ch}^{p2g}$	The conversion coefficient of P2Gs (MW/kg)	$P^{grid,ramp}$	Tie line power ramp rate (MW/h)
$E^{init,p2g}$	Initial stored hydrogen in the container (kg)	D	Diameter of the pipeline (m)
η_{p2g}^{ch}	The P2G charging efficiency	S	The cross − section area of the pipeline (m^2)
η_{p2g}^{dch}	The P2G discharging efficiency		
$P^{Min,Max,gt}$	Min and Max constraint of gas turbine (MW.)		
$P^{gt,ramp}$	Ramp rate limit of gas turbines (MW/h)	$P^{dch,m}$	Discharging power inside a Nanogrid (MW)
V^{min}	Lower bound of node voltage (kV)	SOC^{batt}	Battery SOC level

V^{max}	Upper bound of node voltage (kV)	g^{gt}	Gas turbine′s natural gas burn rate (m^2)
Δh	Height disparity between nodes (m)	$q^{Gen,gt}$	Gas turbine′reactive power output (MVAr)
$d_{i,j}$	The sum of the electrical distances	G^{line}	Natural gas flow rate (m^2)
$Z_{i,j}$	Thevenin impedance distance	Pr^{grid}	Node gas pressure (psi)
$u_{i,j}^{dis}$	Distance unit fee($/per_distance_unit)	e	Node voltage′s real component
a, b, c	constants of the gas turbine′s heat rate funct	f	Node voltage′s imaginary component
λ	Friction coefficient of the Darcy factor	$q^{Dem,MG.}$	Total injected reactive power (MVAr)
Z	The factor of gas compressibility	S^{grid}	apparent power (MVA)
R	Constant of natural gas (J/(kg K))	$P^{p2g,Dch}$	The P2G discharged power (MW)
L	Gas pipeline length (m)	$P^{p2g,ch}$	The P2G charged power (MW)
Temp	Gas flow average temperature (K)	$E^{tot,p2g}$	the total hydrogen in the container (kg)
β_{comp}	Coefficient of gas compressor	$E^{dch,p2g}$	The discharged hydrogen (kg)
η_{comp}	Efficiency of gas compressor	$E^{ch,p2g}$	The charged hydrogen (kg)
$G^{comp,max}$	Maximum permissible gas flow through the compressor (m^2)	$P^{Dem,N}$	Nanogrid demand supplied by the power grid (MW)
$P^{comp,max}$	Maximum allowable gas compressor power demand (MW)	$P^{NG,GT}$	Nanogrids traded energy with gas turbines (MWh)
	Abbreviation	$P^{NG,P2G}$	Nanogrids traded energy with P2Gs (MWh)
P2P	Peer to peer	$P^{P2G,N}$	P2G energy purchased from the power grid (MWh)
DERs	Distributed energy resources	$P^{P2G,GT}$	P2G energy purchased from the gas turbine (MWh)
DR	Demand response	$P^{P2G,NG}$	P2G energy sold to the Nanogrids (MWh)
CDA	Continuous double auction	$P^{N,P2G}$	P2G energy sold to the power grid (MWh)
DSO	Distribution system opera	$P^{GT,P2G}$	Gas turbine energy sold to the P2G (MWh)
MINLP	Mixed integer none leaner programming	$P^{GT,NG}$	Gas turbine energy sold to the Nanogrid (MWh)
FIT	Feed − in tariff rate	S^{P2P}	Final P2P Price ($/MW)
ESS	Energy storage system	$P^{Gen,N}$	Gas turbine generated power to the grid (MW)
TID	$Thevenin\ impedance\ distance$	$P_{i,t}^{comp}$	Gas compressor power demand (MW)
	Decision Variables	$G_{i,t}^{comp}$	Compressor gas flow rate m^2
$q^{dch,n}$	Discharging ESS reactive power to grid (MVAr)	DV	Binary decision variable
$Q^{Dem,N}$	Reactive power supplied by the power grid (MVAr)	G^{grid}	Injected natural gas into the gas grid's nodes (m^2)
$P^{Dem,NG}$	Active power supplied by the power grid (MW)	$Pr_{i,t}^{out}$	Outlet pressure of gas compressor (psi)
P^{cur}	Curtailed power (MW)	$Pr_{i,t}^{in}$	Inlet pressure of gas compressor (psi)
$q^{Dem,DR.}$	Reactive power demand after scheduling (MVAr)	$q_{i,t}^{p2g,dch}$	The P2G discharged reactive power (MVAr)
G^{grid}	Injected natural gas (m^2)	$q_{i,t}^{p2g,ch}$	The P2G charging reactive power (MVAr)
$P^{Gen,gt}$	Gas turbine active power output (MW)	$q_{i,t}^{comp}$	Gas compressor reactive demand (MVAr)
$P^{Dem,DR.}$	The power demand of Nanogrid (MW)	φ^{dis}	network charge $/per distance unit
P^{ch}	ESS′s charging power (MW)	q^{cur}	curtailed reactive power (MVAr)
$P^{Tot,dch}$	Total discharging power (MW)	ψ	traded energy ($/kWh)

I. Introduction

In traditional power systems, electricity flows in a single direction. In such systems, large, centralized power plants generate electricity, and the generated power is transmitted through the grid to consumers [1]. However, due to increasing electricity demand, environmental concerns, and declining fossil fuel reserves, policymakers are advocating a shift from centralized to distributed power systems [2-5] .Recent studies suggest integrating Distributed Energy Resources (DERs) can result in cleaner and more reliable energy systems with substantial environmental benefits [6-8]. Nonetheless, the increasing integration of DERs at the consumer premises transforms power system control, presenting new operational challenges [9, 10].

A microgrid (MG) is a part of the power distribution grid that can be controlled and coordinated, either connected to the main grid or islanded operation [11, 12]. MGs can lower transmission line losses and enhance power quality [13]. They utilize various DERs such as solar panels, wind turbines, micro-hydro systems, and gas turbines as power sources, thereby addressing energy shortages and enhancing grid efficiency [14-18]. The advancement of DER technologies has emphasized energy management within MGs. To mitigate

power fluctuations from renewable DERs, gas turbines with flexible features are increasingly deployed on the demand side to smooth out renewables' intermittent nature. Employing gas turbines to address balancing issues highlights the significance of integrating the operation of electricity and natural gas systems [19].

Local energy trading through the Peer-to-peer (P2P) market is an innovative technology that enables customers to purchase and sell electricity within a local energy market. This P2P market framework provides significant flexibility, enhanced control over energy usage, and lower customer bills. It also allows for more efficient utilization of DERs [20, 21]. The emergence of the energy-sharing market is supported by advancements in information and communication technologies, alongside the deregulation of power distribution grids, which together facilitate P2P energy trading among local energy resources. Research in this area spans multiple domains, including communication infrastructure, market design, policy-making, social science, and trading platforms [22].

The advent of Power-to-Gas (P2G) technology heralds a transformative approach to energy conversion and storage, offering a promising avenue for mitigating renewable energy intermittency and decarbonizing the energy sector. P2G entails the conversion of surplus-generated electricity into hydrogen gaseous fuels through electrolysis and subsequent chemical processes [23]. This innovative technology holds immense potential in addressing the challenges posed by the variable nature of renewable energy sources or market price volatility by storing excess energy in the form of easily transportable and storable gases [23]. Moreover, P2G systems offer versatility by integrating renewable energy into existing gas infrastructure, facilitating its utilization across various sectors, including transportation, industry, and heating.

Battery storage systems represent a pivotal advancement in energy storage, offering scalable and flexible solutions to intermittency and grid stability associated with renewable energy integration [24]. Battery systems utilize electrochemical processes to store surplus electricity, thereby enabling its utilization during periods of high demand or when renewable generation is insufficient [25]. Battery storage enhances grid reliability and resilience while optimizing renewable energy utilization by mitigating curtailment and enabling smoother integration into existing grids [25]. Furthermore, advancements in battery technology, coupled with declining costs, have rendered battery storage an economically viable option for both grid-scale and distributed applications, thereby catalyzing its widespread adoption and deployment [26]. Demand response (DR) mechanisms represent a critical component of modern energy management strategies, offering a means to balance supply and demand in real-time by adjusting electricity consumption patterns in response to grid conditions or price signals. DR initiatives empower consumers to actively participate in grid operations by voluntarily reducing or shifting their electricity usage during peak periods or in response to fluctuating energy prices [27].

Gas-fired generators, renowned for their flexibility, are considered valuable resources for integrating renewable-based distributed energy resources (DERs) into the power grid, thereby linking the power and natural gas systems. This interdependence highlights the importance of coordinating natural gas and electricity networks. Meanwhile, P2P energy market technology is an emerging solution that enables local energy trading among customers, aiding the integration of diverse DERs into the power system. By employing the P2P energy trading model to coupled natural gas and electricity systems, substantial benefits can be realized for all market participants. Many researchers have considered the integrated operation of electricity and natural gas grids.

Wang et al. [28] present a P2P energy trading market designed explicitly for the microgrids (MGs) community, taking into account the operating costs of the power grid during the market-clearing process. Zhang et al. [1] proposed bi-level multi-energy trading (hydrogen and electricity) in the integrated energy systems considering day ahead and real-time balancing markets. It did not consider the electricity and natural gas grid constraints, renewable energy resources, P2Gs, and load flexibility. Crespo-Vazquez et al. [29] offer a framework for P2P energy trading that maintains user preferences and encompasses both day-ahead and intraday markets. They introduce a two-stage stochastic programming model for managing the day-ahead market: in the first stage, users decide the amount of energy they are willing to trade in real-time, and in the second stage, battery operations (charging and discharging) are determined. Authors of [30] proposed the integrated operation of natural gas and electricity grids, facilitating synergy between gas turbines, electricity consumers, and P2Gs. It did not consider both grid constraints. Optimal pricing and market equilibrium are addressed by [31] to create a P2P trading strategy between community MGs and the energy balance service provider. The presented case studies show significant economic benefits for the service provider. Reference [32] developed a novel transactive energy management system framework that integrates P2P and peer-to-grid energy trading through efficient and fair energy pricing strategies. The authors tried to create a peer-to-grid market instead of the FIT rate to facilitate energy trading between prosumers and the power grid. This paper focuses on the energy markets and does not consider the operation of natural gas and electricity networks.

Authors of [33] employed the multi-objective game-theoretic optimization method to facilitate P2P energy trading and applied the Nash equilibrium game to determine the optimal number of participants and payoffs for P2P and peer-to-grid energy trading. Rowe et al. [34] proposed bi-level optimization for an electrical-heat-hydrogen-gas multi-energy

storage system. In the upper level, an MILP was implemented to reduce investment and operation costs. Additionally, the model incorporates grid support criteria at the lower level to reduce network losses. The reviewed paper did not consider batteries, DR, and the gas compressor's role in the integrated energy systems model. The study in [35] introduced a P2P energy trading model that employs neural networks to lower operational costs and implement peak shaving. Despite its notable contributions, the approach lacks integration of trading mechanisms and power network models within the proposed P2P market framework.

Authors in [36] proposed a decomposed P2P energy trading method considering the effect of transacted energy on the power network stability and minimized information exchange between agents and between agents and the grid operator. This paper focused on developing a decentralized framework for P2P energy trading. It did not consider the integrated operation of gas and power networks, ESSs, DR, and P2G.

The authors of [37] explored prosumers' social cooperation through a coalition formation game for the P2P energy market. Reference [38] addressed integrating electricity and natural gas markets by using gas turbines and P2G systems as connecting points between the gas and power grids and examined various clearing strategies to maximize customer profits. Niu et al. [39] proposed a P2P energy trading model in which electricity consumers traded with the electricity producer (transmission system operator) and the natural gas wholesale market (gas supplier). This paper focuses on designing a novel P2P market that allows consumers to trade gas directly from different natural gas suppliers. It did not consider P2G, DR, and the effect of energy transactions on both grids' performance.

Authors of [40] developed an integrated market for power and heat energies, considering electric heating appliances as energy coupling points. This study examined the clearing prices in various energy markets and evaluated how energy consumption patterns influence market competition by employing the AC power flow method.

Reference [41] proposed a method for coupling heating, power, and natural gas energies via a P2P market. However, this paper did not assess the effectiveness of the proposed framework on the functionality of the natural gas and electricity grids. Researchers in [42] designed a P2P energy trading mechanism for prosumers using a coalition graph game, enabling them to form coalitions and determine the quantity and price of traded energy. In this study, the Myerson value rule is used to fairly distribute the total payoff of the P2P scheme among customers. Numerical analysis shows prosumers can benefit from the P2P scheme while adhering to local voltage constraints. Lu et al. [43] present a framework where the power generated by producers is first transmitted to the distribution network, and then purchasers receive the same amount of power minus the distribution network's power losses. Reference [44] proposed a P2P market for sharing a DR between customers. In the first stage, the entity named IEO centrally runs an optimization problem to determine the customer energy schedule for the day ahead market. Due to customers' arbitrary behaviors or renewable power fluctuations, a decentralized P2P market was performed in the second stage to exchange the DR between customers. Also, the reviewed paper did not consider the effect of DR sharing on the performance of the gas and power systems.

Basnet and Zhong [45] suggest a one-hour ahead market where a market operator clears the energy equilibrium price and schedules DERs. In this setup, the transmission network acts as a generator when supplying energy to a community and as a consumer when the community sells its surplus energy. Wang et al. [46] developed a game-theory-based P2P market that allows customers to trade both heat and electricity, considering cooperative behavior among trading agents. This market design explores the synergistic utility of multi-energy trading within an integrated energy system. Zhou et al. [47] propose a two-level congestion management model to meet security constraints. Although their framework provides financial benefits to end customers through participation in the local flexibility market, it does not establish a new framework for this market. Reference [48] integrates various types of energy systems using a two-phase mixed integer linear programming algorithm and hybrid power flow calculation to determine market clearing prices for power, natural gas, and heat energies. Wang et al. [49] propose an innovative risk-averse market-clearing method for integrated power, district heating, and natural gas systems, employing a stochastic framework to mitigate financial risks associated with the intermittency of wind power generation. They use a locational marginal price model to incentivize market participants. Hutty et al. [50] proposed a P2P energy trading framework based on the continuous double auction (CDA) method to trade electricity and heat. This paper considered a CDA-based P2P market to create a local energy market that enabled customers to exchange electricity and heat energies. It did not consider the gas and power networks, DR, and uncertainties.

Zhang et al. [51] proposed a P2P energy trading market for commercial buildings, focusing on multi-energy coupling to enhance energy efficiency and reduce operating costs. However, this study does not address grid constraints and energy transaction fees. Chen et al. [52] introduced a two-level bidding strategy to optimize energy trading within household neighborhoods, taking into account energy storage systems (ESS) and photovoltaic generation. Despite its novel approach, this paper does not consider the impact of energy trading on power grid performance. Jiang et al. [53] proposed a two-stage optimization framework to maximize customer benefits in P2P energy trading. The first stage determines the amount of energy bought or sold in the market. The second stage organizes the market and facilitates energy trading

among customers. However, the paper has some limitations: the two separate stages are not optimal, and the framework's impact on the performance of both networks is not considered.

As shown in Table 1, While we have reviewed many existing works, most reviewed papers conducted in the P2P energy trading frameworks do not consider the coupled operation of electricity and natural gas systems via the P2P energy trading market. Additionally, the few papers that have considered the P2P market framework for the integrated operation of natural gas and electricity networks have explored various methods for designing a decentralized energy trading framework. On the other hand, methods like P2P energy trading are tools that incentivize customers to generate and consume power locally, considering both grids' and customers' benefits. Hence, considering the effects of energy transactions on the performance of gas and power distribution grids is crucial.

Integrating the detailed AC power flow method and natural gas model to evaluate the effect of the P2P energy transaction on the performance of both grids is a vital research aspect not considered in the previous papers. Also, proposing the P2P framework in which the customers' energy schedules are determined based on the market price rather than the power utility price is another research gap that needs to be addressed. Also, considering different energy storage systems such as P2Gs and batteries and using their potential advantages in the P2P market is another research gap. Reference [54] proposed the model and framework for the P2P market based on the CDA method, which was performed in two separate stages. Also, the authors of [4] borrowed the P2P energy market model from the reference [54] and proposed a two-stage framework to integrate the operation of gas and electricity grids through the P2P market framework, considering both network models and constraints. Employing a two-stage framework for P2P energy trading is not optimal, but it is applicable [54]. There are two reasons why this strategy is not optimal for all market players. First, a subscriber's payment cost is determined by the prices specified in the P2P energy trading agreements, not by the electricity prices offered by the power utility used in the objective function. Additionally, the customers choose the amount of electricity to sell or purchase and the bid or ask price in two separate stages instead of jointly at one step [54]. Therefore, a P2P energy trading scheme needs to be developed to schedule DERs based on the P2P market clearing price and consider the effect of each energy transaction on the performance of both grids.

Incentivized by the research gap in the literature, in the first step, we developed a novel joint P2P optimization mechanism for the integrated operation of electricity and natural gas systems considering the AC power flow framework and natural gas steady-state model. The word “joint” implies that the customers' energy is scheduled by the objective function based on the P2P market price. Also, employing both network models (the AC power flow and natural gas steady-state model) enables the network operators to precisely track the energy transaction's effect on the electricity (the voltage profile) and natural gas (node gas pressure) grids. To consider the power grid fee during energy trading and reduce the electricity network losses, we borrowed the Thevenin impedance distance (TID) model from previous literature and engaged it with the optimization problem. Using the TID model enables the network operator to consider the effect of line losses on each energy peer. To harness the different energy storage flexibility through the P2P local energy market, we consider the P2G units and battery storage in the proposed model.

TABLE 1 OVERVIEW OF THE LITERATURE REVIEW

Ref.	Year	IO	P2P	IONPS	AC Power flow	PNUF	DR	P2G
[50]	2024	×	✓	✓	×	×	×	✓
[47]	2022	×	✓	×	✓	×	✓	×
[55]	2021	×	✓	×	×	×	×	×
[1]	2024	✓	✓	×	✓	×	×	×
[56]	2024	×	✓	✓	×	×	×	×
[1]	2024	×	✓	×	×	×	×	×
[57]	2021	×	×	✓	✓	×	✓	×
[22]	2022	×	✓	×	×	×	×	×
[58]	2022	×	✓	×	×	×	×	×
[59]	2022	×	✓	×	✓	×	✓	×
[60]	2022	×	✓	×	✓	×	✓	×
[61]	2022	×	✓	×	×	×	×	×
[62]	2021	×	✓	✓	×	✓	×	×
[53]	2022	×	✓	×	×	×	×	×
[51]	2022	×	✓	✓	×	×	×	×
[22]	2023	×	✓	×	×	×	×	×
[4]	2023	✓	✓	✓	✓	×	×	×
This paper		✓	✓	✓	✓	✓	✓	✓

** Integrated optimization (IO)
Integrated operation of natural gas and power systems (IONPS)
Power network usage fee (PNUF)

In the following, to show the proposed method's superiority and examine its strengths and drawbacks, we compared the presented framework with the benchmark method based on the continuous double auction CDA mechanism, executed in two separate stages [54]. In summary and order of priority, the novelties of this paper are as follows:

- This paper proposes a novel stochastic P2P-based optimization problem for integrated energy microgrid scheduling to facilitate synergy between different DERs (P2Gs, nano grids (NGs), ESSs, and gas turbines) regarding both network constraints.
- Proposing a scenario-based stochastic model for considering natural gas and electricity demands uncertainties to give a better perspective for network operators.
- Considering the electricity network’s usage price based on the electrical distance model, the AC power flow model, the DR, different energy storage

technology (P2G and ESS), and the natural gas steady-state model.

The remainder of this paper is organized as follows: Section 2 introduces the relevant ideas of the presented P2P market design for the incorporated operation of natural gas and electricity networks. Section 3 describes the P2P-based optimization problem (mathematical model) driven by the electric distance between purchasers and vendors. In Section 4, numerical studies are introduced to show the advantages of the presented method. The conclusion and proposed future research aspects are presented in section 5.

II. Methodological framework

This paper introduces the novel electrical distance-based approach for the incorporated operation of natural gas and electricity systems via the P2P market framework at the microgrid level. The proposed microgrid is equipped with a distribution system operator (DSO). Also, we suppose that the DSO is responsible for operating the electricity and natural gas networks [10, 63]. In this regard, the primary target of this paper is to design a joint P2P energy trading-based market for the incorporated operation of electricity and natural gas networks to facilitate the synergy between customers such as consumers (NGs), prosumers (ESSs and P2Gs), and producers (gas turbines). The proposed method is in such a way that the amount of energy to be sold/ purchased in the market is determined based on the market pieces rather than the power utility prices, considering the effect of electrical distance on the transaction fees, the AC power flow, the steady state natural gas grid model and the electricity demand flexibility.

The centralized P2P markets have the advantage of maximizing the welfare of the entire community. Another benefit of centralized P2P frameworks is that the power generation and consumption patterns of peers are more predictable, which reduces uncertainty. The reason is that the coordinator, the DSO, directly controls the operational status of peers [64]. The computational complexity and users' privacy autonomy issues are considered significant drawbacks of centralized methods [64]. Considering that the development of decentralized energy trading is not within the scope of this paper, we employed a simple centralized framework. In this regard, the DSO centrally solves the proposed P2P optimization problem. How to propose the decentralized framework in the joint P2P energy market for the incorporated operation of natural gas and electricity grids remains to be studied, but it is not the focus of this paper. Fig. 1. Illustrates the proposed method's timeline.

As evident from Fig.1, the presented method consists of three major parts. In the first section, the DSO gathers information related to the network components, such as the electricity network and natural gas grid data, customers' related settings, etc. Then, in the second stage, the DSO executes the joint P2P energy trading-based optimization problem to determine the trading schedule for the next 24 hours. In this regard, the targeted period of the optimization problem is the day-ahead market. The presented framework is implemented on the integrated energy microgrid that comprises a 33-bus power distribution grid and a modified 33-node natural gas network. The natural gas and electricity grids are integrated through gas compressors and gas-fired generators. The presented competitive local market price enables customers such as P2Gs to participate in the local energy market, which increases the total social welfare.

The architecture of the proposed method is presented in Fig. 2. The structure of the presented microgrid consists of four main components, including gas turbines (producer), NGs (prosumer), P2Gs (prosumer), the distribution power network (lines and transformers), and natural gas distribution network (lines and compressors). All microgrid components send the required information and settings to the DSO. After gathering information, the DSO solves the P2P-based optimization problem to determine the customer's trading schedules considering the electrical distance between customers, the DR, and both grid constraints. The output of the optimization problem is customers' energy trading schedules, consisting of energy trading plans with other customers or the power grid. The DSO is responsible for balancing bids and offers that are not matched during the P2P market procedure. In this regard, customers' shortage/surplus energy, which is not matched in the P2P energy trading market, is supplied/purchased by the power grid. Employing the AC power flow method and natural gas steady-state model enables the DSO to monitor the detailed effect of energy transactions on the performance of electricity and natural gas grids. The presented P2P-based optimization problem is in such a way that energy transactions between customers reduce the power losses, maintain the node gas pressure in the allowable interval, reduce the total operating expenses of the microgrid, and increase the profit of gas turbines and P2Gs.

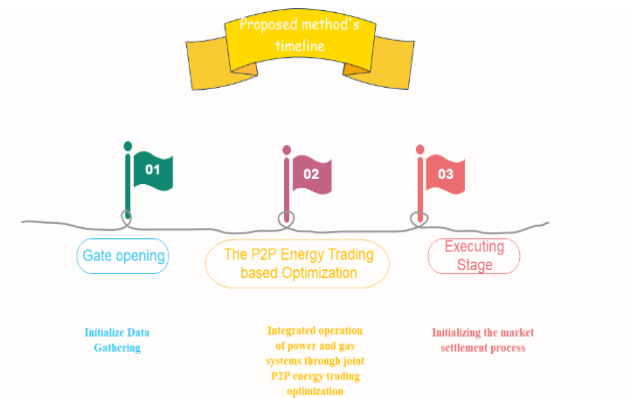

Fig. 1. The presented method timeline.

III. P2P-based optimization problem

As mentioned, this paper considers an integrated energy microgrid consisting of NGs, P2G units, gas turbines, and

ESSs. NGs have power and natural gas demands; natural gas is used for heating and cooking. Also, no control action is placed on the gas loads in NGs. Three types of electrical loads (fixed, emergency, and flexible) are considered at the NGs level. As the name suggests, the fixed loads are noncontrollable and nonadjustable. Emergency loads refer to those groups of power demand that can not be adjusted or curtailed. The difference between fixed and emergency loads is that fixed loads can be curtailed, but emergency loads cannot be interrupted. Flexible loads refer to those groups of electrical loads that can control and adjust their demand profiles across different timescales. Thermostatic loads, ESS, and electric vehicle fleets are examples of flexible loads. The electricity and natural gas load profiles for the next 24 hours are available to the NG operator. Also, NGs are equipped with an ESS, and it is assumed that NGs do not have renewable energy sources. The MG's decision variables are the optimal power demand of NGs (supplied by the power grid and the P2P energy market), ESSs' charging/discharging cycle, optimal charging/discharging cycles of P2Gs (purchased/sold from/to the power grid or the P2P market), and energy generation schedules of gas-fired generators (sold to the electricity grid or local consumers via the P2P energy market).

This paper uses the gas turbine unit as a fossil fuel-based power generation system. The inherent flexibility of gas turbines, characterized by their rapid ramping rate and quick response time, renders them particularly well-suited to managing the intermittency inherent in modern power systems [65]. The DSO gathers various information from the MG's different components. The NGs predicted electricity and natural gas demands for the next 24 hours, P2Gs-related data, gas turbines' rated capacity, the power grid's various data, and related information of the natural gas pipeline are part of the collected information by the DSO. After decision-making and processing, the optimization results are transmitted to the customers as energy trading schedules. The energy trading schedules include energy trading plans between customers and the power grid.

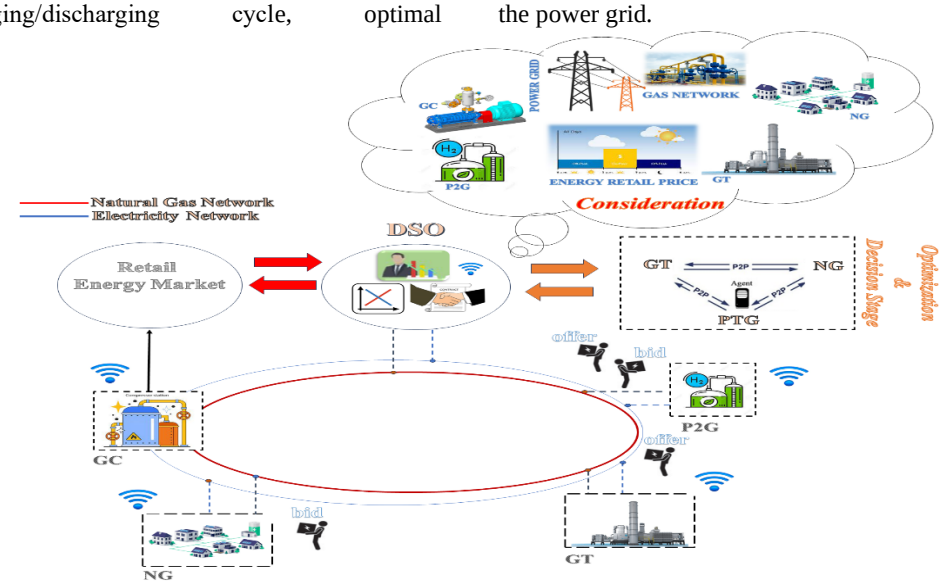

Fig. 2. The overall framework of the proposed method.

The presented framework is based on the mixed integer nonlinear problem (MINLP) optimization programming, which the DSO centrally solves to obtain customers' optimal P2P energy trading schedule. The MINLP is a mathematical optimization approach that involves solving problems with both continuous and discrete (integer) variables where the objective function or some of the constraints are nonlinear. The objective function of the P2P-based optimization problem, shown in Equation (1), is based on the day-ahead market structure.

In the objective function, the first three terms are costs related to energy purchased by the NGs. The second four terms are costs and revenues related to the P2G units. After the P2Gs' related terms, the following terms are the penalty related to the curtailed energy of NGs, the revenue related to selling stored energy to the power grid, and the cost of supplying natural gas from the wholesale natural gas price. The last four terms are revenues related to gas turbines' traded energy and gas compressor operation costs. The gas compressor's electricity demand is supplied only by the power grid through the energy retail price.

For the sake of simplicity, we suppose that the energy stored in the ESSs' is consumed within the NGs or sold to the power grid. The power utility, P2G units, and gas turbines supply the NGs' power demands. Also, the power generated by gas turbines is purchased by the power grid, P2Gs, and NGs. In this regard, the power grid balances surplus production and consumption.

As it is clear from Equation (1), The total operating cost of the microgrid is related to the market price (S^{P2P}), the FIT rate (S^{fit}), the natural gas wholesale price (S^{gas}), and retail energy

price (S^{rit}). The FIT rate and retail price are constant, while the market price is determined in the process of P2P-based optimization. The presented objective function reduces NGs' total payment cost and increases gas turbines' and P2Gs' total revenue. Equation (2) shows that the total power demand of NGs ($P_{s,i,t}^{Dem,NG}$) is supplied by the power grid ($P_{s,i,t}^{Dem,N}$) and the P2P energy trading with gas turbines ($P_{s,i,j,t}^{NG,GT}$) and P2Gs ($P_{s,i,j,t}^{NG,P2G}$). The power grid supplies the NGs' power demand, which is not matched in the P2P market.

$$\begin{aligned}\min\Bigg\{\sum_{s=1}^{n}\Phi_s\Bigg(&\sum_{i}^{N_{ng}}\sum_{t}^{T}P_{s,i,t}^{Dem,N}S_{s,i,t}^{rit}\\&+\sum_{i}^{N_{ng}}\sum_{j}^{N_{gt}}\sum_{t}^{T}P_{s,i,j,t}^{NG,GT}S_{s,i,j,t}^{P2P}\\&+\sum_{i}^{N_{ng}}\sum_{j}^{N_{p2g}}\sum_{t}^{T}P_{s,i,j,t}^{NG,P2G}S_{s,i,j,t}^{P2P}\\&+\sum_{i}^{N_{p2g}}\sum_{j}^{N_{gt}}\sum_{t}^{T}P_{s,i,j,t}^{P2G,GT}S_{s,i,j,t}^{P2P}\\&+\sum_{i}^{N_{p2g}}\sum_{t}^{T}P_{s,i,t}^{P2G,N}S_{s,i,t}^{rit}\\&-\sum_{i}^{N_{p2g}}\sum_{j}^{N_{ng}}\sum_{t}^{T}P_{s,i,j,t}^{P2G,NG}S_{s,i,j,t}^{P2P}\\&-\sum_{i}^{N_{p2g}}\sum_{t}^{T}P_{s,i,t}^{N,P2G}S^{fit}\\&+\sum_{i}^{N_{ng}}\sum_{t}^{T}P_{s,i,t}^{cur}S^{cur}\\&-\sum_{i}^{N_{ng}}\sum_{t}^{T}P_{s,i,t}^{dch,m}S^{fit}\\&+\sum_{i}^{N_{g}}\sum_{t}^{T}G_{s,i,t}^{grid}S^{gas}\\&-\sum_{i}^{N_{gt}}\sum_{t}^{T}P_{s,i,t}^{Gen,N}S^{fit}\\&-\sum_{i}^{N_{gt}}\sum_{j}^{N_{mg}}\sum_{t}^{T}P_{s,i,j,t}^{GT,NG}S_{s,i,j,t}^{P2P}\\&-\sum_{i}^{N_{gt}}\sum_{j}^{N_{p2g}}\sum_{t}^{T}P_{s,i,j,t}^{GT,P2G}S_{s,i,j,t}^{P2P}\\&+\sum_{i}^{N_{gc}}P_{s,i,t}^{comp}S_{i,t}^{rit}\Bigg)\Bigg\}\end{aligned} \tag{1}$$

$$\begin{aligned}P_{s,i,t}^{Dem,NG} = P_{s,i,t}^{Dem,N}&+\sum_{j}^{N_{gt}}P_{s,i,j,t}^{NG,GT}\\&+\sum_{j}^{N_{p2g}}P_{s,i,j,t}^{NG,P2G}\ \forall\ i\in N_{ng},s\\&\in n,t\in T\end{aligned} \tag{2}$$

Equations (3) to (5) determine NGs traded energy (with gas-fired generators and P2G units) and P2Gs purchased energy from gas turbines via the P2P market. Also, to determine purchasers and sellers in P2P energy trading, we employed the binary decision variable ($Dv_{s,i,j,t}$), which is shown in Equation (3) to (5). This binary variable makes the model MINLP. The seller and purchaser at time t are determined through the binary decision variable. For instance, in Equation (3), ($Dv_{s,i,j,t}$) Indicates that the NG (i) at the time period (t) purchases ($P_{s,i,j,t}^{NG,GT}$) kWh from the gas turbine (j). In other words, if ($Dv_{1,1,25,10}$) equals 1, which means that in scenario one, NG "1" trades energy with gas turbine "25" at period 10. Also, the amount of energy that gas turbine "25" sells to NG "1" is determined by solving the optimization problem.

$$\begin{aligned}P_{s,i,j,t}^{NG,GT} = Dv_{s,i,j,t}P_{s,i,j,t}^{GT,NG}\ \forall\ i\in N_{ng},j\in\\N_{gt},s\in n,t\in T\end{aligned} \tag{3}$$

$$\begin{aligned}P_{s,i,j,t}^{NG,P2G} = Dv_{s,i,j,t}P_{s,i,j,t}^{P2G,NG}\ \forall\ i\in N_{ng},j\in\\N_{p2g},s\in n,t\in T\end{aligned} \tag{4}$$

$$\begin{aligned}P_{s,i,j,t}^{P2G,GT} = Dv_{s,i,j,t}P_{s,i,j,t}^{P2G,GT}\ \forall\ i\in N_{p2g},j\in\\N_{gt},s\in n,t\in T\end{aligned} \tag{5}$$

As seen in Constraint (6), the total NGs' power demand ($i\in N_{ng}$) supplied from the gas turbine j via the P2P market at the period *t* must be less than or equal to the energy that gas turbine j is considered to share with NGs ($P_{s,i,j,t}^{GT,NG}$). In other words, gas turbines can not sell energy beyond their generated power at period t. Similar constraints (Inequalities (7) and (8)) are considered for traded power between P2Gs and gas turbines and between NGs and P2Gs.

$$\begin{aligned}\sum_{i}^{N_{ng}}Dv_{s,i,j,t}P_{s,i,j,t}^{GT,NG}\le P_{s,i,j,t}^{GT,NG}\ \forall\ j\in N_{gt},s\in n,t\\\in T\end{aligned} \tag{6}$$

$$\begin{aligned}\sum_{i}^{N_{p2g}}Dv_{s,i,j,t}P_{s,i,j,t}^{GT,P2G}\le P_{s,i,j,t}^{GT,P2G}\ \forall\ j\in N_{gt},s\\\in n,t\in T\end{aligned} \tag{7}$$

$$\begin{aligned}\sum_{i}^{N_{ng}}Dv_{s,i,j,t}P_{s,i,j,t}^{P2G,NG}\le P_{s,i,j,t}^{P2G,NG}\ \forall\ j\in N_{p2g},s\\\in n,t\in T\end{aligned} \tag{8}$$

In the P2P-based optimization problem, we suppose the DSO accesses the whole power distribution grid topology. In this regard, the DSO charges the customers for each energy trading based on the power grid's infrastructure usage. The matched price related to trading energy between customers (i) and (j) is shown in Equation (9). The money paid/received by the purchaser/seller for the power grid usage fee is shown in the second term of Equation (9). The network charges are exogenous costs. In this regard, when the customer (i) is a purchaser, its (φ) is positive, which results in total prices higher than trading prices. When the customer (i) is a seller, its receive price is lower than the traded price since parameter φ is negative.

$$\begin{aligned}S_{s,i,j,t}^{P2P} = \psi_{s,i,j,t}P_{s,i,j,t}^{*,*}\pm\phi_{s,i,j,t}^{dis}P_{s,i,j,t}^{*,*}\quad\forall\ i,j\\\in N_{*},\ \ s\in n,t\in T\end{aligned} \tag{9}$$

The initial term in Equation (9) corresponds to the price determined by the P2P agreement. The subsequent term represents the grid fee paid to the DSO as a grid operation charge [62]. Beyond operational expenses, these incomes can also be allocated for maintenance, compensation for power losses, and investment expenditures. The Unique Cost Allocation Policy is a common approach for charging customers [66]. This policy distributes costs uniformly among community members, ensuring that grid usage fees are applied without discrimination. However, due to its general application, customers in congested areas may not be incentivized to engage in responsible behavior. Consequently, the misconduct of a few customers can negatively impact the entire customer.

In order to allocate costs more precisely, network charges can be proportional to the electric distance between customers. The TID and power transfer distance are two methods for determining the electrical distance between power network buses. The TID is more suitable for radial networks, while the second is more reliable for mesh networks [66]. This study calculates the electrical distance based on the TID, as formerly presented in [66, 67]. The TID between customer (i) and (j) is presented by Equation (10).

$$Z_{i,j} = \left|\mathcal{R}_{i,i} + \mathcal{R}_{j,j} - \mathcal{R}_{i,j} - \mathcal{R}_{j,i}\right| \quad (10)$$

Where the elements of the TID ($\mathbb{R}$) are the components of the impedance matrix (Z_{Bus}), which is the converse of the admittance matrix (Y_{Bus}). As a result of this cost allocation policy, customers will be encouraged to trade with their closest electrical partners. Due to electricity losses, long electric distance trade is more expensive. When network charge is equally shared between both sides of the trade, it becomes [67]:

$$\phi_{i,j}^{dis} = \frac{u^{dis} d_{i,j}}{2} \quad (11)$$

The ($d_{i,j}$) is the sum of the electrical distances between customers (i) and (j). The parameter (u^{dis}), distance unit fee, is presented in ($/per distance unit). As stated before, we considered the TID method to determine the electrical distance between traders. Fig.3 shows a simple radial network to clarify how the DSO considers the electrical distance between customers in the presented P2P-based optimization. The DSO calculates the network charge based on the electric distance ($Z_{i,j}^{th}$) between nodes using Equation (11).

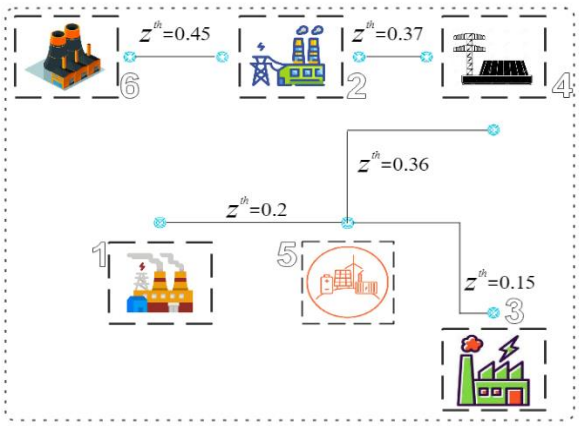

Fig. 3. The sample radial power grid.

The only consumer is placed in node "5" at the simple grid. This customer can trade energy with five producers placed in other nodes with different electric distances. With the assumption that the distance unit fee (u^{dis}) is .01 ($/Km); Table 2 shows the network fee for the illustrative grid in Fig. 3.

TABLE 2 THE SAMPLE RADIAL NETWORK FEE.

node	1	2	3	4	6
$d_{i,j}$	0.2	0.73	0.15	0.36	1.18
$\varphi_{i,j}^{dis}$	$0.001P_{i,j}^{P2P}$	$0.00365P_{i,j}^{P2P}$	$0.00075P_{i,j}^{P2P}$	$0.0018P_{i,j}^{P2P}$	$0.0059P_{i,j}^{P2P}$

As it is clear from Table 2, the network charges gain with increasing the electric distance between purchasers and sellers. So if consumer "5" trades energy with producer "6", its charge is eight times more than trading with producer "3". The market price ($\Psi_{s,i,j,t}$) is bounded by Constraint (12) [46]. This Equation dictates that no consumers are willing to purchase energy above the retail energy price, and no producers are eager to sell energy lower than the FIT rate [46].

$$S^{fit} \le \psi_{s,i,j,t} \le S_t^{rit} \quad \forall\ i,j \in N_*\ s \in n,t \in T \quad (12)$$

We have considered the DR capability in the P2P-based optimization problem to increase customers' profit. In this paper, the load flexibility model is based on [65]. Constraint (13) states that in the period (t) the demand of the NG (i) can be increased by a factor of ($f_{i,t}^{flex,MAX}$). Also, in the following Equations ($P_{s,i,t}^{dem}$) is the NGs predicted load, which is a parameter.

$$P_{s,i,t}^{Dem,DR} \le P_{s,i,t}^{dem} f_{i,t}^{flex,MAX} \quad \forall\ i \in N_{ng}, s \in n, t \in T \quad (13)$$

Similarly, inequality (14) indicates that in the period t, the electrical demand of NGs can be decreased by a factor ($f_{i,t}^{flex,min}$). Equation (15) guarantees that the total energy demand of the NGs (i) does not change after DR. The values

of ($f_{i,t}^{flex,MAX}$) and ($f_{i,t}^{flex,min}$) are determined by the NGs' operator [65].

$$P_{s,i,t}^{Dem,DR} \geq P_{s,i,t}^{dem} f_{i,t}^{flex,MIN} \quad \forall\ i \in N_{ng}, s \in n, t \in T \tag{14}$$

$$\sum_{t}^{T} P_{s,i,t}^{Dem,DR} = \sum_{t}^{T} P_{s,i,t}^{dem} \quad \forall\ i \in N_{ng}, s \in n \tag{15}$$

It is worth noting that we consider the electrical loads with flexible characteristics through simple Equations (13)-(15). Also, in an emergency, the DSO can curtail part of the demand by paying its cost, which is considered in the objective function. Each NG's power balance equation can be found in Equation (16) [4]. The energy demand in NG (i) shall be equal to the imported energy supplied by the power grid, P2G units, and gas turbines represented in Equation (2). The power demand in the NG is divided into two main sections: the power consumed inside NGs ($P_{s,i,t}^{Dem,DR}$) and served to charge the NG's ESS ($P_{s,i,t}^{ch}$).

$$P_{s,i,t}^{Dem,NG} + \left(\eta_{dch} P_{s,i,t}^{dch,n}\right) + P_{s,i,t}^{cur} - \left(\frac{1}{\eta_{ch}} P_{s,i,t}^{ch}\right) - P_{s,i,t}^{Dem,DR} \quad \forall i \in N_{ng}, s \in n, t \in T \tag{16}$$

The mathematical formulas of the NG's ESS are presented in Equations (17)-(18) and Constraint (19) [4]. As it is clear from Equation (17), the stored energy in the ESS can be discharged in the NG ($P_{s,i,t}^{dec,n}$) or sold to the power grid ($P_{s,i,t}^{dec,m}$). As stated before, it is assumed that the energy stored in the ESS can be sold to a power utility or consumed inside the NG.

$$P_{s,i,t}^{Tot,dch} = P_{s,i,t}^{dch,n} + P_{s,i,t}^{dch,m} \quad \forall i \in N_{ng}, s \in n, t \in T \tag{17}$$

Equation (18) calculates each ESS's state of charge (SOC). In order to increase the life span of batteries, their SOC level must remain at a predetermined level, as presented in Constraint (19) [10]. Equation (20) indicates that ESSs are not charged and discharged simultaneously and illustrates charging/discharging limitation [10].

$$SOC_{s,i,t}^{batt} = SOC_{s,i}(0) + \sum_{t=1}^{T} \left(P_{s,i,t}^{ch} - P_{s,i,t}^{Tot,dch}\right) \quad \forall i \in N_{ng}, s \in n \tag{18}$$

$$SOC_{s,i}^{min} \leq SOC_{s,i,t}^{batt} \leq SOC_{s,i}^{max} \ \forall i \in N_{ng}, s \in n, t \in T \tag{19}$$

$$P_{s,i,t}^{ch} \times P_{s,i,t}^{Tot,dch} = 0 \quad \forall\ i \in N_{ng}, s \in n, t \in T$$
$$P_{s,i,t}^{ch} \& P_{s,i,t}^{Tot,dch} \leq P_{ESS}^{max} \quad \forall\ i \in N_{ng}, s \in n, t \in T \tag{20}$$

This paper considers the steady-state natural gas flow model on the day-ahead scheduling time scale. In other words, we assumed that the response time of the natural gas network equals the power grid. According to [68, 69], we can formulate the natural gas network as follows: Injected gas into each grid node is formulated by Equation (21). Gas turbines and NGs are the consumers of the injected natural gas into each node [4, 10].

$$G_{s,i,t}^{grid} = g_{s,i,t}^{gt} + g_{s,i,t}^{load} \quad \forall i \in N_g, s \in n, t \in T \tag{21}$$

As it is clear from Equation (22), the gas turbine's power generation ($P_{s,i,t}^{Gen,gt}$) is sold in the P2P market ($P_{s,i,t}^{GT,NG}$) and ($P_{s,i,t}^{GT,P2G}$) or purchased by the power utility ($P_{s,i,t}^{Gen,N}$).

$$P_{s,i,t}^{Gen,gt} = P_{s,i,t}^{Gen,N} + P_{s,i,t}^{GT,NG} + P_{s,i,t}^{GT,P2G} \ \forall i \in N_{gt}, s \in n, t \in T \tag{22}$$

The performance of thermal plants based on natural gas, coal, and oil fuels is simulated well through quadratic and cubic cost functions [70]. The gas-fired generator natural gas demand is formulated by the quadratic cost function shown in Equation (23) [71]. The fuel cost function coefficients are shown by parameters (a), (b), and (c). The efficiency and construction year of gas turbines determine these coefficients.

$$g_{s,i,t}^{gt} = \alpha_i P_{s,i,t}^{Gen,gt^2} + \beta_i P_{s,i,t}^{Gen,gt} + c_i \forall i \in N_{gt}, s \in n, t \in T \tag{23}$$

The nodal gas flow balance is calculated using Equation (24), which illustrates that injected natural gas equals withdrawn gas. The sum of natural gas injected on gas nodes passes through pipelines. Also, the gas flow is unilateral from the beginning of the gas grid [4].

$$G_{s,i,j,t}^{line} - \sum_{j}^{N_g} G_{s,j,t}^{grid} = 0 \ \forall i, j \in N_g, s \in n, t \in T \ and\ i < j$$
$$G_{s,i,j,t}^{line} + G_{s,j,i,t}^{line} = 0 \tag{24}$$

Since the proposed natural gas grid's diameter is relatively large, we employed the Weymouth function, shown in Equation (25) [29]. This function shows the relationship between node gas pressure and gas flow in the natural gas pipeline. The TEMP represents the average temperature coefficient of a gas flow, which is considered constant. For more information about the parameter of the Weymouth function, refer to the [29].

$$G_{s,i,j,t}^{line} = \frac{1}{4} \frac{\left|Pr_{s,i,t}^{2}(1 - c\Delta h) - Pr_{s,j,t}^{2}\right| D_{i,j,t} S_{i,t}}{\left(1 - \frac{c\Delta h}{2}\right) \lambda ZRL_{i,j} Temp} \ \forall i, j \in N_g, s \in n, t \in T \tag{25}$$

Natural gas grid node pressure must remain within predetermined ranges to ensure gas supply security, and pressure drops compromise this security. Hence, the natural gas grid node pressure is limited by Constraint (26). The power demand of the gas compressor, which depends on the gas flow rate, is illustrated by Equation (27) [4]. The natural gas rate and power demand constraints of gas compressors are presented consecutively by inequalities (28)-(29) [4].

$$Pr^{min} \leq Pr_{s,i,t} \leq Pr^{max} \ \forall i \in N_g, s \in n, t \in T \tag{26}$$

$$P_{s,i,t}^{comp} = \frac{\beta_{comp} G_{s,i,t}^{comp}}{\eta_{comp}} \left[\left(\frac{Pr_{s,i,t}^{out}}{Pr_{s,i,t}^{in}}\right)^{\frac{1}{\beta_{comp}}} - 1\right] \forall i \in N_{gc}, s \in n, t \in T \tag{27}$$

$$G_{s,i,t}^{comp} \leq G^{comp,max} \ \forall\ i \in N_{gc}, s \in n, t \in T \tag{28}$$

$$P_{s,i,t}^{comp} \leq P^{comp,max} \ \forall\ i \in N_{gc}, s \in n, t \in T \tag{29}$$

Electricity is converted into gaseous fuel through P2G technology. The electrolysis process transforms electricity into hydrogen and oxygen. The generation of hydrogen through the

electrolysis process is demonstrated by Equation (30) [72]. Additionally, Equation (31) details the process of discharging P2G units. The total quantity of hydrogen within the container, measured in kilograms, is determined by Equation (32) [72].

$$E_{s,i,t}^{ch,p2g} = P_{s,i,t}^{p2g,ch} \times \mathbb{C}\!\!\!\!\mathbb{f}_{ch}^{p2g} \forall\, i \in N_{p2g}, s \in n, t \in T \quad (30)$$

$$E_{s,i,t}^{dch,p2g} = P_{s,i,t}^{p2g,dch} \times \mathbb{C}\!\!\!\!\mathbb{f}_{dch}^{p2g} \forall\, i \in N_{p2g}, s \in n, t \in T \quad (31)$$

$$E_{s,i,t}^{tot,p2g} = E_{s,i,t}^{init,p2g} + E_{s,i,t}^{ch,p2g} - E_{s,i,t}^{dch,p2g} \;\forall\, i \in N_{p2g}, s \in n, t \in T \quad (32)$$

Equation (33) indicates that the P2P market and the power grid supply the required power for charging P2Gs. Also, Equation (34) represents that the stored energy in the hydrogen containers can be bought by NGs through the local energy market or the power grid. P2Gs are not allowed to be charged and discharged simultaneously, as represented by Equation (35) [72]. Equation (36) bounds the charging and discharging power of P2Gs [72].

$$\frac{1}{\eta_{p2g}^{ch}} P_{s,i,t}^{p2g,ch} = \sum_{j}^{N_{gt}} P_{s,i,j,t}^{P2G,GT} + P_{s,i,t}^{P2G,N} \;\forall\, i \in N_{p2g}, s \in n, t \in T \quad (33)$$

$$\eta_{p2g}^{dch} P_{s,i,t}^{p2g,dch} = \sum_{j}^{N_{ng}} P_{s,i,j,t}^{P2G,NG} + P_{s,i,t}^{N,P2G} \forall\, i \in N_{p2g}, s \in n, t \in T \quad (34)$$

$$P_{s,i,t}^{p2g,ch} \times P_{s,i,t}^{p2g,dch} = 0 \;\; \forall\, i \in N_{p2g}, s \in n, t \in T \quad (35)$$

$$P_{s,i,t}^{p2g,ch} \& P_{s,i,t}^{p2g,dch} \le P_{p2g}^{max} \quad (36)$$

Equations (37)-(43) illustrate the constraints of the power grid with multiple gas turbines and NGs. Each NG's power demand and gas turbine's generated power regulation affect power flow and the power grid node's voltage [73]. Equations (37) and (38) represent the power flow balance equations for active and reactive powers in the power distribution grid [74].

$$\begin{aligned} P_{s,i,t}^{Dem,MG} + P_{s,i,t}^{Gen,gt} + P_{s,i,t}^{dec,n} + P_{s,i,t}^{cur} & - P_{s,i,t}^{dem,DR} + P_{s,i,t}^{p2g,dch} - P_{s,i,t}^{p2g,ch} \\ & - P_{s,i,t}^{comp} \\ & = e_{s,i,t} \sum_{j}^{N_e} \left(G_{i,j} e_{s,j,t} - B_{i,j} f_{s,j,t}\right) \\ & + f_{s,i,t} \sum_{j}^{N_e} \left(G_{i,j} e_{s,j,t} + B_{i,j} f_{s,j,t}\right) \;\; \forall i \\ & \in N_e, s \in n, t \in T \end{aligned} \quad (37)$$

$$\begin{aligned} q_{s,i,t}^{Dem,MG} + q_{s,i,t}^{Gen,gt} + q_{s,i,t}^{dec,n} + q_{s,i,t}^{cur} & - q_{s,i,t}^{dem,DR} + q_{s,i,t}^{p2g,dch} - q_{s,.i,t}^{p2g,ch} \\ & - q_{s,i,t}^{comp} \\ & = f_{s,i,t} \sum_{j}^{N_e} \left(G_{i,j} e_{s,j,t} - B_{i,j} f_{s,j,t}\right) \\ & - e_{s,i,t} \sum_{j}^{N_e} \left(G_{i,j} e_{s,j,t} + B_{i,j} f_{s,j,t}\right) \;\; \forall i \\ & \in N_e, s \in n, t \in T \end{aligned} \quad (38)$$

As shown in Equations (37) and (38), the power injections at the nodes are quadratic functions of the nodes' voltages' rectangular coordination [75]. The ramp rate of tie-line power measures how quickly a power system can adjust its power output in response to changes in demand, which is the essential metric for ensuring the stability of a power system [74]. Constraint (39) formulates the tie line power ramp rate based on (MW/h) [74].

$$\left|P_{s,i,t}^{Dem,N} - P_{s,i,t-1}^{Dem,N}\right| \le P_i^{grid,ramp} \forall i \in N_e, s \in n, t \in T \quad (39)$$

In order to ensure that the voltage magnitude at each node in the power system remains within an acceptable range, Constraint (40) is employed, which is essential to guarantee reliable power system operation and avoid costly equipment damage [74].

$$\left(V_i^{min}\right)^2 \le e_{s,i,t}^2 + f_{s,i,t}^2 \le (V_i^{max})^2 \forall i \in N_e, s \in n, t \in T \quad (40)$$

Apparent power constraint refers to the limitations of a power system caused by factors such as insufficient capacity, network congestion, or high demand. It can create problems such as power outages, reliability issues, and higher costs. Constraint (41) represents apparent power constraints related to each node [74].

$$\left(P_{s,i,t}^{Dem,N}\right)^2 + \left(Q_{s,i,t}^{Dem,N}\right)^2 \le \left(S_{s,i,t}^{Dem,N}\right)^2 \forall i \in N_e, s \in n, t \in T \quad (41)$$

Constraints (42) and (43) demonstrate the gas turbine's output and ramping rate constraints; these constraints are essential for maintaining the gas turbine's efficiency and avoiding damage to the machinery [74].

$$P_i^{Min,gt} \le P_{s,i,t}^{Gen,gt} \le P_i^{Max,gt} \;\forall i \in N_{gt}, s \in n, t \in T \quad (42)$$

$$\left|P_{s,i,t}^{Gen,gt} - P_{s,i,t-1}^{Gen,gt}\right| \le P_i^{gt,ramp} \;\; \forall i \in N_{gt}, s \in n, t \in T \quad (43)$$

IV. Simiulation and results

A. Assumption

A modified 33-bus natural gas grid and the IEEE 33-node power distribution network are employed to evaluate the presented framework [4]. Characteristics of the natural gas network are chosen from [76]. The number of the electricity network and gas grid nodes is equal [4, 10]. Also, it is assumed that node 0 is the slack bus in the electricity distribution network. The studied microgrid has three types of customers: NGs, P2Gs, and gas-fired generators [4]. In the examined network, it is supposed that all nodes of the natural gas grid have the same altitude. Also, the natural gas grid beside the gas turbines supplies the fixed gas loads in the NGs. The required data for simulation is presented in Table 3.

Fig. 5 represents the time of use of the electricity tariff. The predicted electricity and natural gas demands are borrowed from [4, 77]. The power and natural gas loads are aggregated demands randomly shared between NGs. The calorific value of natural gas is employed to convert gas loads to (MW). Also, it is assumed that each NG is equipped with an ESS.

TABLE 3 REQUIRED PARAMETERS FOR SIMULATION.

Parameter	Value	Parameter	Value
u^{dis}	0.1 ($/km)	SOC_i^{max}, SOC_i^{min}	90%, 20%
Pr^{max}, Pr^{min}	90-30 (psi)	S^{gas}	0.06014 ($/m^3)
S^{fit}, S^{cur}	0.14, 3.5 ($/km)	$P_i^{Min,gt}, P_i^{Max,gt}$	1000-2000 (kW)
$batt^{cap}$	300-1000 (kWh)	$p2g^{cap}$	200 (kg)
$\mathbb{C}f_{ch}^{p2g}, \mathbb{C}f_{dch}^{p2g}$	1/40 (kW/kg)	$P_{p2g}^{max}, P_{ESS}^{max}$	1210,600 (kW)
$\eta_{p2g}^{ch}, \eta_{p2g}^{dch}$	0.85	η_{ch}, η_{dch}	0.9
$\mathbb{f}_{i,t}^{flex,MAX}, \mathbb{f}_{i,t}^{flex,MIN}$	130%,70%	$\beta_{comp}, \eta_{comp}$	4.7,0.85%
α, b, c	2.148, 2.212, 0.1085	$P_i^{gt,ramp}, P_i^{grid,ramp}$	200,250 (kW)
$\lambda, Z, TEMP, R$	0, 33, 288 (K), 8.314 J/(mol·K)	$\Delta h, \cos(\theta)$	0,0.866 (lag)

Also, the power distribution grid parameters, NGs' ESS specifications, gas turbines' data, and the natural gas grid parameters can be found in [21]. The power grid will supply the remaining demand, which is not matched in the P2P market. As stated before, the scheduling stage, Equations (1)-(43), is performed one day earlier than the executed day. The studied grid's architecture is presented in Fig. 4. The studied microgrid has fifteen NGs, fourteen gas turbines, four P2G units, and one gas compressor located at the beginning of the natural gas network. Also, in the illustrated studied microgrid architecture, LDs refer to NGs. Fig. 5 represents the time of use of the electricity tariff. The predicted electricity and natural gas demands are borrowed from [4, 77].

B. Computational performance

The presented optimization problem is implemented in the Generalized Algebraic Modeling System (GAMS) environment on a computer with a Core i5 system, a 2.50 GHz CPU, and 12 GB of RAM. Due to the nature of the presented optimization problem, which is nonlinear and nonconvex, we solved the presented problem with the global optimizer ANTIGONE solver [78]. The complexity of such problems requires a sophisticated approach, as traditional solvers often fall short of providing feasible and optimal solutions. ANTIGONE's robust framework addresses these challenges by employing advanced algorithms that can efficiently navigate the intricate landscape of nonlinearity and nonconvexity [78]. This solver uses techniques such as branch-and-bound, cutting planes, and outer approximation, which are essential for finding global optima in highly complex optimization scenarios. ANTIGONE uses the CPLEX for solving relaxations, the CONOPT for Finding feasible points, and the LAPACK for Addressing linear systems [78].

TABLE 4 SOLVERS PERFORMANCE.

Modeling	ANTIGONE	DICOPT
Solving Time (min)	15	13
Number of iteration	-	4
Solution gap (%)	17.27%	21.98%

$Gap = 100.\left(\frac{UpperBound - LowerBound}{|LowerBound|}\right)$

To validate the results of the ANTIGONE, we used the DICOPT solver, which decomposes the MINLP problem into sub-problems (NLP) and master problems (MIP). The proposed optimization problem has 99849 variables and 74544 constraints, with 172424 Jacobian elements, of which 26088 are nonlinear.

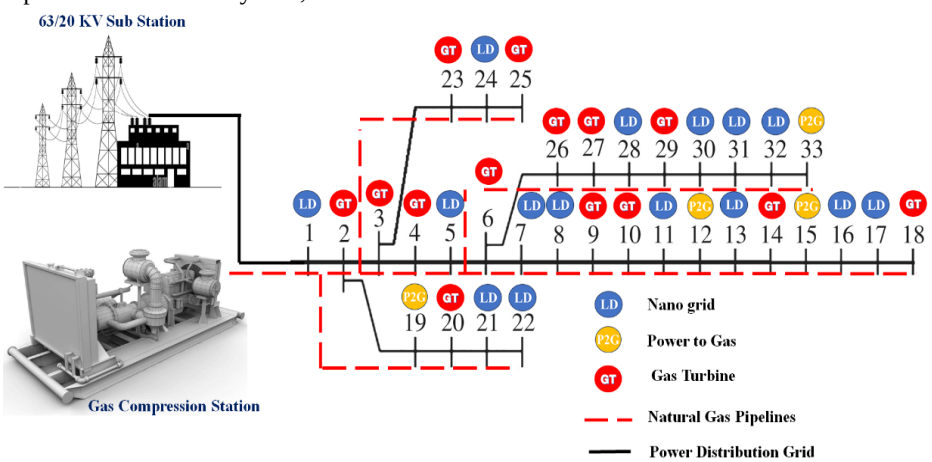

Fig. 4. The studied network architecture.

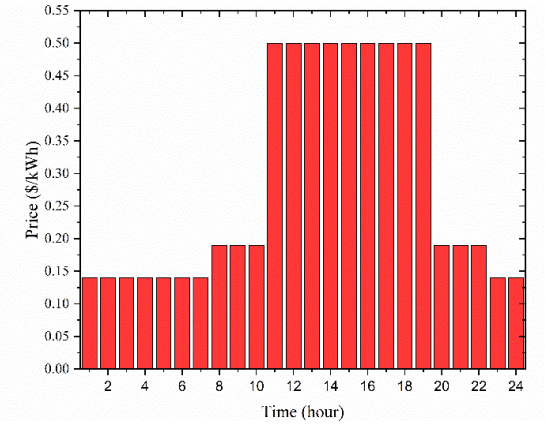

Fig. 5. The electricity tariff.

To assess the performance of the proposed method, we divide the simulations into two sections. Initially, we evaluate the simulation for a single trading period. Subsequently, we extend the simulation to 24 trading periods. Before illustrating the results of the proposed case study, we present a concise description of the method used as a benchmark framework. The proposed method is compared with one common mechanism in the P2P energy trading market, performed in two stages. The technique used as a benchmark framework is the CDA mechanism, comprehensively described in [54], and its implementation procedure is described in Appendix (A.1). Considering that the presented optimization model is based on the scenario-based stochastic optimization problem, a description related to creating scenarios and reducing scenarios is given in Appendix (A.2).

It is worth noting that the benchmark method does not consider the electric distance between purchasers and sellers in the matching process. As a result, the cheapest seller will be sorted first in purchasers' priority lists, while the highest buyer will be sorted first among sellers' preference lists. In the P2P energy trading model based on the CDA framework, through the optimization problem, stage one, the energy schedules of customers are determined. The energy schedules of customers contained the NGs' energy demand pattern and the generated electricity schedules of gas-fired generators. In the following, these schedules are returned to subscribers, and through the CDA method, subscribers trade energy and reach the P2P energy trading agreements.

C. case study (one-period optimization)

In the first case study, we compare the proposed framework with the CDA method for the integrated operation of electricity and natural gas grids at 11 AM. The architecture of the proposed network and the placement of the customers in the low-voltage network are presented in Fig. 4. It is worth noting that both methods use the same input data, which is presented in the previous subsection. In this case, we run the proposed optimization problem, Equations (1)-(43), for one period. The procedure for implementing the CDA framework, the benchmark method, for the integrated operation of gas and power grids is thoroughly described in [4, 54] and Appendix (A1).

Figs. 6 and 7 show traded energy flows during 11 AM between customers without the P2P market and with the CDA-based P2P market, respectively. Without the P2P market, customers trade energy with the power grid. The power grid purchases and sells energy from and to the customers based on the energy retail price, which is not competitive compared to the P2P market price.

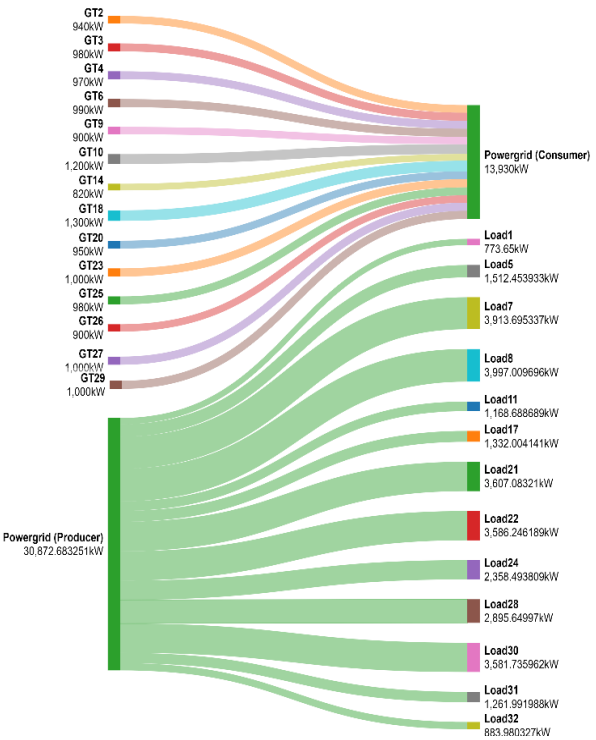

Fig. 6. Energy transactions between customers and the power grid without the P2P market.

As stated, we compare the proposed framework with the previous P2P market-based model as a benchmark method, performed in separate stages. The energy traded flow between customers in the benchmark method is shown in Fig. 7. The power grid balances the energy shortage via retail price (the TOU tariff and the FIT rate). Without the P2P market (Fig. 6) and the CDA-based P2P energy market (Fig. 7), P2Gs do not participate in the energy trading process. Without the P2P market, due to P2G units' conversion efficiency on both sides (charge and discharge), it is not cost-effective for P2Gs to be charged through the power grid via the TOU tariff and discharged to the grid via the FIT rate. Additionally, considering that the previous P2P market model (CDA-based) is executed in two distinct stages (scheduling and trading), a MINLP optimization problem based on the energy retail price is solved during the scheduling stage, similar to the case without the P2P market. Customers engage in energy trading in the subsequent trading stage, which is determined in the

scheduling stage. In this context, similar to the scenario without a P2P market, P2Gs do not participate in energy trading.

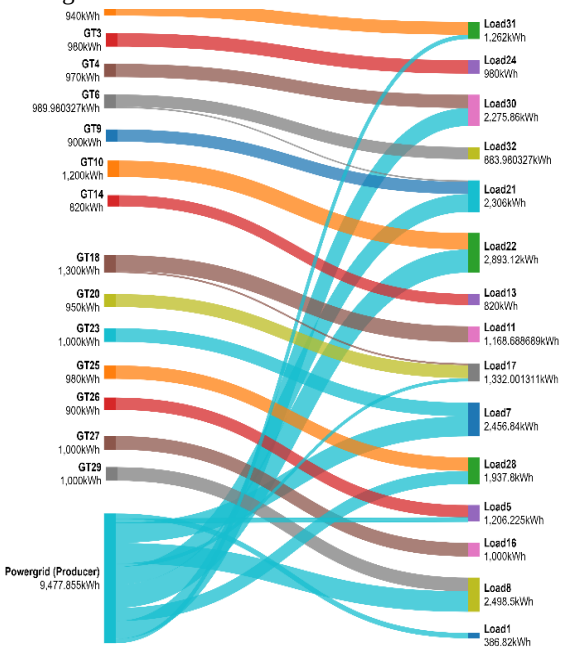

Fig. 7. The flow of the traded energy (the benchmark method).

Figs. 8 and 9 illustrate the proposed method's traded energy flow between customers (NGs, gas-fired units, P2Gs, and the power grid) for different scenarios. There are two significant differences between the proposed method (Figs. 8 and 9) and the previous framework (Fig. 7). First, NGs trade energy with the closest producers in the presented method due to employing the electrical distance model based on the TID framework. Implementing the TID model leads to a situation in which far-off trades impose higher customer costs (reducing gas turbines and P2Gs' revenue and increasing payment costs of NGs). Second, since the proposed method is executed in one stage, the energy consumption and production schedules are determined based on the market competitive price, which leads to the participation of P2Gs in the P2P market.

The right-hand sides of Figs. 8 and 9 represent the energy trading flow in scenarios two and four consecutively. Also, the left-hand side of Figs 8 and 9 illustrate the transacted energy flow in scenarios one and three, respectively. Due to the higher predicted power demand shown in Fig. a3, the volume of traded energy in scenario four is the highest, followed by scenarios two, three, and one. It is worth noting that scenario one has the highest predicted demand for natural gas (Fig. (a4)), which is one reason for reducing traded energy in scenario one. In other words, the DSO limits gas turbines' generated power due to high natural gas demand at period 11 of scenario one to keep node gas pressure in the desired range.

P2Gs are charged during off-peak periods (1-7) through different markets, and due to higher energy prices, they are willing to trade the stored energy during peak hours (11-19). P2Gs supply NGs' power demand through correlation with gas turbines. In other words, when gas turbines can not meet the energy demand of NGs, NGs trade energy with P2Gs. In this regard, P2Gs trade energy with NGs during hour 11 since gas turbines' generated power is reduced due to high natural gas demand in scenario one (Fig (a4))).

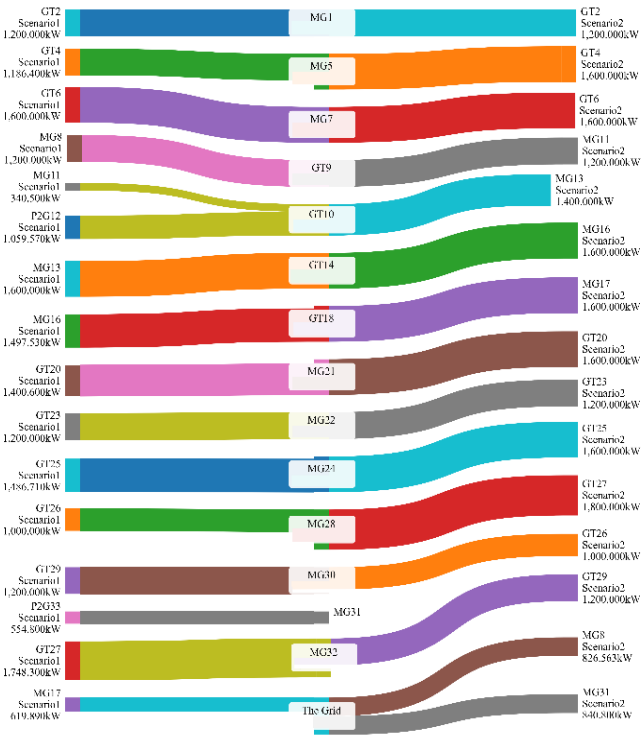

Fig. 8. The flow of the traded energy in scenarios one and two (the proposed method).

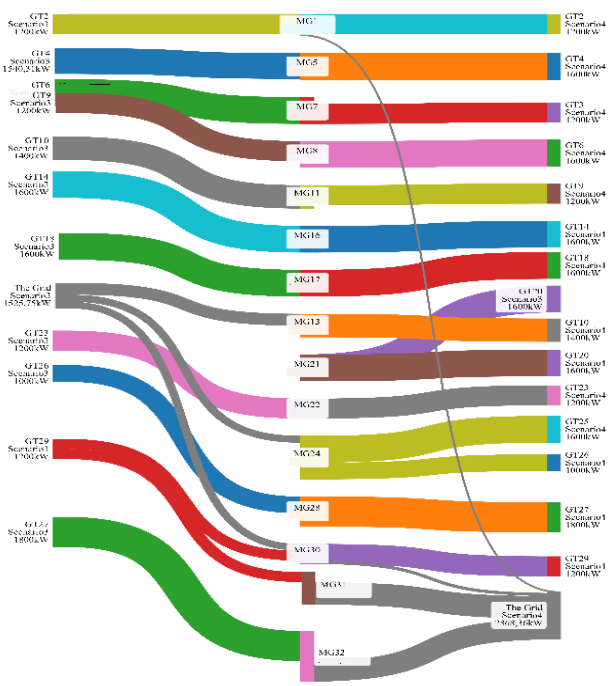

Fig. 9. The flow of the traded energy in scenarios three and four (the proposed method).

Also, due to the high electricity demand in scenario four, the traded energy between the power grid and NGs in scenario four is about 13% of the energy demand of NGs at hour 11, which is the highest among scenarios. Also, it is worth noting that the volume of traded energy in the proposed method is increased by about 40.21% compared to the benchmark method.

Power losses occur during electricity transmission from one bus to another, particularly in P2P energy trading, where electricity is transferred from producers to NGs. As electricity flows through power lines and transformers, some energy is lost due to resistance in the wires and transformers. This phenomenon can result in reduced yields for participants in P2P energy trading. In this context, we evaluate the impact of incorporating the TID model into the proposed method by comparing it with the benchmark framework. Each line's power loss is calculated by dividing energy loss by the line flow. The active power loss in the proposed method and benchmark framework is 26.73% and 47.97358%, consecutively. The power loss reduction in the presented method is mainly due to employing the TID framework in the P2P energy trading process.

The operational cost of the entire network is calculated as the total payment costs of NGs, including the traded energy with gas turbines, P2G units, and power utility, minus the total revenue generated by gas turbines and P2G units from selling power to the grid and NGs. The operating cost of the entire network (hour 11) in the proposed method and benchmark framework is 750.86 ($) and 4738.5 ($), respectively.

D. 24-hour optimization

This section evaluates the performance of the presented method for the entire period of the next day. First, the energy purchased and supplied by the studied network's customers (NGs, gas turbines, and P2Gs) is analyzed. Figs. 10 to 13 illustrate the electricity demand of NGs provided by the power grid and the local market's producers for scenarios one to four consecutively. In the following Figs (10-13), the orange, green, and purple curves are supplied electricity by the power grid and purchased energy from gas-fired generators and P2G units, respectively. As energy traded between P2Gs and NGs clearly shows, P2Gs trade energy mainly after hour 12 due to high natural gas demand (Fig. (a4)). In other words, P2Gs complement gas-fired generators in supplying NGs' energy demand during peak hours.

The upstream grid-supplied NGs power demand during the off-peak period (hours 1-7). With the increase of the energy tariff starting from the mid-peak period (hours 8 to 11), the electricity imported from the power grid decreases. Due to the high energy tariffs, the proportion of energy imported from the power grid during peak periods is minimal, accounting for 20.11%, 11%, 20%, and 20% in scenarios one through four, respectively. After peak periods (hour 20), the amount of imported electricity from the power grid gradually increases.

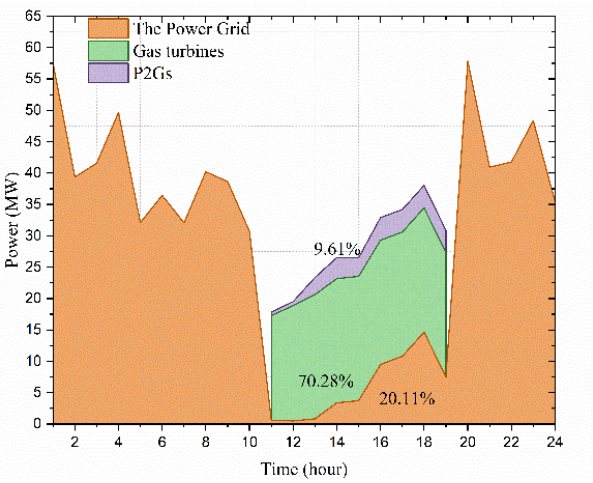

Fig. 10. NGs traded energy in scenario one.

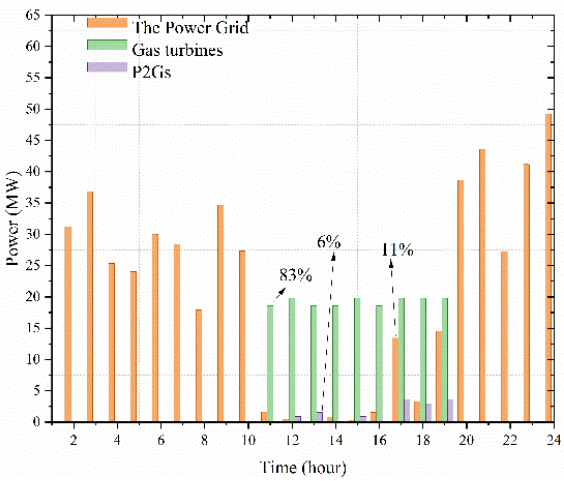

Fig. 11. NGs traded energy in scenario two.

The operational cost of gas-fired generators depends on the gas compressor's electricity demand and gas turbines' natural gas demand. Hence, since the power grid supplies the gas compressor through the electricity tariff, selling power to the grid is cost-effective for gas-fired generators only during off-peak periods. Also, since the P2P market price is cleared between a range in which the TOU and the FIT rates are its upper and lower bounds, respectively (constraint (12)), there is no significant difference between the TOU rate and the P2P market price during off-peak hours. On the other hand, since P2Gs can store energy, they purchase energy from gas-fired generators during off-peak periods and trade the stored energy with NGs during peak hours. Briefly, in off-peak hours, gas turbines trade energy with the power grid and P2Gs, and during peak hours, NGs trade energy with P2Gs, gas turbines, and the power grid. Also, during peak periods, about (70% to 80%), (10% to 20%), and (5% to 10%) of the NGs' power demand is supplied by gas turbines, the power grid, and P2Gs, consecutively.

Due to high electricity prices in mid-peak and peak periods, gas-fired generators trade energy in the P2P market during

these hours. P2Gs are charged during off-peak and mid-peak periods and sell their stored energy to NGs during peak periods. The power grid balances the shortage of energy production. Also, the total operating cost of both networks for the proposed method and the benchmark framework is 115343.2 ($) and 218779.44 ($), respectively. The total operation cost of the entire network in the proposed method is reduced by 47% compared to the benchmark method. The participation of the P2Gs and the increasing generated power of gas-fired generators are the reasons for the significant reduction of the operation cost compared to the previous method.

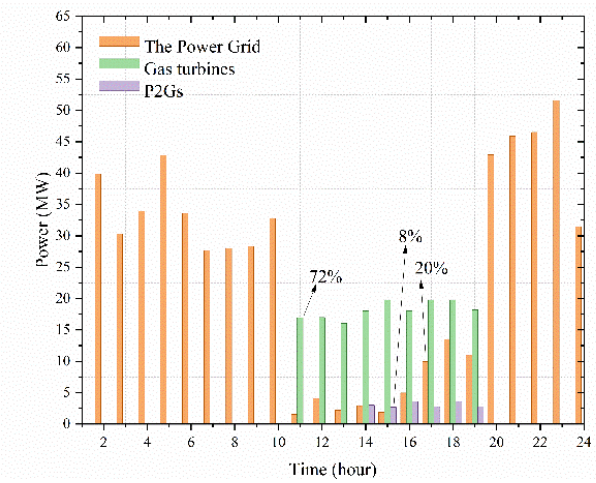

Fig. 12. NGs traded energy in scenario three.

The charging/discharging cycles and the stored hydrogen of the total P2G units are illustrated in Figs. 14-15, consecutively. During periods 1 to 10, P2Gs are charged by the gas turbines through the P2P market (upper side of Fig. 14). By 11 AM, hydrogen containers are charged to approximately 80% of their capacity. With the initiation of the peak periods, the P2Gs trade energy with NGs through the P2P market. The purchased and sold energy costs in the P2P market are 3025.8 ($) and 6916.1 ($), respectively. In this regard, the total P2G revenue from participation in the P2P market is 3891.32 ($/day). The charging energy of P2Gs' is highest in scenario one since during peak hours (periods 11 to 19), the predicted electricity demand of scenario one is highest. In other words, since NGs are only customers for P2G units, their higher energy demand causes P2Gs to be willing to increase their stored energy to trade with NGs during peak hours.

Figs. 16 to 19 represent gas turbines' traded energy in scenarios one to four, respectively. Also, gas compressor power demand is shown in Fig. 20. Gas turbines trade energy with the power grid and P2Gs during off-peak periods. Due to the low electricity tariff during these periods (off-peak), NGs' are not interested in trading energy in the P2P market. Since the gas compressor purchases its required energy from the power grid through the energy retail price, the volume of gas turbines traded energy with the power grid considerably decreases after off-peak periods.

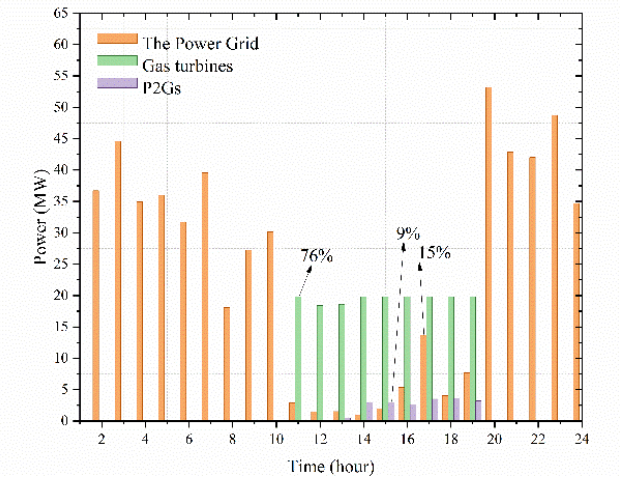

Fig. 13. NGs traded energy in scenario four.

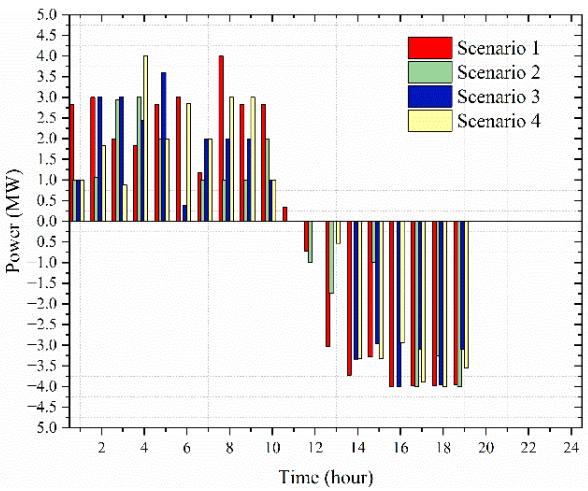

Fig. 14. P2Gs charge and discharge.

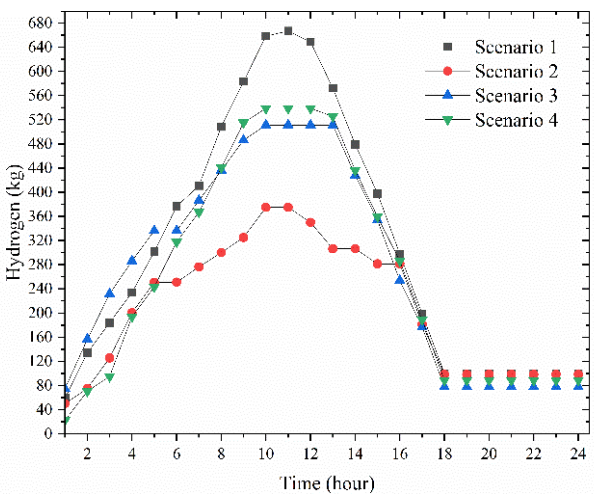

Fig. 15. The stored hydrogen in the containers.

Gas turbines' energy trading with P2Gs continues even in mid-peak periods (hours 8-10). Since P2Gs will sell the stored energy during peak periods, purchasing electricity during mid-

peak periods is cost-effective. Gas-fired generators trade energy with NGs during peak periods. In other words, selling energy via the P2P market at competitive prices makes energy production for gas turbines during peak periods affordable. The cost of supplying natural gas and gas compressor electricity demand are 12993.4 and 4981.3 ($), respectively.

The income of the total gas turbines from selling energy to the power grid (through the FIT rate), P2Gs (P2P market), and NGs (P2P market) are 26829.3, 2733.582, and 42526.41 ($), consecutively. The total revenue of gas-fired generators in the proposed framework and the benchmark method are 59075.71 and 55200.45 ($). Hence, the total revenue of gas-fired generators in the proposed framework is increased by about 7%.

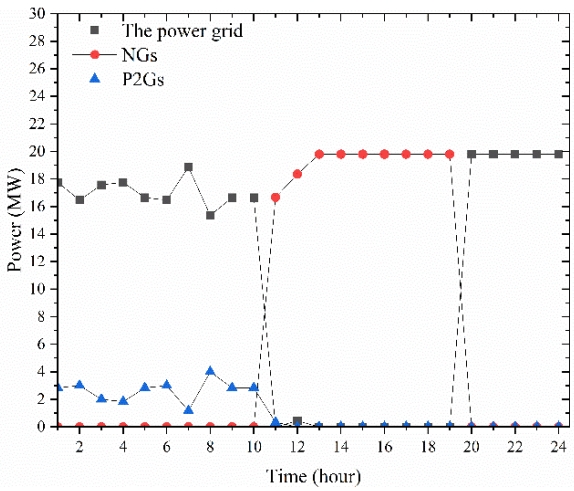

Fig. 16. Gas-fired generators traded energy in scenario one.

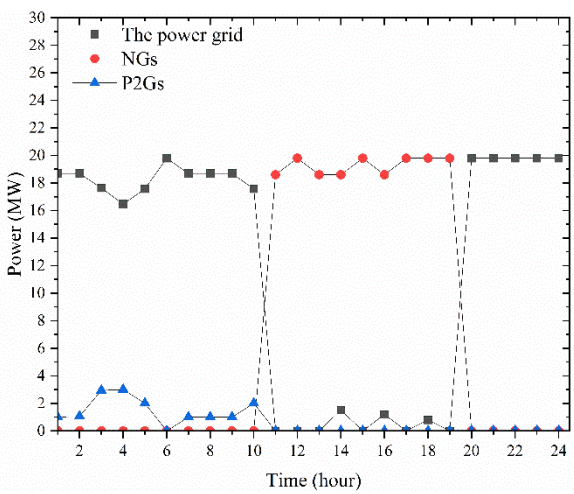

Fig. 17. Gas-fired generators traded energy in scenario two.

Also, as it is clear from Fig. 20, the power demand of the gas compressor is dependent on predicted natural gas demand for different scenarios (Fig. (a4)). Figs. 21 and 22 illustrate the total charging and discharging cycles and the state of charge of entire ESSs for different scenarios. Each NG is equipped with an ESS, which is charged during off-peak periods or hours when NGs trade energy with gas turbines via the P2P market. In order to maximize the usage of gas-fired generators during peak periods, ESSs are charged. Notably, ESS's charging power is supplied by NGs purchased energy. In other words, NGs store a part of the traded energy with the power grid during off-peak periods in ESSs and use it during high energy price periods. Also, Fig. 23 represents the average node gas pressure for different natural gas nodes. As it is clear, during the synergy between natural gas and electricity grids, the presented method guarantees the performance of the natural gas network. Gas pressure reduction alongside nodes (1 to 18) is higher in scenario four, followed by scenarios one, two, and three. The difference between scenarios is caused by differences in predicted natural gas demand for different scenarios, shown in Fig. (a4).

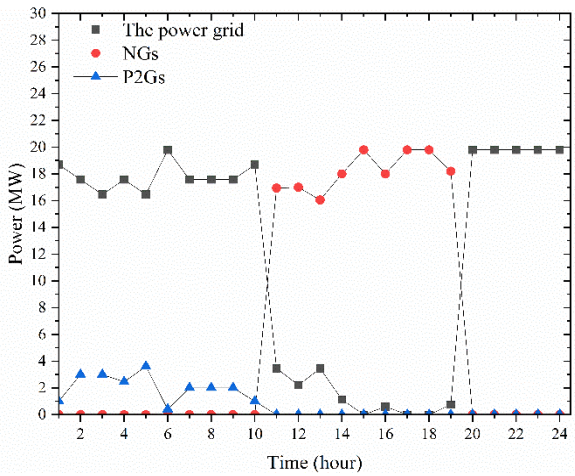

Fig. 18. Gas-fired generators traded energy in scenario three.

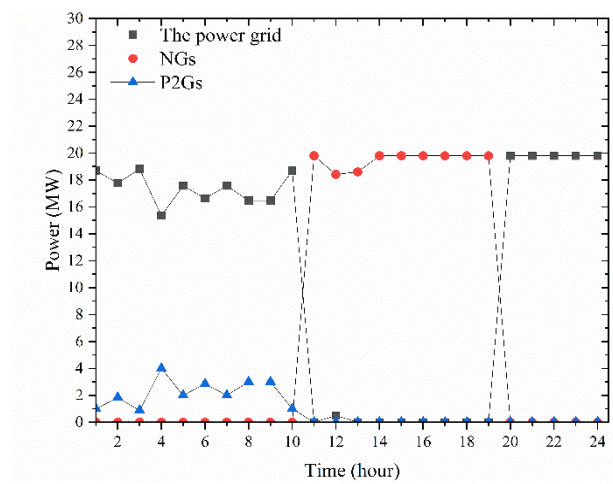

Fig. 19. Gas-fired generators traded energy in scenario four.

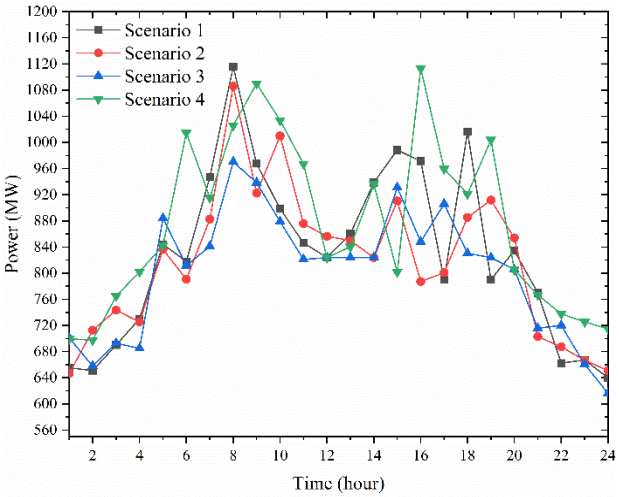

Fig. 20. Gas compressor power demand.

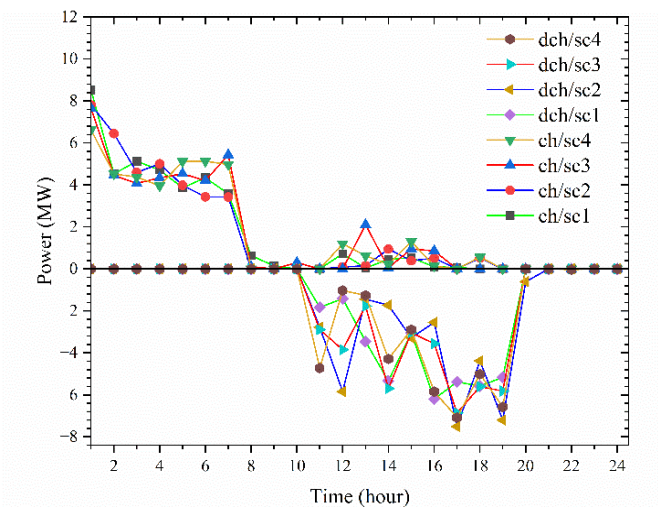

Fig. 21. Total ESSs charging and discharging cycles.

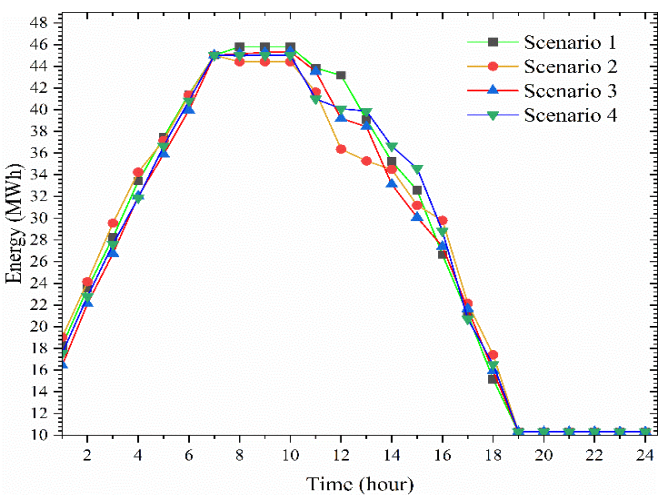

Fig. 22. The state of charge of entire ESSs.

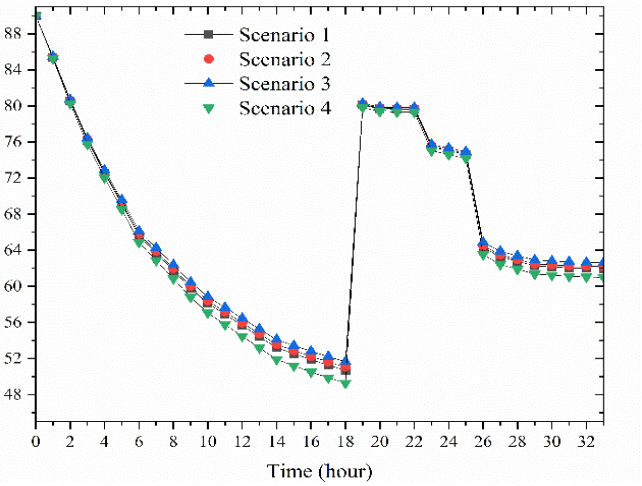

Fig. 23. The average node gas pressure.

V. Conclusion

Due to the importance of coupled operation of the natural gas and electricity grids, this paper proposed a novel stochastic P2P market-based method to integrate the operation of electricity and natural gas networks considering P2G storages, electrical distance, ESSs, DR, and both grid constraints. The presented method was compared with the previous framework as a benchmark method.

In the first step, 1000 random scenarios are generated based on normal PDF. In the following, generated scenarios are reduced by the backward method to four scenarios representing their original generation. Finally, the proposed method is solved for 4 reduced scenarios, and its results are analyzed. The case study was initiated by running the optimization problem for one single trading period. The results of the single-period optimization revealed that employing the TID model in the presented method led to electrically closer trades, reduced power losses by about 44%, and the proposed framework increased the volume of the traded energy by about 40%. Also, it was concluded that without the presented P2P market, P2Gs did not participate in the P2P energy trading process. The separation between the scheduling and trading stage in the benchmark method was the reason for P2Gs not participating.

In the following, the case study was performed for 24 hours. The results revealed the optimum performance of the proposed framework. The total operating cost of the entire network was reduced by about 47%, and the total revenue of gas turbines was increased by about 7% compared to the benchmark method. Also, the entire P2G revenue was 3891 ($), which was zero in the benchmark method. The proposed method could be enhanced by considering electric vehicle parking lots, heat networks, and renewable energy resources.

Appendix (A.1)

A coalition of consumers, producers, and the DSO performs CDA-based P2P energy trading. Unlike the proposed method, the CDA-based P2P energy trading framework is implemented in two distinct stages. In the first step, called the scheduling stage, NGs' electricity energy demands, P2Gs' charging-discharging cycles, and gas turbines' energy production for the next day are determined. Scheduling stage results are obtained by solving the presented optimization in section three, supposing that the customers can only trade with the power grid. In stage two (trading stage), these scheduling results are sent back to customers, and they, based on these energy schedules and the CDA framework, trade energy with each other. Stage two is implemented as follows:

Step 1: Once customers receive the results of the scheduling stage, they initiate energy trading for the next 24 hours by sending bids/offers. The structure of customers' bids is shown by Equation (a1).

$$b_t\left(S_{b,t}, \rho_{b,t}, \delta_{b,t}, \tau_{b,t}\right) \quad \text{(a1)}$$

Where purchaser ($S_{b,t}$) that want to buy ($\rho_{b,t}$) energy in price ($\delta_{b,t}$) at time ($\tau_{b,t}$). Similarly, vendor offer is illustrated by Equation (a2).

$$O_t\left(S_{s,t}, \rho_{s,t}, \delta_{s,t}, \tau_{s,t}\right) \quad \text{(a2)}$$

Step 2: After all offers/bids are received by the DSO for the time slot (t), the DSO creates the order book for the present time slot. The order book is an electronic data sheet that is made for each traded period (hear 24 traded period). In the order book, offers/bids are sorted based on price and arrival time. Offers are sorted in ascending order, and bids are sorted in descending order.

Step 3: Once the order book is ready, if the following relation is satisfied, the purchaser (b_t) and seller (O_t) are chosen for energy trade.

$$\delta_{s,t} \le \delta_{b,t} \quad \text{(a3)}$$

Step 4: The amount of matched energy transaction is calculated by Equation (a4). The following formula indicates the Constraint related to the volume of traded energy. In other words, the minimum preferred energy of the purchaser or seller limits the volume of traded energy. Also, Equation (a5) calculates the matched energy price.

$$\rho_{matched} = min\{\rho_{b,t}, \rho_{s,t}\} \quad \text{(a4)}$$

$$\delta_{matched} = \frac{\delta_{b,t} + \delta_{s,t}}{2} \quad \text{(a5)}$$

Step 5: fully matched bids and offers are eliminated from the order book. Those bids and offers that are not completely matched are updated by Equations (a6) and (a7).

$$b_t^{'}(S_{b,t}, \rho_{b,t}, \delta_{b,t}^{'}, \tau_{b,t}) \qquad if\ \rho_{b,t} - \rho_{s,t} > 0 \quad \text{(a6)}$$

$$o_{s,t}^{'}(S_{s,t}, \rho_{s,t}, \delta_{s,t}^{'}, \tau_{s,t}) \qquad if\ \rho_{p,t} - \rho_{s,t} < 0 \quad \text{(a7)}$$

Step 6: Repeat steps 1 to 5 for all bids/offers in traded period (t) and continue to period (t+1) if all offers and bids in period (t) are matched.

Appendix (A.2)

Due to considering the uncertainties related to natural gas and power demands, this paper employs the scenario-based stochastic optimization problem. In the first step, 1000 random scenarios (initial samples) are created to represent variations in electricity and natural gas demand. Due to the nonlinear nature of the proposed optimization problem, solving the optimization problem for all created scenarios is time-consuming and impossible. In this regard, the backward reduction method is employed to reduce the number of initial scenarios to four.

The normal distribution function (PDF) is employed to deal with the uncertainty of natural gas and electricity demand, as shown in Equation (a8) [79]. Natural gas and power demand of the studied network is described through mean value (μ) and standard deviation (σ). The σ value for creating natural gas and electricity scenarios is equal to 20%.

$$f(\rho^{g,e}) = \frac{1}{\sqrt{2\pi} \times \sigma^{g,e}} e^{\left(\frac{\rho - \mu^{g,e}}{2\sigma^{g,e^2}}\right)} \quad \text{(a8)}$$

The 1000 generated scenarios for natural gas and electricity demands based on normal PDF are illustrated in Figs. (a1) and (a2), respectively. Original scenarios are reduced by the backward reduction method, which is comprehensively described in [80]. Through the backward method, 1000 initial scenarios are reduced to four, of which their occurrence probabilities are 0.37, 0.25, 0.18, and 0.2, respectively.

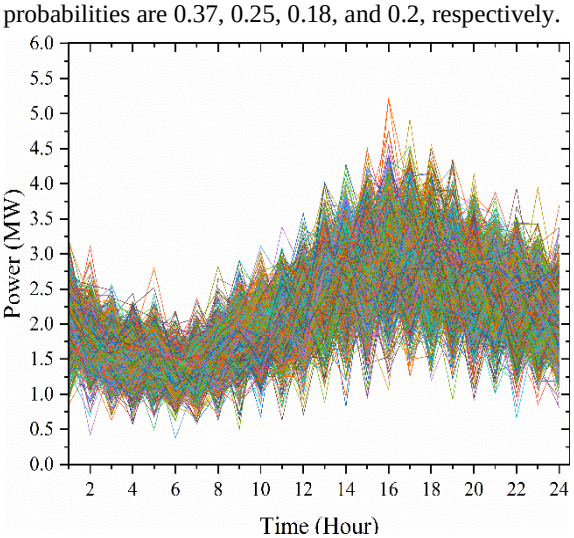

Fig. (a1). Original scenario for electricity demand.

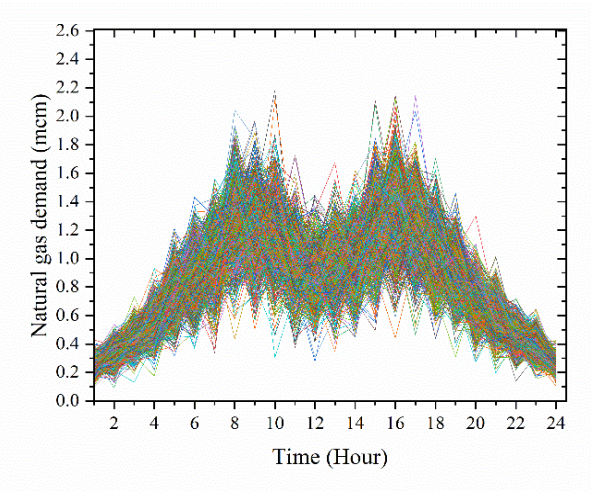

Fig. (a2). Original scenarios for natural gas demand.

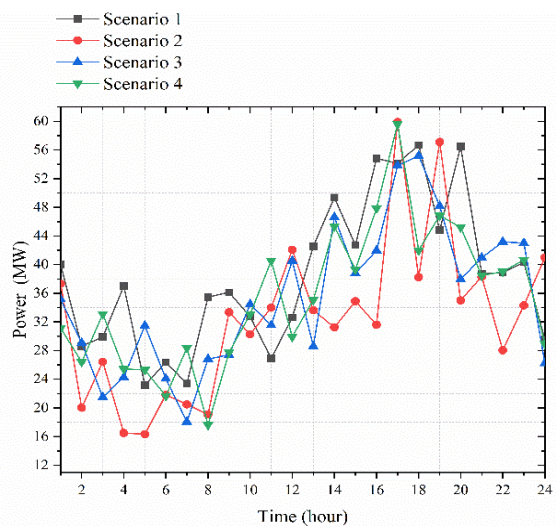

Fig. (a3). Reduced scenarios for natural gas demand.

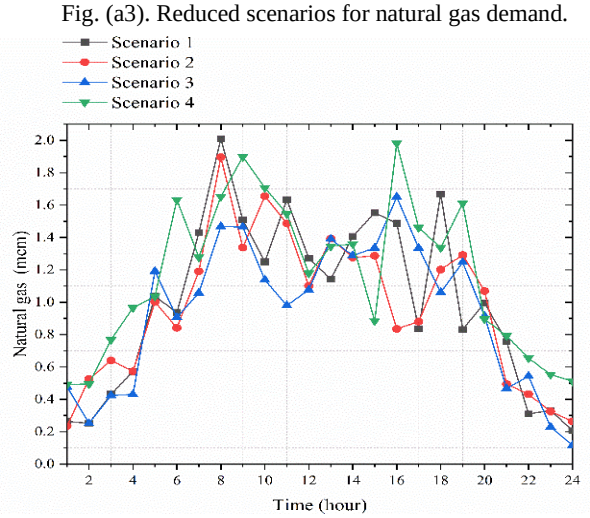

Fig. (a4). Reduced scenarios for natural gas demand.

REFERENCES

[1] R. Zhang, S. Bu, and G. Li, "Multi-market P2P trading of cooling–heating-power-hydrogen integrated energy systems: An equilibrium-heuristic online prediction optimization approach," *Applied Energy*, vol. 367, p. 123352, 2024.

[2] J. Chen, B. Sun, Y. Li, R. Jing, Y. Zeng, and M. Li, "Credible capacity calculation method of distributed generation based on equal power supply reliability criterion," *Renewable Energy*, vol. 201, pp. 534-547, 2022.

[3] Y. Shang, L. Zhu, F. Qian, and Y. Xie, "Role of green finance in renewable energy development in the tourism sector," *Renewable Energy*, vol. 206, pp. 890-896, 2023.

[4] M. Feili and M. T. Ameli, "Integrated operation of gas and power system through the P2P market mechanism," *IET Smart Grid*, vol. 6, no. 4, pp. 359-379, 2023.

[5] A. Masoudi, M. Simab, H. Akbarj, S. A. Saeed, and T. Daemi, "Maximizing the Electric Vehicles' Owners Profit Considering Optimal Charging and Discharging Management in the Distribution Networks Using Dynamic Programming," *International Journal of Industrial Electronics Control and Optimization*, vol. 5, no. 2, pp. 109-121, 2022.

[6] M. F. Akorede, H. Hizam, and E. Pouresmaeil, "Distributed energy resources and benefits to the environment," *Renewable and sustainable energy reviews*, vol. 14, no. 2, pp. 724-734, 2010.

[7] T. Cai, M. Dong, K. Chen, and T. Gong, "Methods of participating power spot market bidding and settlement for renewable energy systems," *Energy Reports*, vol. 8, pp. 7764-7772, 2022.

[8] M. Shafiee, A.-A. Zamani, and M. Sajadinia, "Using improved DDAO algorithm to solve economic emission load dispatch problem in the presence of wind farms," *International Journal of Industrial Electronics Control and Optimization*, vol. 6, no. 3, pp. 161-169, 2023.

[9] C. Wang, J. Wu, J. Ekanayake, and N. Jenkins, *Smart electricity distribution networks*. CRC Press, 2017.

[10] M. Feili, M. T. Ameli, and M. Shafiekhah, "Coupled Energy Systems Operation Through MINLP Framework Considering Systems Constraints and Demand Response," in *2023 13th Smart Grid Conference (SGC)*, 2023: IEEE, pp. 1-8.

[11] Z. Zhang, F. M. Altalbawy, M. Al-Bahrani, and Y. Riadi, "Regret-based multi-objective optimization of carbon capture facility in CHP-based microgrid with carbon dioxide cycling," *Journal of Cleaner Production*, vol. 384, p. 135632, 2023.

[12] Y. Duan, Y. Zhao, and J. Hu, "An initialization-free distributed algorithm for dynamic economic dispatch problems in microgrid: Modeling, optimization and analysis," *Sustainable Energy, Grids and Networks*, p. 101004, 2023.

[13] A. Taghieh, A. Mohammadzadeh, C. Zhang, N. Kausar, and O. Castillo, "A type-3 fuzzy control for current sharing and voltage balancing in microgrids," *Applied Soft Computing*, vol. 129, p. 109636, 2022.

[14] Z. Shi, H. Liang, S. Huang, and V. Dinavahi, "Distributionally robust chance-constrained energy management for islanded microgrids," *IEEE Transactions on Smart Grid*, vol. 10, no. 2, pp. 2234-2244, 2018.

[15] M. Ghiasi, Z. Wang, M. Mehrandezh, S. Jalilian, and N. Ghadimi, "Evolution of smart grids towards the Internet of energy: Concept and essential components for deep decarbonisation," *IET Smart Grid*, 2022.

[16] Z. Shuai *et al.*, "Microgrid stability: Classification and a

review," *Renewable and Sustainable Energy Reviews,* vol. 58, pp. 167-179, 2016.
[17] Y. Zahraoui, T. Korõtko, A. Rosin, T. E. K. Zidane, H. Agabus, and S. Mekhilef, "A Competitive Framework for The Participation Of Multi-Microgrids in The Community Energy Trading Market: A Case Study," *IEEE Access,* 2024.
[18] M. Vosoogh, M. Rashidinejad, A. Abdollahi, and M. Ghaseminezhad, "Efficient networked microgrid management considering plug-in electric vehicles and storage units," *International Journal of Industrial Electronics Control and Optimization,* vol. 4, no. 2, pp. 245-255, 2021.
[19] H. Mei, Y. Li, C. Suo, Y. Ma, and J. Lv, "Analyzing the impact of climate change on energy-economy-carbon nexus system in China," *Applied Energy,* vol. 262, p. 114568, 2020.
[20] D. Forfia, M. Knight, and R. Melton, "The view from the top of the mountain: Building a community of practice with the gridwise transactive energy framework," *IEEE Power and Energy Magazine,* vol. 14, no. 3, pp. 25-33, 2016.
[21] M. Feili and M. T. Ameli, "Integrated operation of gas and power system through the P2P market mechanism," *IET Smart Grid,* 2023.
[22] B. Zheng, W. Wei, Y. Chen, Q. Wu, and S. Mei, "A peer-to-peer energy trading market embedded with residential shared energy storage units," *Applied Energy,* vol. 308, p. 118400, 2022.
[23] O. Jogunola *et al.*, "Peer-to-Peer Local Energy Market: Opportunities, Barriers, Security and Implementation Options," *IEEE Access,* 2024.
[24] R. Safipour and M. Oukati Sadegh, "Optimal Planning of energy storage systems using symbiotic organisms search algorithm," *International Journal of Industrial Electronics Control and Optimization,* vol. 1, no. 1, pp. 19-26, 2018.
[25] Y. Meng, J. Qiu, C. Zhang, G. Lei, and J. Zhu, "A Holistic P2P market for active and reactive energy trading in VPPs considering both financial benefits and network constraints," *Applied Energy,* vol. 356, p. 122396, 2024.
[26] J. Hao, T. Huang, Y. Sun, X. Zhan, Y. Zhang, and P. Wu, "Optimal Prosumer Operation with Consideration for Bounded Rationality in Peer-to-Peer Energy Trading Systems," *Energies,* vol. 17, no. 7, p. 1724, 2024.
[27] A. Tiwari, B. K. Jha, and N. M. Pindoriya, "Multi-objective optimization based demand response program with network aware peer-to-peer energy sharing," *International Journal of Electrical Power & Energy Systems,* vol. 157, p. 109887, 2024.
[28] X. Wang *et al.*, "Congestion management under peer-to-peer energy trading scheme among microgrids through cooperative game," *Energy Reports,* vol. 8, pp. 59-66, 2022.
[29] J. L. Crespo-Vazquez, T. AlSkaif, Á. M. González-Rueda, and M. Gibescu, "A community-based energy market design using decentralized decision-making under uncertainty," *IEEE Transactions on Smart Grid,* vol. 12, no. 2, pp. 1782-1793, 2020.
[30] G. Sun, J. Sun, S. Chen, Z. Wei, and H. Zang, "Market-based coordination of regional electric and natural gas systems: A peer-to-peer energy trading model," *CSEE Journal of Power and Energy Systems,* 2022.
[31] Z. Wang, X. Yu, Y. Mu, H. Jia, Q. Jiang, and X. Wang, "Peer-to-Peer energy trading strategy for energy balance service provider (EBSP) considering market elasticity in community microgrid," *Applied Energy,* vol. 303, p. 117596, 2021.
[32] M. H. Ullah and J.-D. Park, "DLMP integrated P2P2G energy trading in distribution-level grid-interactive transactive energy systems," *Applied Energy,* vol. 312, p. 118592, 2022.
[33] L. Ali, S. Muyeen, H. Bizhani, and A. Ghosh, "A multi-objective optimization for planning of networked microgrid using a game theory for peer-to-peer energy trading scheme," *IET Generation, Transmission & Distribution,* vol. 15, no. 24, pp. 3423-3434, 2021.
[34] K. Rowe, G. Mokryani, K. Cooke, F. Campean, and T. Chambers, "Bi-level optimal sizing, siting and operation of utility-scale multi-energy storage system to reduce power losses with peer-to-peer trading in an electricity/heat/gas integrated network," *Journal of Energy Storage,* vol. 83, p. 110738, 2024.
[35] D. Peng, H. Xiao, W. Pei, H. Sun, and S. Ye, "A novel deep learning based peer-to-peer transaction method for prosumers under two-stage market environment," *IET Smart Grid,* 2022.
[36] N. Tarashandeh and A. Karimi, "Peer-to-peer energy trading under distribution network constraints with preserving independent nature of agents," *Applied Energy,* vol. 355, p. 122240, 2024.
[37] W. Tushar *et al.*, "A coalition formation game framework for peer-to-peer energy trading," *Applied Energy,* vol. 261, p. 114436, 2020.
[38] C. Wang, W. Wei, J. Wang, F. Liu, and S. Mei, "Strategic offering and equilibrium in coupled gas and electricity markets," *IEEE Transactions on Power Systems,* vol. 33, no. 1, pp. 290-306, 2017.
[39] M. Niu, C. Gao, G. Muñoz-Delgado, and J. Contreras, "A cross-carrier multilateral trading model for integrated electricity and natural gas systems," *Applied Energy,* vol. 354, p. 122064, 2024.
[40] A. G. Daryan, A. Sheikhi, and A. A. Zadeh, "Peer-to-Peer Energy sharing Among Smart Energy Hubs in an integrated Heat-Electricity Network," *Electric Power Systems Research,* vol. 206, p. 107726, 2022.
[41] S. Ge, J. Li, X. He, and H. Liu, "Joint energy market design for local integrated energy system service procurement considering demand flexibility," *Applied Energy,* vol. 297, p. 117060, 2021.
[42] M. I. Azim, W. Tushar, and T. K. Saha, "Coalition graph game-based P2P energy trading with local voltage management," *IEEE Transactions on Smart Grid,* vol. 12, no. 5, pp. 4389-4402, 2021.
[43] T. Lu, Z. Wang, Q. Ai, and W.-J. Lee, "Interactive model for energy management of clustered microgrids," *IEEE Transactions on Industry Applications,* vol. 53, no. 3, pp. 1739-1750, 2017.
[44] K. Wang *et al.*, "Embedding P2P transaction into demand response exchange: A cooperative demand response management framework for IES," *Applied Energy,* vol. 367, p. 123319, 2024.
[45] A. Basnet and J. Zhong, "Integrating gas energy storage system in a peer-to-peer community energy market for enhanced operation," *International Journal of Electrical Power & Energy Systems,* vol. 118, p. 105789, 2020.
[46] N. Wang, Z. Liu, P. Heijnen, and M. Warnier, "A peer-to-peer market mechanism incorporating multi-energy coupling and cooperative behaviors," *Applied Energy,* vol. 311, p. 118572, 2022.
[47] W. Zhou, Y. Wang, F. Peng, Y. Liu, H. Sun, and Y. Cong, "Distribution network congestion management considering time sequence of peer-to-peer energy trading," *International Journal of Electrical Power & Energy*

Systems, vol. 136, p. 107646, 2022.
[48] Y. Chen, W. Wei, F. Liu, and S. Mei, "A multi-lateral trading model for coupled gas-heat-power energy networks," *Applied energy*, vol. 200, pp. 180-191, 2017.
[49] H. Wang, C. Wang, M. Q. Khan, G. Zhang, and N. Xie, "Risk-averse market clearing for coupled electricity, natural gas and district heating system," *CSEE Journal of Power and Energy Systems*, vol. 5, no. 2, pp. 240-248, 2019.
[50] T. D. Hutty and S. Brown, "P2P trading of heat and power via a continuous double auction," *Applied Energy*, vol. 369, p. 123556, 2024.
[51] H. Zhang, S. Zhang, X. Hu, H. Cheng, Q. Gu, and M. Du, "Parametric optimization-based peer-to-peer energy trading among commercial buildings considering multiple energy conversion," *Applied Energy*, vol. 306, p. 118040, 2022.
[52] T. Gokcek, I. Sengor, B. P. Hayes, and O. Erdinc, "A hierarchical approach for P2P energy trading considering community energy storage and PV-enriched system operator," *IET Generation, Transmission & Distribution*, vol. 16, no. 23, pp. 4738-4749, 2022.
[53] A. Jiang, H. Yuan, and D. Li, "A two-stage optimization approach on the decisions for prosumers and consumers within a community in the Peer-to-peer energy sharing trading," *International Journal of Electrical Power & Energy Systems*, vol. 125, p. 106527, 2021.
[54] Y. Zhou, J. Wu, G. Song, and C. Long, "Framework design and optimal bidding strategy for ancillary service provision from a peer-to-peer energy trading community," *Applied Energy*, vol. 278, p. 115671, 2020.
[55] N. Hashemipour, P. C. del Granado, and J. Aghaei, "Dynamic allocation of peer-to-peer clusters in virtual local electricity markets: A marketplace for EV flexibility," *Energy*, vol. 236, p. 121428, 2021.
[56] Y. Xia, Q. Xu, J. Fang, Y. Huang, L. Shi, and F. Wu, "Surrogate model enabled integrated energy system trading in buildings considering bidding characteristics," *Energy and Buildings*, vol. 306, p. 113939, 2024.
[57] C. S. Lai, M. Yan, X. Li, L. L. Lai, and Y. Xu, "Coordinated Operation of Electricity and Natural Gas Networks with Consideration of Congestion and Demand Response," *Applied Sciences*, vol. 11, no. 11, p. 4987, 2021.
[58] S. Rezaei and A. Ghasemi, "Stochastic scheduling of resilient interconnected energy hubs considering peer-to-peer energy trading and energy storages," *Journal of Energy Storage*, vol. 50, p. 104665, 2022.
[59] M. Khorasany, A. S. Gazafroudi, R. Razzaghi, T. Morstyn, and M. Shafie-khah, "A framework for participation of prosumers in peer-to-peer energy trading and flexibility markets," *Applied Energy*, vol. 314, p. 118907, 2022.
[60] M. Mehdinejad, H. Shayanfar, and B. Mohammadi-Ivatloo, "Peer-to-peer decentralized energy trading framework for retailers and prosumers," *Applied Energy*, vol. 308, p. 118310, 2022.
[61] S. Malik, M. Duffy, S. Thakur, B. Hayes, and J. Breslin, "A priority-based approach for peer-to-peer energy trading using cooperative game theory in local energy community," *International Journal of Electrical Power & Energy Systems*, vol. 137, p. 107865, 2022.
[62] J. Guerrero, B. Sok, A. C. Chapman, and G. Verbič, "Electrical-distance driven peer-to-peer energy trading in a low-voltage network," *Applied Energy*, vol. 287, p. 116598, 2021.
[63] D. Alkano and J. M. Scherpen, "Distributed supply coordination for power-to-gas facilities embedded in energy grids," *IEEE Transactions on Smart Grid*, vol. 9, no. 2, pp. 1012-1022, 2016.
[64] Y. Zhou, J. Wu, C. Long, and W. Ming, "State-of-the-art analysis and perspectives for peer-to-peer energy trading," *Engineering*, vol. 6, no. 7, pp. 739-753, 2020.
[65] V. Shabazbegian, H. Ameli, M. T. Ameli, G. Strbac, and M. Qadrdan, "Co-optimization of resilient gas and electricity networks; a novel possibilistic chance-constrained programming approach," *Applied Energy*, vol. 284, p. 116284, 2021.
[66] T. Baroche, P. Pinson, R. L. G. Latimier, and H. B. Ahmed, "Exogenous cost allocation in peer-to-peer electricity markets," *IEEE Transactions on Power Systems*, vol. 34, no. 4, pp. 2553-2564, 2019.
[67] D. J. Klein and M. Randić, "Resistance distance," *Journal of mathematical chemistry*, vol. 12, no. 1, pp. 81-95, 1993.
[68] D. Huo, C. Gu, K. Ma, W. Wei, Y. Xiang, and S. Le Blond, "Chance-constrained optimization for multienergy hub systems in a smart city," *IEEE Transactions on Industrial Electronics*, vol. 66, no. 2, pp. 1402-1412, 2018.
[69] M. Geidl and G. Andersson, "Optimal power flow of multiple energy carriers," *IEEE Transactions on power systems*, vol. 22, no. 1, pp. 145-155, 2007.
[70] A. Theerthamalai and S. Maheswarapu, "An effective non-iterative "λ-logic based" algorithm for economic dispatch of generators with cubic fuel cost function," *International Journal of Electrical Power & Energy Systems*, vol. 32, no. 5, pp. 539-542, 2010.
[71] F. Fang, Q. H. Wang, and Y. Shi, "A novel optimal operational strategy for the CCHP system based on two operating modes," *IEEE Transactions on power systems*, vol. 27, no. 2, pp. 1032-1041, 2011.
[72] H. Mehrjerdi, "Peer-to-peer home energy management incorporating hydrogen storage system and solar generating units," *Renewable Energy*, vol. 156, pp. 183-192, 2020.
[73] R. Habibifar, H. Ranjbar, M. Shafie-Khah, M. Ehsan, and J. P. Catalão, "Network-constrained optimal scheduling of multi-carrier residential energy systems: a chance-constrained approach," *Ieee Access*, vol. 9, pp. 86369-86381, 2021.
[74] Y. Jiang *et al.*, "Coordinated operation of gas-electricity integrated distribution system with multi-CCHP and distributed renewable energy sources," *Applied energy*, vol. 211, pp. 237-248, 2018.
[75] G. L. Torres, V. H. Quintana, and G. Lambert-torres, "Optimal power flow in rectangular form via an interior point method," in *Proc. of 1996 IEEE North American Power Symposium*, 1996: Citeseer.
[76] V. Shabazbegian, H. Ameli, M. T. Ameli, and G. Strbac, "Stochastic optimization model for coordinated operation of natural gas and electricity networks," *Computers & Chemical Engineering*, vol. 142, p. 107060, 2020.
[77] M. Feili and M. Mameli, "Simultaneous operation of electricity and natural gas systems through the P2P energy trading mechanism," *Journal of Modeling in Engineering*, vol. 21, no. 75, pp. 205-224, 2023.
[78] R. Misener and C. A. Floudas, "ANTIGONE: algorithms for continuous/integer global optimization of nonlinear equations," *Journal of Global Optimization*, vol. 59, no. 2, pp. 503-526, 2014.
[79] F. S. Gazijahani, S. N. Ravadanegh, and J. Salehi, "Stochastic multi-objective model for optimal energy exchange optimization of networked microgrids with presence of renewable generation under risk-based

strategies," *ISA transactions*, vol. 73, pp. 100-111, 2018

[80] Z. Li and C. A. Floudas, "Optimal scenario reduction framework based on distance of uncertainty distribution and output performance: II. Sequential reduction," *Computers & Chemical Engineering*, vol. 84, pp. 599-610, 2016.

Meysam Feili received his B.Sc. and M.Sc degrees in electrical engineering, with a focuse on power systems, in 2013 and 2017, respectively. Now, he is a researcher at the Center of Excellence in Power System Studies at Shahid Beheshti University. His current research interests are power distribution systems operation, integrating renewable energies, the local energy markets, and multi-vector energy systems.

Mohammad Taghi Ameli received his B.Sc. degree in electrical engineering from the Technical College of Osnabrück, Germany, in 1988 and his M.Sc. and Ph.D. degrees from the Technical University of Berlin, Berlin, Germany, in 1992 and 1997, respectively. He is a Professor in the Department of Electrical Engineering and the chair of the Research Institute for Electrical Networks at Shahid Beheshti University. He has been the Editor-in-Chief of the International Journal of Research and Technology in Electrical Industry (IJRTEI) since 2020. His research interests include the operation, planning, and control of power and energy systems, integrating renewable energies into the energy system, and smart grids.

IECO

This page intentionally left blank.

International Journal Of
Industrial Electronics Control and Optimization
Print ISSN: 3517-2645
Online ISSN: 3568-2645
Homepage: https://ieco.usb.ac.ir/

A New Quadratic CUK-Based Step-Up DC/DC Converter Without Right Hand Plane Zero

Hossein Gholizadeh [1] | Sara Hasanpour[2*]

[1]School of Electrical and Computer Engineering, University of Tehran, Tehran, Iran.
[2*]Department of Electrical Engineering, Ramsar Branch, Islamic Azad University, Ramsar, Iran.
Corresponding author's email: Sara.Hasanpour@iau.ac.ir

Article Info

Article type:
Research Article

Article history:
Received: 09-May-2024
Received in revised form: 30-July-2024
Accepted: 06-August-2024
Published online: 21-March-2025

Keywords:
CUK-Based,
Step-up dc-dc converter,
Quadratic.

ABSTRACT

In this paper, a new transformerless high step-up DC/DC converter with low input current ripple for renewable energy generation systems. This introduced circuit is based on a conventional quadratic boost converter with a CUK circuit. Therefore, the advantages of Cuk and quadratic boost converters such as continuity of the input and output currents have been maintained. In this suggested topology, switched capacitor and switched inductor techniques are also considered to obtain high voltage gains. The series connection of an inductor with the load causes the converter to have no right half plane zeros (RHPZ) in the transfer function; Thus, the proposed structure is able to provide fast dynamic behavior under the load variation than the other typical counterparts. The other advanced features of the introduced topology are its ultra-high voltage gain, continuous input current with low ripple, low voltage stress, and common ground between the input source and output load. The voltage conversion ratio of the suggested topology for both ideal and non-ideal modes has been provided. The operating principle, steady-state analysis along with comparison study of the proposed converter are discussed in detail. Finally, to confirm the theoretical analysis, a 80 W (20 V/ 160 V) hardware prototype is established.

I. Introduction

In recent decades, due to the importance of energy management, the use of renewable energy sources (RES) and batteries have been paid more attention. RESs are used in many applications such as renewable energy, energy harvesting, uninterruptible power supply (UPS), data centers, medical implantable devices, industrial, lighting technology, medical and military, automotive and railway technology, portable devices, gadgets, space and avionics, telecommunications, and physics research. Because of the low output voltage level of resources (< 48 V), the use of high voltage gain DC/DC converters as an interface circuit to create a desired output voltage is necessary [1-2]. For step-up dc-dc structures, high step-up capability and low input current ripple requirements are necessary for that are applied in RES applications [2]. Moreover, due to simple structure, and compact design, non-isolated structures of step-up converters are preferred for low-power applications.

In past years, conventional step-up power topologies such as Boost, SEPIC and Buck-Boost circuits with simple structures and low component counts have been introduced for high-voltage gain applications. However, in these converters, strong limitation on voltage conversion ratio limits their applications. Moreover, due to the use of a diode in the output side of the circuit, which leads to the discontinuity of the output current, a right half plane zero (RHPZ) is created, which leads to non-minimum phase (NMP) behavior in their transfer function and slow dynamic response [3, 4].

So far, many modified high voltage gain DC-DC topologies have been introduced. In these topologies, to raise the voltage conversion ratio, some effective boosting methods including voltage-lift, switched inductors (SI), switched capacitors (SC), cascading technique, voltage multipliers (VM) and coupled-inductor (CI) have been used [1, 2, 5]. It should be noted that

in CI-based converters, the leakage inductance of the CI often causes high voltage spikes across the power switch which should be limited by adding auxiliary clamp circuits to the converter [6,7].

In recent years, many non-isolated transformerless converters with high voltage gain have been introduced. In [8, 9], two new types of quadratic boost step-up DC-DC converters are introduced. However, low voltage gain along with high input current ripple are demerits of the mentioned circuits, which limits their applications for RES systems. Using two power switches, high voltage gain DC-DC converter with low input current ripple and low voltage stress are suggested in [16-21]. In addition, in [22-23], some quadratic high-gain DC-DC converters based on extended capacitor-diode networks are presented. However, the lack of common ground between the input and output sides is the main disadvantage of these circuits. To solve the mentioned problem, ultrahigh step-up quadratic single-switch converters with continuous input current ripple are suggested in [24-28]. In addition, new non-isolated single-switch high gain converters with low input current ripple and common ground are proposed in [25-28]. Nevertheless, due to RHPZ, these converters are not able to provide a fast transient response.

One of the methods to eliminate the RHPZ is the continuity of the current on the output side of the circuit. For this purpose, in [29-32], step-up DC/DC converters with fast dynamic response and low input current ripple for low-power applications are presented. However, the mentioned circuits suffer from a low voltage gain ratio along with using two power switches. In [33] and [34], two new types of high-voltage gain DC-DC converters are suggested. However, because of the NMP feature, these structures are not able to provide a fast transient response.

Keeping in mind the merits and demerits of the discussed high step-up converters, this paper suggests a new topology of a non-isolated single-switch quadratic high voltage gain DC-DC converter without RHPZ for renewable energy source applications. The advantages of the proposed converter are as follows:

1- High voltage gain.
2- Common ground connection.
3- Low input current ripple.
4- A single power switch structure.
5- Minimum phase behavior.

II. Operational principles of the converter

The circuit diagram of the proposed circuit is shown in Fig. 1. In this introduced converter, there are seven didoes (D_1-D_7), one power switch (S), six capacitors (C_1-C_5, and C_o), along with four inductors (L_1-L_4). Regarding this figure, the proposed topology is a modified structure of a conventional quadratic boost topology, and a CUK converter. Thus, the proposed structure maintains the benefits of the quadratic boost and Cuk circuits such as continuity of the input and output current waveforms, and high voltage gain ratio. Moreover, in order to achieve high voltage gains under low voltage stress, voltage boosting techniques SC and SI are also considered in the converter. Therefore, high output DC voltages can be created at low duty cycles, which leads to efficiency improvement. Also, to restrict the voltage stress rate across the power switch (S), a simple passive clamp circuit including the diode D_7 and the capacitor C_5 is used. To simplify the analysis of the presented circuit, all switching devices are considered ideal. Fig. 2 shows the theoretical key waveforms of the proposed converter in one switching period. Furthermore, the circuit has two operating modes continuous conduction mode (CCM), which are depicted in Fig. 3.

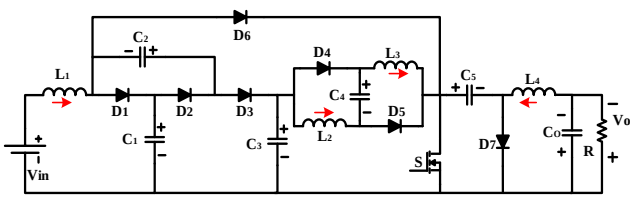

Fig. 1. The circuit configuration of the proposed converter.

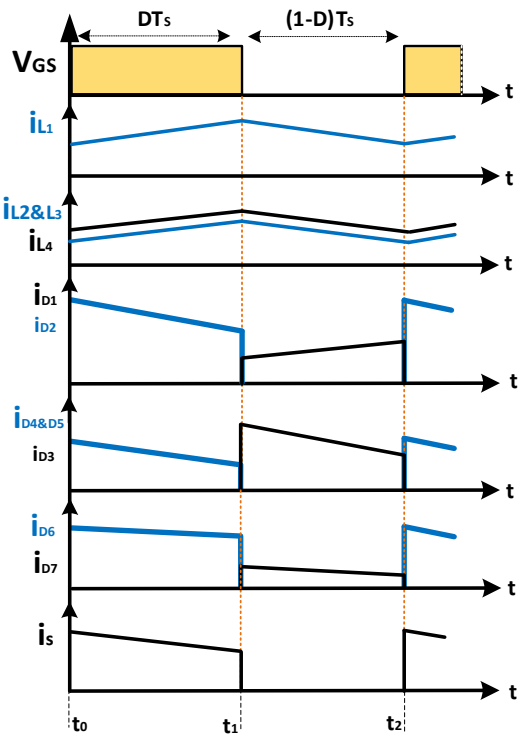

Fig. 2. The time-domain key waveforms of the converter.

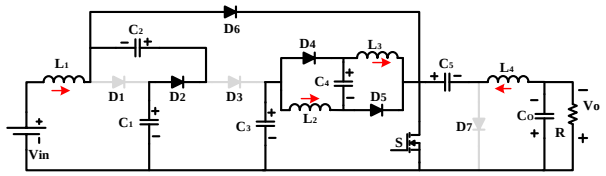

(a)

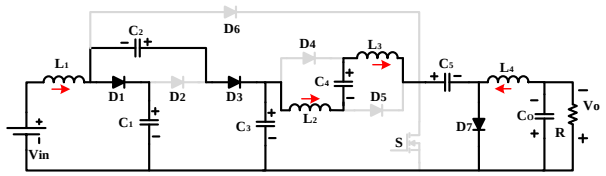

(b)

Fig. 3. Equivalent circuits of the introduced converter; (a) Mode-1, (b) Mode-2.

Mode-1 [t_0 - t_1]: At t = t_0, the single power switch S is turned ON by applying PWM pulses. From Fig. 3-(a), during operating mode, the diodes D_2, D_4, D_5, and D_6 are also conducting, while other diodes of the circuit are off. In this time interval, the input inductor (L_1) is charging from the input DC voltage source; thus, its current is increased linearly. Furthermore, the middle inductors L_1, L_2 and also the capacitor C4 are charged from the voltages across the capacitor C_3 through the diodes D_4, D_5 and the power switch. Besides, the output inductance (L_4) gets charged due to the positive voltage induced from the capacitor C_5. Moreover, the capacitor C_2 receives energy from the capacitor C_1 through the power switch and diodes D_2 and D_6.

Mode-2 [t_1 - t_2]: As shown in Fig 3 (b), in the second operating mode, as soon as the active switch (S) at time $t = t_1$ is turned OFF, the diodes D_1, D_3 and D_7 begin to conduct. In this mode, the capacitors C_1 and C_3 start to charge from the input inductor current. moreover, the energies stored in the inductors L_2 and L_3 along with the capacitor C_4 are released to the capacitor C_5. During this interval, the output inductor (L_4) charges the output capacitor C_o.

III. Steady-State Analysis

A. Steady-State Equations

The voltage of the inductors and also the current of the converter capacitors during both operation modes can be stated as follows:

$$L_1 \frac{di_{L1}}{dt} = D(V_{in}) + (1-D)(V_{in} - V_{C1}) \quad (1)$$

$$L_2 \frac{di_{L2}}{dt} = D(V_{C3}) + (1-D)(V_{C3} + V_{C4} - \acute{V}) \quad (2)$$

$$L_3 \frac{di_{L3}}{dt} = D(V_{C3}) + (1-D)(\acute{V} - V_{C5}) \quad (3)$$

$$L_4 \frac{di_{L4}}{dt} = D(V_{C5} - V_o) + (1-D)(-V_o) \quad (4)$$

$$C_1 \frac{dV_{C1}}{dt} = D(-i_{D2}) + (1-D)(i_{L1} - i_{D3}) \quad (5)$$

$$C_2 \frac{dV_{C2}}{dt} = D(i_{D2}) + (1-D)(-i_{D3}) \quad (6)$$

$$C_3 \frac{dV_{C3}}{dt} = D(-i_{L2} - i_{D4}) + (1-D)(i_{D3} - i_{L3}) \quad (7)$$

$$C_4 \frac{dV_{C4}}{dt} = D(i_{D4} - i_{L3}) + (1-D)(-i_{L3}) \quad (8)$$

$$C_5 \frac{dV_{C5}}{dt} = D(-i_{L4}) + (1-D)i_{L3} \quad (9)$$

$$C_o \frac{dV_{Co}}{dt} = D(i_{L4} - I_o) + (1-D)(i_{L4} - I_o) \quad (10)$$

Which, D denotes duty cycle of the power switch (S).

A. Average Voltage and Current of the Energy Storage Components

By applying the volt-second balance principle across the circuit inductors of the converter and using (1)-(4), the average voltage across the capacitors of the converter can be achieved as follows:

$$\boldsymbol{V_{C1} = V_{C2} = \frac{V_{in}}{1-D}} \quad (11)$$

$$\boldsymbol{V_{C3} = V_{C4} = \frac{2V_{in}}{1-D}} \quad (12)$$

$$\boldsymbol{V_{C5} = \frac{4V_{in}}{(1-D)^2}} \quad (13)$$

$$\boldsymbol{V_{Co} = \frac{4DV_{in}}{(1-D)^2}} \quad (14)$$

Moreover, using the current second balance of the circuit capacitors, the average current value of the inductors of the converter can be obtained as follows:

$$\boldsymbol{I_{L1} = \frac{4DI_o}{(1-D)^2}} \quad (15)$$

$$\boldsymbol{I_{L2} = I_{L3} = \frac{DI_o}{1-D}} \quad (16)$$

$$\boldsymbol{I_{L4} = I_o} \quad (17)$$

According to equation (14), the voltage gain ratio of the suggested topology is increased exponentially versus the duty cycle in quadratic form, which leads to create an ultra-high voltage gain ratio.

B. Considering Parasitic Elements

Equation (14) shows the ideal voltage gain ratio of the proposed topology. However, the parasitic resistances of the components including inductors (r_L), switches (r_S), and diodes (r_D) are affected to the performance of each topology. The presence of parasitic resistors causes a drop in the voltage gain ratio of the converter, especially in high duty cycles. In the proposed topology, after the inclusion of these parasitic components, the non-ideal voltage gain is obtained as follow:

$$\frac{V_o}{V_{in}} = \frac{4D}{(1-D)^2}\left(1 - \frac{r_L}{R}\frac{4D}{(1-D)^4} - \frac{r_s}{R}\frac{4D^2}{(1-D)^4} - \frac{r_D}{R}\frac{4D}{(1-D)^3}\right) \quad (18)$$

Regarding (14) and (18), the ideal and non-ideal voltage gains of the presented topology have been compared in Fig. 4. From this figure, in the duty cycle range 0<D<0.5, the value of the ideal voltage gain is almost close to the non-ideal gain; thus,

their difference can be ignored.

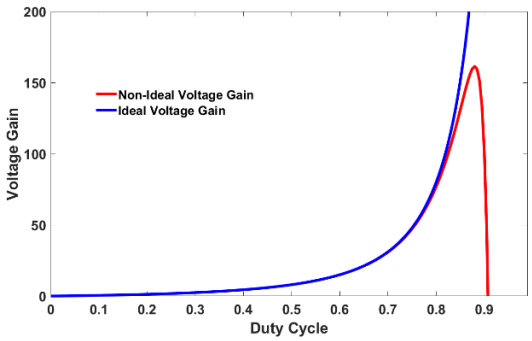

Fig. 4. Ideal voltage and non-ideal voltage gains of the proposed converter.

C. DCM Performance Analysis

D.1. Boundary Between CCM and DCM

In the proposed circuit, the boundary condition between CCM and DCM performances occurs when the input current reaches zero at the end of the switch period, in which case the currents of the diodes D_1 and D_3 fall to zero at $t=t_2$. Fig. 5 shows the current waveforms of the input inductor and the diodes D_1 and D3 at the boundary operation. With the help of converter operation modes, the slope of m_1 and m_2 of the input inductor current can be obtained as follows:

$$m_1 = \frac{V_{in}}{L_{1B}} \quad (19)$$

$$m_2 = \frac{-DV_{in}}{L_{1B}(1-D)} \quad (20)$$

Given the average value of input inductor current, and using (19) - (20), the boundary condition of the input inductance is derived as:

$$L_{1(min)} = \frac{DR}{2.f.M_{CCM}{}^2} \quad (21)$$

Regarding (21), the voltage gain, output load, and switching frequency affect the boundary condition value of the L_1.

D.2. Discontinuous Conduction Mode (DCM)

Fig. 6 illustrates the current waveforms of the input inductor and the diodes D_1 and D_3 under DCM mode. In DCM operation, according to the structure of the proposed topology and also by applying the volt-second balance principle on L_1, the average voltages of C_1 and C_2 are derived as follows:

$$V_{C1} = V_{C2} = \frac{1-\Delta}{1-D-\Delta} V_{in} \quad (22)$$

Which Δ is the time duration $t_2<t<t_3$, which the diodes D_1 and D_3 turn-off. In addition, the voltages of the other capacitors are achieved as:

$$V_{C3} = V_{C4} = \frac{2(1-\Delta)}{1-D-\Delta} V_{in} \quad (23)$$

Eventually, the voltage gain of the converter in DCM operation is obtained as follows:

$$M_{DCM} = \frac{V_o}{V_{in}} = \frac{(1-\Delta)4D}{(1-D)(1-D-\Delta)} \quad (24)$$

From (24), the time duration $1-\Delta$ as a function of the proposed converter parameters can be determined as:

$$1-\Delta = \frac{Q(M_{DCM})^2}{D} \quad (25)$$

Which, Q is defined as:

$$Q = \frac{2L_1 f_s}{R} \quad (26)$$

With substituting (59) into (56) and after rearranging, the voltage gain of the suggested circuit at DCM condition is calculated as:

$$M_{DCM} = \frac{V_o}{V_{in}} = \frac{4QD+2D\sqrt{Q(4Q+(1-D)^2)}}{2Q(1-D)} \quad (27)$$

D. Efficiency Interpretation

The power loss mechanism of the suggested circuit is provided in this part. The key parasitic parameters of the proposed circuit are listed in Table 1. The power loss of the power switch can be taken by

$$P_S = \frac{1}{2T_s}.V_{DS}(i_S^{t=on}.t_{on}) + \frac{1}{2T_s}.V_{DS}(i_S^{t=off}.t_{off}) + r_{DS(on)}.I^2_{S(RMS)} \quad (28)$$

$$P_s = \frac{16D}{(1-D)^4}\frac{r_S}{R}P_o \quad (29)$$

Here, $i_S^{t=on}$, $i_S^{t=off}$ are the switch current values at turn-on, turn-off instants. Also, the power loss of the diodes can be achieved as given below:

$$P_{Di} = r_{Di}.I^2_{D(RMS)} + V_{FDi}.I_{D(AVG)} \quad (30)$$

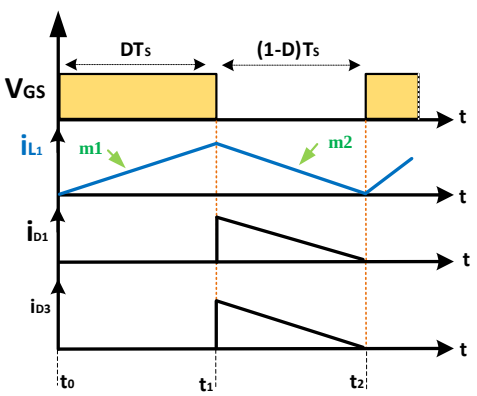

Fig. 5. The current waveforms of L_1 and Diodes D_1 and D_3 at the boundary condition between CCM and DCM mode.

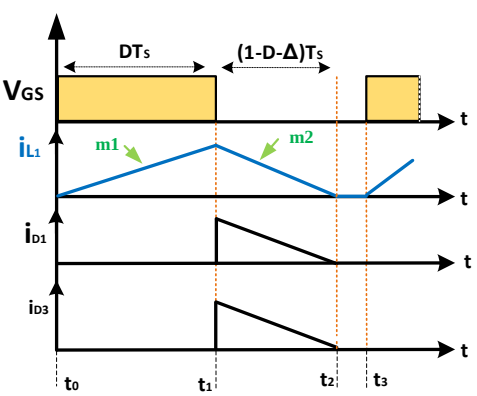

Fig. 6. The current waveforms of L_1, D_1 and D_3 at DCM.

$$x(t) =$$

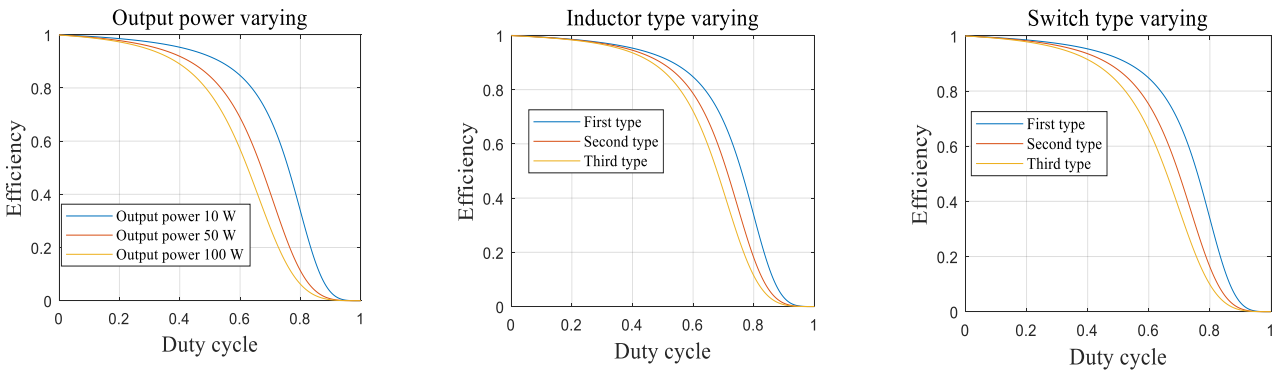

(a) (b) (c)

Fig. 7. Theoretical efficiency of the presented converter versus duty cycle and parasitic parameters.

$$P_D = \frac{10D-6D^2}{(1-D)^2} V_{FD.} I_o \quad (31)$$

Besides, the power dissipation of the circuit capacitor is:

$$P_{Cap.i} = r_{Ci}.I_{Ci(RMS)}^2 \quad (32)$$

$$P_C = \frac{11D+D^3}{(1-D)^3}\frac{r_D}{R}P_o \quad (33)$$

Finally, the power loss of the magnetic components can be estimated as:

$$P_{Li} = r_{L_i}.I_{L_i}^2 + P_{Core} \quad (34)$$

$$P_L = \frac{3D^4-8D^3+24D^2-4D+1}{(1-D)^4}\frac{r_L}{R}P_o \quad (35)$$

Fig. 7 (a)-(c) shows the effect of the parasitic parameters of the proposed circuit versus the duty cycle per the theoretical efficiency. From these figures, the proposed converter can provide high power-handling capacities at high voltage gains.

TABLE 1 THE PARASITIC PARAMETERS OF THE CONVERTER.

Parameter	Description
$r_{DS(ON)}$	ON-state resistance of the active switch (MOSFET)
t_{on} , t_{off}	Turn-on and turn-off times of the switch
T_s	The switching cycle time of the single switch
ESR_i	Equivalent Series Resistance of the converter capacitors
V_{FDi}	Threshold voltage of the converter diodes
r_D	Diodes' Resistance in Forwarding State
r_{Lin}, r_{Ni}	Parasitic resistances of the magnetic components (L_{in},and CI)

IV. Derivation of the Small-Signal Model

In this part, the small signal derivation along with analyzes of the low-frequency behavior of the presented topology are provided. For this purpose, the state-space averaging technique is used [35]. In order to simple modeling of the circuit, the state-space averaging method is used. The state variables of the system include the inductor currents and capacitor voltages. Thus, the state vector of the proposed converter is defined as:

$$[i_{L1} \quad i_{L2} \quad i_{L3} \; i_{L4} \quad V_{C1} \quad V_{C2} \quad V_{C3} \quad V_{C4} \quad V_{C5} \quad V_{Co}] \quad (36)$$

To obtain the state equations of the converter, it is necessary to consider the parasitic resistances of the middle capacitors r_{C1}, r_{C2}, r_{C3}, and r_{C4} in series with the capacitors. According to the converter structure, the state equations of operating mode *I* ($t_0<t<t_1$) are expressed as:

$$L_1\frac{di_{L_1}}{dt} = V_{in} \quad (37)$$

$$L_2\frac{di_{L_2}}{dt} = L_3\frac{di_{L_3}}{dt} = -X_1 r_{C4} i_{L_2} - X_1 r_{C4} i_{L_3} + X_0 r_{C4} V_{C3} + (1 - X_0 r_{C4}) V_{C4} \quad (38)$$

$$L_4\frac{di_{L_4}}{dt} = V_{C5-}V_{Co} \quad (39)$$

$$C_1\frac{dV_{C1}}{dt} = X_3(V_{C2} - V_{C1}) \quad (40)$$

$$C_2\frac{dV_{C2}}{dt} = X_3(V_{C1} - V_{C2}) \quad (41)$$

$$C_3\frac{dV_{C3}}{dt} = (X_1 - 1)i_{L_2} + (X_1 - 1)i_{L_3} - X_0 V_{C3} + X_0 V_{C4} \quad (42)$$

$$C_4\frac{dV_{C4}}{dt} = -X_1 i_{L_2} - X_1 i_{L_3} + X_0 V_{C3} - X_0 V_{C4} \quad (43)$$

$$C_5\frac{dV_{C5}}{dt} = -i_{L_4} \quad (44)$$

$$C_o\frac{dV_{Co}}{dt} = i_{L_4} - \frac{V_{Co}}{R} \quad (45)$$

The state equations of mode *II* ($t_2<t<t_3$), are given as:

$$L_1\frac{di_{L_1}}{dt} = V_{in} - X_3 X_4 i_{L_1} + X_3 r_{C3} i_{L_2} + (-1 + X_3)V_{C1} + X_3 V_{C2} - X_3 V_{C3} \quad (46)$$

$$L_2\frac{di_{L_2}}{dt} = L_3\frac{di_{L_3}}{dt} = 0.5[X_2 r_{C3} V_{C1} - X_6 i_{L_1} + (r_{C4} + X_2 r_{C3}{}^2) i_{L_2} - X_1 r_{C4} i_{L_3} + (1 - X_2 r_{C3})V_{C3} + V_{C4} - V_{C5}] \quad (47)$$

$$L_4\frac{di_{L_4}}{dt} = -V_{Co} \quad (48)$$

$$C_1\frac{dV_{C1}}{dt} = X_2(r_{C2} + r_{C3})i_{L_1} - X_2 r_{C3} i_{L_2} + X_2(-V_{C1} - V_{C2} + V_{C3}) \quad (33)$$

$$C_2\frac{dV_{C2}}{dt} = [X_2(r_{C2} + r_{C3}) - 1]i_{L_1} - X_2 r_{C3} i_{L_2} + X_2(-V_{C1} -$$

$V_{C2} + V_{C3})$ (49)

$$C_3 \frac{dV_{C3}}{dt} = -[X_2(r_{C2} + r_{C3}) - 1]i_{L_1} + (X_2 r_{C3} - 1)i_{L_2} + X_2(V_{C1} + V_{C2} - V_{C3}) \quad (50)$$

$$C_4 \frac{dV_{C4}}{dt} = -i_{L_2} \quad (51)$$

$$C_5 \frac{dV_{C5}}{dt} = i_{L_2} \quad (52)$$

$$C_o \frac{dV_{Co}}{dt} = i_{L_4} - \frac{V_{Co}}{R} \quad (53)$$

Where, X_0-X_6 are defined as follows:

$$X_0 = \frac{1}{r_{c3}+r_{c4}} \quad ,X_1 = \frac{r_{c3}}{r_{c3}+r_{c4}} \quad , \quad X_2 = \frac{1}{r_{c1}+r_{c2}+r_{c3}} \quad ,$$

$$X_3 = \frac{r_{c1}}{r_{c1}+r_{c2}+r_{c3}} \quad (54)$$

$$X_4 = r_{c2} + r_{c3} \quad ,X_5 = \frac{1}{r_{c1}+r_{c2}} \quad , \quad X_6 = 0.5(r_{c4} - X_2 {r_{c3}}^2 - r_{c3}) \quad (55)$$

The simulation results of the frequency response (Bode plot) control-to-output voltage (V_o/d) transfer function of the presented circuit is provided in Fig. 8. Also, the dominant pole and zero map of the transfer function is depicted in Fig. 9. The values of simulation parameters are selected as V_{in}=20V, D=0.5, R=200 Ω, L_1= 0.2mH, L_2= L_3= 8mH, L_4= 5mH, C_1= C_4= C_5=200uF, C_2=220uF, C_3=C_o=100uF and r_{C1}=0.1 Ω r_{C2}=0.2 Ω, r_{C3}=0.1 Ω, r_{C4}=0.1Ω. Regarding these figures, the suggested converter is stable without right half-plane (RHP) zero (minimum phase behavior (MP). This behavior is due to the use of an inductor in the output of the circuit (L_4), which leads to the continuity of the circuit current on the output side and therefore the MP behavior. It is noteworthy that one of the prominent features of most current-fed high step-up converters is NMP behavior which led to an inverse response, narrow bandwidth, low transient response and destabilization in higher voltage gain.

V. Comparison with Other Topologies

In this part, a comparative study between the presented quadratic high voltage gain converter and other similar converters is provided. For this purpose, some typical key indicators including the number of components, voltage conversion ratio, input current ripple, minimum phase

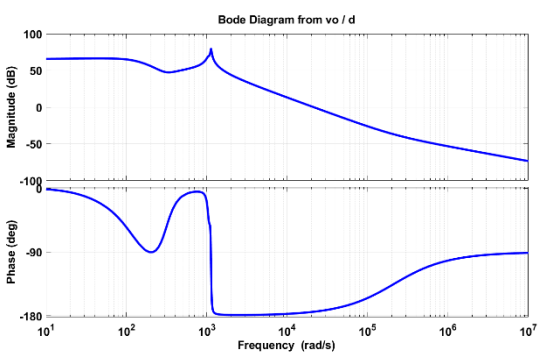

Fig. 8. Bode diagram Control-to-output transfer function $G_{vo\text{-}d}$

of the proposed converter.

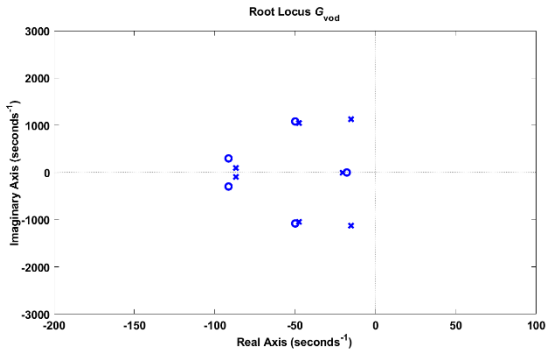

Fig. 9. Root locus graph for control-to-output voltage transfer function G_{vod}.

behavior, and voltage stress are considered, which are summarized in Table 2. From the table, the converters in [3], [29]-[32] have minimum phase (MP) behavior which leads to a fast transient response. Also, low input current ripple is the main demerit of the converters in [17], [19], [32] and [3] that limits their applications for RES. Moreover, converters [28] and [12] suffer from the lack of common ground between input DC source and output load.

Fig. 10 represents the voltage gain comparison of the converters given in the comparison table. Regarding this figure, the proposed converter along with the converters in [11], [12], [17] and [25] can provide higher output DC voltage gains than the other counterparts. However, these converters suffer from a high input current ripple (in [17]), the lack of common ground (in [12]), NMP behavior (in [11], [12], [19], and [25]) and use two active switches (in [17]). Also, among MP structures, the proposed converter has a higher voltage gain. Moreover, the experimental efficiency along with the characteristics of the circuit implemented in different converters was prepared in the comparison table. According to the table, compared to other converters, the proposed converter is able to provide proper efficiency.

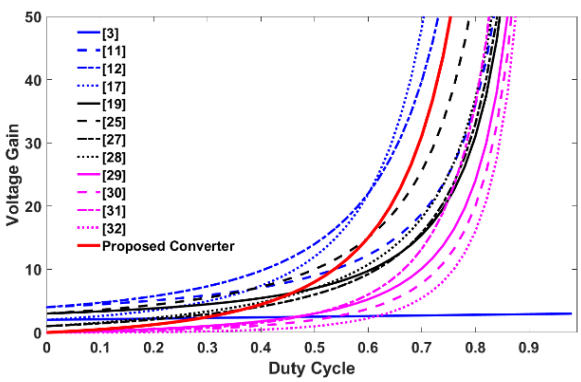

Fig. 10. Total voltage gain comparison.

TABLE 2 PERFORMANCE COMPARISON OF THE PROPOSED CONVERTER WITH OTHER COUNTERPARTS.

Converter	No. of Components S/D/C/L	Voltage Gain	Low Input Current Ripple	Minimum Phase Behavior	Maximum Voltage Stress on Switch	Maximum Voltage Stress on Diodes	Common Ground	Sample prototype specifications Vin/Vo/f/ Po/Eff.
[3]	2/4/5/1	2+D	No	Yes	$\frac{V_o}{2+\mathrm{D}}$	$\frac{V_o}{2+\mathrm{D}}$	Yes	26V/44V/50 KHz/100W/92.8%
[11]	1/5/4/2	$\frac{(2-D)^2}{(1-D)^2}$	Yes	No	$\frac{V_o}{2-\mathrm{D}}$	$\frac{V_o}{2-\mathrm{D}}$	Yes	10V/70V/50 KHz/ 200W/88%
[12]	1/9/5/3	$\frac{4-2\mathrm{D}+2D^2}{(1-D)^2}$	Yes	No	$\frac{(1+D)V_o}{4-2\mathrm{D}+2D^2}$	$\frac{(1+D)V_o}{4-2\mathrm{D}+2D^2}$	No	-
[17]	2/5/4/3	$\frac{2-\mathrm{D}}{(1-D)^3}$	No	No	$\frac{1-\mathrm{D}}{2-D}V_o$	$\frac{1}{(1-D)^2}V_o$	Yes	24V/340V/20KHz/ 500W/93%
[19]	2/3/3/2	$\frac{3-3\mathrm{D}+D^2}{(1-D)^2}$	No	No	$\frac{V_o}{3-3\mathrm{D}+D^2}$	$\frac{(2-D)V_o}{3-3\mathrm{D}+D^2}$	Yes	20V/190V/25 KHz/ 123W/94%
[25]	1/6/4/3	$\frac{3-\mathrm{D}}{(1-D)^2}$	Yes	No	$\frac{2V_o}{3-\mathrm{D}}$	$\frac{(1+D)V_o}{3-\mathrm{D}}$	Yes	20V/200V/50 KHz/ 100W/89%
[27]	1/5/6/4	$\frac{1+2\mathrm{D}-2D^2}{(1-D)^2}$	Yes	No	$\frac{V_o}{1+2\mathrm{D}-2D^2}$	$\frac{V_o}{1+2\mathrm{D}-2D^2}$	Yes	24V/222V/50 KHz/ 200W/90%
[28]	1/6/8/5	$\frac{1+3\mathrm{D}-3D^2}{(1-D)^2}$	Yes	No	$\frac{V_o}{1+3\mathrm{D}-3D^2}$	$\frac{V_o}{1+3\mathrm{D}-3D^2}$	No	20V/200V/50 KHz/ 180W/90%
[29]	2/2/3/3	$\frac{\mathrm{D}(2-\mathrm{D})}{(1-D)^2}$	Yes	Yes	$\frac{V_o}{\mathrm{D}(2-\mathrm{D})}$	V_o	Yes	-
[30]	2/2/3/3	$\frac{\mathrm{D}}{(1-D)^2}$	Yes	Yes	$\frac{V_o}{\mathrm{D}}$	$\frac{V_o}{\mathrm{D}}$	Yes	18V/48V/40 KHz/ 48W/89%
[31]	2/3/4/3	$\frac{\mathrm{D}(1+\mathrm{D})}{(1-D)^2}$	Yes	Yes	$\frac{V_o}{\mathrm{D}}$	$\frac{V_o}{\mathrm{D}}$	Yes	-
[32]	2/2/3/3	$\frac{D^2}{(1-D)^2}$	No	Yes	$\frac{V_o}{\mathrm{D}}$	$\frac{V_o}{\mathrm{D}}$	Yes	20V/100V/50 KHz/ 100W/92%
Proposed Converter	1/7/6/4	$\frac{4D}{(1-D)^2}$	Yes	Yes	$\frac{V_o}{\mathrm{D}}$	$\frac{V_o}{\mathrm{D}}$	Yes	20V/160V/50 KHz/ 80W/93%

V. Design Considerations

In this part, the design considerations of the presented topology are discussed. Duty cycle of the power switch is achieved from the desired voltage gain ratio (14) as:

$$D = \frac{2G+4-4\sqrt{1+G}}{2G} \quad (56)$$

In (40), G is the voltage conversion ratio of the circuit. Due to the degrading effects of high current ripple from RES such as short lifetime, circuit design in CCM with low input current ripple is preferred. Considering allowable input current ripple ($\Delta I_{in} \approx 20\%.I_{in}$), the minimum value of the input inductance L_1 of the converter can be determined as:

$$L_1 > \frac{V_{L1}.D}{\Delta I_{in}.f_s} = \frac{V_{in}.D}{\Delta I_{in}.f_s} \quad (57)$$

Where, f_s is the switching frequency of the single power switche. Moreover, the proper values of the other inductors of the proposed circuit (L_2, L_3 and L_4) are calculated as:

$$L_2 > \frac{2D.V_{in}}{\Delta I_{L2}.(1-D)f_s} \quad (58)$$

$$L_3 > \frac{2D.V_{in}}{\Delta I_{L3}.(1-D)f_s} \quad (59)$$

$$L_4 > \frac{(1-D).V_o}{\Delta I_{L4}.f_s} \quad (60)$$

Based on the allowable output voltage ripple (ΔV_{Co}), the value of the output capacitance C_o can be given as:

$$\boldsymbol{C_o > \frac{(1-D).V_o}{8.L_4\Delta V_{co}.f_s^2}} \quad (61)$$

Furthermore, the proper values of the other used capacitors in the presented circuit can be designed as:

$$C_1 > \frac{2D.I_o}{\Delta V_{C1}(1-D)f_s} \quad (62)$$

$$C_2 > \frac{2D.I_o}{\Delta V_{C2}(1-D)f_s} \quad (63)$$

$$C_3 > \frac{D(1+D).I_o}{\Delta V_{C3}(1-D)f_s} \quad (64)$$

$$C_4 > \frac{D.I_o}{\Delta V_{C4}f_s} \quad (65)$$

$$C_5 > \frac{D.I_o}{\Delta V_{C5}f_s} \quad (66)$$

With the help of this non-ideal voltage gain, the real maximum voltage rates across the semiconductor elements can be determined as follows:

$$V_S = V_{D7} = \frac{4V_{in}}{(1-D)^2} = \frac{V_o}{D}.\alpha \quad (67)$$

$$V_{D1} = V_{D2} = V_{D3} = \frac{V_{in}}{1-D} = \frac{(1-D)V_o}{4D}.\alpha \quad (68)$$

$$V_{D4} = V_{D5} = \frac{2V_{in}}{1-D} = \frac{(1-D)V_o}{2D}.\alpha \quad (69)$$

Which, α is defined as:

$$\alpha = \frac{1}{\left(1-\frac{r_L}{R}\frac{4D}{(1-D)^4}-\frac{r_S}{R}\frac{4D^2}{(1-D)^4}-\frac{r_D}{R}\frac{4D}{(1-D)^3}\right)} \quad (70)$$

VI. Experimental Validation

In order to verify the performance of the introduced circuit, an 80W sample prototype with an input voltage of V_{in}=20 V and V_o=160V was built in the laboratory. The specifications of the components used to implement this sample prototype are summarized in Table *3*.

Fig.11 (a) shows the DC voltage of the output load of the converter in the sample prototype of the introduced circuit. Also, the measured voltage stresses of the switching components (MOSFET and diodes) components are presented in Fig. 11 (b)-(e). The current waveforms of the switching components of the proposed converter are illustrated in Fig. 11 (f)-(l). Also, Fig. 11 (m) presents the experimental results of the dynamic responses of the output voltage and the output

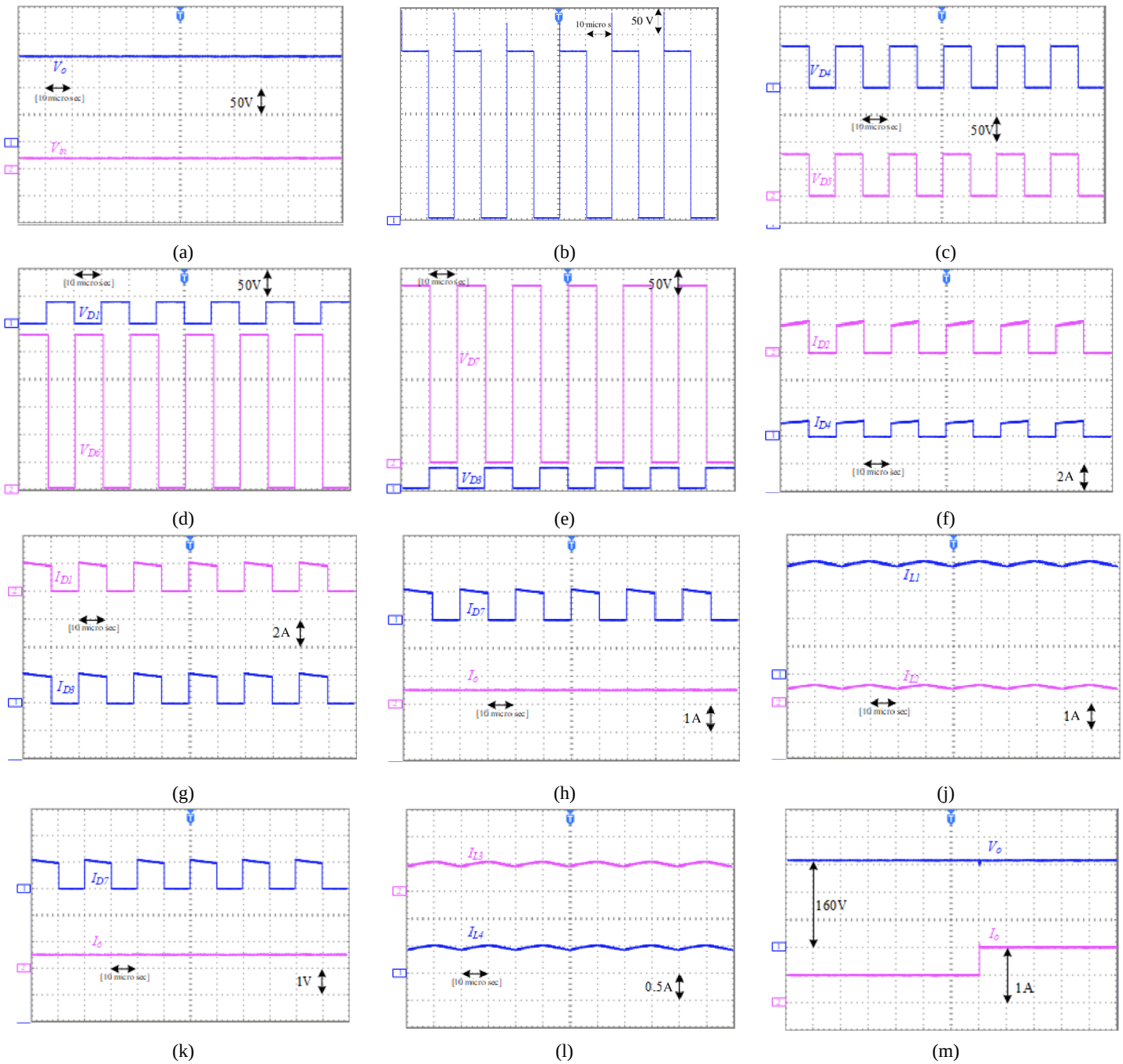

Fig. 11. Experimental results. (a)V_o and V_{in} (b) V_s (c) V_{D4}, V_{D5}, (d) V_{D1}, V_{D6}, (e) V_{D7}, V_{D3}, (f) I_{D2}, I_{D4}, (g) I_{D1}, I_{D3}, (h) I_{D7}, I_o, (j) I_{L1}, I_{L2}, (k) I_{D7}, I_o, (l) I_{L3}, I_{L4}, (m) Dynamic response of the output voltage along with the output load current of the proposed circuit under the output load changing from R_L=320Ω to R_L=160Ω.

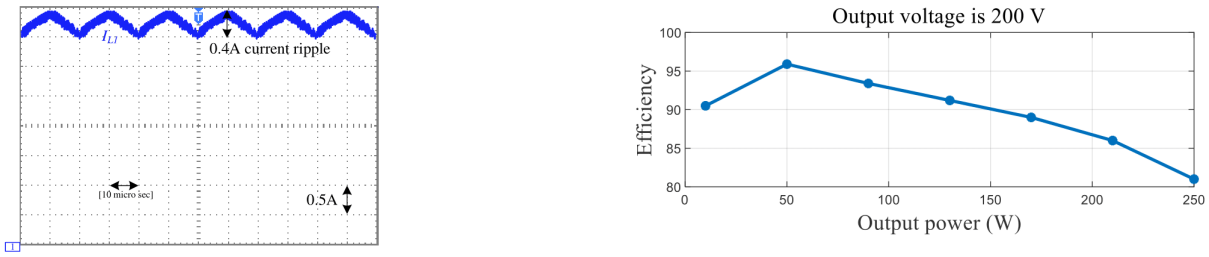

(a) (b)

Fig.12. (a) Current ripple value of the input inductor, (b) Experimental efficiency of the proposed converter versus the output power.

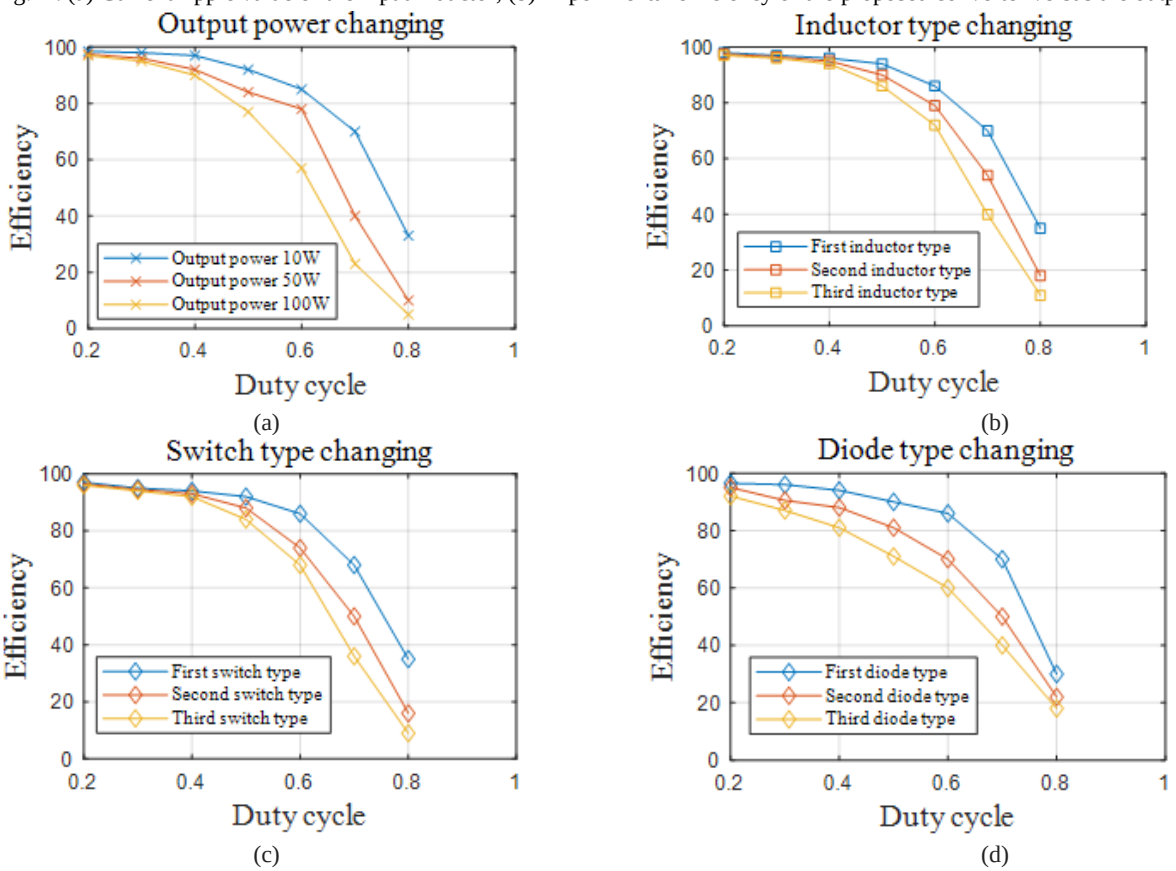

(a) (b) (c) (d)

Fig.13 . Experimental results of the efficiency versus, (a) output power, (b) inductor types, (c) power switch type.

TABLE *3* KEY PARAMETERS OF PROTOTYPE SETUP.

Parameter	Values
Output Power (P_{out})	80 W
Input Voltage (V_{in})	20 V
Output Voltage (V_o)	160 V
Switching Frequency (f_s)	50 kHz
Capacitors C_1 –C_o	190 µF
Power Switch S	IRFP250
Input Inductor L_{in}	210 µH / EE42/21/20
Inductors L_2, L_3, L_4	2 mH
Diodes D_1 – D_7	SFF100-04CT

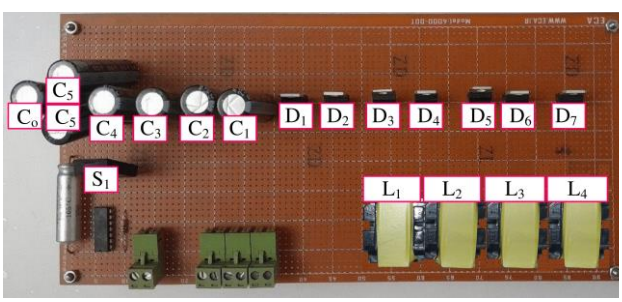

Fig. 14. Picture of the proposed converter prototype.

load current of the introduced circuit at a step change in the output load from R_L=320Ω to R_L=160Ω.

In addition, according to Fig. 12 (a), the input current is continuous with low ripple. From this figure, the value of input current ripple in the proposed converter is about 0.4A.

Moreover, the experimental efficiency of the proposed converter under the output power is provided in Fig. 12 (b). regarding this figure, the maximum efficiency of the suggested topology is about 0.93%.

I. Conclusion

A new transformerloss high voltage gain of quadratic CUK-based DC-DC converter with low input current ripple has been suggested in this paper. The introduced circuit provides unique features, including minimum phase behavior, high voltage gain ratio, enough high efficiency, and common ground between the source and load sides. Operating principles along with the steady-state analysis of the proposed converter are thoroughly explained. Then the converter is compared with other similar circuits, and the advantages of the suggested topology are shown. Moreover, the low-frequency behavior of the introduced circuit is obtained and its minimum phase feature is analyzed. The experimental results from a sample prototype 80*W*, 20V-160V have verified the feasibility of the presented converter design. Moreover, the sensitivity analysis of the efficiency and voltage gain at different inductors, switches and diodes are provided.

REFERENCES

[1] G. Zhang, H. Chen, S. S. Yu, N. Jin, and Y. Zhang, "Generalized flexible voltage pumping module for extra high step high voltage gain converters in electric vehicles," IEEE Trans. on Vehicular Tech., vol. 70, pp. 6463-6471, 2021.

[2] S. Moosavi, "Efficiency improvement and inrush current reduction in a non-isolated DC-DC converter," International Journal of Industrial Electronics Control and Optimization, vol. 2, no. 2, pp. 137-144, 2019.

[3] M. Soltani, A. Mostaan, Y. P. Siwakoti, P. Davari, and F. Blaabjerg, "Family of step-up DC/DC converters with fast dynamic response for low power applications," IET Power Electronics, vol. 9, pp. 2665-2673, 2016.

[4] M. Eskandarpour Azizkandi, F. Sedaghati, and H. Shayeghi, "A New Boost DC-DC Converter Based on a Coupled Inductor and Voltage Multiplier Cells," International Journal of Industrial Electronics Control and Optimization, vol. 2, no. 4, pp. 265-278, 2019.

[5] S. Hasanpour, A. Baghramian, and H. Mojallali, "A new high-gain coupled-inductor SEPIC converter for a microgrid system," in Power Electronics, Drive Systems & Technologies Conference, 2017, pp. 294-299.

[6] S. Hasanpour, Y. P. Siwakoti, and F. Blaabjerg, "A new high efficiency high step-up DC/DC converter for renewable energy applications," IEEE Trans. on Ind. Electron., vol. 70, pp. 1489-1500, 2022.

[7] S. Hasanpour, "New structure of single-switch ultra-high-gain DC/DC converter for renewable energy applications," IEEE Trans. on Power Electron., vol. 37, pp. 12715-12728, 2022.

[8] R. Sharifi Shahrivar, H. Gholizadeh, A. Siadatan, and S. E. Afjei, "Design and Implementation of a Modified Boost Topology with High Voltage Ratio and Efficiency Besides the Lower Semiconductors Stresses," Research and Technology in the Electrical Industry, vol. 1, pp. 75-84, 2022.

[9] N. Totonchi, H. Gholizadeh, S. Mahdizadeh, and E. Afjei, "A high step up DC-DC converter based on the cascade boost, voltage multiplier cell and self lift luo converter," in Smart Grid Conference (SGC), 2020, pp. 1-5.

[10] H. Gholizadeh, N. Totonchi, R. S. Shahrivar, S. Mahdizadeh, E. Afjei, and A. Abbasi, "Design and implementation of a transformerless high step-up dc-dc converter based on conventional boost converter and voltage multiplier cells," in Power Electronics, Drive Systems, and Technologies Conference (PEDSTC), 2021, pp. 1-5.

[11] S. Khan, A. Mahmood, M. Zaid, M. Tariq, C.-H. Lin, J. Ahmad, et al., "A high step-up dc-dc converter based on the voltage lift technique for renewable energy applications," Sustainability, vol. 13, p. 11059, 2021.

[12] S. Chakraborty and A. Kumar, "A multilevel based high gain switched inductor quadratic DC-DC boost converter," IFAC-PapersOnLine, vol. 55, pp. 448-453, 2022.

[13] P. E. Babu, S. Vemparala, T. Pavithra, and S. Kumaravel, "Switched LC network-based multistage ultra gain DC-DC converter," IEEE Access, vol. 10, pp. 64701-64714, 2022.

[14] N. Prabaharan, T. Santhosh, R. Rajesh, M. Salem, and S. Mekhilef, "A new High Gain Non-Isolated DC-DC Converter for Photovoltaic System," in IEEE IAS Global Conference on Renewable Energy and Hydrogen Technologies (GlobConHT), 2023, pp. 1-5.

[15] S. Mahdizadeh, M. T. Monfared, S. E. Fazeli, and M. T. Bina, "A Single Switch Common-ground Ultra-high Gain Non-isolated DC-DC Converter," in Power Electronics, Drive Systems, and Technologies Conference (PEDSTC), 2023, pp. 1-5.

[16] S. Naresh, S. Peddapati, and M. L. Alghaythi, "Non-isolated high gain quadratic boost converter based on inductor's asymmetric input voltage," IEEE Access, vol. 9, pp. 162108-162121, 2021.

[17] B. Krishna and V. Karthikeyan, "Ultra-voltage gain step-up DC-DC converter for renewable energy micro-source applications," IEEE Trans. on Energy Conversion, vol. 37, pp. 947-957, 2021.

[18] S. Mahdizadeh and E. Afjei, "A Quadratic high gain non-isolated DC-DC converter suitable for renewable applications," in Smart Grid Conference (SGC), 2021, pp. 1-6.

[19] K. Varesi, N. Hassanpour, and S. Saeidabadi, "Novel high step-up DC–DC converter with increased voltage gain per devices and continuous input current suitable for DC microgrid applications," International Journal of Circuit Theory and Applications, vol. 48, pp. 1820-1837, 2020.

[20] S. Gopinathan, V. S. Rao, and S. Kumaravel, "Enhanced Voltage Gain Boost DC-DC Converter with Reduced Voltage Stress and Core Saturation," IEEE Trans. on Circuits and Systems II: Express Briefs, 2023.

[21] N. Subhani, Z. May, M. K. Alam, I. Khan, M. A. Hossain, and S. Mamun, "An Improved Non-Isolated Quadratic DC-DC Boost Converter With Ultra High Gain Ability," IEEE Access, vol. 11, pp. 11350-11363, 2023.

[22] M. Baba, A. Giridhar, and B. Narasimharaju, "Active switched-capacitor based ultra-voltage gain quadratic boost DC-DC converters," International Journal of Circuit Theory

In addition, the experimental efficiency of the proposed circuit at different output powers, switch and inductor types at V_o =160 V are measured which are presented in Fig. 13. A Photograph of the sample prototype of the proposed converter is also presented in Fig. 14.

and Applications, vol. 51, pp. 1389-1416, 2023.
[23] S. Gopinathan, V. S. Rao, and K. Sundaramoorthy, "Family of non-isolated quadratic high gain DC–DC converters based on extended capacitor-diode network for renewable energy source integration," IEEE Journal of Emerging and Selected Topics in Power Electronics, vol. 10, pp. 6218-6230, 2022.
[24] M. T. Monfared, H. Gholizadeh, S. M. Kalamialhashem, S. Amini, S. A. A. Afjei, and S. E. Afjei, "A Cubic Transformer-less DC-DC Converter with Continuous Input Current: Mathematical model, Simulation, and Experimental," in Power Electronics, Drive Systems, and Technologies Conference (PEDSTC), 2022, pp. 19-25.
[25] H. Gholizadeh and L. Ben-Brahim, "A new non-isolated high-gain single-switch DC–DC converter topology with a continuous input current," Electronics, vol. 11, p. 2900, 2022.
[26] H.-D. Liu, A. S. Jana, and C.-H. Lin, "An improved high gain continuous input current quadratic boost converter for next-generation sustainable energy application," IEEE Trans. on Circuits and Systems II: Express Briefs, 2023.
[27] R. Rajesh, N. Prabaharan, and T. Santhosh, "Design and Analysis of a Non-isolated DC-DC Converter with a High-voltage Conversion Ratio," IEEE Trans. on Circuits and Systems II: Express Briefs, 2022.
[28] R. Rajesh and N. Prabaharan, "Design of New Nonisolated High Gain Converter for Higher Power Density," International Transactions on Electrical Energy Systems, vol. 2023, 2023.
[29] H. Gholizadeh, S. A. Gorji, E. Afjei, and D. Sera, "Design and implementation of a new cuk-based step-up DC–DC converter," Energies, vol. 14, p. 6975, 2021.
[30] M. Okati, M. Eslami, M. Jafari Shahbazzadeh, and H. Shareef, "A new transformerless quadratic buck–boost converter with high-voltage gain ratio and continuous input/output current port," IET Power Electronics, vol. 15, pp. 1280-1294, 2022.
[31] A. H. S. Mahdizadeh, "A Non-inverting Transformerless Semi-Quadratic Buck-Boost Converter," in International Conference on Power, Energy and Electrical Engineering (CPEEE), 2022.
[32] H. Gholizadeh, S. A. Gorji, and D. Sera, "A Quadratic Buck-Boost Converter With Continuous Input and Output Currents," IEEE Access, vol. 11, pp. 22376-22393, 2023.
[33] M. Ehsani, M. Saeidi, H. Radmanesh, and A. Abrishamifar, "Comparisons between generalized predictive control and linear controllers in multi-input DC-DC boost converter," International Journal of Industrial Electronics Control and Optimization, vol. 3, no. 1, pp. 27-34, 2020.
[34] H. Shojaeian, S. Hasanzadeh, and M. Heydari, "High efficient and high step-up dual switches converter based on three coupled inductors," International Journal of Industrial Electronics Control and Optimization, vol. 1, no. 2, pp. 143-152, 2018.
[35] S. Hasanpour, A. Baghramian, and H. Mojallali, "Reduced - order small signal modelling of high - order high step - up converters with clamp circuit and voltage multiplier cell," IET Power Electronics, vol. 12, no. 13, pp. 3539-3554, 2019.

Hossein Gholizadeh's birthplace is Tabriz, Iran, and his date of birth is October 3, 1996. The individual completed their secondary education in mathematics at Ferdousi High School of Tabriz, recognized as one of the prominent high schools in Iran. This academic achievement was attained in 2015. In 2019, he obtained a Bachelor of Science in Electrical Engineering from Shahid Beheshti University in Tehran, Iran. Furthermore, he commenced pursuing a Master's degree without being required to take an entrance examination due to his exceptional academic achievement, which earned him the highest rank. The individual in question has pursued a Master's in power electronics and electrical machines at Shahid Beheshti University. The focus of his research lies in the examination of non-isolated high step-up DC-DC converter topologies. The individual in question was the research group head focused on designing DC-DC converters in the University of Shahid Beheshti Power Electronics Lab. He provides instruction to undergraduate and graduate students interested in the topology of DC-DC converters. The individual maintains an ongoing research partnership with International Qatar University, Deakin University in Australia, and Queensland University in Australia. Significantly, the individual attained the fifth position in the national PhD entrance examination of the Islamic Republic of Iran. Currently, he holds the position of the head of the DC-DC converters' design subgroup within the power electronics group at Tehran University.

Sara Hasanpour was born in Iran, in 1979. She received the B.S. degree in electron ic engineering from Azad Islamic University, Lahijan Branch, Iran, in 2002, the M.S. degree from the Isfahan University of Technology, Isfahan, Iran, in 2005, and the Ph.D. degree in power electronics engineering from University of Guilan, Rasht, Iran, in 2019. She received the best Ph.D. thesis award in power electronics engineering in Iran, awarded by the Power Electronics Society of Iran, 2020. She is currently assistant professor at Azad Islamic University, Ramsar Branch, Ramsar, Iran. Her major research interests include design and implementation of step-up/step-down switch-mode DC/DC converters with high-power density, renewable energy technologies, control and modeling of switched-mode DC/DC converters and electronic ballasts.

IECO

This page intentionally left blank.

International Journal Of
Industrial Electronics Control and Optimization
Print ISSN: 3517-2645
Online ISSN: 3568-2645
Homepage: https://ieco.usb.ac.ir/

An Analytical Approach to Min-Time Control of Discrete-Time Linear Systems with Constrained Input

Valiollah Ghaffari
Department of Electrical Engineering, Persian Gulf University, Bushehr, Iran
Corresponding author's email: vghaffari@pgu.ac.ir

Article Info

Article type:
Research Article

Article history:
Received: 12-June-2024
Received in revised form: 18-September-2024
Accepted: 23-September-2024
Published online: 21-March-2025

Keywords:
Constrained systems,
Discrete-time models,
Min-time control,
State transition matrix.

ABSTRACT

Employing discrete-time techniques, the min-time control of continuous-time dynamical systems is mainly studied through an analytical framework. To this aim, the exact discrete-time model of the linear time-invariant systems is specified through a zero-order hold. The optimal solution could be directly determined from some necessary conditions. However, the structure of the optimum control sequences is derived by utilizing the well-known Pontryagin principle. Employing the state transition matrix, the states of the control system are computed at the switching times. The switching times of the control signal would be found from a set of nonlinear algebraic equations. Accordingly, the transformation of the system's states, from a known initial point to a specific value, would be accomplished in the minimum possible time. Applying the proposed scheme, the exact (integer) values of the switching times and the final time are numerically determined from the solution of an algebraic equation. Several discrete-time and continuous-time examples are discussed and simulated to show the feasibility and effectiveness of the suggested procedure in the dynamical systems. The simulation results confirm the method's advantages over the existing ones.

NOMENCLATURE

$x(t)$	The states of continuous-time system	$A_c,\ B_c$	The matrices of continuous-time system
$u(t)$	The inputs of continuous-time system	$A,\ B$	The matrices of discrete -time system
x_k	The states of discrete-time system	m	Number of control inputs
u_k	The inputs of discrete-time system	n	Number of system's states
T_s	Sampling-time	$\|.\|$	Two-norm of a matrix
N	Number of samples	$\det(.)$	Determinant

I. Introduction

In the optimal control, satisfying some constraints on the inputs and the outputs, the profile of the system's input is reshaped to minimize a known cost function. Deriving necessary and sufficient optimality conditions, the optimal control can be formulated in the dynamical descriptions. Most times, there may not be a systematic guideline to the solution of the optimal control. Hence the approximated techniques have been interested in the control applications.

The control efforts may be not optimally found in many applications. Moreover, the optimal control does not have a unique solution. As an example, in the linear time-invariant (LTI) model without input limitation, the min-time control has not an optimum solution [1]. Considering quadratic cost functions, the optimal control of the unconstrained LTI systems has a unique solution. Due to the emergence of a two-point boundary value problem, determining the optimum solution exactly may have some complexities via the analytical ways [1]. Because of such difficulty, it may be of interest to focus on suboptimal or near-to-optimal control policies [2-5]. Numerical methods like the wavelet tool and iterative mechanisms may be utilized to determine the approximated solution [6, 7]. Using semi-definite programming, an optimal control is addressed for piecewise affine systems [8].

In the min-time problems, the input shape is selected such that the goal would be satisfied in the minimum time. Usually, the bang-bang compensator is reduced to a min-time control. Compared to the other forms like minimum fuel or energy, the solution of the min-time has extra obstacles. The min-time control has been applied in the aerospace vehicles [9]. The optimal guidance issues may be treated as a control system [10-12]. Hence, achieving the exact solutions would be helpful in such cases. The phase plane is a graphical tool for the min-time control in the second-order systems. Although the phase plane is efficient, it cannot be generalized to the high-order models [1]. In the constrained models, a numerical framework is developed for finding the solution of the optimal control problems [13].

There have been some attempts to the min-time issues. As an example, the min-time is studied in controlling a stepping motor [14]. The min-time control is robustly assessed in constrained discrete-time descriptions [15]. Employing a non-smooth optimization, the min-time problem is discussed in discrete-time linear systems [16]. The algebraic solution is examined in min-time velocity planning [17]. The min-time control is optimally found in the LTI model with real poles [18]. The fast solution of the min-time problem is computed in low-thrust transfer with eclipses [19]. Based on lattice theory, the min-time is solved in speed planning [20]. The solution of the HJB min-time is revealed via multilevel techniques [21]. Insuring dead-beat property, an optimal control law is designed in continuous-time dynamical systems [22]. The min-time control of Boolean networks is performed via a fast graphical approach [23]. Concerning smooth transition in communication topology, the minimum time formation control is studied in an underwater vehicle [24]. Based on Pontryagin principle and penalty functions, the predictive control is formulated in continuous-time nonlinear systems [25].

The min-time problem with a limited input signal may not have a solution due to the imposed nonlinearity. However, the optimum control effort can be explicitly obtained in the feasible cases. Recently, relying on a state transition matrix, the min-time control is formulated and solved in the constrained continuous-time systems [26]. Thinking of such an idea, the control input would contain some additive pulses at the calculated time-instants. So, the control aims may disappear due to the sensitivity to the inaccurate and approximated time-instants. Such a drawback can be significantly handled in the discrete-time form. Hence, this point motivates the author to study the min-time property in the LTI plant under input limitations and sampled-data control. Thus the minimum time and the switching instants will be computed by the addressed algebraic equation. As a result, the optimal control signal can be explicitly determined in typical LTI systems. Compared to the previous studies, finding some integer numbers, corresponding to the switching instants, would be the main advantage of the current work. Therefore, the sensitivity of the overall performance is effectively diminished via the discrete-time models. To implement such an idea, the optimal inputs are first computed from an algebraic equation. Then the corresponding differential or difference equations are solved via a recursive scheme.

The structure of the paper is divided as follows: In Section 2, the well-known min-time control is formulated in the discrete-time linear systems with a constrained input. To compute the optimal control signal, the key results of the paper are presented in Section 3. To show the method's feasibility, some examples are analytically reported and simulated in Section 4. The concluding points are briefly provided in the last section.

II. Problem statement

Consider the following constrained LTI systems:

$$\dot{x} = A_c x + B_c u, \tag{1}$$

where $x(t) \in \mathbb{R}^n$ is the state vector and $u(t) \in \mathbb{R}^m$ is the control effort. In (1), the input signals are constrained by $|u_i(t)| \leq 1$, $i = 1,2,\dots,m$, while the matrices $A_c \in \mathbb{R}^{n\times n}$ and $B_c \in \mathbb{R}^{n\times m}$ are some given terms. It is desired to find an input $u(t)$ such that the states of the dynamic (1) move from the initial point x_0 to the final value $x(t_f)$ in the minimum possible time. So the cost function that is to be optimized is $J = \int_0^{t_f} 1\mathrm{d}t$.

It is established that the control signal involves some square pulses at some time-instants [26]. Notwithstanding, the switching times should be calculated with special precaution. To handle such a complexity, (1) is discretized under sampling-time T_s. Imagining a zero-order hold (ZOH) in the system's input, the equivalent discrete-time model can be found as

$$x_{k+1} = Ax_k + Bu_k, \tag{2}$$

where $A = e^{A_c T_s}$ and $B = \int_0^{T_s} e^{A_c \tau} B_c \mathrm{d}\tau$. Moreover, the cost function would be rewritten as $J = T_s \sum_{k=0}^{N-1} 1$. Concerning the control limitation ($u_k = [u_{1k} \quad u_{2k} \quad \dots \quad u_{mk}]^T$, $|u_{ik}| \leq 1$, $i = 1,2,\dots,m$) and $t_f = NT_s$, N input control sequences will be determined to transform the system's states from x_0 to x_N in the minimum time.

Assumption 1. To guarantee the control aim in the minimum time, the following condition holds:

$$\|x_N\| \leq \|A\|^N \|x_0\| + \|B\| \frac{\|A\|^N - 1}{\|A\| - 1}. \tag{3}$$

The right hand side of (3) with respect to N would be increasing if $\mathrm{Ln}(\|A\|)\left(\|x_0\| + \frac{\|B\|}{\|A\|-1}\right) > 0$. Based on the discrete-time state transition matrix, to fulfill the control aims, an analytical framework is developed in the next section.

III. Main results

The control aims would be fulfilled by finding some appropriate control signals u_k. To this, the main results of this paper is presented as follows:

Theorem 1. In the LTI system (2) with Assumption 1, for some sequences u_k, $k = 0,1,\dots,n-1$ with $|u_{ik}| = 1$, $i = 1,2,\dots,m$, if there exists integer numbers k_i, $i = 1,\dots,n$, such that the following identity has a solution:

$$\begin{aligned} &x_N + (A-I)^{-1}Bu_{n-1} \\ &= A^{k_n}(x_0 + (A-I)^{-1}Bu_0) \\ &+ \sum_{i=1}^{n-1} A^{k_n-k_i}(A-I)^{-1}B(u_i - u_{i-1}), \end{aligned} \tag{4}$$

where $k_n = N$ and $x_{k_n} = x_N$, then, by applying the control sequence:

$$u_k = \begin{cases} u_0, & 0 \le k < k_1 \\ u_1, & k_1 \le k < k_2 \\ \vdots & \\ u_{n-1}, & k_{n-1} \le k \le k_n \end{cases} \tag{5}$$

the system's states move from x_0 to x_N in the minimum possible time.

Proof. To solve the optimization issue, as reported in [1], the Hamiltonian function is constructed as

$$H = 1 + \lambda_{k+1}^T(Ax_k + Bu_k). \tag{6}$$

Hence the stationary condition would be reduced to

$$\frac{\partial H}{\partial u} = B^T\lambda_{k+1} = 0. \tag{7}$$

As a consequence, it fails to find the optimum inputs. The Pontryagin principle is utilized as follows [27]:

$$H(x_k^*, u_k^*, \lambda_{k+1}^*) \le H(x_k^*, u_k, \lambda_{k+1}^*). \tag{8}$$

Then the following condition is obtained:

$$\begin{aligned} &\lambda_{k+1}^{*T}Bu_k^* \le \lambda_{k+1}^{*T}Bu_k,\ |u_{ik}| \le 1, \\ &i = 1,2,\dots,m. \end{aligned} \tag{9}$$

Accordingly, the optimal control sequences are found as $u_k^* = -\text{sign}(\lambda_{k+1}^{*T}B)$. Therefore, the control signals are kept within the boundaries of the limitations (i,e,. $u_{ik}^* = \pm 1$, $i = 1,2,\dots,m$). Drawing the phase diagram of the open-loop system corresponding to $u_{ik}^* = +1$ and $u_{ik}^* = -1$, it is shown that there are at most $n-1$ switching instants (namely, $k_1, k_2, \dots, k_{n-1}$) in the control signal [18]. Resultantly, the control sequences are interpreted as the following:

$$u_k = \begin{cases} u_0, & 0 \le k < k_1 \\ u_1, & k_1 \le k < k_2 \\ \vdots & \\ u_{n-1}, & k_{n-1} \le k \le k_n \end{cases} \tag{10}$$

The state values at the mentioned instants are calculated as follows:

$$\begin{cases} x_{k_1} = A^{k_1}x_0 + (A^{k_1-1}B + \cdots + B)u_0 \\ x_{k_2} = A^{k_2-k_1}x_{k_1} + (A^{k_2-k_1-1}B + \cdots + B)u_1 \\ \vdots \\ x_{k_n} = A^{k_n-k_{n-1}}x_{k_{n-1}} \\ \quad + (A^{k_n-k_{n-1}-1}B + \cdots + B)u_{n-1} \end{cases} \tag{11}$$

where $k_n = N$ and $x_{k_n} = x_N$.

The explicit response of the discrete-time system (2) is

$$x_k = A^k x_0 + \sum_{i=0}^{k-1} A^{k-i-1}Bu_i. \tag{12}$$

Utilizing the triangular inequality, the two-norm of x_k may be written as:

$$\|x_k\| \le \|A\|^k\|x_0\| + \sum_{i=0}^{k-1}\|A\|^{k-i-1}\|B\|. \tag{13}$$

So the last condition would be directly obtained from (12). In the condition which $\det(A-I) \ne 0$ holds, we have:

$$\begin{aligned} &I + A + A^2 + \cdots + A^{q-1} = (A^q - I)(A-I)^{-1} \\ &= (A-I)^{-1}(A^q - I). \end{aligned} \tag{14}$$

The optimal control may have not a solution. For example, there is not a feasible solution in the following conditions:

$$\|x_N\| > \|A\|^N\|x_0\| + \|B\|\frac{\|A\|^N - 1}{\|A\| - 1}. \tag{15}$$

The right side of (15) with respect to N would be increasing if $\|A\| > 1$ holds. Moreover, guaranteeing $\|A\| < 1$, such the sequence could be increasing if $\frac{\|B\|}{1-\|A\|} < \|x_N\| - \|x_0\|$. Using the property $\|A\|^N < 1$, the condition $\|x_0\| + \|B\|\frac{1}{1-\|A\|} < \|x_N\|$ leads to (15).

The identities (11) are characterized as:

$$\begin{cases} x_{k_1} = A^{k_1}x_0 + (A^{k_1} - I)(A-I)^{-1}Bu_0 \\ x_{k_2} = A^{k_2-k_1}x_{k_1} + (A^{k_2-k_1} - I)(A-I)^{-1}Bu_1 \\ x_{k_3} = A^{k_3-k_2}x_{k_2} + (A^{k_3-k_2} - I)(A-I)^{-1}Bu_2 \\ \vdots \\ x_{k_n} = A^{k_n-k_{n-1}}x_{k_{n-1}} \\ \quad + (A^{k_n-k_{n-1}} - I)(A-I)^{-1}Bu_{n-1} \end{cases} \tag{16}$$

The identity (11) may be modified in a compact form. As an example, for the second-order case (i.e., $n = 2$), we have:

$$\begin{aligned} &x_{k_2} = A^{k_2}x_0 + (A^{k_2} - A^{k_2-k_1})(A-I)^{-1}Bu_0 \\ &+ (A^{k_2-k_1} - I)(A-I)^{-1}Bu_1. \end{aligned} \tag{17}$$

Thus

$$\begin{aligned} &x_{k_2} + (A-I)^{-1}Bu_1 \\ &= A^{k_2}(x_0 + (A-I)^{-1}Bu_0) \\ &+ A^{k_2-k_1}(A-I)^{-1}B(u_1 - u_0). \end{aligned} \tag{18}$$

Similarly, for the third order model (i.e., $n = 3$), we have:

$$\begin{aligned} &x_{k_3} = A^{k_3}x_0 + (A^{k_3} - A^{k_3-k_1})(A-I)^{-1}Bu_0 \\ &+ (A^{k_3-k_1} - A^{k_3-k_2})(A-I)^{-1}Bu_1 \\ &+ (A^{k_3-k_2} - I)(A-I)^{-1}Bu_2. \end{aligned} \tag{19}$$

Then

$$\begin{aligned} &x_{k_3} + (A-I)^{-1}Bu_2 \\ &= A^{k_3}(x_0 + (A-I)^{-1}Bu_0) \\ &+ A^{k_3-k_1}(A-I)^{-1}B(u_1 - u_0) \\ &+ A^{k_3-k_2}(A-I)^{-1}B(u_2 - u_1). \end{aligned} \tag{20}$$

Therefore, for a typical order n, the optimality condition is generalized as:

$$\begin{aligned} &x_N + (A-I)^{-1}Bu_{n-1} \\ &= A^{k_n}(x_0 + (A-I)^{-1}Bu_0) \\ &+ \sum_{i=1}^{n-1} A^{k_n-k_i}(A-I)^{-1}B(u_i - u_{i-1}). \end{aligned} \tag{21}$$

It completes the proof. □

Remark 1. The addressed strategy can be divided to $2^{m\times n}$ cases. In each one, it leads to a set of n variables and n equations. Thus the min-time solution would be exactly found for a typical description. Moreover, such a process is performed in an off-line way. Accordingly, the complexity due

to the execution time may be handled via powerful software packages along with upgrading the hardware.

Remark 2. Although the above closed-forms are corresponding to $\det(A-I)\neq 0$, employing (11), similar conclusions can be obtained for the discrete-time systems with $\det(A-I)=0$.

Remark 3. Mathematically, the transition time among the switching signal happens in zero seconds. However, jumping from $u_{ik}=-1$ to $u_{ik}=+1$ may be challenging points in practice. Additionally, by smoothing such a sharpness, the minimum time property would disappear in the system's response.

IV. Numerical examples

In this section, to validate the applicability of the suggested procedure, several min-time examples are studied in discrete-time and continuous-time models. All simulations are performed via Matlab R2016b.

Example 1. Consider the discrete-time model (2) with the following data:

$$A=\begin{bmatrix}0.7 & 0.3\\ 0.1 & 0.5\end{bmatrix},\quad B=\begin{bmatrix}0.1\\ 0.5\end{bmatrix}.$$

It is of interest to move the system's state from $x_0=[1\quad -1]^T$ to $x_N=[3\quad 1]^T$ in a minimum time. To find the optimal control, the state transition matrix is calculated as the following:

$$A^k=\mathcal{Z}^{-1}\{(zI-A)^{-1}z\}=\begin{bmatrix}\frac{3}{4}(0.8)^k+\frac{1}{4}(0.4)^k & \frac{3}{4}(0.8)^k-\frac{3}{4}(0.4)^k\\ \frac{1}{4}(0.8)^k-\frac{1}{4}(0.4)^k & \frac{1}{4}(0.8)^k+\frac{3}{4}(0.4)^k\end{bmatrix}. \quad (22)$$

The optimum solution would be computed from the following equation:

$$x_N+(A-I)^{-1}Bu_1=A^{k_2}(x_0+(A-I)^{-1}Bu_0)+A^{k_2-k_1}(A-I)^{-1}B(u_1-u_0). \quad (23)$$

Then

$$\begin{bmatrix}9\\3\end{bmatrix}-\begin{bmatrix}5\\4\end{bmatrix}u_1=A^{k_2}\left(\begin{bmatrix}3\\-3\end{bmatrix}-\begin{bmatrix}5\\4\end{bmatrix}u_0\right)-A^{k_2-k_1}\begin{bmatrix}5\\4\end{bmatrix}(u_1-u_0). \quad (24)$$

Subsequently, the identity (24) is investigated in the following cases:

A) When $u_0=+1$ and $u_1=+1$, then (24) may lead to $36(0.8)^{k_2}=-12$ and $19(0.4)^{k_2}=7$.

B) If $u_0=+1$ and $u_1=-1$, then (24) would be reduced to

$$\begin{cases}2(0.8)^{k_2-k_1}-(0.8)^{k_2}=\frac{7}{3}\\ 19(0.4)^{k_2}-14(0.4)^{k_2-k_1}=-7\end{cases}. \quad (25)$$

C) Substituting $u_0=-1$ and $u_1=+1$, (24) is simplified as

$$\begin{cases}(0.8)^{k_2}-2(0.8)^{k_2-k_1}=\frac{1}{3}\\ 5(0.4)^{k_2}+14(0.4)^{k_2-k_1}=7\end{cases}. \quad (26)$$

D) If $u_0=-1$ and $u_1=-1$, then (24) would lead to $36(0.8)^{k_2}=84$ and $5(0.4)^{k_2}=-7$.

Accordingly, it is clear that there is not a solution in all the cases. This problem may be checked by concerning the allowable upper bound as the following:

$$\xi_N=\|A\|^N\|x_0\|+\|B\|\frac{\|A\|^N-1}{\|A\|-1},\ N\geq 1. \quad (27)$$

In this example, we have:

$\|A\|=0.8319,\ \|B\|=0.5099,\ \|x_0\|=1.4142.$

Thus (27) is determined as

$$\xi_N=3.0333-1.6191(0.8319)^N,\ N\geq 1. \quad (28)$$

Checking $\mathrm{Ln}(\|A\|)\left(\|x_0\|+\frac{\|B\|}{\|A\|-1}\right)=0.298>0$, it is clear that ξ_N is an increasing sequence ($\xi_N<3.0333$). The mentioned condition is obtained via differentiation of $\xi_N=\|A\|^N\|x_0\|+\|B\|\frac{\|A\|^N-1}{\|A\|-1}$ with respect to N. In Example 1, $\|x_N\|=3.1623>\xi_N$. So, Assumption 1 does not hold and there is not a solution to the min-time control of Example 1.

Example 2. Consider the min-time control of the following discrete-time model:

$A=\begin{bmatrix}0.7 & 0.3\\ 0.1 & 0.5\end{bmatrix}$, $B=\begin{bmatrix}1\\2\end{bmatrix}$, $x_0=\begin{bmatrix}1\\-1\end{bmatrix}$ and $x_N=\begin{bmatrix}-7\\-5\end{bmatrix}$.

In Example 2, $\|A\|=0.8319$, $\|B\|=2.2361$, and $\|x_0\|=1.4142$. Using Assumption 1, (3) is reduced to $(0.8319)^N\leq 0.3953$. So, there exists the integer $N\geq 6$ such that Assumption 1 holds. Similar to Example 1, the state transition matrix is

$$A^k=\begin{bmatrix}\frac{3}{4}(0.8)^k+\frac{1}{4}(0.4)^k & \frac{3}{4}(0.8)^k-\frac{3}{4}(0.4)^k\\ \frac{1}{4}(0.8)^k-\frac{1}{4}(0.4)^k & \frac{1}{4}(0.8)^k+\frac{3}{4}(0.4)^k\end{bmatrix}.$$

The optimal control is derived via the following algebraic equation:

$$x_N+(A-I)^{-1}Bu_1=A^{k_2}(x_0+(A-I)^{-1}Bu_0)+A^{k_2-k_1}(A-I)^{-1}B(u_1-u_0).$$

Then

$$\begin{bmatrix}-21\\-15\end{bmatrix}-25\begin{bmatrix}1.1\\0.7\end{bmatrix}u_1=A^{k_2}\left(\begin{bmatrix}3\\-3\end{bmatrix}-25\begin{bmatrix}1.1\\0.7\end{bmatrix}u_0\right)-A^{k_2-k_1}25\begin{bmatrix}1.1\\0.7\end{bmatrix}(u_1-u_0). \quad (29)$$

To quantify the optimum solution, the following cases are taken into account:

A) If $u_0=+1$ and $u_1=+1$, then (29) would lead to $(0.8)^{k_2}=1.8$ and $37(0.4)^{k_2}=49$.

B) When $u_0=+1$ and $u_1=-1$, then (29) may be reduced to

$$\begin{bmatrix}26\\10\end{bmatrix}=\begin{bmatrix}-135(0.8)^{k_2}+37(0.4)^{k_2}+270(0.8)^{k_2-k_1}-50(0.4)^{k_2-k_1}\\ -45(0.8)^{k_2}-37(0.4)^{k_2}+90(0.8)^{k_2-k_1}+50(0.4)^{k_2-k_1}\end{bmatrix}$$

It may be modified as:

$$\begin{cases}2(0.8)^{k_2-k_1}-(0.8)^{k_2}=0.2\\ 50(0.4)^{k_2-k_1}-37(0.4)^{k_2}=1\end{cases}. \quad (30)$$

C) If $u_0=-1$ and $u_1=+1$, then (29) could be simplified as:

$$-4\begin{bmatrix}48.5\\32.5\end{bmatrix}$$
$$=\begin{bmatrix}135(0.8)^{k_2}-13(0.4)^{k_2}-270(0.8)^{k_2-k_1}+50(0.4)^{k_2-k_1}\\45(0.8)^{k_2}+13(0.4)^{k_2}-90(0.8)^{k_2-k_1}-50(0.4)^{k_2-k_1}\end{bmatrix}$$

It equals to

$$\begin{cases}2(0.8)^{k_2-k_1}-(0.8)^{k_2}=1.8\\50(0.4)^{k_2-k_1}-13(0.4)^{k_2}=49\end{cases}. \quad (31)$$

D) Substituting $u_0=-1$ and $u_1=-1$, (29) leads to $(0.8)^{k_2}=0.2$ and $13(0.4)^{k}=1$.

Consequently, no solution is anticipated in Cases A, C and D for (29). There is also a solution for Case B. But it is not an integer. However, taking $k_1=8$ and $k_2=18$, the final value $x_N=[-6.9538\quad -5.0951]^T$ would be touched in Example 2. The induced errors are directly related to the integer values of k_1 and k_2. Although it is not an exact solution, it is sufficiently near to the desired final point. As shown in Fig 1, the optimum control sequences are found as

$$u_k=\begin{cases}+1,\ 0\le k<8\\-1,\ 8\le k<18\end{cases} \quad (32)$$

Moreover, the states of Example 2 are illustrated in Fig 1.

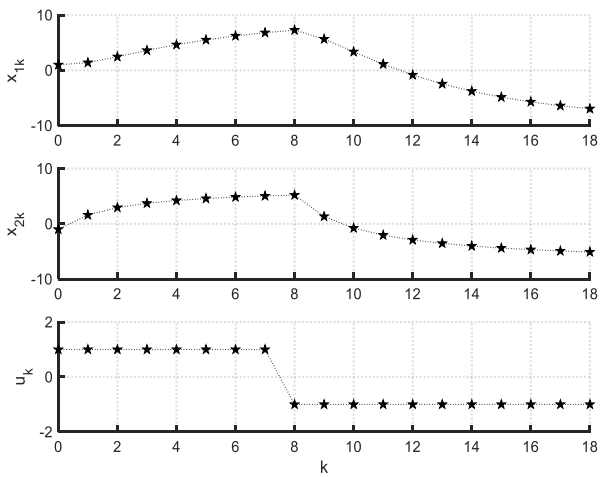

Fig 1. The states and control input of Example 2

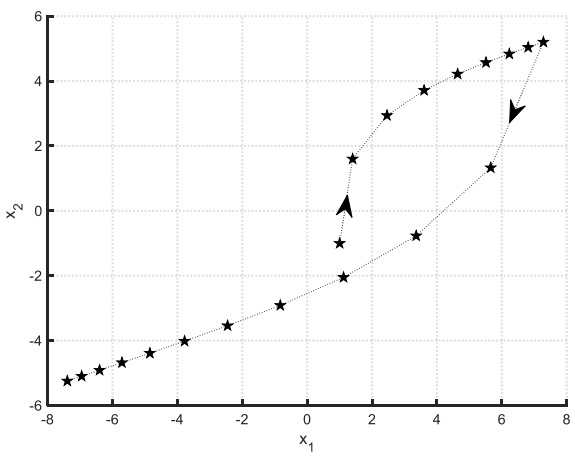

Fig 2. The state's trajectory in Example 2

In the phase plane, the corresponding trajectory is plotted as seen in Fig 2. Accordingly, the control aims are effectively verified via the min-time control signal (32).

Example 3. Consider the following second-order continuous-time dynamic:

$$\ddot{y}=u, \quad (33)$$

where y is the position and u is the acceleration. The acceleration is limited by $|u(t)|\le 1$. It is desired to move the system's states from $y(0)=1$, $\dot{y}(0)=-1$ to $y(t_f)=2$, $\dot{y}(t_f)=0$ in the possible minimum time. The state-space representation is

$$\dot{x}=\begin{bmatrix}0&1\\0&0\end{bmatrix}x+\begin{bmatrix}0\\1\end{bmatrix}u. \quad (34)$$

Including the block ZOH, the equivalent discrete-time description is

$$x_{k+1}=\begin{bmatrix}1&T_s\\0&1\end{bmatrix}x_k+\begin{bmatrix}\frac{1}{2}T_s^2\\T_s\end{bmatrix}u_k. \quad (35)$$

Taking the sampling-time $T_s=1$, the discrete-time model is found as:

$$A=\begin{bmatrix}1&1\\0&1\end{bmatrix},\ B=\begin{bmatrix}\frac{1}{2}\\1\end{bmatrix} \quad (36)$$

The condition (3) is simplified as $1.1817\le(1.6180)^N$. So, Assumption 1 can hold for integer $N\ge 1$ in Example 3. To move the states from $x_0=[1\quad -1]^T$ to $x_N=[2\quad 0]^T$ in a minimum time, the optimality condition is written as the following:

$$\begin{cases}x_{k_1}=A^{k_1}x_0+(A^{k_1-1}+\cdots+I)Bu_0\\x_N=A^{k_2-k_1}x_{k_1}+(A^{k_2-k_1-1}+\cdots+I)Bu_1\end{cases} \quad (37)$$

The singular condition $\det(A-I)=0$ takes place in this example. The condition (37) can be written as:

$$x_N=A^{k_2}x_0+A^{k_2-k_1}(A^{k_1-1}+\cdots+I)Bu_0 \\ +(A^{k_2-k_1-1}+\cdots+I)Bu_1. \quad (38)$$

The state transition matrix is disclosed as

$$A^k=\begin{bmatrix}1&k\\0&1\end{bmatrix}. \quad (39)$$

The identity (38) is reduced to

$$\begin{bmatrix}2\\0\end{bmatrix}=\begin{bmatrix}1&k_2\\0&1\end{bmatrix}\begin{bmatrix}1\\-1\end{bmatrix} \\ +\begin{bmatrix}1&k_2-k_1\\0&1\end{bmatrix}\left(\begin{bmatrix}1&k_1-1\\0&1\end{bmatrix}+\cdots+I\right)\begin{bmatrix}\frac{1}{2}\\1\end{bmatrix}u_0 \\ +\left(\begin{bmatrix}1&k_2-k_1-1\\0&1\end{bmatrix}+\cdots+I\right)\begin{bmatrix}\frac{1}{2}\\1\end{bmatrix}u_1. \quad (40)$$

It may be simplified as:

$$\begin{bmatrix}2\\0\end{bmatrix}=\begin{bmatrix}1&k_2\\0&1\end{bmatrix}\begin{bmatrix}1\\-1\end{bmatrix} \\ +\begin{bmatrix}1&k_2-k_1\\0&1\end{bmatrix}\begin{bmatrix}k_1&\frac{k_1(k_1-1)}{2}\\0&k_1\end{bmatrix}\begin{bmatrix}\frac{1}{2}\\1\end{bmatrix}u_0 \\ +\begin{bmatrix}k_2-k_1&\frac{(k_2-k_1)(k_2-k_1-1)}{2}\\0&k_2-k_1\end{bmatrix}\begin{bmatrix}\frac{1}{2}\\1\end{bmatrix}u_1. \quad (41)$$

Then

$$\begin{cases}(2k_2-k_1)k_1u_0+(k_2-k_1)^2u_1=2+2k_2\\k_1u_0+(k_2-k_1)u_1=1\end{cases} \quad (42)$$

To determine the optimal control, the following cases are briefly studied:

A) $u_0=+1,\ u_1=+1$

B) $u_0 = +1,\ u_1 = -1$
C) $u_0 = -1,\ u_1 = +1$
D) $u_0 = -1,\ u_1 = -1$

There is no solution for Cases A, C and D. However, $k_1 = 1 + \frac{\sqrt{6}}{2} = 2.2247$ and $k_2 = 1 + \sqrt{6} = 3.4495$ is found for Case B. Unfortunately, it is not an integer number. Nevertheless, choosing $k_1 = 2$ and $k_2 = 3$, the continuous-time control effort is specified as follows:

$$u(t) = \begin{cases} +1, & 0 \le t < 2 \\ -1, & 2 \le t < 3 \end{cases}. \tag{43}$$

Applying the control signal (43), the final states of (33) are touched at $x_N = [1.5 \quad 0]^T$, while it slightly differs from the desired point. Such an error is specifically caused due to the integer values of the switching instants. To show the merit of the suggested idea, the results are compared with a similar continuous-time approach [26]. In both cases, the states and control efforts of the model are depicted in Fig 3. In the phase plane, the trajectory is plotted in Fig 4.

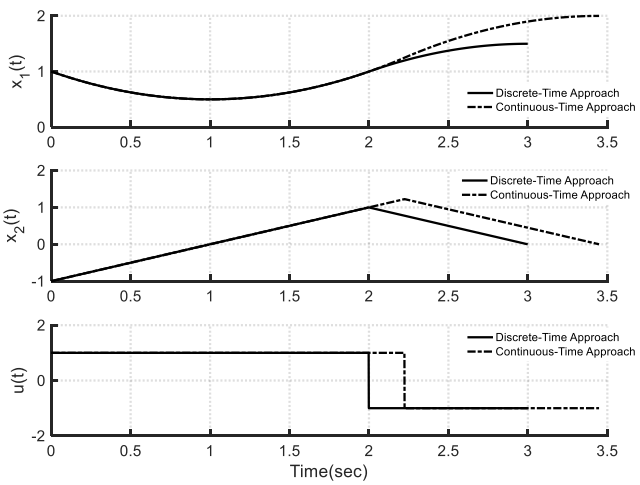

Fig 3. The states and control input in Example 3

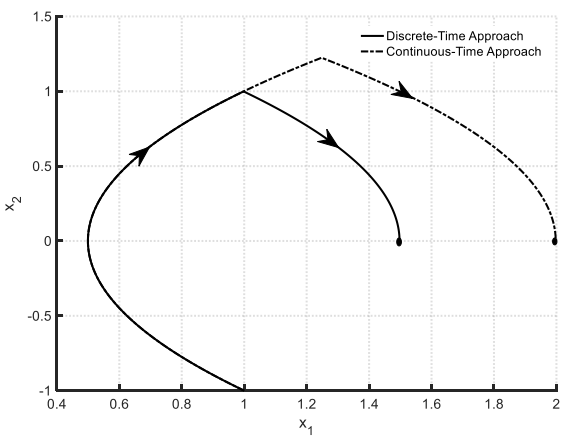

Fig 4. The state's trajectory in Example 3

Compared to a similar idea [26], finding integer switching times would be the main advantage of the suggested control methodology.

Example 4. Consider the min-time control of the following system:

$$\ddot{y} = 2u, \tag{44}$$

with $y(0) = 1$, $\dot{y}(0) = 0$, $y(t_f) = 8$, $\dot{y}(t_f) = -10$ and $|u(t)| \le 1$. The state-space equation would be found as the following:

$$\dot{x} = \begin{bmatrix} 0 & 1 \\ 0 & 0 \end{bmatrix} x + \begin{bmatrix} 0 \\ 2 \end{bmatrix} u. \tag{45}$$

The equivalent discrete model is

$$x_{k+1} = \begin{bmatrix} 1 & T_s \\ 0 & 1 \end{bmatrix} x_k + \begin{bmatrix} T_s^2 \\ 2T_s \end{bmatrix} u_k. \tag{46}$$

Taking the sampling period $T_s = 1$, we have:

$$A = \begin{bmatrix} 1 & 1 \\ 0 & 1 \end{bmatrix},\ B = \begin{bmatrix} 1 \\ 2 \end{bmatrix},\ x_0 = \begin{bmatrix} 1 \\ 0 \end{bmatrix},\ x_N = \begin{bmatrix} 8 \\ -10 \end{bmatrix}.$$

The inequality (3) is found as $3.5564 \le (1.6180)^N$. So, Assumption 1 insures for any integer $N > 3$. The optimal control is found from the following conditions:

$$\begin{cases} x_{k_1} = A^{k_1} x_0 + (A^{k_1 - 1} + \cdots + I) B u_0 \\ x_N = A^{k_2 - k_1} x_{k_1} + (A^{k_2 - k_1 - 1} + \cdots + I) B u_1 \end{cases} \tag{47}$$

It is written as:

$$\begin{aligned} x_N &= A^{k_2} x_0 + A^{k_2 - k_1}(A^{k_1 - 1} + \cdots + I) B u_0 \\ &+ (A^{k_2 - k_1 - 1} + \cdots + I) B u_1. \end{aligned} \tag{48}$$

In this case, the state transition matrix is given by

$$A^k = \begin{bmatrix} 1 & k \\ 0 & 1 \end{bmatrix}.$$

The identity (48) is arranged as:

$$\begin{aligned} \begin{bmatrix} 8 \\ -10 \end{bmatrix} &= \begin{bmatrix} 1 & k_2 \\ 0 & 1 \end{bmatrix} \begin{bmatrix} 1 \\ 0 \end{bmatrix} \\ &+ \begin{bmatrix} 1 & k_2 - k_1 \\ 0 & 1 \end{bmatrix} \begin{bmatrix} k_1 & \frac{k_1(k_1 - 1)}{2} \\ 0 & k_1 \end{bmatrix} \begin{bmatrix} 1 \\ 2 \end{bmatrix} u_0 \\ &+ \begin{bmatrix} k_2 - k_1 & \frac{(k_2 - k_1 - 1)(k_2 - k_1)}{2} \\ 0 & k_2 - k_1 \end{bmatrix} \begin{bmatrix} 1 \\ 2 \end{bmatrix} u_1. \end{aligned} \tag{49}$$

Then

$$\begin{cases} (2k_1 k_2 - k_1^2) u_0 + (k_2 - k_1)^2 u_1 = 7 \\ 2k_1 u_0 + (2k_2 - 2k_1) u_1 = -10 \end{cases}. \tag{50}$$

To determine the optimal control, (50) is solved in the following cases:

A) $u_0 = +1,\ u_1 = +1$
B) $u_0 = +1,\ u_1 = -1$
C) $u_0 = -1,\ u_1 = +1$
D) $u_0 = -1,\ u_1 = -1$

It is seen that there is no feasible solution for Cases A, C and D. However, $k_1 = 4$ and $k_2 = 13$ is found for Case B. In the continuous-time form, the control signal is depicted as:

$$u(t) = \begin{cases} +1, & 0 \le t < 4 \\ -1, & 4 \le t < 13 \end{cases} \tag{51}$$

The states and input of the model (45) are computed as depicted in Fig 5. Furthermore, the trajectory is plotted in the phase plane as seen in Fig 6.

In Example 4, since the switching instants are integer, the outcomes of the proposed discrete-time idea would be the same as the continuous-time approach [26]. Thus the required

objectives are completely fulfilled via the calculated control effort (51).

In low-order systems, (4) can be solved via the analytic methods as seen in Examples 1-4. However, in complex equations, the nonlinear problem would be solved via numerical iterative methods. Moreover, Matlab's commands like fzero, fsolve, and others can be utilized to find the roots of (4).

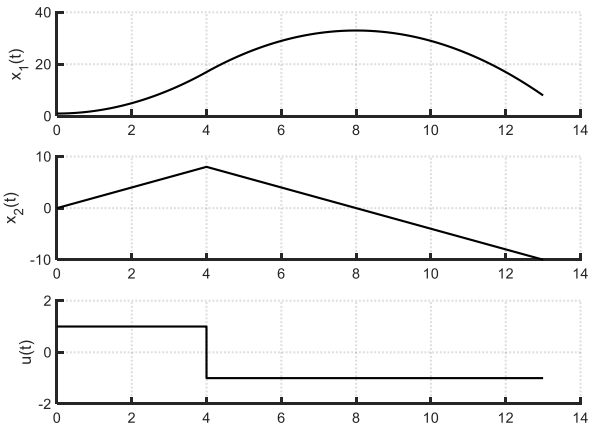

Fig 5. The states and control input in Example 4

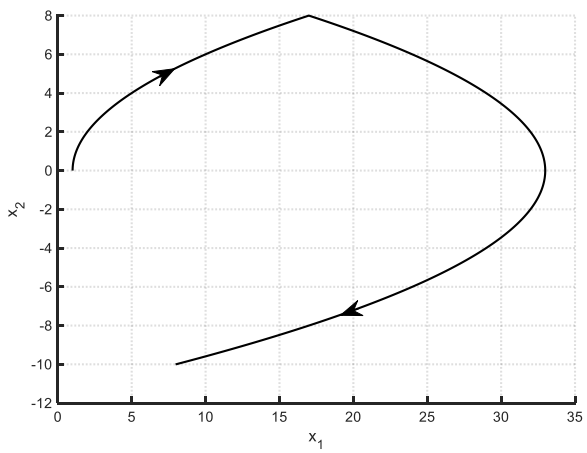

Fig 6. Trajectory in Example 4

Example 5. Consider a discrete-time min-time problem with the following data:

$A = \begin{bmatrix} 0.6 & 0.7 & 0 \\ 0 & -0.3 & 0.3 \\ -0.2 & 0.2 & 0.4 \end{bmatrix}$, $B = \begin{bmatrix} 1 & 0 \\ 0 & 1 \\ 1 & 1 \end{bmatrix}$, $x_0 = \begin{bmatrix} 2 \\ -1 \\ 3 \end{bmatrix}$ and $x_N = \begin{bmatrix} 4.3 \\ 1.4 \\ 2.6 \end{bmatrix}$.

Employing Assumption 1 with $\|A\| = 0.9541$, $\|B\| = 1.7321$, and $\|x_0\| = 3.7417$, (3) is reduced to $(0.9541)^N \leq 0.9566$. So, there exists always integer N for satisfying Assumption 1. In this case, the optimal control would be derived from the following equation:

$$x_N + (A-I)^{-1}Bu_2 = A^{k_3}(x_0 + (A-I)^{-1}Bu_0)$$
$$+A^{k_3-k_1}(A-I)^{-1}B(u_1-u_0)$$
$$+A^{k_3-k_2}(A-I)^{-1}B(u_2-u_1).$$

Then

$$\begin{bmatrix} 4.3 \\ 1.4 \\ 2.6 \end{bmatrix} + \begin{bmatrix} -2.8182 & -1.9091 \\ -0.1818 & -1.0909 \\ -0.7879 & -1.3939 \end{bmatrix} u_2$$
$$= A^{k_3}\left(\begin{bmatrix} 2 \\ -1 \\ 3 \end{bmatrix} + \begin{bmatrix} -2.8182 & -1.9091 \\ -0.1818 & -1.0909 \\ -0.7879 & -1.3939 \end{bmatrix} u_0 \right)$$
$$+A^{k_3-k_1} \begin{bmatrix} -2.8182 & -1.9091 \\ -0.1818 & -1.0909 \\ -0.7879 & -1.3939 \end{bmatrix} (u_1-u_0)$$
$$+A^{k_3-k_2} \begin{bmatrix} -2.8182 & -1.9091 \\ -0.1818 & -1.0909 \\ -0.7879 & -1.3939 \end{bmatrix} (u_2-u_1).$$

Accordingly, among all the possible cases, a feasible solution of the mentioned equation is numerically found as $k_1 = 3$, $k_2 = 8$ and $k_3 = 12$ which corresponded to $u_0 = [-1 \quad +1]^T$, $u_1 = [+1 \quad -1]^T$ and $u_2 = [+1 \quad +1]^T$. Thus the optimum sequences are obtained as follows:

$$u_{1k} = \begin{cases} -1, & 0 \leq k < 3 \\ +1, & 3 \leq k \leq 12 \end{cases} \tag{52}$$

and

$$u_{2k} = \begin{cases} +1, & 0 \leq k < 3 \\ -1, & 3 \leq k < 8 \\ +1, & 8 \leq k \leq 12 \end{cases} \tag{53}$$

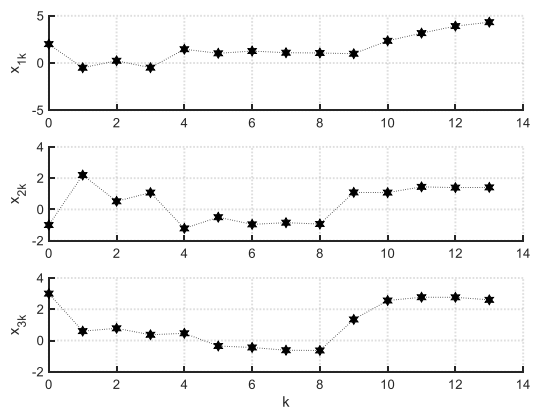

Fig 7. The states of the discrete-time model in Example 5

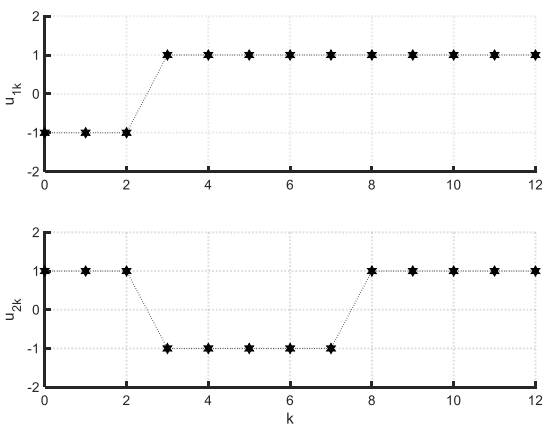

Fig 8. The calculated control inputs in Example 5

Solving the discrete-time model, the states of Example 5 are illustrated in Fig 7. Moreover, the calculated control inputs are

plotted in Fig 8. Consequently, the requirements are fulfilled in Example 5 through the computed control inputs.

V. Conclusion

The movement of the system's states in the minimum time is analytically investigated in the sampled-data control description. Hence, the amplitude of the optimum control signal is firstly derived from the Pontryagin principle. Using the state transition matrix, the system's states are computed at the switching times. Finally, corresponding to the switching times, some integer parameters are exactly determined via the addressed algebraic equation. Moreover, the minimum final time is calculated for the optimal control problem. The effectiveness of the suggested procedure is verified in several discrete-time and continuous-time control examples.

References

[1] F. L. Lewis, D. Vrabie, and V. L. Syrmos, Optimal control. John Wiley & Sons, 2012.

[2] R. Kosut, "Suboptimal control of linear time-invariant systems subject to control structure constraints," IEEE Transactions on Automatic Control, vol. 15, no. 5, pp. 557-563, 1970.

[3] W. L. Garrard, "Suboptimal feedback control for nonlinear systems," Automatica, vol. 8, no. 2, pp. 219-221, 1972.

[4] S. Nasini and R. Nessah, "An almost exact solution to the min completion time variance in a single machine," European Journal of Operational Research, vol. 294, no. 2, pp. 427-441, 2021.

[5] A. Polyakov and J.-P. Richard, "Suboptimal LMI-based solution of minimum time control problem," IFAC Proceedings Volumes, vol. 47, no. 3, pp. 2475-2480, 2014.

[6] T. Abualrub, I. Sadek, and F. El Nachar, "Wavelet based approximations in the optimal control of parabolic problems," Journal of Control Theory and Applications, vol. 11, pp. 103-107, 2013.

[7] G. Colombo and T. T. Le, "Higher order discrete controllability and the approximation of the minimum time function," Discrete and Continuous Dynamical Systems, vol. 35, no. 9, pp. 4293-4322, 2015.

[8] M. Akbarian, N. Eghbal, and N. Pariz, "A Novel method for optimal control of piecewise affine systems using semi-definite programming," International Journal of Industrial Electronics Control and Optimization, vol. 3, no. 1, pp. 59-68, 2020.

[9] M. R. Jardin and A. E. Bryson Jr, "Methods for computing minimum-time paths in strong winds," Journal of Guidance, Control, and Dynamics, vol. 35, no. 1, pp. 165-171, 2012.

[10] C.-H. Lee, M.-J. Tahk, and J.-I. Lee, "Generalized formulation of weighted optimal guidance laws with impact angle constraint," IEEE Transactions on Aerospace and Electronic Systems, vol. 49, no. 2, pp. 1317-1322, 2013.

[11] S. Gutman, "On optimal guidance for homing missiles," Journal of Guidance and Control, vol. 2, no. 4, pp. 296-300, 1979.

[12] J. Zhang, Q. Xiao, and L. Li, "Solution space exploration of low-thrust minimum-time trajectory optimization by combining two homotopies," Automatica, vol. 148, p. 110798, 2023.

[13] Z. Shabani and H. Tajadodi, "A numerical scheme for constrained optimal control problems," International Journal of Industrial Electronics Control and Optimization, vol. 2, no. 3, pp. 233-238, 2019.

[14] A. Luo, "Minimun time optimal control of stepping motor," Journal of Central South University of Technology, vol. 2, pp. 54-58, 1995.

[15] G. Pin and T. Parisini, "Robust minimum-time constrained control of nonlinear discrete-time systems: New results," in IEEE Conference on Decision and Control and European Control Conference, 2011, pp. 1710-1715.

[16] D. Chen, L. Bako, and S. Lecoeuche, "The minimum-time problem for discrete-time linear systems: a non-smooth optimization approach," in IEEE International Conference on Control Applications, 2012, pp. 196-201.

[17] G. Lini, A. Piazzi, and L. Consolini, "Algebraic solution to minimum-time velocity planning," International Journal of Control, Automation and Systems, vol. 11, pp. 805-814, 2013.

[18] S. Bichiou, M. K. Bouafoura, and N. benhadj Braiek, "Minimum time control synthesis for high order LTI systems," in International Conference on Electrical Sciences and Technologies in Maghreb, 2014, pp. 1-6.

[19] M. Cerf, "Fast solution of minimum-time low-thrust transfer with eclipses," Proceedings of the Institution of Mechanical Engineers, Part G: Journal of Aerospace Engineering, vol. 233, no. 7, pp. 2699-2714, 2019.

[20] L. Consolini, M. Laurini, M. Locatelli, and A. Minari, "A solution of the minimum-time speed planning problem based on lattice theory," Journal of the Franklin Institute, vol. 357, no. 12, pp. 7617-7637, 2020.

[21] G. Ciaramella and G. Fabrini, "Multilevel techniques for the solution of HJB minimum-time control problems," Journal of Systems Science and Complexity, vol. 34, no. 6, pp. 2069-2091, 2021.

[22] V. Ghaffari, "Control Law Design with Dead-beat Property in Continuous-Time Dynamical Systems," International Journal of Industrial Electronics Control and Optimization, vol. 2, no. 3, pp. 189-196, 2019.

[23] S. Gao, J.-e. Feng, Z. Li, and C. Xiang, "Minimum-Time Control of Boolean Control Networks: A Fast Graphical Approach," IEEE Transactions on Circuits and Systems II: Express Briefs, 2023.

[24] J. Yan, C. Wu, X. Yang, C. Chen, and X. Guan, "Minimum Time Formation Control of AUVs with Smooth Transition in Communication Topology," IEEE Robotics and Automation Letters, 2024.

[25] M. Pagone, M. Boggio, C. Novara, A. Proskurnikov, and G. C. Calafiore, "Continuous-time nonlinear model predictive control based on Pontryagin Minimum Principle and penalty functions," International Journal of Control, pp. 1-17, 2024.

[26] V. Ghaffari, "The Exact Solution of Min-Time Optimal Control Problem in Constrained LTI Systems: A State Transition Matrix Approach," AUT Journal of Modeling and Simulation, vol. 51, no. 2, pp. 103-110, 2019.

[27] R. E. Kopp, "Pontryagin maximum principle," in Mathematics in Science and Engineering, vol. 5: Elsevier, 1962, pp. 255-279.

Valiollah Ghaffari received the B.Sc., M.Sc., and Ph.D. degrees in electrical engineering from Shiraz University, Shiraz, Iran, in 2006, 2009, and 2014, respectively. He is currently an Associate Professor with the Department of Electrical Engineering, Persian Gulf University. His research interests include robust control, nonlinear control, adaptive control, and model predictive control.

International Journal Of
Industrial Electronics Control and Optimization
Print ISSN: 3517-2645
Online ISSN: 3568-2645
Homepage: https://ieco.usb.ac.ir/

A New Hybrid Intelligent Method for Accurate Short Term Electric Power Production Forecasting from Uncertain Renewable Energy Resources

Gholamreza Memarzadeh[1] | Farshid Keynia[2] | Faezeh Amirteimoury[3] | Rasoul Memarzadeh [4] | Hossein Noori[5]

Department of Electrical Engineering, Faculty of Engineering, Vali-e-Asr University of Rafsanjan, Rafsanjan, Iran.[1,4]
Department of Energy Management and Optimization, Institute of Science and High Technology and Environmental Sciences, Graduate University of Advanced Technology, Kerman, Iran.[2]
Department of Computer Engineering, Kerman Branch, Islamic Azad University, Kerman, Iran[3].
Department of Civil Engineering, Faculty of Engineering, Vali-e-Asr University of Rafsanjan, Rafsanjan, Iran[4]
Corresponding author's email: g.memarzadeh@vru.ac.ir

Article Info

Article type:
Research Article

Article history:
Received: 10-May-2024
Received in revised form: 23-August-2024
Accepted: 09-September-2024
Published online: 21-March-2025

Keywords:
Gated Recurrent Unit,
LSTM,
MRMI Feature Selection,
Renewable energy resources.

ABSTRACT

In recent years, there has been a significant increase in the utilization of renewable resources for electricity generation. Consequently, accurate short-term forecasting of renewable power production has become crucial for power system operations. However, Renewable Power Production Forecasting (RPPF) presents unique challenges due to the intermittent and uncertain nature of renewable energy sources. This paper proposes a novel approach to short-term RPPF. The proposed model integrates various techniques, including Long Short-Term Memory (LSTM), Gated Recurrent Unit (GRU), Autoregressive Integrated Moving Average (ARIMA), Multi-Layer Perceptron (MLP), and Adaptive Neuro-Fuzzy Inference System (ANFIS). The aim is to enhance the accuracy and predictive performance of renewable power production forecasts. The suggested hybrid model employs the Modified Relief-Mutual Information (MRMI) feature selection technique to identify the most influential input data for prediction. Subsequently, the combined model generates a 24-hour ahead RPP prediction using a weighted output approach. By capitalizing on the strengths of each individual model, the combined method mitigates their weaknesses, thereby improving the overall efficiency of the forecasting process. The accuracy and performance of the proposed method are evaluated through two case studies involving solar farm power generation at the Mahan, Iran and Rafsanjan, Iran sites. The results demonstrate the effectiveness of the hybrid model in enhancing the accuracy of short-term RPPF. By combining multiple forecasting methods and utilizing the MRMI feature selection technique, the proposed method significantly improves prediction accuracy.

I. Introduction

Renewable energy sources, increasingly crucial for global electricity production due to their environmental benefits, reliability, and cost-effectiveness, are gaining prominence. [1]. Among them, solar photovoltaic (PV) is one of the most widely used. Solar energy, produced by photovoltaic panels, is a clean and inexpensive energy source that reduces reliance on harmful fossil fuels [2-4]. Despite these advantages, integrating significant PV energy into power systems poses operational challenges that affect electricity prices. Unlike traditional energy sources, PV systems exhibit heightened uncertainty in electricity generation, substantially impacting their profitability within the electricity market. Moreover, the variable and unpredictable nature of solar power presents challenges for grid operators and market participants in effectively managing and pricing electricity. Therefore, the uncertain nature of PV makes it difficult to predict accurately. Various methods have been proposed in recent years for PV

power forecasting. These methods can be categorized into four groups: physical, statistical, artificial intelligence, and hybrid models. Physical models, which utilize meteorological and geographical data, are generally less effective for short-term RPPF. However, they often yield better results in long-term forecasting [5-7]. Statistical models used for short-term RPPF try to find the relationship between input and output [8-11]. Statistical models outperform physical models in RPPF. However, they cannot catch long-term dependencies within data. Artificial intelligence models such as artificial neural networks [12-16], support vector machine (SVM) [17], and fuzzy logic [18] are more accurate in short-term RPPF. They use historical data on meteorological conditions in order to forecast future solar radiation levels [19]. However, deep neural networks were shown to be much more efficient in short-term RPPF [20-26]. For instance, Liu et al. [27] integrated a deep network model with a feature selection technique in order to enhance the prediction accuracy. Sharadga et al. [28] studied different prediction methods for PV power output, including statistical and artificial intelligence-based approaches, to compare their performance. Alaraj et al. [29] introduced an ensemble approach using machine learning to forecast solar photovoltaic power, considering meteorological parameters. Authors in [30] combined a naïve Bayes algorithm, MLP, and LSTM to forecast solar power generation for the next hour and hourly for the following days. Zhu et al. [31] proposed a short-term wind power forecasting method based on a new hybrid model to enhance the accuracy of wind power prediction. Xiong et al. [32] developed a hybrid model combining complementary ensemble empirical mode decomposition (CEEMD), sample entropy (SE), random forest (RF), improved reptile search algorithm (IRSA), bidirectional long short-term memory (BiLSTM) network, and extreme learning machine (ELM) for wind power prediction. Chen et al. [33] presented a method for forecasting using multiple steps. They used ensemble empirical mode decomposition (EEMD) and improved K-harmonic mean clustering optimized by the Cuckoo search algorithm (CSA). Moreno et al. [34] developed a method called WSF that combines a decomposition model with LSTM for forecasting. Duan et al. [35] proposed a combined short-term wind speed forecasting model based on CNN-RNN and linear regression optimization to account for error. Kosana et al. [36] implemented a hybrid forecasting framework using improved complete ensemble empirical mode decomposition with adaptive noise (ICEEMDAN), BiLSTM, and autoencoder for wind speed forecasting.

Liu et al. [37] developed a system for wind speed forecasting that includes various techniques. They used ensemble empirical mode decomposition with adaptive noise (CEEMDAN) as a data preprocessing technique, the C-C method as a feature selection method, a multi-objective grey wolf optimizer (MOGWO) as a parameter optimization algorithm, and a multi-input multi-output least squares support vector machine (MIMOLSSVM) as a forecasting model. They also used evaluation metrics for interval WSF. Cai et al. [38] proposed a wind power mid-long-term forecasting method considering various wind energy characteristics to effectively predict future climate information. Scott et al. [39] explored machine learning techniques for forecasting PV generation systems. The method presented by Theocharides et al. [40] involved combining machine learning techniques with statistical post-processing to forecast solar power for the next day. In a similar vein, Heo et al. [41] proposed a multi-channel convolutional neural network approach to predict monthly photovoltaic power. Their method included utilizing raster image data to account for regional influences. Hu et al. [42] proposed a hybrid approach for short-term wind speed predictions. Their approach is based on a preprocessing algorithm and optimization theory. Aly [43] used recurrent Kalman filter (RKF), Fourier series (FS), wavelet transform (WT), and artificial neural network (ANN) for WSF and WPF. Juardo et al. [44] proposed an improved encoder-decoder-based CNN model for probabilistic short-term load and PV forecasting. Brester et al. [45] evaluated neural network models for site-specific solar PV forecasting using numerical weather prediction data and weather observations. The taxonomy of some of reviewed papers based on different aspects of their works has been listed in Table 1.

The proposed model combines several powerful forecasting techniques, including LSTM, GRU, ARIMA, MLP, and ANFIS. Furthermore, we employ the MRMI method for input selection to enhance the accuracy of our predictions. By leveraging the strengths of these diverse models, our hybrid approach aims to overcome the challenges posed by the intermittency and uncertainty inherent in renewable resources. Through the weighted combination of model outputs, we generate reliable and accurate predictions for the next 24 hours of renewable power production. The important contributions of proposed paper can be summarized as follows:

1- Hybrid forecasting models incorporating LSTM, GRU, ARIMA, MLP, and ANFIS are developed to accurately predict renewable power production for the next 24 hours. By combining the strengths of these individual models, the hybrid approach effectively compensates for their respective weaknesses, significantly enhancing overall forecasting performance.

2- In this study, the MRMI feature selection technique is introduced to identify input data with the highest predictive value for the LSTM, GRU, MLP, and ANFIS models.

content while minimizing redundancy. This approach ensures that the chosen input variables effectively capture essential aspects of renewable power production data, thereby improving the accuracy of forecasting models. By applying the MRMI feature selection technique, we enhance the performance and robustness of the LSTM, GRU, MLP, and

TABLE 1 CLASSIFICATION OF THE EVALUATED PAPERS

Ref.	Uncertain parameter	Prediction horizon	Feature selection	Model	Error
[30]	PV power	1 step ahead	×	naïve bayes algorithm- MLP-LSTM	MAPE index is between 8.76%
[31]	Wind power	1 step ahead	×	Temporal convolutional network	RMSE index is between 87.9475 to 100.0070 for three different data set
[32]	Wind power	1 step ahead	✓	ELM and BiLSTM models	MAPE index is between 5.34% to 35.07%
[33]	Wind speed	multi-step ahead	×	EEMD-Clustring-MLP	MAPE index is between 6.10% to 13.84%
[34]	Wind speed	multi-step ahead	×	Decomposition model-LSTM	MAPE index is between 5.62% for 12 hour ahead forecasting
[35]	Wind speed	1 step ahead	×	CNN-RNN	MAPE index is between 2.5481% to 6.0137%
[36]	Wind speed	multi-step ahead	×	CNN-BiLSTM	Performance is improved by 21% and 48%
[37]	Wind speed	1 step ahead interval forecasting	×	CEEMDAN-C-C feature selection-(MOGWO)-(MIMOLSSVM)	Coverage Probability (CP) is 6.73%
[38]	Wind power	1 step ahead	×	GWO-LSTM	MAPE index is 10.75% to to 18.24%
[39]	PV power	multi-step ahead	✓	Machine learning algorithms	RMSE index is 32 for random forest model
[42]	Wind speed	multi-step ahead	×	Hybrid model based on persistence model (PM)-AR-ARMA-ANN	MAPE is 34.28% for three step ahead forecasting
[43]	Wind speed and power	1 step ahead	×	Hybrid model based on RKF-FS-WT-ANN	MAPE is 3.6153%
[44]	Net load	multi-step ahead	×	CNN	RMSE index is 5.88
[45]	PV power	1 step ahead	×	ANN	RMSE index is 153.188

ANFIS models. The selected input data with the highest predictive value enable the models to focus on the most influential factors for RPPF. This contributes to more accurate and reliable predictions, facilitating better decision-making in areas such as energy planning, grid management, and renewable resource allocation. In summary, the MRMI feature selection technique makes a valuable contribution to the overall forecasting process, ensuring that the LSTM, GRU, MLP, and ANFIS models are equipped with the most relevant and non-redundant input data for accurate renewable power production prediction.

3- The paper presents a strong solution for predicting solar power generation in the next 24 hours. It introduces a reliable method that can be applied effectively to RPPF. This method is versatile and can be used for various renewable energy sources, such as wind and solar power. By forecasting power production for the next 24 hours, it provides valuable insights for energy grid operators, renewable energy developers, and policymakers. In summary, this paper offers a comprehensive and effective approach for RPPF, especially for predicting solar power generation. Using hybrid models, feature selection techniques, and a 24-hour prediction horizon, it serves as a valuable tool for improving energy planning, grid management, and the utilization of renewable energy.

The rest of the paper is organized in the following manner. In Section 2, we provide an overview of the framework used in the proposed method. The methodology of the proposed model is explained in detail in Section 3. Finally, in Section 4, we present the numerical results obtained from the study.

II. Methodology

Using the aforementioned hybrid model, the day-ahead prediction is obtained from the weighted sum of the outputs of each proposed prediction model. The presented hybrid model

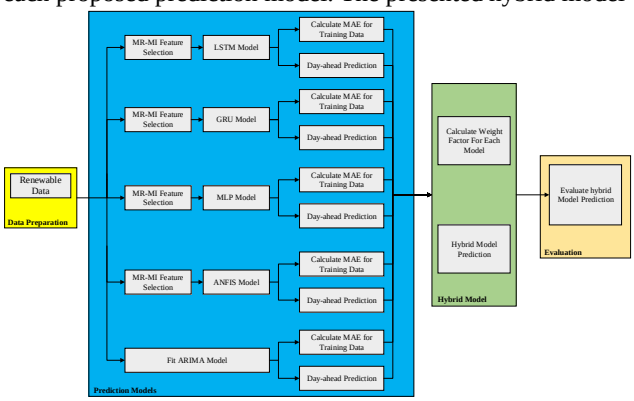

Fig. 1. Framework of the proposed hybrid model

significantly enhances the accuracy of RPPF. Combining multiple models allows each to compensate for the others'

weaknesses, thereby improving forecasting efficiency. To implement the hybrid model, input data with the highest importance values are selected for LSTM, GRU, MLP, and ANFIS models using the MRMI feature selection method. These models then predict renewable power production for the next 24 hours. Unlike the other models, ARIMA does not undergo feature selection but establishes a relationship between input and output. Finally, the hybrid model's output is determined by applying appropriate weighting factors to the individual model outputs.

The framework of the proposed method is illustrated in Figure 1.

Here are the specific details of the proposed method.

Data preparation:

First, historical data is collected and standardized during the initial phase. Next, to forecast a particular day, the artificial intelligence models prepare training and target matrices. The training matrix has dimensions of 1200 by 400, while the target matrix is 1200 by 1. Specifically, training samples are selected up to the day preceding the last day of each month for which a prediction is needed. The ARIMA model, in contrast, operates as a statistical model for time series, representing the current series as a linear combination of past observations.

Prediction models:

The artificial intelligence models utilize the MRMI feature selection module to choose training samples with the highest predictive value. This MRMI method helps identify data with the potential to accurately predict outcomes. Conversely, the ARIMA model aims to establish a relationship between input and output variables. Specifically, the ARIMA model attempts to fit a model based on the historical time series data available before the prediction day. The Mean Absolute Error (MAE) value is calculated for each prediction model using the training data. This calculation determines the weight coefficient of each model in the hybrid model. Furthermore, each prediction model generates forecasts for the next 24 hours.

Hybrid model:

In this model, the weight coefficient for each prediction model within the hybrid model is determined using the method described in Section 3.7. The weight coefficient quantifies the importance or contribution of each model to generating accurate predictions. By multiplying each model's weight coefficient by its respective prediction output, the hybrid model produces forecasts for the next 24 hours. This combination of weighted predictions from multiple models enhances the overall forecasting accuracy of the hybrid model.

Evaluation

It is essential to evaluate the performance of the implemented method using key metrics. The efficiency of the hybrid model is validated by three error indices: Mean Absolute Percentage Error (MAPE), Mean Absolute Error (MAE), and Root Mean Square Error (RMSE). These established metrics provide objective measures to assess the precision of forecasting models. The error indices defined by Equations (1), (2), and (3) are used to measure the performance of the hybrid model. These metrics enable the evaluation of the hybrid model's accuracy in forecasting renewable power production over the next 24 hours. Analyzing these measures is crucial for assessing the reliability and efficiency of the proposed approach. Analyzing these measures is essential in assessing the reliability and efficiency of the proposed approach.

$$MAPE = \frac{1}{N}\sum_{i=1}^{N}\frac{\left|S_i^{Real} - S_i^{For}\right|}{S_i^{Real}} \times 100\% \quad (1)$$

$$MAE = \frac{1}{N}\sum\left|S_i^{Real} - S_i^{For}\right| \quad (2)$$

$$RMSE = \sqrt{\frac{1}{N}\sum_{i=1}^{N}(S_i^{Real} - S_i^{For})^2} \quad (3)$$

Where N represents the total number of hours in each day, S_i^{Real} is the real value at the time i, S_i^{For} is the predicted value at the time i.

III. Problem description

A. MRMI feature selection approach

In this section, we propose the MR-MI approach to select the most suitable features. Feature selection is a widely employed method in machine learning, where a subset of the available data features is chosen for use in the learning algorithm. The forecasting process often requires a large amount of input data, including historical data. However, this data might contain unnecessary inputs that complicate the prediction of power system parameters, leading to decreased performance. Additionally, as the number of input features increases, more historical data is generally needed. However, the available historical data for forecasting is often limited. Therefore, it is essential to use a feature selection method to refine potential inputs, ensuring that only the most informative features are selected while filtering out less important ones. In this paper, we propose a feature selection method that begins by examining the similarity between input and output. Any candidate features showing only slight similarity to the target are discarded. Then, for each selected input from the previous step, if two inputs are closely related, one is chosen and the other is removed. In other words, the remaining features after these two steps are relevant and non-redundant candidates.

B. LSTM model

The study proposes using an LSTM network consisting of two layers, each with 100 hidden units. This design effectively captures complex behaviors and relationships within the data, leading to improved prediction performance. The LSTM has a unique advantage in its ability to preserve information across longer time sequences, making it particularly useful for forecasting time-series data, such as renewable power

production. By retaining contextual information, the model can make accurate predictions for the following 24 hours. The chosen configuration strikes a balance between model complexity and computational efficiency, demonstrating the effectiveness of deep learning techniques in accurately forecasting renewable power production [46].

C. GRU model

The GRU offers an alternative to the more intricate LSTM model, providing a streamlined architecture with fewer trainable parameters [47]. The GRU incorporates two gates—the reset gate and the update gate—in contrast to the three gates in the LSTM, namely, the input gate, the forget gate, and the output gate. Unlike LSTM units, GRU gates do not have dedicated memory cells within each unit, resulting in a less complex architecture. Consequently, GRU models typically exhibit higher runtime efficiency compared to LSTM models. In this research, we propose using a GRU network with two layers, each containing 100 hidden units. By configuring the network with multiple layers and a sufficient number of hidden units, the GRU model can effectively capture complex patterns and relationships in the data. Although the GRU has a simpler structure than the LSTM, it still performs robustly in handling temporal dependencies and making precise predictions. The use of two layers with 100 hidden units ensures reliability without overburdening computational resources. The simplified architecture of the GRU network, combined with the chosen configuration, facilitates efficient training and prediction for RPPF. In summary, this study demonstrates the effectiveness of alternative recurrent neural network architectures, such as GRU, in capturing temporal dependencies and making accurate predictions. GRU's reduced complexity, computational benefits, and ability to handle sequential data make it a valuable tool for tasks like forecasting renewable power production.

D. MLP model

Artificial neural networks are computational models that mimic the operation of the human brain, consisting of interconnected neurons. In this study, we have utilized a MLP neural network, trained using the Levenberg-Marquardt (LM) learning algorithm. The LM algorithm is widely acknowledged as a highly efficient and effective learning mechanism for MLP models. The specific MLP neural network employed in this research adopts a feed-forward structure, where information flows unidirectionally from the input layer to the output layer. The model comprises two layers: the input layer, which receives the input data, and the output layer, which generates predictions. Additionally, hidden layers can be integrated between these two layers to capture intricate patterns and relationships within the data. Many applications opt for a two-layer MLP architecture because it strikes a balance between model complexity and learning capacity. However, it is important to note that the specific architecture and number of hidden units in each layer may vary depending on the complexity of the problem. In this study, the chosen architecture and configuration are determined based on the requirements and characteristics of the RPPF task. By utilizing MLP neural networks and the LM learning algorithm, this paper aims to harness the computational power of artificial neural networks to effectively learn and model the relationships between input variables and the desired output. The combination of MLP and LM provides a reliable and efficient approach for capturing complex patterns and making accurate predictions in RPPF.

E. ANFIS model

ANFIS is a hybrid artificial neural network model that integrates the principles of fuzzy logic and neural networks [48]. The ANFIS model combines the ability of fuzzy logic to handle linguistic rules with the powerful learning capabilities of neural networks. This fusion allows ANFIS to effectively capture and model complex relationships within the data. In this paper, the ANFIS network is utilized to enhance the performance of the forecasting model. The main parameters of the ANFIS network include the fuzzy inference system generation method, set to Fuzzy C-Means clustering (FCM), and the number of clusters, set to 10.

F. ARIMA model

The ARIMA function generates an ARIMA object that defines the functional form and stores the parameter values of an ARIMA*(p,D,q)* model for analyzing a univariate time series data, denoted as y_t [49]. The ARIMA model considered in this paper is represented by the following form:

$$\begin{aligned}(1-\varphi_1 L-\varphi_2 L^2-\cdots\\ -\varphi_{24}L^{24})(1-L)^2 y_t\\ =c\\ +(1+\theta_1 L+\theta_2 L^2\\ +\cdots+\theta_{24}L^{24})\varepsilon_t\end{aligned} \quad (4)$$

Where, φ is parameter of non-seasonal autoregressive model, L is difference operator, c is model constant, θ is parameter of non-seasonal moving average model, and ε_t is the random variable.

G. Hybrid model

The paper presents a hybrid model that combines multiple prediction models to improve the accuracy of RPPF. This approach leverages the distinct strengths of each model while addressing their limitations, resulting in a forecasting technique that is both more effective and reliable. Traditionally, hybrid models assign equal weight coefficients to each prediction model, regardless of their performance, which can lead to suboptimal results. In this paper, we propose a new method where different weight coefficients are assigned to each model based on their MAE values. The MAE is calculated using the training results of each model, and the weight coefficients are determined through a specific equation.

$$\omega_i = \frac{\frac{1}{MAE_i}}{\sum_{i=1}^{n} \frac{1}{MAE_i}} \quad (5)$$

Where, ω_i is the weight coefficient of each prediction model, and *n* is the number of prediction models. Now that the weight coefficient of each prediction model is determined, the prediction of the hybrid model for the next 24 hours is calculated from the following equation:

$$Y_{Hybrid} = \sum_{i=1}^{n} \omega_i * y_i \quad (6)$$

Where, Y_{Hybrid} is the prediction of hybrid model for next 24 hours, and y_i is the result of *ith* prediction model for next 24 hours.

TABLE 2 RESULTS OF DIFFERENT PREDICTION MODELS FOR DAY-AHEAD PVPF FOR MAHAN PV POWER PLANT

Prediction model	Last day of March			Last day of June			Last day of September			Last day of December		
	MAE (MW)	RMSE (MW)	MAPE (%)	MAE (MW)	RMSE (MW)	MAPE (%)	MAE (MW)	RMSE (MW)	MAPE (%)	MAE (MW)	RMSE (MW)	MAPE (%)
ARIMA	0.5118	0.0910	24.5340	0.5343	0.6968	7.7187	0.0943	0.0619	7.5581	0.3935	0.1592	45.6098
MRMI-MLP	0.6582	0.5349	28.8859	0.7004	0.8772	7.2929	0.0454	0.1311	1.1040	0.4385	0.3412	54.9586
MRMI-ANFIS	0.7382	0.4848	30.5026	0.5116	0.6683	7.4918	0.1302	0.0722	2.6813	0.2185	0.1524	21.9730
MRMI-GRU	0.4280	0.0104	15.4680	1.1261	1.3156	12.8132	0.1240	0.0378	7.4690	0.2680	0.1297	25.4004
MRMI-LSTM	0.6975	0.5031	27.5882	0.9203	1.2134	10.2564	0.0537	0.0050	2.9719	0.1895	0.1355	19.1905
Hybrid model	**0.3376**	**0.0809**	**13.7206**	**0.1941**	**0.1291**	**7.3995**	**0.0811**	**0.0388**	**4.2464**	**0.1747**	**0.0468**	**29.4023**

IV. Simulation results

This section focuses on assessing the efficiency of the hybrid model in forecasting renewable energy generation, specifically for PV power production. To ensure the precision and effectiveness of the hybrid model, a variety of datasets are employed. Initially, historical solar production data from the Mahan and Rafsanjan photovoltaic power plants for 2020 are used to forecast future solar production. The study includes two case studies, each using distinct solar data to thoroughly evaluate the capabilities of the proposed hybrid model. To assess the proposed techniques, we utilized MATLAB R2020b, a widely used programming platform renowned for its applications in scientific research and data analysis. The goal of this study is to provide a comprehensive understanding of the hybrid model's efficiency and usability in forecasting renewable power production. To achieve this, we used real datasets and implemented the model on a well-established software platform.

A. PVPF of Mahan PV power plant

In the first case study, we performed day-ahead photovoltaic power forecasting (PVPF) using hourly data from the Mahan PV power plant. To evaluate the effectiveness of our method, we selected the last days of March, June, September, and December 2020 for analysis, consistent with the approach used in our previous case studies.

Table 2 presents the results of various prediction models for day-ahead photovoltaic power forecasting (PVPF). In this case study, six models are considered: ARIMA, MRMI-MLP, MRMI-ANFIS, MRMI-GRU, MRMI-LSTM, and the hybrid model. The results in Table 2 indicate that the hybrid model performs well in PVPF, demonstrating its capability to forecast PV power production with acceptable accuracy. The error indices further support this claim, as the hybrid model exhibits the best performance among the forecasting models on the last day of March. In contrast, the other methods do not outperform the hybrid model on that day. This underscores the limitations of relying solely on a single model for predicting different days with varying characteristics. Utilizing a hybrid model enhances the reliability and accuracy of the predictions, making it a preferable approach. The weights assigned to each model in the hybrid model are detailed in Table 3.

TABLE 3 WEIGHT COEFFICIENT OF EACH PREDICTION MODEL FOR MAHAN PV POWER PLANT

Month	ω_{ARIMA}	ω_{MLP}	ω_{ANFIS}	ω_{GRU}	ω_{LSTM}
Last day of March	0.208	0.113	0.296	0.098	0.285
Last day of June	0.241	0.106	0.311	0.087	0.255
Last day of September	0.2	0.1	0.3	0.1	0.3
Last day of December	0.261	0.102	0.275	0.107	0.254

The results of different seasons of the year have been compared. To use the results of the mentioned paper, the average MAPE error of different months for a season has been selected.

The graph in Figure 2 shows actual and predicted solar power generation at the end of each month using different models.

TABLE 4 MAPE ERROR OF DIFFERENT MONTHS

Prediction model	Spring	Summer	Autumn	Winter
MRIG-LSTM [50]	40.6012	18.5967	39.0396	35.5622
WT-MRIG-LSTM [50]	16.4554	7.6746	18.3332	17.8109
WT-MRIG-ELM [50]	14.3944	8.8431	25.4246	9.5635
ARIMA	24.5340	7.7187	7.5581	45.6098
MRMI-MLP	28.8859	7.2929	1.1040	54.9586
MRMI-ANFIS	30.5026	7.4918	2.6813	21.9730
MRMI-GRU	15.4680	12.8132	7.4690	25.4004
MRMI-LSTM	27.5882	10.2564	2.9719	19.1905
Hybrid model	13.7206	7.3995	4.2464	29.4023

. It is evident that the forecasts exhibit a higher margin of error, particularly during the final days of December and March, due to the highly variable weather conditions in these months compared to earlier days. It is important to note that all the models analyzed in the study focus solely on solar power production and do not account for other influencing factors. Despite this limitation, the hybrid model demonstrates reliability in predicting solar power generation for the following day. Its performance is commendable given the complex and fluctuating weather conditions during these months.

Figure 3 displays regression plots of different prediction models for the last day of December. In addition to the previously mentioned indexes, R2 has also been used to demonstrate the effectiveness of the proposed method for PVPF. The graph shows that the MRMI-LSTM prediction model has the highest R2 value. However, the hybrid model's R2 value is not significantly different from the MRMI-LSTM model. This suggests that the hybrid model performs well in accurately forecasting the PV power production, as the forecasted and real values are very close to each other. In conclusion, the previously mentioned methods are capable of effectively forecasting PV power production for the Mahan PV power plant.

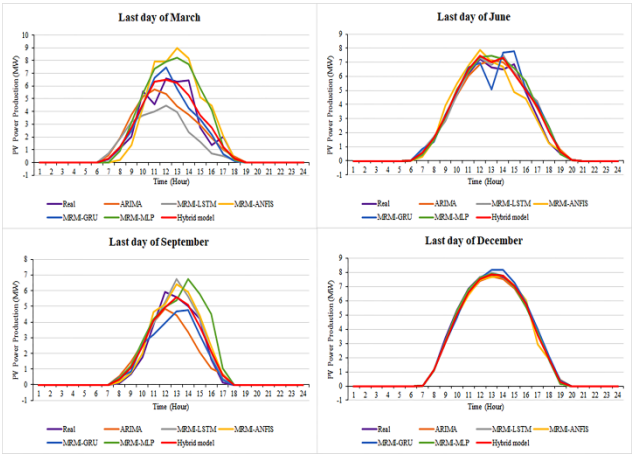

Fig. 2. Assessing various prediction models for Mahan PV power plant

B. *PVPF of Rafsanjan PV power plant*

In the second case study, hourly PV power production data from the Rafsanjan PV power plant in 2020 is used for day-ahead photovoltaic power forecasting (PVPF). The Rafsanjan PV power plant has a nominal capacity of 1.2 MW. As in the previous case studies, the last days of March, June, September, and December 2020 are selected for forecasting day-ahead PV power production using the proposed method.

Table 5 presents the results of different prediction models for day-ahead PVPF, similar to the previous case studies. The results clearly show that the hybrid model performs well in forecasting PV power production, demonstrating acceptable accuracy and outperforming other models based on the error indices. For example, on the last day of September, the MRMI-MLP model shows the best performance among the different forecasting models. However, the hybrid model performs comparably to the MRMI-MLP model and surpasses other methods. This underscores the limitations of relying solely on a single model for predicting days with varying characteristics. The use of a hybrid model improves the reliability and accuracy of the predictions. The weights assigned to each model in the hybrid model are detailed in Table 6.

Figure 4 illustrates the results for each month using different models. It is evident that the forecast error is relatively higher on the last days of December and March. These days are characterized by changing weather conditions, where factors such as temperature, radiation, and cloud cover significantly impact the forecasts. Despite these challenges, the hybrid model demonstrates its effectiveness in predicting day-ahead PV power production. The error values obtained from this method are within an acceptable range, indicating both accuracy and reliability.

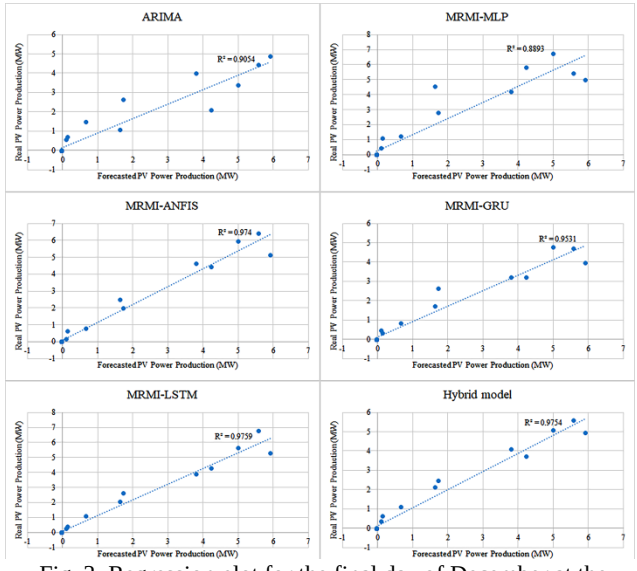

Fig. 3. Regression plot for the final day of December at the Mahan PV power plant

It is also worth noting that the day-ahead forecast relies heavily on the hybrid model, which greatly contributes to the precision of the predictions. This underscores the importance of using the hybrid model to achieve accurate day-ahead forecasts.

Figure 5 shows the R^2 index used to measure accuracy for the final day of December across different prediction models. Among the models considered, the MRMI-ANFIS prediction model achieves the highest R^2 value, indicating a strong correlation between the forecasted and actual values. This suggests that the MRMI-ANFIS model is highly accurate and reliable. Overall, the results confirm that the proposed method is effective in accurately predicting the PV power production for the Rafsanjan PV power plant.

I. Conclusion

In this paper, a hybrid model called RPPF is introduced, combining multiple forecasting models—ARIMA, MRMI-MLP, MRMI-ANFIS, MRMI-GRU, and MRMI-LSTM—to improve day-ahead predictions. By leveraging the strengths of these models and mitigating their weaknesses, the hybrid approach enhances forecasting accuracy and efficiency.

The MRMI technique is employed within the hybrid model to select the most predictive input data for the LSTM, GRU, MLP, and ANFIS models. To evaluate the model's performance, two case studies are conducted on PV power production in Mahan and Rafsanjan for the year 2020.

The results demonstrate that the hybrid model achieves satisfactory accuracy, as indicated by metrics like MAPE, MAE, and RMSE. These findings not only validate the effectiveness of the hybrid model but also highlight its potential for reliable and efficient forecasting of renewable power production. Future research could explore the applicability of this approach in other sectors of the energy system and consider additional factors that may impact the forecasting process. Additionally, prediction accuracy could be further improved by combining these methods within a closed-loop framework.

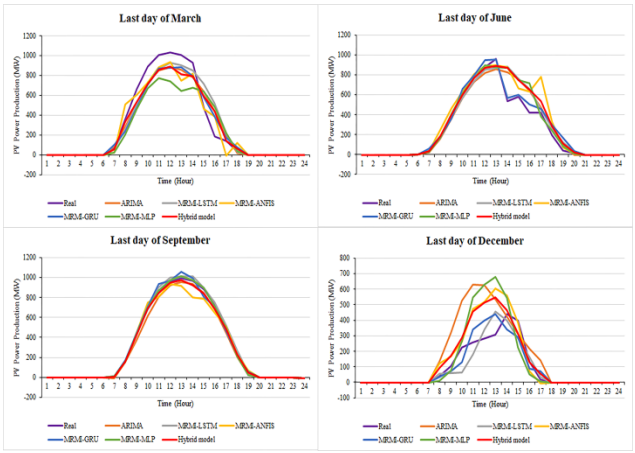

Fig. 4. Assessing various prediction models for Rafsanjan PV power plant

TABLE 5 RESULTS OF DIFFERENT PREDICTION MODELS FOR DAY-AHEAD PVPF FOR RAFSANJAN PV POWER PLANT

Prediction model	Last day of March			Last day of June			Last day of September			Last day of December		
	MAE (kW)	RMSE (kW)	MAPE (%)	MAE (kW)	RMSE (kW)	MAPE (%)	MAE (kW)	RMSE (kW)	MAPE (%)	MAE (kW)	RMSE (kW)	MAPE (%)
ARIMA	61.4656	20.6792	16.8260	48.5279	23.6963	22.5864	20.3033	19.7646	14.4021	77.5209	68.9528	67.3614
MRMI-MLP	95.3771	51.4258	22.0480	44.7761	33.7007	15.6763	5.4595	0.9276	4.7864	61.6852	34.4639	28.3559
MRMI-ANFIS	60.3823	23.8531	26.5322	61.3149	55.6033	19.2720	26.3523	15.3333	17.1840	48.3347	39.7238	32.1484
MRMI-GRU	60.2453	25.8259	18.6621	27.3876	24.4896	30.4020	16.0709	4.5092	15.7852	31.8057	0.0912	22.3722
MRMI-LSTM	63.3539	9.7691	17.8139	49.0751	32.8670	27.3831	13.7650	12.3796	15.2571	29.4512	7.0599	16.5769
Hybrid model	56.2347	23.5854	14.5869	46.7227	39.9648	19.3358	10.4980	7.4080	7.4487	41.4546	34.3694	27.6639

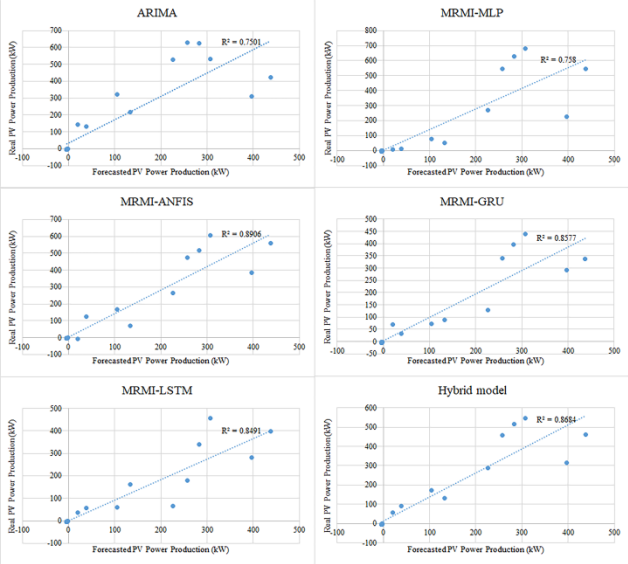

Fig. 5. Regression plot for last day of December for Rafsanjan PV power plant by different prediction models

TABLE 6 WEIGHT COEFFICIENT OF EACH PREDICTION MODEL FOR RAFSANJAN PV POWER PLANT

Month	ω_{ARIMA}	ω_{MLP}	ω_{ANFIS}	ω_{GRU}	ω_{LSTM}
Last day of March	0.260	0.132	0.249	0.111	0.248
Last day of June	0.218	0.101	0.302	0.106	0.273
Last day of September	0.194	0.120	0.283	0.099	0.304
Last day of December	0.205	0.115	0.311	0.101	0.268

REFERENCES

[1] M. Vosoogh, M. Rashidinejad, A. Abdollahi, and M. Ghaseminezhad, "Efficient networked microgrid management considering plug-in electric vehicles and storage units," International Journal of Industrial Electronics Control and Optimization, Vol. 4, No. 2, pp. 245-255, 2021.

[2] Z. Allal, H. N. Noura, and K. Chahine, "Machine Learning Algorithms for Solar Irradiance Prediction: A Recent Comparative Study," e-Prime - Advances in Electrical Engineering, Electronics and Energy, Vol. 7, p. 100453, 2024.

[3] H. B, V. G, Vaibhav, K. S. Anantharaju, and R. K. Pai, "Machine learning in the era of smart automation for renewable energy materials," e-Prime - Advances in Electrical Engineering, Electronics and Energy, Vol. 7, p. 100458, 2024.

[4] S. M. Hadad Baygi and J. Farzaneh, "Application of Artificial intelligence techniques for optimum design of hybrid grid-independent PV/WT/battery power system," International Journal of Industrial Electronics Control and Optimization, Vol. 3, No. 3, pp. 275-289, 2020.

[5] J. d. S. Catalão, H. M. I. Pousinho, and V. M. F. Mendes, "Short-term wind power forecasting in Portugal by neural networks and wavelet transform," Renewable energy, Vol. 36, No. 4, pp. 1245-1251, 2011.

[6] M. G. De Giorgi, A. Ficarella, and M. Tarantino, "Error analysis of short term wind power prediction models," Applied Energy, Vol. 88, No. 4, pp. 1298-1311, 2011.

[7] J. Jung, S. Han, and B. Kim, "Digital numerical map-oriented estimation of solar energy potential for site selection of photovoltaic solar panels on national highway slopes," Applied Energy, Vol. 242, pp. 57-68, 2019.

[8] O. Ait Maatallah, A. Achuthan, K. Janoyan, and P. Marzocca, "Recursive wind speed forecasting based on Hammerstein Auto-Regressive model," Applied Energy, Vol. 145, pp. 191-197, 2015.

[9] D. Yang, V. Sharma, Z. Ye, L. I. Lim, L. Zhao, and A. W. Aryaputera, "Forecasting of global horizontal irradiance by exponential smoothing, using decompositions," Energy, Vol. 81, pp. 111-119, 2015.

[10] J. L. Torres, A. García, M. De Blas, and A. De Francisco, "Forecast of hourly average wind speed with ARMA models in Navarre (Spain)," Solar Energy, Vol. 79, No. 1, pp. 65-77, 2005.

[11] F. Besharat, A. A. Dehghan, and A. R. Faghih, "Empirical models for estimating global solar radiation: A review and case study," Renewable and Sustainable Energy Reviews, Vol. 21, pp. 798-821, 2013/05/01/ 2013.

[12] J. Wang, P. Du, T. Niu, and W. Yang, "A novel hybrid system based on a new proposed algorithm—Multi-Objective Whale Optimization Algorithm for wind speed forecasting," Applied Energy, Vol. 208, pp. 344-360, 2017.

[13] W. Sun and M. Liu, "Wind speed forecasting using FEEMD echo state networks with RELM in Hebei, China," Energy Conversion and Management, Vol. 114, pp. 197-208, 2016.

[14] T. Niu, J. Wang, K. Zhang, and P. Du, "Multi-step-ahead wind speed forecasting based on optimal feature selection and a modified bat algorithm with the cognition strategy," Renewable Energy, Vol. 118, pp. 213-229, 2018.

[15] H. Shao, X. Deng, and F. Cui, "Short - term wind speed forecasting using the wavelet decomposition and AdaBoost technique in wind farm of East China," IET Generation, Transmission & Distribution, Vol. 10, No. 11, pp. 2585-2592, 2016.

[16] H. You, R. Jia, X. Chen, and L. Huang, "A design of ultra-short-term power prediction algorithm driven by wind turbine operation and maintenance data for LSTM-SA neural network," Journal of Renewable and Sustainable Energy, Vol. 15, No. 4, 2023.

[17] A. K. Yadav and S. Chandel, "Solar radiation prediction using Artificial Neural Network techniques: A review," Renewable and sustainable energy reviews, Vol. 33, pp. 772-781, 2014.

[18] G. Perveen, M. Rizwan, and N. Goel, "Comparison of intelligent modelling techniques for forecasting solar energy and its application in solar PV based energy system," IET Energy Systems Integration, Vol. 1, No. 1, pp. 34-51, 2019.

[19] O. M. Babatunde, J. L. Munda, Y. Hamam, and C. G. Monyei, "A critical overview of the (Im)practicability of solar radiation forecasting models," e-Prime - Advances in Electrical Engineering, Electronics and Energy, Vol. 5, p. 100213, 2023.

[20] Q. Yu and Z. Li, "Correlated load forecasting in active distribution networks using Spatial - Temporal Synchronous Graph Convolutional Networks," IET Energy Systems Integration, Vol. 3, No. 3, pp. 355-366, 2021.

[21] M. Khodayar, O. Kaynak, and M. E. Khodayar, "Rough deep neural architecture for short-term wind speed forecasting," IEEE Transactions on Industrial Informatics,

Vol. 13, No. 6, pp. 2770-2779, 2017.
[22] Q. Hu, R. Zhang, and Y. Zhou, "Transfer learning for short-term wind speed prediction with deep neural networks," Renewable Energy, Vol. 85, pp. 83-95, 2016.
[23] H.-z. Wang, G.-q. Li, G.-b. Wang, J.-c. Peng, H. Jiang, and Y.-t. Liu, "Deep learning based ensemble approach for probabilistic wind power forecasting," Applied energy, Vol. 188, pp. 56-70, 2017.
[24] L. Zeng, X. Lan, and S. Wang, "Short-term wind power prediction based on the combination of numerical weather forecast and time series," Journal of Renewable and Sustainable Energy, Vol. 15, No. 1, 2023.
[25] X. Yang, Z. Zhao, Y. Peng, and J. Ma, "Research on distributed photovoltaic power prediction based on spatiotemporal information ensemble method," Journal of Renewable and Sustainable Energy, Vol. 15, No. 3, 2023.
[26] Y. Sun, V. Venugopal, and A. R. Brandt, "Short-term solar power forecast with deep learning: Exploring optimal input and output configuration," Solar Energy, Vol. 188, pp. 730-741, 2019.
[27] X. Liu, H. Zhang, X. Kong, and K. Y. Lee, "Wind speed forecasting using deep neural network with feature selection," Neurocomputing, Vol. 397, pp. 393-403, 2020.
[28] H. Sharadga, S. Hajimirza, and R. S. Balog, "Time series forecasting of solar power generation for large-scale photovoltaic plants," Renewable Energy, Vol. 150, pp. 797-807, 2020.
[29] M. Alaraj, A. Kumar, I. Alsaidan, M. Rizwan, and M. Jamil, "Energy production forecasting from Solar photovoltaic plants based on meteorological parameters for Qassim region, Saudi Arabia," Ieee Access, Vol. 9, pp. 83241-83251, 2021.
[30] S. S. Pattanaik, A. K. Sahoo, R. Panda, and S. Behera, "Life cycle assessment and forecasting for 30kW solar power plant using machine learning algorithms," e-Prime - Advances in Electrical Engineering, Electronics and Energy, Vol. 7, p. 100476, 2024.
[31] J. Zhu, L. Su, and Y. Li, "Wind power forecasting based on new hybrid model with TCN residual modification," Energy and AI, Vol. 10, p. 100199, 2022.
[32] J. Xiong, T. Peng, Z. Tao, C. Zhang, S. Song, and M. S. Nazir, "A dual-scale deep learning model based on ELM-BiLSTM and improved reptile search algorithm for wind power prediction," Energy, Vol. 266, p. 126419, 2023.
[33] X.-J. Chen, J. Zhao, X.-Z. Jia, and Z.-L. Li, "Multi-step wind speed forecast based on sample clustering and an optimized hybrid system," Renewable Energy, Vol. 165, pp. 595-611, 2021.
[34] S. R. Moreno, R. G. da Silva, V. C. Mariani, and L. dos Santos Coelho, "Multi-step wind speed forecasting based on hybrid multi-stage decomposition model and long short-term memory neural network," Energy Conversion and Management, Vol. 213, p. 112869, 2020.
[35] J. Duan et al., "A combined short-term wind speed forecasting model based on CNN–RNN and linear regression optimization considering error," Renewable Energy, Vol. 200, pp. 788-808, 2022.
[36] V. Kosana, K. Teeparthi, and S. Madasthu, "Hybrid wind speed prediction framework using data pre-processing strategy based autoencoder network," Electric Power Systems Research, Vol. 206, p. 107821, 2022.
[37] T. Liu, Q. Zhao, J. Wang, and Y. Gao, "A novel interval forecasting system for uncertainty modeling based on multi-input multi-output theory: A case study on modern wind stations," Renewable Energy, Vol. 163, pp. 88-104, 2021.
[38] Z. Cai, S. Dai, Q. Ding, J. Zhang, D. Xu, and Y. Li, "Gray wolf optimization-based wind power load mid-long term forecasting algorithm," Computers and Electrical Engineering, Vol. 109, p. 108769, 2023.
[39] C. Scott, M. Ahsan, and A. Albarbar, "Machine learning for forecasting a photovoltaic (PV) generation system," Energy, Vol. 278, p. 127807, 2023.
[40] S. Theocharides, G. Makrides, A. Livera, M. Theristis, P. Kaimakis, and G. E. Georghiou, "Day-ahead photovoltaic power production forecasting methodology based on machine learning and statistical post-processing," Applied Energy, Vol. 268, p. 115023, 2020.
[41] J. Heo, K. Song, S. Han, and D.-E. Lee, "Multi-channel convolutional neural network for integration of meteorological and geographical features in solar power forecasting," Applied Energy, Vol. 295, p. 117083, 2021.
[42] W. Hu et al., "New hybrid approach for short-term wind speed predictions based on preprocessing algorithm and optimization theory," Renewable Energy, Vol. 179, pp. 2174-2186, 2021.
[43] H. H. Aly, "A novel deep learning intelligent clustered hybrid models for wind speed and power forecasting," Energy, Vol. 213, p. 118773, 2020.
[44] M. Jurado, M. Samper, and R. Rosés, "An improved encoder-decoder-based CNN model for probabilistic short-term load and PV forecasting," Electric Power Systems Research, Vol. 217, p. 109153, 2023.
[45] C. Brester, V. Kallio-Myers, A. V. Lindfors, M. Kolehmainen, and H. Niska, "Evaluating neural network models in site-specific solar PV forecasting using numerical weather prediction data and weather observations," Renewable Energy, Vol. 207, pp. 266-274, 2023.
[46] F. Keynia and G. Memarzadeh, "A new financial loss/gain wind power forecasting method based on deep machine learning algorithm by using energy storage system," IET Generation, Transmission & Distribution, Vol. 16, No. 5, pp. 851-868, 2022.
[47] G. Memarzadeh and F. Keynia, "A new short-term wind speed forecasting method based on fine-tuned LSTM neural network and optimal input sets," Energy Conversion and Management, Vol. 213, p. 112824, 2020.
[48] S. Kouhi and F. Keynia, "A new cascade NN based method to short-term load forecast in deregulated electricity market," Energy Conversion and Management, Vol. 71, pp. 76-83, 2013.
[49] N. Darjani, and H. Omranpour, . "Comprehensive learning polynomial auto-regressive model based on optimization with application of time series forecasting," International Journal of Industrial Electronics Control and Optimization, Vol. 5, No. 1, pp. 43-50, 2022.
[50] G. Memarzadeh and F. Keynia, "Solar power generation forecasting by a new hybrid cascaded extreme learning method with maximum relevance interaction gain feature selection," Energy Conversion and Management, Vol. 298, p. 117763, 2023.

Gholamreza Memarzadeh was born in Rafsanjan, Iran. He received the B.S. and M.S. degrees in electrical engineering from Shahid Bahonar University, kerman, Iran, and Ph.D. degree in electrical engineering from the Graduate University of Advanced Technology, Kerman, Iran in 2012, 2015, and 2022, respectively. He is currently an Assistant Professor with the Department of Electrical Engineering of Vali-e-Asr university of Rafsanjan.

Farshid Keynia was born in Kerman, Iran. He received the B.S. degrees from Shahid Bahonar University, kerman, Iran, M.S. and Ph.D. degree in electrical engineering from Semnan University, Semnan, Iran, in 1996, 2001 and 2011, respectively. He is currently an Associate Professor with the Department of Energy, Institute of Science and High Technology and Environmental Sciences, Graduate University of Advanced Technology, Kerman, Iran.

Faezeh Amirteimoury received her the B.Sc degrees from Shahid Bahonar University, kerman, Iran in 2011 and M.Sc. dgree from Islamic Azad University of Kerman, Kerman, Iran in 2022. She is currently a software engineer working for an IT company and a researcher in the field of AI.

Rasoul Memarzadeh was born in Rafsanjan, Iran. He received the B.S. degree in Civil Engineering from Vali-e-Asr University of Rafsanjan, Iran in 2009. He received M.S. degree in Civil (hydraulic) Engineering from the Khaje Nasirodin Toosi University of Technology, Tehran, Iran in 2012, and PhD degree in the same field from the Shahid Bahonar University, Kerman, Iran in 2017. He is currently an Assistant Professor with the Department of Civil Engineering of Vali-e-Asr university of Rafsanjan.

Hossein Noori was born in Rafsanjan, Iran. He received B.S., M.S. and Ph.D. degrees in communication engineering from Isfahan University of Technology, Isfahan, Iran, Shahid Bahonar University, kerman, Iran and Tarbiat Modares University, Tehran, Iran, respectively. He is currently an Assistant Professor with the Department of Electrical Engineering of Vali-e-Asr university of Rafsanjan.

IECO

This page intentionally left blank.

International Journal Of
Industrial Electronics Control and Optimization
Print ISSN: 3517-2645
Online ISSN: 3568-2645
Homepage: https://ieco.usb.ac.ir/

Assessment of Economic, Technical, Social and Environmental Impact of Flexibility-based Smart Microgrid Operation

Faezeh Gholipour Zarandi[1] | Masoud Rashidinejad[2] | Amir Abdollahi[3] | Ali Yazhari Kermani[4]

Department of Electrical Engineering, Shahid Bahonar University of Kerman, Kerman, Iran.[1,2,3,4]
Corresponding author's email: Mrashidi@uk.ac.ir

Article Info

Article type:
Research Article

Article history:
Received: 16-May-2024
Received in revised form: 26-July-2024
Accepted: 06-August-2024
Published online: 21-March-2025

Keywords:
Flexibility,
Battery Aging,
Smart Microgrid,
Uncertainty,
Lexicographic Method

ABSTRACT

The proliferation of renewable energy sources, with their inherent uncertainty in smart microgrids, necessitates the use of flexible resources to maintain grid stability. However, implementing these flexibility-based approaches can have a multidimensional impact, including economic, technical, social, and environmental considerations. This study investigates these effects, with a particular focus on how flexibility provision influences battery aging, which is a critical aspect since batteries are the primary source of flexibility in microgrids. Here, a Lexicographic approach is used to optimize the multi-objective operation problem by minimizing costs while maximizing flexibility. Batteries act as the main source of flexibility and compensate for the uncertainty associated with solar energy production; therefore, it is important to investigate the battery's aging upon flexibility provision. The analysis shows a trade-off between flexibility and economic efficiency. Hence, from an economic point of view, increasing reliance on batteries and micro turbine production to improve flexibility leads to higher operating costs. From a social perspective, the proposed approach increases microgrid reliability by minimizing the cost of energy not supplied. Considering the technical aspect, the results indicate that increasing the use of batteries in order to increase microgrids' flexibility accelerates their aging, hence decreasing their corresponding state of health. Further, the simulation results show that flexibility comes with an environmental cost. Therefore, increasing reliance on micro turbine production and the possibility of purchasing energy from sources with more emissions to provide the required flexibility can lead to an increase in the cost of pollution.

I. Introduction

The growing concern over climate change and the depletion of fossil fuels has driven a global shift towards Renewable Energy Resources (RERs). Solar power, with its abundance and clean energy generation, has emerged as a frontrunner in this transition. However, the inherent variability of solar energy introduces challenges to grid stability. Unlike traditional power plants fueled by coal or natural gas, solar power generation fluctuates throughout the day, depending on sunshine availability. This variability can disrupt the delicate balance between supply and demand within a power grid, potentially leading to voltage fluctuations, outages, and equipment damage [1].

In order to address these challenges and ensure the seamless integration of RERs like solar power, the concept of flexibility has received a great amount of attention in the literature covering smart microgrids operation [2]. A smart microgrid is a localized, self-contained power system that integrates Distributed Energy Resources (DERs) like solar panels, wind turbines, and energy storage systems [3]. Flexibility, in this context, refers to a microgrid's ability to adapt to real-time changes in power supply and demand. This

adaptation can involve various strategies, such as adjusting power generation from renewable resources, strategically utilizing energy storage systems, and dynamically managing consumer load profiles [4].

Previous studies have explored the concept of flexibility from various perspectives, highlighting its multifaceted nature and providing a comprehensive overview of the challenges and opportunities associated with integrating RERs into power systems. Their work emphasizes the need for flexibility as a key enabler for a reliable and efficient grid with a high penetration of renewables [5]. The integration of renewable energy sources generally leads to control challenges. From this point of view, it is very important to create control measures against the uncertainties of renewable resources in order to maintain and improve flexibility. For instance, in [6] the proposed strategy is based on deep learning to maintain the stability of the system against the fluctuations in the production of renewable power plants, which examines the technical and economic aspects of flexibility.

Building upon these definitions, researchers have introduced several metrics to quantify the energy system's flexibility. For example, [7] proposes a Flexibility Requirement Index (FRI) that considers a system's ability to manage power imbalances over different time horizons. Similarly, [8] presents the System Flexibility Index (SFI) as a measure of a system's capability of rapid response to power fluctuations. These metrics offer valuable tools for assessing and comparing the flexibility of different microgrid configurations. Beyond definitions and metrics, research efforts have delved into the practical implementation of flexibility strategies. In this regard, [9] explores the potential of demand response programs as a means to enhance flexibility. Demand response programs incentivize consumers to adjust their electricity consumption patterns during peak demand periods, thereby alleviating pressure on the grid. In [10], four different flexibility evaluation indicators are defined, which show the matching of power supply and demand with the effect of error in load forecasting. In [11] several flexibility indices are defined for real-time operations, which are modeled as the cost of flexibility in the objective function, and the economic trade-off between the cost of production and the cost of flexibility provides an acceptable level of flexibility.

Numerous studies have also investigated the role of energy storage systems, particularly batteries, in providing flexibility within microgrids. For instance, [12] analyzes the techno-economic feasibility of using battery storage to manage the variability of RERs. On the other hand, it highlights the trade-off between flexibility benefits and the cost associated with battery deployment and operation. Similarly, [13] focuses on the technical challenges of battery degradation due to increased cycling for flexibility purposes. This research explores strategies to mitigate battery aging and optimize battery utilization within microgrids.

Despite significant advancements in understanding and implementing flexibility within smart microgrids, further research opportunities still exist. Flexibility services, by considering the preferences of end users, can also include the social perspective in addition to technical and economic perspectives. In [14], a two-level optimization is defined for systematic evaluation to provide flexibility, where the consumers play a role in providing flexibility. In [15] flexibility is examined from the technical point of view in addition to the economic point of view. In this study, the power generation and transmission capacity is considered as a technical constraint and the results show that technical challenges are of particular importance in flexibility studies along with economic challenges. In [16], the authors examine the effect of flexibility on system reliability. Although the results show that the improvement of flexibility has a positive effect on reliability indicators, the increase of social satisfaction resulting from this planning has not been directly addressed in these studies. On the other hand, in [17], flexibility in the power grid has been investigated by considering gas-fired fast ramp power plants as a resource of flexibility. In these studies, in addition to determining the trade-off between cost and flexibility, it is also possible to check the pollution constraints, which has not been addressed in these studies. Table 1 summarizes the main topic of flexibility studies in previous literature. Flexibility studies are often looking for optimal solutions to increase flexibility, while the technical, economic, social and environmental evaluation of flexibility improvement is of special importance, which has not been dealt with in a comprehensive and integrated way in previous studies.

TABLE 1 OVERVIEW OF THE PREVIOUS LITERATURE IN FLEXIBILITY STUDIES

Ref.	Year	Aspects of flexibility provision				Battery aging	Multi objective Optimization
		Technical	Economic	Social	Environmental		
[4]	2017	×	✓	×	×	×	×
[5]	2021	×	✓	×	×	×	✓
[6]	2024	×	✓	×	✓	×	×
[7]	2021	✓	✓	×	×	×	×
[8]	2019	×	✓	✓	×	×	×
[9]	2023	✓	✓	×	✓	×	×
[10]	2023	✓	✓	×	×	×	✓
[11]	2019	×	✓	✓	×	×	×
[12]	2020	✓	✓	×	×	✓	✓
[13]	2018	✓	✓	×	×	✓	✓
[14]	2024	✓	✓	✓	×	×	×
[15]	2022	✓	✓	×	×	×	×
[16]	2022	×	✓	×	×	×	×
[17]	2020	×	✓	×	×	×	×
Current study		✓	✓	✓	✓	✓	✓

This paper investigates the multi-objective optimization problem in smart microgrids, considering both economic costs and system flexibility. In order to facilitate the multi-objective optimization a lexicographic approach is employed to prioritize objectives. Here, two primary cases are analyzed. The first case is defined by assigning the higher priority to the operation cost. Following the same principle, the second case prioritizes flexibility. Moreover, the uncertainty associated with photovoltaic (PV) generation is incorporated into the model. Key contributions and points that make this paper stand out against previous literature can be summarized as follows.

Comprehensive assessment of flexibility:

- This study extensively investigates the economic, technical, social, and environmental impacts of flexibility-based smart microgrid operations, providing a comprehensive view. Here, the trade-off between flexibility and costs, as well as the environmental implications of increased gas-fired power plant operation (for fast ramping capabilities), are analyzed. Also, social impacts are assessed through metrics such as outage duration and customer satisfaction index.
- Battery Aging Focus: This study emphasizes the impact of flexibility provision on battery aging, which is crucial since batteries are the primary source of flexibility in microgrids. Hence in this paper, the impact of flexibility on battery aging (as a flexible resource) is evaluated.
- Lexicographic Method: This paper employs a Lexicographic approach for multi-objective optimization, balancing cost and flexibility in smart microgrid operations.

Also, the uncertainties in PV generation are modeled using Monte Carlo simulation in MATLAB software, while the optimization problem is solved using the GAMS environment.

In essence, this research provides valuable insights into the trade-offs involved in optimizing smart microgrids, with a particular focus on the role of flexibility and its impact on various system aspects.

The rest of this paper is organized as follows: The methodology and modeling are introduced in the section II. Section III presents optimization results. Likewise, section IV provides more detailed discussions and analysis. Finally, the conclusion is given in section V.

II. Methodology

A. Smart Microgrid Optimization

In order to investigate the problem of flexible operation, a multi-objective function is defined for smart microgrid structure [8]. The first objective function is to minimize operation costs. The operating costs of the microgrid are shown in (1). In this regard, $cost^{E}$ is the cost of energy purchased from the upstream network, $cost^{ESS}$ is the cost of charging and discharging the battery and $cost^{ENS}$ is the cost of Energy Not Supplied (ENS).

In (2), $\pi^{N}_{t,s}$ is the price of purchasing energy from the upstream network and $p^{N}_{t,s}$ is the power exchanged with the upstream network. Time and scenario indices are represented by t and s. Here, T is the time interval of 1...24 hours. In (3), π^{ESS} is the price of battery charging and discharging. In the same equation, $p^{ch}_{t,s}$ and $p^{dis}_{t,s}$ are the charging and discharging power of the battery, respectively. Likewise, (4) constitutes the cost of ENS where $\pi^{ENS}_{t,s}$ represents the price of ENS and $p^{ENS}_{t,s}$ shows amount of ENS. [18].

$$F_1^{C} = Min\left\{OC = \sum_{s}\sum_{t=1}^{24}\left\{\begin{matrix} cost^{E} + cost^{ESS} \\ + cost^{ENS} \end{matrix}\right\}\right\} \quad (1)$$

$$cost^{E} = \{\pi^{N}_{t,s} p^{N}_{t,s}\} \qquad \forall t \in T \quad (2)$$

$$cost^{ESS} = \left\{\pi^{ESS}{}_{t,s}\left(p^{ch}_{t,s} + p^{dis}_{t,s}\right)\right\} \qquad \forall t \in T \quad (3)$$

$$cost^{ENS} = \left\{\pi^{ENS}_{t,s} p^{ENS}_{t,s}\right\} \qquad \forall t \in T \quad (4)$$

The second objective which aims to maximize the flexibility of the system by considering the flexibility index, is shown in (5). In this equation, $C^{a}_{(i,t)}$ and $p^{*}_{(i,t)}$ demonstrate the available capacity and instantaneous required power [8].

$$F_2^{F} = Max\left\{SFI = \sum_{s}\sum_{t=1}^{24}\frac{C^{a}_{(t,s)}}{p^{*}_{(t,s)}(t_{C^{*}_{(t,s)}} - t_{(t,s)})}\right\} \quad (5)$$

Battery degradation and aging occurs through an internal electrochemical process [10]. The degradation process occurs during operation as well as when the battery is not in the duty cycle. Hence, aging or State of Health (SOH) refers to the degree of battery damage compared to its initial state. SOH is defined in (6), where ξ_{tot} is the total battery cell capacity loss and Q_{nom} is the nominal battery capacity [19].

$$SOH = \left(1 - \frac{\xi_{tot}}{0.2Q_{nom}}\right) \quad (6)$$

The total battery aging is presented in (7) that is consisted of two parts: cycle aging and life-time aging, which are shown as ξ_{cyc} and ξ_{cal}, respectively [20].

$$\xi_{tot} = \xi_{cyc} + \xi_{cal} \quad (7)$$

$$\xi_{cyc} = \sum_i \left(k_{s1} SOC_{dev,i} e^{\left(k_{s2} SOC_{dev,i}\right)} \right) \times e^{\frac{-Ea}{R}\left(\frac{1}{T}-\frac{1}{T_{ref}}\right)} Q_{proc,i} \quad (8)$$

$$SOC_{avg,i} = \frac{1}{\Delta Q_{proc,i}} \int_{Q_{proc,i-1}}^{Q_{proc,i}} SOC \, dQ_{proc} \quad (9)$$

$$SOC_{dev,i} = \sqrt{\frac{1}{\Delta Q_{proc,i}} \int_{Q_{proc,i-1}}^{Q_{proc,i}} \left(SOC - SOC_{avg,i}\right)^2 dQ_{proc}} \quad (10)$$

Arrhenius equation is used in (8), which is a well-established principle in chemistry, to explain the effect of temperature on battery aging. This equation includes the base temperature of the cell (T_{ref}) and T defines the temperature during operation. R is the gas constant, E_a is a parameter that represents the activation energy, and $Q_{proc,i}$ is the processed charge at the end of i^{th} event. In this regard the value deviation from the reference state of charge is shown as SOC_{dev}. k_{sn} SOC during a specific cycle is shown using SOC_{avg}. In (10), SOC_{dev} is fully described [20].

$$\frac{d\xi_{cal}}{dt} = k(T, SOC) = \left(1 + \frac{\xi_{cal}(t)}{Q_{nom}}\right)^{-\alpha(T)} \quad (11)$$

$$k(T, SOC) = k_A e^{\frac{-E_A}{R}\left(\frac{1}{T}-\frac{1}{T_{ref}}\right)} SOC + k_B e^{\frac{-E_B}{R}\left(\frac{1}{T}-\frac{1}{T_{ref}}\right)} \quad (12)$$

$$\xi_{cal} = Q_{nom}\left(\left(\frac{k(T, SOC)(1+\alpha(T))t}{Q_{nom}} + 1\right)^{\frac{1}{1+\alpha(T)}} - 1\right) \quad (13)$$

The calendar aging structure uses Arrhenius equations. In this regard, calendar aging is influenced by an empirical equation between SOC and temperature. For describing the calendar aging of batteries $K\sqrt{t}$ is often used. Also, parameter $\alpha(T)$ is provided which is related to temperature. The $\alpha(T)$ parameter follows the experimental data using non-linear regression. ξ_{cal} calendar aging at the time t is calculated in (11). $k(T, SOC)$ expresses the kinetic dependence of capacity reduction based on temperature and SOC. Kinetic dependence is shown in (12). In this equation, k_A and k_B are model parameters, E_A and E_B are experimental parameters that determine the activation energy SOC and temperature are assumed constant in these equations. Therefore, (11) is rewritten as (13) [21].

$$P_{t,s}^{MT} + P_{t,s}^{G} + P_{t,s}^{PV} + ENS_{t,s} + P_{t,s}^{dis} = P_{t,s}^{ch} + P_{t,s}^{D} + P_{t,s}^{S} \quad (14)$$

$$SoC_{t,s} = SoC_{t-1,s} + \frac{\left(P_{t,s}^{ch}\eta^{ch} - \frac{P_{t,s}^{dis}}{\eta^{dis}}\right)}{E} \quad (15)$$

$$SoC_{Min} \le SoC_{t,s} \le SoC_{Max} \quad (16)$$

$$P_t^{ch} \le u_{t,s}^{ch} P^{ch\_Max} \quad (17)$$

$$P_{t,s}^{dis} \le u_{t,s}^{dis} P^{dis\_Max} \quad (18)$$

$$u_{t,s}^{ch} + u_{t,s}^{dis} = 1 \quad (19)$$

$$P^{MT\_min} \le P_{t,s}^{MT} \le P^{MT\_Max} \quad (20)$$

$$P_D^{MT} \le P_{t,s}^{MT} - P_{t-1,s}^{MT} \le P_U^{MT} \quad (21)$$

$$0 \le P_{t,s}^{B} \le P_B^{Max} \quad (22)$$

$$0 \le P_{t,s}^{s} \le P_s^{Max} \quad (23)$$

$$MCe = \varepsilon . \sum_s \sum_t \upsilon . P_{t.s}^{B} + \sigma . P_{t.s}^{MT} \quad (24)$$

Load balance constraint is shown in (14). In this equation, $P_{t,s}^{MT}$ is the micro turbine (MT) production power, $P_{t,s}^{G}$ is the power purchased from the upstream network, $P_{t,s}^{D}$ is the microgrid load, and $P_{t,s}^{S}$ is the power sent to the upstream network. This constraint balances the power at time t and under scenario s. The process of changing battery's SOC is explained in (15). In this equation, η^{ch} and η^{dis} are the charging and discharging efficiency of the battery, respectively. Maximum and minimum limit of SOC is shown in (16). In this equation, SOC_{Max} and SOC_{Min} are the maximum and minimum limits of SOC, sequentially. The charging and discharging power limits are explained in (17) and (18), respectively. In these equations, the maximum charge and discharge power of the battery are shown by P^{ch_Max} and P^{dis_Max}. (18) introduces two binary variables, denoted as

$u_{t,s}^{ch}$ and $u_{t,s}^{dis}$. These variables can only take on the values of 0 or 1. Variable $u_{t,s}^{ch}$ represents the charging state of the battery ($u_{t,s}^{ch}$ = 1 indicates charging), while variable $u_{t,s}^{dis}$ represents the discharging state ($u_{t,s}^{dis}$ = 1 indicates discharging). This mathematical relationship enforces the constraint that the battery cannot be in both charging and discharging states simultaneously. (20) defines the upper and lower boundaries of MT, which P^{MT_Max} and P^{MT_min} are the maximum and minimum production power values of the MT. Furthermore, the MT ramp speed limit is explained by (21). In this equation, P_U^{MT} and P_D^{MT} show the ramp-up and ramp-down of the MT. The limit of buying and selling power from the main network are shown by (22) and (23). These equations state that the power purchased from the upstream and the power sent to the upstream is less than the values of P_B^{Max} and P_s^{Max}, respectively [21]. The carbon emission cost is the equivalent emission cost for electricity purchased from the upstream grid and the MT. If υ and σ are the equivalent emission factors for upstream grid electricity and MT electricity, and ε is the CO_2 processing cost per kg, then the carbon emission cost is expressed as (24) [22].

B. *Modeling the output power of the solar power plant with the Monte Carlo method*

Previous research has shown that the beta distribution function provides the most accurate and closest values for radiation modeling compared to other distribution functions used for this purpose. The probability density distribution function for the beta distribution is as provided in (25) where B can be expressed by the gamma function (Γ) which is shown in (26). Also, α and β are parameters of beta probability distribution function. After fitting the beta distribution function to the historical data, the parameters of the beta distribution function are obtained with the help of MATLAB Learning Toolbox. After obtaining the probability distribution function, the solar radiation is predicted for the required time interval with the help of the inverse transformation of the beta function. (27) presents the amount of solar power resulting from different amounts of radiation. In this equation; G is the modeled solar radiation in terms of w/m^2, G_{std} is solar radiation in the standard environment. In addition, R_c is a certain amount of radiation. Finally, P_{sn} is the nominal output power of solar panels, which is determined according to the structure of the panel [23].

$$f(x) = \frac{x^{\alpha-1}(1-x)^{\beta-1}}{B(\alpha,\beta)} \tag{25}$$

$$B(\alpha,\beta) = \frac{\Gamma(\alpha)\Gamma(\beta)}{\Gamma(\alpha+\beta)} \tag{26}$$

$$P_{pv} = \begin{cases} P_{sn}\dfrac{G^2}{G_{std}+R_c} & 0 \le G \le R_c \\ P_{sn}\dfrac{G}{G_{std}} & R_c \le G \le G_{std} \\ P_{sn} & G_{std} \le G \end{cases} \tag{27}$$

C. *Mathematical approach: Lexicographic Method*

Multi-objective optimization problems are challenging due to the inherent conflicts between the objective functions. Multi-objective optimization problems inherently lack a single solution that can simultaneously achieve optimal values for all objectives. The Lexicographic method serves as an efficient approach to optimize these problems by relying on a pre-defined ordering among the objectives. This method involves sequentially solving a series of single-objective optimization problems after prioritizing the objectives. At each stage, one objective is optimized while considering the constraints imposed by the previously optimized objectives. This process continues until all objectives are optimized in the desired order. The implementation of the Lexicographic method consists of optimizing the objective with the first priority at the beginning and obtaining the optimum value of $F_1(x) = F_1^*$. Then, the second step is to optimize the objective with the second priority by adding the constraint $F_1(x) \le F_1^*$ (for minimization objectives) to preserve the optimal solution of the first optimization. Hence, minimizing $F_2(x) = F_2^*$ subject to $F_1(x) \le F_1^*$ will be the optimal solution for the multi-objective problem that shown in (28) [24]:

$$\begin{aligned} &Min\, F_i(x) = \\ &\quad subject\ to: F_j(x) \le F_j(x_j^*) \\ &\quad j = 1,2,\ldots,i-1 \\ &\quad i = 1,2,\ldots,n \end{aligned} \tag{28}$$

where i presents an objective status in the preferred order and $F_j(x_j^*)$ denotes the optimal value of $F_j(x)$ [24].

III. Test Results

The structure investigated in this paper includes a smart microgrid containing an MT, a PV and an energy storage. In this structure, the battery plays the role of the energy storage, and working alongside the MT, it is also a source of flexibility in addition to supplying energy. In this research, the problem of flexibility-based operation is investigated using the Lexicographic method in two cases, with cost priority in the first case and flexibility in the second one. Hence, in the first case, the cost objective is minimized initially, and the flexibility objective is optimized with an additional constraint of $Cost(x) \le Cost^*$ which leads to the optimum value

considering both objectives. Likewise, the second case assigns the flexibility with a higher priority and optimizes the operation cost in accordance to that. In this regard, the scheduling results of the MT, battery and the exchanged energy with the upstream network are presented in this section. In addition, the effect of providing flexibility using the battery on its aging and health is numerically compared in both cases. In order to examine the results obtained from solving the stochastic scheduling problem, 1000 scenarios are generated using Monte Carlo, and the number of these scenarios has been reduced to 10 using the k-means method. The utilized historical data were acquired from the modified Rye microgrid [25]. Fig. 1 shows the production power of the solar power plant in the 10 scenarios. In addition, the probability of these scenarios is shown in Table 2.

Fig. 2 shows the electrical demand of the studied microgrid in a 24-hour period. Additionally, in order to exchange energy with the upstream network, the corresponding prices are shown in Fig. 3. It's worth mentioning that the electrical demand and electricity prices are acquired from [26]. Although these values can have considerable uncertainties, in this study they are regarded as deterministic entities for the ease of calculation. This is since the main idea of this research is to provide a comprehensive study regarding different aspects of flexibility provision and considering the uncertainties of PV generation can sufficiently impose a high amount of flexibility requirement.

Fig. 4 shows the scheduling of the smart microgrid energy resources in the first case. Since in this case the scheduling cost is prioritized, as can be observed in this figure, the MT is operating at its minimum capacity for most of the time intervals. On the other hand, the battery is discharged in certain hours and charged in hours with the lowest price of energy purchased from the upstream network.

Since there are spikes in the consumption profile at some hours such as 8 and 22, it is necessary for the network to have the required flexibility in order to supply the load. Hence, the fast-ramp resource (battery) is discharged for this purpose.

Fig. 5 shows the values of ENS for the two cases. In this optimization problem, the maximum amount of ENS is limited to 50 kW. However, despite setting the Value of the Lost Load (VOLL) equal to 2 $\$/_{kW}$, due to the consideration of the cost of pollution, the optimization results show that there is unsupplied energy in several time intervals.

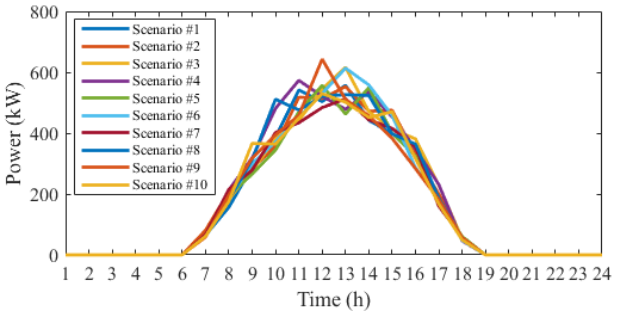

Fig. 1. Production power of the solar power plant in the 10 scenarios

TABLE 2 PV SCENARIOS AND THE CORRESPONDING PROBABILITIES

Scenario	***1***	***2***	***3***	***4***	***5***
Probability	0.105	0.09	0.102	0.123	0.103
Scenario	**6**	**7**	**8**	**9**	**10**
Probability	0.095	0.097	0.102	0.106	0.077

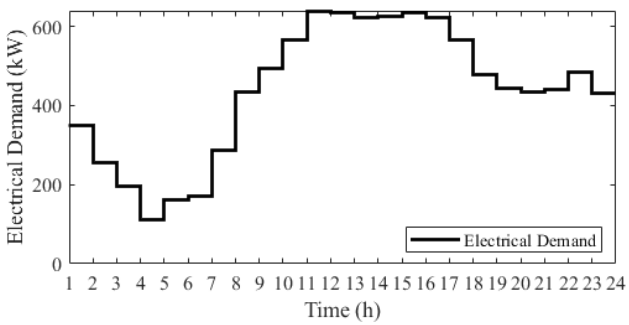

Fig. 2. Electrical demand

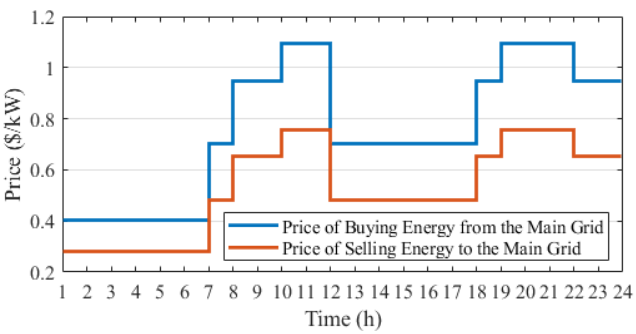

Fig. 3. Main grid energy trading price

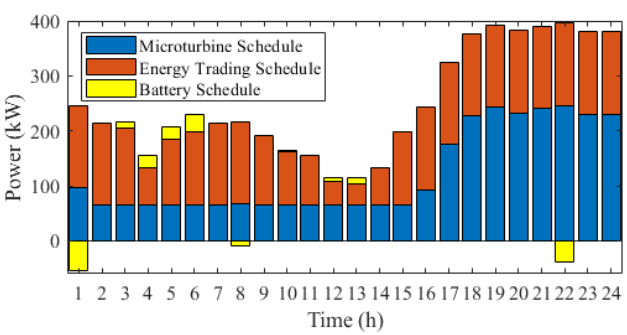

Fig. 4. Scheduling of smart microgrid energy resources in the first case

Similarly, Fig. 6 shows the scheduling results in the second case. Since flexibility is a priority in this case, as can be seen in the figure, fast-ramp resources (batteries) have many time intervals of energy production. Therefore, the flexibility of the network is increased and a greater share of the load profile is supplied. This result can also be seen in Fig. 5. It can be seen that during these hours the value of ENS has decreased which indicates more demand coverage.

Assigning priorities to each of the objective functions in the flexibility-based optimization problem has different effects from economic, social, environmental and technical points of view. In this paper, the economic aspect considers the cost of operation. The social aspect is defined in the form of the cost of ENS. Likewise, the environmental and the technical aspects are modeled in the form of the emission cost of the MT and the upstream network, and battery aging, respectively. Table 3 presents the comparison of two cases from economic, social, and environmental aspects as well as grid flexibility index.

It is clear that in the second case, by assigning the higher priority to flexibility and increasing the presence of fast-ramp resources, as well as increasing the purchase of energy from the upstream network, the cost of operation increases drastically. Furthermore, due to the increase in the production of resources and the purchase of energy, the cost of emission increases compared to case 1. This increase is 27.9% for operating cost and 8.5% for emission cost. In this case, due to the improvement of flexibility, load supply has been better and the total cost of unsupplied energy has decreased by 20.8%, which demonstrates a rise in social welfare.

It should be noted that providing flexibility using the battery increases its aging. Bearing in mind that the degradation of the battery health in a 24-hour period is very small, these changes are shown in Fig. 7 for both cases in a one-year period considering how the battery had to perform in the 24-hour operation time interval. As shown in the figure, by prioritizing the flexibility index and consequently charging and discharging the battery in more cycles, the aging rate of the battery increases.

IV. Discussion and Analysis

The findings of this study reveal a significant trade-off between flexibility and economic efficiency in microgrids. The increased reliance on batteries and micro turbine production to enhance flexibility results in higher operating costs, with a notable 27.9% increase in overall expenses. This economic impact underscores the need for careful consideration of cost management strategies when implementing flexibility measures.

From a technical perspective, the provision of flexibility accelerates battery aging, leading to a reduction in their state of health by more than 20% over a year. This technical challenge highlights the importance of developing advanced battery management systems and exploring alternative energy storage solutions to ensure long-term sustainability.

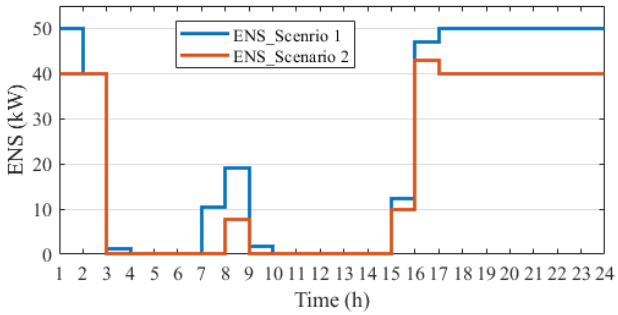

Fig. 5. Values of ENS in the two cases

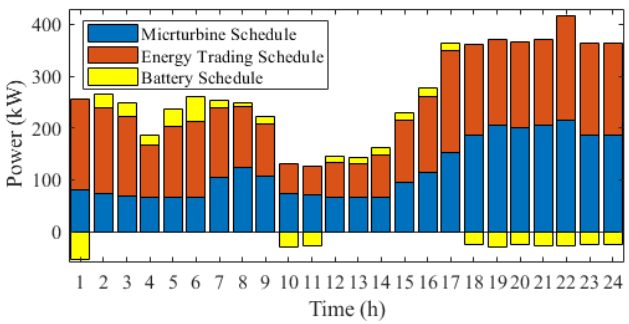

Fig. 6. Scheduling of the smart microgrid energy resources in the second case

TABLE 3 COMPARISON IN TERMS OF ECONOMIC, SOCIAL, AND ENVIRONMENTAL ASPECTS AS WELL AS NETWORK FLEXIBILITY INDEX.

Priority cases	*Operation Cost*	*Emission Cost*	*Total ENS Cost*	*Flexibility Index*
Case 1	32964.64	4601.52	1163.45	0.637
Case 2	42170.05	4990.22	921.68	0.78

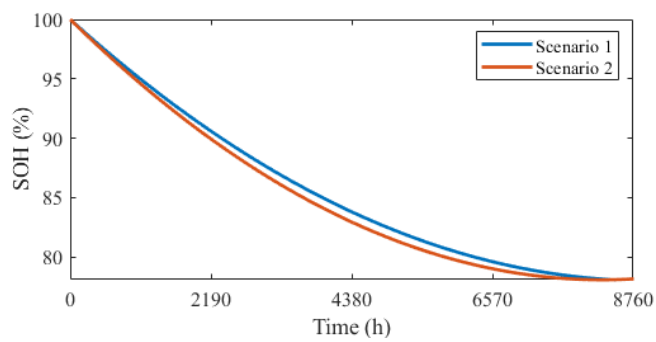

Fig. 7. Battery degradation in both cases in one-year period.

Socially, the proposed approach enhances microgrid reliability by minimizing the cost of energy not supplied, resulting in a 20.8% improvement in social welfare. This improvement in reliability is crucial for maintaining the quality of life and economic stability in communities reliant on microgrids.

However, the environmental impact of increased flexibility cannot be overlooked. The reliance on micro turbine

generation and higher-emission energy sources leads to an 8.5 % rise in pollution costs. This environmental cost necessitates the exploration of cleaner energy alternatives and the implementation of stringent emission control measures. cleaner energy alternatives and the implementation of stringent emission control measures.

V. Conclusions

In this study, the effects of implementing approaches based on flexibility in smart microgrids, considering the economic, technical, social and environmental consequences have been investigated. For this purpose, the lexicographic method was used to solve the optimization problem with the aim of optimizing operations by minimizing costs and at the same time maximizing flexibility. In this research, the battery is considered as the main source of flexibility. The simulation performed compares microgrid resource planning as well as operation cost, emission cost, unsupplied energy cost, microgrid flexibility index and in addition compares the impact of flexibility provision on battery aging in two cases. Considered cases are proposed by setting priorities for cost and flexibility in the lexicographic method. The results show that prioritizing cost flexibility from an economic point of view, increasing reliance on batteries and MT production to improve flexibility leads to a 27.9% increase in operating costs. From a social perspective, the proposed approach increases microgrid reliability by providing a 20.8% reduction in the cost of unsupplied energy. From a technical perspective, the results show that increasing the use of batteries accelerates their aging. On the other hand, it was observed that with a 14.3 % increase in flexibility, the emission cost also increased by 8.5%.

REFERENCES

[1] G. G. Kim et al., "Prediction Model for PV Performance With Correlation Analysis of Environmental Variables," in IEEE Journal of Photovoltaics, vol. 9, no. 3, pp. 832-841, May 2019, doi: 10.1109/JPHOTOV.2019.2898521.

[2] S. B. Q. Naqvi and B. Singh, "An Improved Power Quality PV-Battery System Coupled to Weak Grid with Feed-in Tariff Flexibility and PV Intermittency Flattening," 2020 IEEE 5th International Conference on Computing Communication and Automation (ICCCA), Greater Noida, India, 2020, pp. 583-588, doi: 10.1109/ICCCA49541.2020.9250834.

[3] D. Liu, X. Kong, D. Kong, S. Quan, C. YONG and D. Dong, "Bi-level optimized operation strategy for interconnected microgrids," 2019 22nd International Conference on Electrical Machines and Systems (ICEMS), Harbin, China, 2019, pp. 1-6, doi: 10.1109/ICEMS.2019.8921519.

[4] T. Xing, Q. Caijuan, Z. Liang, G. Pengjiang, G. Jianfeng and J. Panlong, "A comprehensive flexibility optimization strategy on power system with high-percentage renewable energy," 2017 2nd International Conference on Power and Renewable Energy (ICPRE), Chengdu, China, 2017, pp. 553-558, doi: 10.1109/ICPRE.2017.8390596.

[5] T. T. Pedersen, M. Victoria, M. G. Rasmussen and G. B. Andresen, "Exploring flexibility of near-optimal solutions to highly renewable energy systems," 2021 IEEE 48th Photovoltaic Specialists Conference (PVSC), Fort Lauderdale, FL, USA, 2021, pp. 0387-0391, doi: 10.1109/PVSC43889.2021.9518745.

[6] S. Paesschesoone, N. Kayedpour, C. Manna and G. Crevecoeur, "Improving Energy Flexibility in Photovoltaic-Battery Systems through Switching Reinforcement Learning Control," 2024 IEEE Conference on Technologies for Sustainability (SusTech), Portland, OR, USA, 2024, pp. 57-62, doi: 10.1109/SusTech60925.2024.10553555.

[7] M. MansourLakouraj, M. J. Sanjari, M. S. Javadi, M. Shahabi and J. P. S. Catalão, "Exploitation of Microgrid Flexibility in Distribution System Hosting Prosumers," in IEEE Transactions on Industry Applications, vol. 57, no. 4, pp. 4222-4231, July-Aug. 2021, doi: 10.1109/TIA.2021.3073882.

[8] S Poorvaezi Roukerd, A Abdollahi and M Rashidinejad, "Probabilistic-possibilistic flexibility-based unit commitment with uncertain negawatt demand response resources considering Z-number method", International Journal of Electrical Power & Energy Systems,Volume 113, 2019, Pages 71-89, ISSN 0142-0615.

[9] M. Yu, J. Jiang, X. Ye, X. Zhang, C. Lee and S. H. Hong, "Demand Response Flexibility Potential Trading in Smart Grids: A Multileader Multifollower Stackelberg Game Approach," in IEEE Transactions on Systems, Man, and Cybernetics: Systems, vol. 53, no. 5, pp. 2664-2675, May 2023, doi: 10.1109/TSMC.2022.3218039.

[10] S. Luo, J. Zhou, N. Feng, Y. Su, D. Yang and B. Wang, "Power System Flexibility Assessment Method for Matching Supply and Demand with Flexibility," 2023 8th International Conference on Power and Renewable Energy (ICPRE), Shanghai, China, 2023, pp. 107-112, doi: 10.1109/ICPRE59655.2023.10353889.

[11] H. Berahmandpour, S. M. Kouhsari and H. Rastegar, "A New Flexibility Index in Real Time Operation Incorporating Wind Farms," 2019 27th Iranian Conference on Electrical Engineering (ICEE), Yazd, Iran, 2019, pp. 549-553, doi: 10.1109/IranianCEE.2019.8786492.

[12] X. Tang, Y. Hu and Z. Chen, "Multi-objective optimal configuration model of energy storage system considering flexibility and economy in distribution network," 2020 International Conference on Smart Grids and Energy Systems (SGES), Perth, Australia, 2020, pp. 374-378, doi: 10.1109/SGES51519.2020.00072.

[13] A. Wang, J. Liu, and W. Wang, “Flexibility-based

improved model of multi-energy hubs using linear weighted sum algorithm," J. Renew. Sustain. Energy, vol. 10, no. 1, p. 15901, Jan. 2018, doi: 10.1063/1.5005571.

[14] S. Ramírez-López, G. Gutiérrez-Alcaraz, M. Gough, M. S. Javadi, G. J. Osório and J. P. S. Catalão, "Bi-Level Approach for Flexibility Provision by Prosumers in Distribution Networks," in IEEE Transactions on Industry Applications, vol. 60, no. 2, pp. 2491-2500, March-April 2024, doi: 10.1109/TIA.2023.3330683.

[15] C. Fournely, M. Pečjak and T. Medved, "New method for evaluating the value of flexibility and new services for DSOs on the LV network," 2022 18th International Conference on the European Energy Market (EEM), Ljubljana, Slovenia, 2022, pp. 1-5, doi: 10.1109/EEM54602.2022.9921072.

[16] Y. Peng, Q. Zhou, X. Qin, B. Ding and Y. Zhang, "Power System Flexibility Indicators Considering Reliability in Electric Power System with High-Penetration New Energy," 2022 5th International Conference on Power and Energy Applications (ICPEA), Guangzhou, China, 2022, pp. 469-474, doi: 10.1109/ICPEA56363.2022.10052215.

[17] K. Oikonomou, M. Parvania and R. Khatami, "Deliverable Energy Flexibility Scheduling for Active Distribution Networks," in IEEE Transactions on Smart Grid, vol. 11, no. 1, pp. 655-664, Jan. 2020, doi: 10.1109/TSG.2019.2927604.

[18] B. Mohammadi-ivatloo and F. Jabari, Operation, Planning, and Analysis of Energy Storage Systems in Smart Energy Hubs. 2018. doi: 10.1007/978-3-319-75097-2.

[19] C. Guenther, B. Schott, W. Hennings, P. Waldowski, and M. A. Danzer, "Model-based investigation of electric vehicle battery aging by means of vehicle-to-grid scenario simulations," J. Power Sources, vol. 239, pp. 604–610, 2013, doi: https://doi.org/10.1016/j.jpowsour.2013.02.041.

[20] L. Lam and P. Bauer, "Practical Capacity Fading Model for Li-Ion Battery Cells in Electric Vehicles," IEEE Trans. Power Electron., vol. 28, no. 12, pp. 5910–5918, doi: 579 10.1109/TPEL.2012.2235083.

[21] L. Vankudoth, A. Q. H. Badar, R. Kumar Chauhan and M. Hossain, "Economic Analysis of Energy Scheduling and Trading in Multiple-Microgrids Environment," 2021 XVIII International Scientific Technical Conference Alternating Current Electric Drives (ACED), Ekaterinburg, Russia, 2021, pp. 1-6, doi: 10.1109/ACED50605.2021.9462285.

[22] Ma, T., Wu, J., & Hao, L. (2017). Energy flow modeling and optimal operation analysis of the micro energy grid based on energy hub. Energy conversion and management, 133, 292-306.

[23] A. Sangwongwanich, Y. Yang and F. Blaabjerg, "High-Performance Constant Power Generation in Grid-Connected PV Systems," in IEEE Transactions on Power Electronics, vol. 31, no. 3, pp. 1822-1825, March 2016, doi: 10.1109/TPEL.2015.2465151.

[24] L. Lai, L. Fiaschi, M. Cococcioni and K. Deb, "Solving Mixed Pareto-Lexicographic Multiobjective Optimization Problems: The Case of Priority Levels," in IEEE Transactions on Evolutionary Computation, vol. 25, no. 5, pp. 971-985, Oct. 2021, doi: 10.1109/TEVC.2021.3068816.

[25] P. Aaslid, "Rye microgrid load and generation data, and meteorological forecasts.," Zenodo (CERN European Organization for Nuclear Research). Jun. 21, 2021. doi: 10.5281/zenodo.4448894.

[26] A. Yazhari Kermani, A. Abdollahi, and M. Rashidinejad, "Cyber-secure energy and flexibility scheduling of interconnected local energy networks with introducing an XGBoost-assisted false data detection and correction method," International Journal of Electrical Power & Energy Systems, vol. 155, p. 109683, Jan. 2024, doi: 10.1016/j.ijepes.2023.109683.

Faezeh Gholipour Zarandi received her B.Sc. degree in electrical engineering from Sirjan University of Technology, Sirjan, Iran in 2017 and her M.Sc. degree in electrical engineering from Shahid Bahonar University, Kerman, Iran in 2022. Currently, she is working towards her Ph.D. degree in electrical engineering at Shahid Bahonar University, Kerman, Iran. Her research interests are energy systems' flexibility, energy management, data de-aggregation and microgrid scheduling.

Masoud Rashidinejad received his B.Sc. degree in electrical engineering and M.Sc. degree in systems engineering from the Isfahan University of Technology, Khomeyni Shahr, Iran, and his Ph.D. degree in electrical engineering from Brunel University, London, the UK in 2000. Prof. Rashidinejad is a professor with the department of electrical engineering, Shahid Bahonar University, Kerman, Iran. His research interests include power system optimization, power system planning, electricity restructuring, energy efficiency, and energy management in smart electricity grids.

Amir Abdollahi received his B.Sc. degree in electrical engineering from Shahid Bahonar University, Kerman, Iran in 2007, his M.Sc. degree in electrical engineering from the Sharif University of Technology, Tehran, Iran in 2009, and his Ph.D. degree in electrical engineering from Tarbiat Modares University, Tehran, in 2012. Dr. Abdollahi is currently an Associate Professor with the Department of Electrical Engineering, Shahid Bahonar University. His current research interests include demand side management, planning, reliability, and economics in smart electricity grids.

Ali Yazhari Kermani was born in Kerman, Iran, in 1994. He received his B.S. degree in Electrical Power Systems Engineering from the Department of Electrical Engineering, Shahid Bahonar University of Kerman, Kerman, Iran, in 2017 and his M.S. degree from Kerman University of Advanced Technology (KGUT), Kerman, Iran, in 2019. He is currently working towards his Ph.D. in the Department of Electrical Engineering and is working with the Reliability and Monitoring of Uncertain Power Systems laboratory in Shahid Bahonar University of Kerman, Kerman, Iran. His current research interests include multi-microgrid systems, data-driven energy and flexibility scheduling, power systems' cyber security and data mining.

International Journal Of
Industrial Electronics Control and Optimization
Print ISSN: 3517-2645
Online ISSN: 3568-2645
Homepage: https://ieco.usb.ac.ir/

Flexibility-Constrained Energy Management of Smart Energy Hubs Considering Peer to Peer Transactive Energy and Demand Response program

Ali Riki | Mahmoud Oukati Sadegh | Omid Narouei

Faculty of Engineering, University of Sistan and Baluchestan, Zahedan, Iran.[1,2,3]
Corresponding author's email: oukati@ece.usb.ac.ir

Article Info

Article type:
Research Article

Article history:
Received: 02-July-2024
Received in revised form: 04-September-2024
Accepted: 19-September-2024
Published online: 21-March-2025

Keywords:
Demand Response,
Energy Management,
Flexibility,
Smart Energy Hubs.

ABSTRACT

The concept of an energy hub (EH) has been utilized to address the issue of performing concurrent operations of various energy generation and transmission infrastructures. This subject is exceedingly respected within the field of microgrids (MG). One of the primary concerns for investors is the efficient utilization of EH to effectively manage energy carriers, particularly in transactions with the upstream grid. In this paper the proposed smart energy hubs (SEH) manage dispatchable generation, i.e. Combined Cooling, Heat, and power (CCHP), and non-dispatchable generation, i.e. Photovoltaic (PV). SEHs consider Ice Storage Conditioner (ISC) as well as Thermal Energy Storage System (TESS) as the Energy Storage System (ESS). To mitigate dependence on gas and electricity utility companies, a peer-to-peer (P2P) energy sharing strategy has been executed. The implementation of demand response (DR) is directed toward shiftable electrical loads. The thermodynamic model of heating and cooling loads is developed with flexibility as integrated demand response (IDR) based on the desired temperature. The objective of optimization is to minimize operation and environmental costs subjected to numerous technical constraints. The flexibility constraint serves in particular to enhance the flexibility of the interrelationships between MG and the upstream network. The suggested model incorporates the probabilistic nature of PV generation as well as the electrical, thermal, and cooling demands in various scenarios. The proposed model is a Mix Integer Non-Linear Problem (MINLP), which was solved using SCIP solver in GAMS software. Implementation of the proposed framework on the typical EHs shows the impact of P2P transactive energy and flexibility constraint performance on elements such as operation costs, emissions and flexibility of the system.

Sets		$P_{EES}^{ch}(h,t,s)$	Real power charged by EES (kW).
H	Set of hubs.	$P^{EC}(h,t,s)$	Electrical power consumed by EC unit (kW).
T	Set of hours in the operation period.	$H^{HRU}(h,t,s)$	Thermal power generated by HRU (kW).
S	Set of scenarios.	$P_{TESS}^{dis}(h,t,s)$	Thermal power discharged by TESS (kW).
$j \in H$	Subset of hubs.	$H^{AC}(h,t,s)$	heating power consumed by AC unit (kW).
Variables		$P_{TESS}^{ch}(h,t,s)$	Thermal power charged by TESS (kW).
$P_{gas}^{PGU}(h,t,s)$	Gas purchased from gas grid fired by PGU (kW).	$P^{L}(h,t,s)$	Electric loads before DR (kW).
$P_{gas}^{AB}(h,t,s)$	Gas purchased from gas grid fired by AB (kW).	$\overline{H}^{air}$,$\underline{H}^{air}$	upper/lower bound of indoor heat (kW).
$P_{e}^{PGU}(h,t,s)$	Real power generated by PGU (kW).	$\overline{H}^{ws}$,$\underline{H}^{ws}$	upper/lower bound of hot water (kW).
$H^{AB}(h,t,s)$	Thermal power generated by AB	$\overline{C}^{air}$,$\underline{C}^{air}$	upper/lower bound of injected cooling power

	(kW).		(kW).
Parameters		α_s	Parameter of the Beta PDF.
$\rho(s)$	Probability of occurrence of the scenario s.	μ_s	Mean of forecasted solar irradiance (kW/m2).
$\rho_e(h,t)$	Electricity price "sell and purchase" ($/kWh).	σ_s	Standard deviation of forecasted solar irradiance (kW/m2).
$\rho_g(h,t)$	Gas price ($/kWh).	η^{pv}	Efficiency of PV module.
$\eta_e^{PGU}(h)$	Efficiency for electricity generation for co-product heat of PGU.	S^{pv}	Area of PV module (m2).
$\eta_h^{AB}(h)$	Efficiency for heat generation of AB.	η^{sol}	Efficiency of PV module.
$\varphi_{in}(h)$	Equivalent emission coefficients for electricity (kg/kWh).	μ_d	Standard deviation of forecasted demands (kW).
$\varphi_g(h)$	Equivalent emission coefficients for natural gas (kg/kWh).	$\eta^{TRA}(h)$	Efficiency of transformer.
ρ^{EDR}	compensation price of Electrical DR.	$K^{ISC}(h)$	Performance coefficient of ISC.
ρ^{HairDR}	compensation price of indoor heating DR.	$K^{AC}(h)$	Performance coefficient of AC.
ρ^{CDR}	compensation price of cooling DR.	**Abbreviations**	
$\overline{P}_{ESS}^{ch}$,$\overline{P}_{ESS}^{dis}$	Maximum real power charged /discharged by ESS (kW).	DR	Demand response
$\eta_{ESS}^{ch}(h)$	Charging efficiency of ESS.	SEH	Smart energy hub
$\eta_{ESS}^{dis}(h)$	Discharging efficiency of ESS.	CCHP	Combined Cooling, Heat, and power
$\overline{E}^{EES}(h)$	Maximum energy in ESS (kWh).	ISC	Ice Storage Conditioner
$\underline{P}_{PGU}$,$\overline{P}_{PGU}$	Minimum/Maximum allowable real power generated by PGU unit (kW).	TESS	Thermal energy storage system
$\underline{H}_{HRU}$,$\overline{H}_{HRU}$	Minimum/Maximum allowable thermal power generated by HRU unit (kW).	ESS	Energy Storage System
$\overline{H}_{AB}(h)$	Maximum allowable thermal power generated by AB (kW).	IDR	Integrated Demand Response
$\overline{H}_{AC}(h)$	Maximum allowable cooling power generated by AC (kW).	MINLP	Mixed Integer Non-linear Program
$\overline{P}^{ELE}(h)$	Maximum real power imported from the upstream grid after transformer (kW).	P2P	Peer-To-Peer
$f_b(si)$	Beta PDF of si.	MES	Multi-energy systems
si	Solar irradiance (kW/m2).	DG	Dispatchable generation
MGO	Micro grid operator	EV	Electrical Vehicle
RES	Renewable energy sources	QPSO	Quantum Particle Swarm Optimization
MCE	Multi-carrier energy	SPCAES	Solar-Powered Compressed Air Energy Storage
HSS	Hydrogen storage system	DRC	downside risk constraint
RO	Robust optimization	P2G	power-to-gas
TDR	Thermal demand response	ADMM	Alternating Direction Method of Multipliers
EDR	Electrical demand response	AB	Auxiliary Boiler
EMS	energy management system	PGU	Power Generation Unit
IGDT	information gap decision theory	AC	Absorption chiller
CHP	combined heat and power	EC	Electrical Chiller
WT	wind turbine	HRU	Heat Recovery Unit
PDF	Probability Density Function		

I. Introduction

A. Motivation and incitement

Traditional energy systems such as power, natural gas, heat and cooling systems are mostly planned and operated separately. Lack of coordination among traditional energy systems hinders the economical and efficient operation of the entire system. by development of the energy Internet [1], the coupling of various energy sources (electricity, gas, heat and cooling) has become much tighter, and the interaction between energy sources, power grid, and consumers is constantly intensified. This makes the coordinated operation of multiple energy sources an increasingly urgent task. For MESs, supplying and converting different energy sources can improve the flexibility and stability of the overall system. In

addition, MESs can increase the efficiency of energy consumption by coupling multiple energy sources [2]. For the supply, conversion and storage of different types of energy and load demand and their relationship in a MES, a system called EH is used and applied to all carriers [3]. Considering the use of different technologies, DGs and ESSs in MG Based on EH, energy management may create many challenges for MGO in the future.

On the other hands Finding improved ways to use environmentally friendly RES is of great interest, especially in developed countries. Because these solutions can curb the harmful effects of CO_2 emissions, which pose a challenge to an environment that is already experiencing alarming scales of global warming. Photovoltaics accounted for 48% of the total new power capacity added in 2019, as the share of RESs to meet power demand increases [4]. Although their presence provides some benefits to the power system, variable power generation in PV systems increases the net load ramp rate of the power system. For example, on July 16, 2020, in California, increased demand combined with a drop in PV production toward evening led to an 11 MW increase in ramp rate over three hours [5]. In such systems, the MGO must make new decisions to reduce the ramp rate of the system. Due to the increasing installation of PV systems, one of the main solutions to reduce system ramp rates is collaboration between MGO and individual customers. To this end, MGO may limit the ramp rate of power exchanged by EH with the upstream grid by setting flexibility constraints [6]. The flexibility constraint is the absolute value of the ramp rate for power purchased from the grid minus the ramp rate for power sold to the grid as less than or equal to the maximum ramp rate limit. With this constraint, the ramp rate is defined as the capacity to buy/sell from/to the grid at time step t minus these values at time step t-1. Therefore, this paper aims to model the flexibility-constrained energy management problem of SEHs equipped with RESs, considering DR and P2P energy to reduce emission costs and increase system flexibility.

B. Literature review

The mounting prevalence of distributed generation and the emergence of MCE systems have engendered an augmented demand for EH systems within the power grid. An EH is a new idea implemented in a MCE system to transmit, receive and store different types of energy. In addition, load distribution is a pivotal optimization issue in the energy systems, whereby it plays a significant role in mitigating the consumption of non-renewable energy sources, environmental pollution, and system operating costs. Numerous investigations have been undertaken in the realm of EH management with relation to this matter. At first, the issue of energy management was explored in the absence of any contemplation environmental pollution. The article by [7] centers on examining the notion of a hydrogen-based smart micro EH while taking into account the inclusion of IDR and a fuel cell-based HSS. The purpose of the model being proposed is to achieve the minimization of the overall EH cost through the implementation of a RO strategy, taking into account the uncertainty of electricity prices.in another development, a hybrid interval-stochastic framework was proposed by [8] to create robust programming of EH which thermal energy market, TDR program and EDR program are considered to manage flexible energy management in order to reduce operation cost. Authors proposed a cooperative framework in which a network of EHs collaborate together and share their resources in order to reduce their costs. In contrast to techniques predicated upon Nash-equilibrium points, which merely identify equilibrium points without ensuring the optimality of the solution, the cooperative strategy employed in [9] herein provides a means of obtaining the optimal solution for the given problem. The study documented in reference [10], was examined the efficacy of ice storage as a nascent and evolving mechanism for energy storage with the aim of enhancing performance and diminishing the operation cost of EHs. Moreover, the stochastic behavior of ice storage was compared with deterministic conditions. A rule-based EMS based on the modifications of the traditional load following and circuit charging was developed in [11] to effectively coordinate the operation of an integrated multi-carrier hybrid energy system. A novel optimization framework based on a hybrid IGDT and RO was developed in [12] to handle the optimal self-scheduling of the EH within a medium-term horizon for large consumers. The purpose of this framework was to efficiently address the intricate binary variables and cope with the worst-case scenarios associated with the generation of wind turbines and the uncertainties in the day-ahead electricity market. Furthermore, authors in [13] were offered a linear max–min–max robust optimization-based decision-making tool that incorporates both uncertainties of the electricity market price and the wind generation. As indicated in the present discourse, the optimal load distribution in energy systems not only engenders a reduction in operational costs, but also facilitates a diminution in the consumption of non-renewable energy sources, thereby mitigating the production of deleterious substances in the environment. In this regard, the article [14] has proposed an optimal load distribution model for the EH, which aims to reduce the total cost of the EH, including operating costs and CO_2 emission costs of the system. The investigated energy hub includes the unit of CHP, gas boiler, PV systems and WT, and EV and the issue of uncertainty related to EVs was dealt with through the application of RO from a methodological viewpoint. authors in [15] were examined the design and performance of an EH to meet the heating, cooling, electricity, and freshwater demands of a coastal city. A thorough thermodynamic examination of the EH was being undertaken to consider the economic and emissions perspective in conjunction with the availability of RESs. In a recent study, a robust approach based on QPSO was

employed to minimize the total cost of the EH system [16]. The investigation focused on evaluating the reduction of fuel consumption and pollutant emissions through the implementation of a TESS within the residential EH. In another development, a model for EH was considered for the purpose of the optimal operation of the MG with multiple energy carrier infrastructures for day-ahead [17]. The objective of optimization was to reduce operation and environmental expenses while taking into account various technical constraints. More specifically, the influence of SPCAES as a new ESS on the effectiveness and productivity of the EH, as well as on environmental expenses, was examined. Article [18] demonstrated the implementation of an emission cost model, which incorporates penalty factors, in regulating the usage of RESs by residential EH towards mitigating pollution emissions. As a measure to mitigate the risks arising from potential uncertainties faced by the decision-maker, a risk-aversion strategy, specifically the DRC, was adopted. Furthermore, the researchers of [19] posited an energy hub equipped with P2G technology, wherein patrons partake in an IDR program. The findings demonstrated that the P2G technology effectively mitigates CO_2 emissions via the consumption of CO_2 emanating from the CHP system and boiler. It appears that the interchanging of energy between EHs will augment the flexibility of the system while concurrently mitigating its operational costs. On the other hand, P2P energy transaction, allowing EHs to trade energy with each other in a direct manner, plays a pivotal role in mitigating the utilization of non-renewable energy sources and, consequently, in reducing carbon emissions. Despite the fact that the involvement of numerous EHs enhances flexibility and mitigates system costs, the equitable and compelling allocation of benefits remains a considerable challenge. Hereupon, the article [20] presents a market mechanism designed for the operation of multiple EHs, which relies on a P2P transaction system. The application of cooperative game theory led to the development of a just and persuasive method of distributing payoffs. The problem concerning the allocation of payoffs was structured as a two-stage problem. In the first stage, the allocation of payoffs was ascertained with the objective of minimizing the worst-case excess. Subsequently, the coalition with the highest excess was found and reintroduced into the first-phase problem. Moreover, a potential solution was presented in [21] for energy transaction through a P2P model among interconnected SEHs. EHs had the capacity to exchange both electrical and thermal energy with one another, thereby resulting in a reduction in expenditure and a decrease in reliance on gas and electricity service providers. The research conducted by Article [22] sought to investigate a completely decentralized approach to electricity trading in the framework of transactive energy markets. The proposed model presents a theoretical framework for P2P trading, which facilitates services among clients in a decentralized manner. the decentralized power flow issue was approached through the utilization of the ADMM. in article [23] the authors were focused to evaluate the significance of P2P energy transactions in conjunction with on-site flexibility resources for industrial sites. This study seeks to examine the potential impact of P2P energy transactions on uncertain parameters in light of the substantial peak power charges associated with grid power usage. Studies conducted to energy management of the EH can be categorized through multifaceted approaches. TABLE 1 presents a compilation of recent scholarly investigations pertaining to the perspectives outlined above. The presented table also outlines the unique aspects of the current work in relation to prior research.

TABLE 1 COMPREHENSIVE COMPARISON OF THIS PAPER TO LITERATURE REVIEW.

Reference	Flexibility-constrained	P2P transaction	Emission costs	Multi-carrier energy	Demand response	Uncertainty
[7]	×	×	×	✓	✓	✓
[8]	×	×	×	×	✓	✓
[9]	×	×	×	✓	✓	×
[10]	×	×	×	✓	✓	×
[11]	×	×	✓	✓	×	×
[12]	×	×	×	×	✓	✓
[13]	×	×	×	✓	×	✓
[14]	×	×	✓	×	✓	✓
[15]	×	×	✓	✓	×	×
[16]	×	×	✓	✓	×	✓
[17]	×	×	✓	✓	×	✓
[18]	×	×	×	✓	✓	✓
[19]	×	×	✓	×	✓	×
[20]	×	✓	×	✓	×	✓
[21]	×	✓	×	×	×	✓
[22]	×	✓	×	✓	×	✓
[23]	×	✓	✓	✓	✓	×
Current paper	✓	✓	✓	✓	✓	✓

C. Contributions and organization

The aforementioned research has demonstrated the impact of MCE systems on the flexibility and stability of the system. Additionally, it was determined that the implementation of P2P energy and DR concepts resulted in a decrease of both operational and environmental costs for the system. Nevertheless, the stochastic nature of PV systems, which contributes to the heightened ramp rate of the system's net load, implies a void in our current research. The current investigation endeavors to explore the utilization of flexibility-constrained concepts within SEHs, with a focus on P2P energy trading and DR. This is pursued with the ultimate objective of augmenting system flexibility and diminishing both environmental and operational costs. Particularly, the study aimed at the following objectives:

- Modeling 3 CCHP-based EHs optimal operation involving DR programs and P2P energy transaction,
- In order to enhance the overall flexibility of a system, the application of the flexibility-constrained concept is recommended and
- This approach involves taking into account the scenario-based performance of various elements, such as PV systems and loads.

The following organization is considered for the rest of the paper. In Section 2, the SEHs architecture is described and problem is formulated. The mathematical model and solution algorithm are presented in Section 3. Section 4 presents and discusses the simulation results and finally, Section 5 addresses the conclusion of the study.

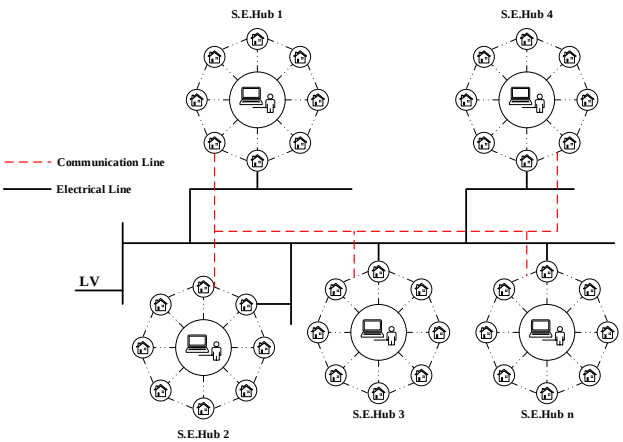

Fig. 1. Transactive framework for multiple SEHs

II. SEHs architecture and problem formulation

A. SEH architecture

An MCE framework for multiple SEHs is shown in Fig. 1. All SEHs are networked and can trade electrical energy with other hubs via the networked infrastructure. They also communicate with each other through a communication network to determine the optimal energy trading profile. Hubs are equipped with an EMS that facilitates the identification of the most effective strategy for scheduling their energy generation, consumption, and energy share. In general, Each SEH is composed of CCHP, PV, AB, ISC, ESSs and a multitude of loads pertaining to electrical, heating, and cooling functions. In an effort to enhance realism, the implementation of hubs exhibiting distinct components has been attempted. Thus, it can be posited that SEHs 1, 2, and 3 have drawn inspiration from [17], [24], and [25], correspondingly. The general schema of the proposed SEHs is depicted in Fig. 2 . The CCHP system is composed of various fundamental components, including but not limited to the PGU, HRU, and AC. The implementation of ISC has become commonplace in various cooling applications. This innovative technology has been found to be effective in reducing peak power supply tension during peak hours, as reported by previous studies [25]. In this study, the ISC consisted of a single-duty chiller (operable only in ice-making mode) and an ice storage tank that melted the stored ice only during peak hours. Additionally, the ISC could not operate in both ice-making and ice-melting modes simultaneously. Furthermore, it should be noted that the CCHP system was operated in a hybrid load mode [26]. The present inquiry pertains to a system encompassing three distinct categories of energy requisites, namely those associated with electricity, heat, and cooling. The present study posited that the MG operator possessed unfettered access to all pertinent data. according to Fig. 2, the primary portion of the natural gas streams into the PGU to generate electricity and heat. Subsequently, the second phase is initiated whereby AB triggers the generation of thermal energy. In fact, natural gas dispatch is expressed as:

$$P_{gas} = P_{gas}^{PGU} + P_{gas}^{AB} \quad (1)$$

Electricity P_e^{PGU} and heat H^{HRU} are generated through the firing of natural gas P_{gas}^{PGU} in the gas turbine as follows:

$$P_e^{PGU} = \eta_e^{PGU} \times P_{gas}^{PGU} \quad (2)$$

$$H^{HRU} = \eta_h^{PGU} \times P_{gas}^{PGU} \quad (3)$$

AB consumes natural gas for the purpose of heat generation in the subsequent manner:

$$H^{AB} = \eta_h^{AB} \times P_{gas}^{AB} \quad (4)$$

Electricity is transferred between the SEH and the upstream grid via the transformer. In the event of insufficient electricity, the SEH will procure electricity from the upstream electrical grid. Conversely, in instances of electricity surplus, the electrical hub vends the excess electricity to the upstream grid.

$$P^{ELE} = \eta^{TRA} \times P^{GRD} \quad (5)$$

The succeeding equation delineates the ice-making capacity of the chiller:

$$P_{ISC}^{dis} = K^{ISC} \times P^{ISC} \quad (6)$$

The process of injecting co-product heat H^{HRU} from PGU into the HRU results in the accumulation of heat at the heating hub. Specifically, the heating hub assembles the output heat of HRU, represented as $\eta^{HRU} \times H^{HRU}$, along with the heat emanating from AB. Subsequently, a fraction of the thermal energy, which is directed towards AC, is utilized to facilitate cooling:

$$C^{AC} = K^{AC} \times H^{AC} \quad (7)$$

Additionally, the electric chiller consumes electrical power to produce cooling energy and this process can be mathematically expressed as follows:

$$C^{EC} = K^{EC} \times P^{EC} \quad (8)$$

B. problem formulation

This subsection entails an elaboration of the problem

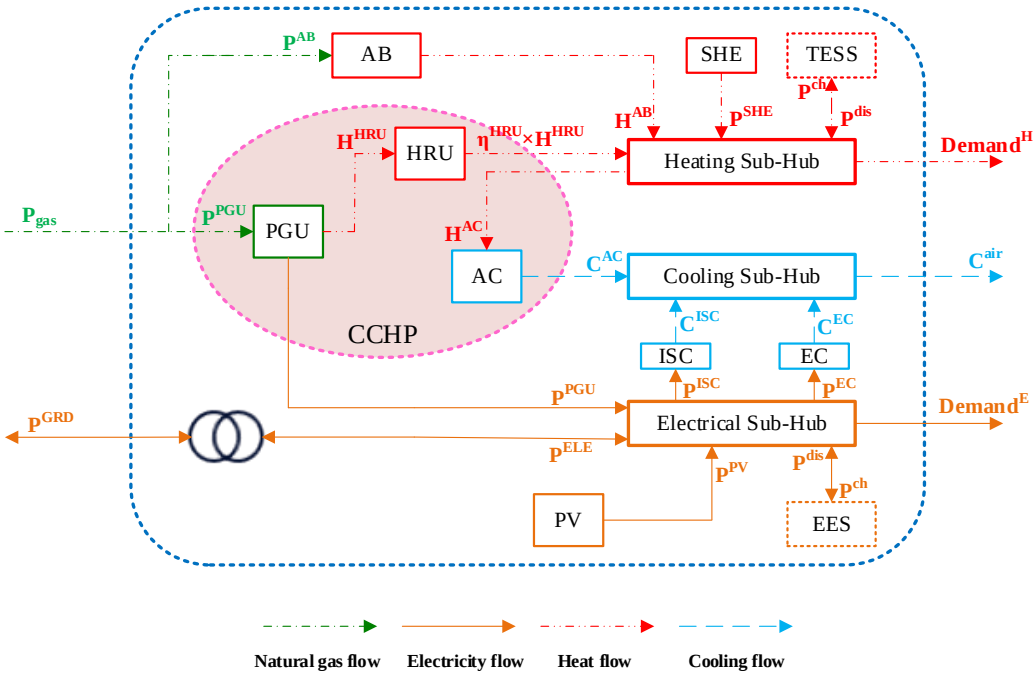

Fig. 2. General scheme of SEHs

formulation encompassing the objective function as well as the inherent constraints of the network and generation units.

2.2.1. objective functions

The following equations demonstrate the proposed objective function, which represents the operating costs of the MG (including all three SEHs) in the day-ahead market. It consists of six components: the net purchase cost of electricity and gas, the CO_2 emission cost and the compensation cost of shiftable electrical loads and flexible heating and cooling loads. This study considers operating cost minimization from the perspective of MGO seeking to economically and technically optimize the use of MG components. These components encompass CCHP, PV, TESS, ESS and ISC. In this analysis, the focus is strictly on operational costs, while disregarding investment costs associated with these MG components. The objective function can be presented in the following formulation:

$$f = \sum_{s} \rho(s) \times \sum_{h} \sum_{t} \begin{bmatrix} C_{pe}(h,t,s) + C_{pg}(h,t,s) + \\ C_{oe}(h,t,s) + C^{EDR}(h,t,s) + \\ C^{HDR}(h,t,s) + C^{CDR}(h,t,s) \end{bmatrix} \quad (9)$$

$$C_{pe}(h,t,s) = \rho_e(h,t) \times P^{GRD}(h,t,s) \quad (10)$$

$$C_{pg}(h,t,s) = \rho_g(h,t) \times \left[\frac{P_e^{PGU}(h,t,s)}{\eta_e^{PGU}(h)} + \frac{H^{AB}(h,t,s)}{\eta_h^{AB}(h)}\right] \quad (11)$$

$$C_{oe}(h,t,s) = \theta(h) \times \begin{bmatrix} \varphi_{in}(h) \times P^{GRD}(h,t,s) + \\ \varphi_g(h) \times \left(\frac{P_e^{PGU}(h,t,s)}{\eta_e^{PGU}(h)} + \frac{H^{AB}(h,t,s)}{\eta_h^{AB}(h)}\right) \end{bmatrix} \quad (12)$$

$$C^{EDR}(h,t,s) = \rho^{EDR} \times \Delta P^{sh,dn}(h,t,s) \quad (13)$$

$$\begin{aligned} &C^{HDR}(h,t,s) = C^{HairDR}(h,t,s) + \\ &C^{HwsDR}(h,t,s) = \rho^{HairDR} \times \\ &\left|H^{air}(h,t,s) - H^{air,forecast}(h,t,s)\right| \\ &+\rho^{HwsDR} \times \left|H^{ws}(h,t,s) - H^{ws,forecast}(h,t,s)\right| \end{aligned} \quad (14)$$

$$\begin{aligned} &C^{CDR}(h,t,s) = \rho^{CDR} \times \\ &\left|C^{air}(h,t,s) - C^{air,forecast}(h,t,s)\right| \end{aligned} \quad (15)$$

Constraints: The proposed optimization problem considers the following constraints:

Flexibility constraint: The SEH's flexibility constraint is modeled using Equation (16):

$$\left|\begin{matrix} P^{buy}(h,t,s) - P^{buy}(h,t-1,s) - \\ (P^{sell}(h,t,s) - P^{sell}(h,t-1,s)) \end{matrix}\right| \leq P^{Flexibility}(h,t) \quad (16)$$

whereby the power traded between the system and the upstream grid during time step t, in comparison with time step

t-1, is constrained to be less than or equal to the flexibility limitation.

P2P transaction constraint: The SEHs operate on a P2P basis, wherein participants are able to engage in transactions involving the purchase or sale of electrical energy based on their respective preferences. $e_h^{el} = \{e_{h,j,t}^{el},\ \forall h,j \in H,\ \forall t \in T\}$ indicates the electrical energy sharing of SEH h with j on timeslot t. If power is purchased from SEH j, $e^{el}(h,j,t)$ will be positive, and otherwise if SEH h sells to j and $e^{el}(h,j,t)$ is negative. An Energy Sharing Profile between S.E.s must satisfy the following constraints:

$$e^{el}(h,j,t,s) + e^{el}(j,h,t,s) = 0 \quad (17)$$

$\Pi_h = \{\pi_{h,j},\ \forall h,j \in H\}$ also specifies payments for energy trades between SEHs. The payment among SEH h with j, must be equal but with opposite signs, so the payment among SEHs must satisfy the bellow constraint:

$$\pi(h,j,s) + \pi(j,h,s) = 0 \quad (18)$$

The exclusion of the trading cost of energy between hubs from the optimization (1) is justified by its negligible impact on the overall social cost of the hubs. This factor solely involves the transfer of payments between the hubs and does not contribute to the calculation of the total social cost. For example, \$12 is a payment hub h makes to j, so hub j receives \$12 and h pay \$12. Therefore, it follows that the aggregate cost incurred in relation to energy sharing remains constant.

DR programs: The DR programs facilitate the energy supply by implementing measures to regulate energy consumption among end users via various strategies and initiatives. This article examines a price-based IDR system for shiftable electric loads, and two IDR programs for flexible thermal loads.

a) Shiftable electrical loads: There are two primary programs in which the customer may participate, namely incentive-based and price-based programs. This paper presents an examination of price-based DR, a technique employed by customers who adjust their energy consumption by transferring some of their loads to alternate periods, influenced by the pricing signal. It is noteworthy that the modeling methodology employed in this study presents an IDR mechanism, wherein it is possible to transfer shiftable loads from periods of peak demand to periods of reduced activity. The mathematical formulation of the load shifting approach is demonstrated in equations (19) -(23).

$$Demand^E(h,t,s) = P^L(h,t,s) + \Delta P^{sh,up}(h,t,s) - \Delta P^{sh,dn}(h,t,s) \quad (19)$$

$$\sum_{t=1}^{N} \Delta P^{sh,up}(h,t,s) - \sum_{t=1}^{N} \Delta P^{sh,dn}(h,t,s) = 0 \quad (20)$$

$$0 \le \Delta P^{sh,up}(h,t,s) \le \overline{\Delta P}^{sh,up}(h,t) \times \psi^{sh,up}(h,t,s) \quad (21)$$

$$0 \le \Delta P^{sh,dn}(h,t,s) \le \overline{\Delta P}^{sh,dn}(h,t) \times \psi^{sh,dn}(h,t,s) \quad (22)$$

$$\psi^{sh,up}(h,t,s) + \psi^{sh,dn}(h,t,s) \le 1 \quad (23)$$

The terms $\Delta P^{sh,up}(h,t,s)$ and $\Delta P^{sh,dn}(h,t,s)$ a are positive variables demonstrating increased and reduced loads, respectively.

b) Flexible heating loads: The present article explicates two distinct categories of heating loads, namely indoor heating loads and hot water loads.

$$Demand^H(h,t,s) = H^{air}(h,t,s) + H^{ws}(h,t,s) \quad (24)$$

The mathematical representation of heating loads relies on their thermodynamic model in a manner that temperature plays a fundamental part in determining the fulfillment of heating requirements [27]. The proposed methodology broadens the range of options available to SEHs for energy transactions in meeting their heating requirements. It is worth noting that the method in question entails a comprehensive analysis of all heating loads, while simultaneously operating under the assumption that the integration form of DR is utilized. the mathematical modeling of indoor heating DR is shown in equations (25) -(28).

$$\underline{H}^{air}(h,t,s) \le H^{air}(h,t,s) \le \overline{H}^{air}(h,t,s) \quad (25)$$

$$\underline{H}^{air}(h,t,s) = H^{air,forecast}(h,t,s) - \phi^H(h,t) \times H^{air,forecast}(h,t,s) \quad (26)$$

$$\overline{H}^{air}(h,t,s) = H^{air,forecast}(h,t,s) + \phi^H(h,t) \times H^{air,forecast}(h,t,s) \quad (27)$$

$$0 \le \phi^H(h,t) \le \overline{\phi}^H \quad (28)$$

The second type of heating load is the hot water, which is one of the necessary consumptions. The aforementioned analysis is also applicable to hot water modeling:

$$\underline{H}^{ws}(h,t,s) \le H^{ws}(h,t,s) \le \overline{H}^{ws}(h,t,s) \quad (29)$$

$$\underline{H}^{ws}(h,t,s) = H^{ws,forecast}(h,t,s) - \phi^{ws}(h,t) \times H^{ws,forecast}(h,t,s) \quad (30)$$

$$\overline{H}^{ws}(h,t,s) = H^{ws,forecast}(h,t,s) + \phi^{ws}(h,t) \times H^{ws,forecast}(h,t,s) \quad (31)$$

$$0 \le \phi^{ws}(h,t) \le \overline{\phi}^{ws} \quad (32)$$

c) Flexible cooling loads: The present study considers the cooling load as defined by the air conditioning system, which is dependent on the temperature of the enclosed space. The objective of this study is to decrease the ambient temperature within the given space through the introduction of cool air into the surrounding environment. The identical thermodynamic framework is utilized in the calculation of cooling loads, with one modification in the principal equation:

$$\underline{C}^{air}(h,t,s) \le C^{air}(h,t,s) \le \overline{C}^{air}(h,t,s) \quad (33)$$

$$\underline{C}^{air}(h,t,s) = C^{air,forecast}(h,t,s) - \phi^{C}(h,t) \times C^{air,forecast}(h,t,s) \quad (34)$$

$$\overline{C}^{air}(h,t,s) = C^{air,forecast}(h,t,s) + \phi^{C}(h,t) \times C^{air,forecast}(h,t,s) \quad (35)$$

$$0 \le \phi^{C}(h,t) \le \overline{\phi}^{C} \quad (36)$$

Energy balance at SEHs: The expression for the balance of electrical power at the electrical hub is presented as follows:

$$P^{ELE}(h,t,s) + P^{PV}(h,t,s) + P_e^{PGU}(h,t,s) + P_{EES}^{dis}(h,t,s) + \sum_j e^{el}(h,j,t,s) = Demand^{E}(h,t,s) + P^{ISC}(h,t,s) + P_{EES}^{ch}(h,t,s) + P^{EC}(h,t,s) \quad (37)$$

Furthermore, the heat balance is expressed in the subsequent manner:

$$\eta^{HRU}(h) \times H^{HRU}(h,t,s) + H^{AB}(h,t,s) + P_{TESS}^{dis}(h,t,s) = Demand^{H}(h,t,s) + H^{AC}(h,t,s) + P_{TESS}^{ch}(h,t,s) \quad (38)$$

Moreover, the expression of the cooling energy balance can be stated as:

$$C^{AC}(h,t,s) + C^{EC}(h,t,s) + C_{ISC}^{dis}(h,t,s) = C^{air}(h,t,s) \quad (39)$$

ESS operation constraints: In the context of the operation of ESSs in an SEH environment, emphasis has been placed on several limitations, which take the form of generic models, as documented in academic sources such as [26] and [28]. It should be highlighted that within the framework under consideration, ESS pertains to the composite entities of EES, TESS, and ISC.

$$0 \le P_{ESS}^{ch}(h,t,s) \le \overline{P}_{ESS}^{ch}(h) \times U_{ESS}^{ch}(h,t,s) \quad (40)$$

$$0 \le P_{ESS}^{dis}(h,t,s) \le \overline{P}_{ESS}^{dis}(h) \times U_{ESS}^{dis}(h,t,s) \quad (41)$$

$$U_{ESS}^{ch}(h,t,s) + U_{ESS}^{dis}(h,t,s) \le 1 \quad (42)$$

$$E_{ESS}(h,t,s) = E_{ESS}(h,t-1,s) - P_{ESS}^{dis}(h,t,s) \times \eta_{ESS}^{dis}(h) + \left(\frac{P_{ESS}^{ch}(h,t,s)}{\eta_{ESS}^{ch}(h)}\right) \quad (43)$$

$$0 \le E_{ESS}(h,t,s) \le \overline{E}^{EES}(h) \quad (44)$$

$$E_{ESS}(h,0,s) = E_{ESS}(h,24,s) \quad (45)$$

Generation limits for PGU and HRU: The electrical and heating power generated by CCHP in SEHs must adhere to a set of predetermined limits [26], [29]:

$$\underline{P}_{PGU}(h) \le P_e^{PGU}(h,t,s) \le \overline{P}_{PGU}(h) \quad (46)$$

$$\underline{H}_{HRU}(h) \le H^{HRU}(h,t,s) \le \overline{H}_{HRU}(h) \quad (47)$$

AB and AC operation limits: The heating and cooling power produced by AB and AC are required to fall within predetermined minimum and maximum thresholds, as shown below [26]:

$$0 \le H^{AB}(h,t,s) \le \overline{H}_{AB}(h) \quad (48)$$

$$0 \le H^{AC}(h,t,s) \le \overline{H}_{AC}(h) \quad (49)$$

Power limits for the transformer: The output real power of transformers should meet the following conditions:

$$0 \le P^{ELE}(h,t,s) \le \overline{P}^{ELE}(h) \quad (50)$$

Uncertainty modeling: This section expounds on the uncertainty models used for the output power of PVs, and electrical, heating, and cooling demands.

Solar irradiance modeling: A common approach in analyzing the distribution of solar irradiance at any given hour is to employ a bimodal distribution model, which is characterized by the linear combination of two unimodal distributions. The Beta PDF serves as a suitable choice for each of these unimodal distributions. The sources cited as [30] and [31], present the following information:

$$f_b(si) = \begin{cases} \frac{\Gamma(\alpha_s+\beta_s)}{\Gamma(\alpha_s)\Gamma(\beta_s)} \times si^{(\alpha_s-1)} \times (1-si)^{(\beta_s-1)} & 0 \le si \le 1,\ \alpha_s \ge 0,\ \beta_s \ge 0 \\ 0 & otherwise \end{cases} \quad (51)$$

$$\beta_s = (1-\mu_s) \times \left(\frac{\mu_s \times (1+\mu_s)}{\sigma_s^2} - 1\right) \quad (52)$$

$$\alpha_s = \frac{\mu_s \times \beta_s}{(1-\mu_s)} \quad (53)$$

In order to forecast the average and variance of solar irradiance at hourly intervals, researchers refer to historical data sourced from the neighboring meteorology station [31], [32]. The Beta PDF is defined as a range spanning from (51) to (53) for each hour, with respect to its respective mean and standard deviation. Various factors, namely solar irradiance, surface area, efficacy of PV modules, and solar collectors, are pivotal in determining the generated power of PV and solar collector units. The computation of the output power for both PV and solar collector units is carried out utilizing the Beta PDF across various conditions [30], [31], [33]:

$$P_{pv}(si) = \eta^{pv} \times S^{pv} \times si$$
$$P_{SHE}(si) = \eta^{sol} \times S^{sol} \times si \quad (54)$$

Modelling the electrical, heating, and cooling demands: The modelling of uncertainty in the forecast of electrical, heating, and cooling demands is carried out using a Normal PDF, as follows [31], [34]:

$$f_d(\ell) = \frac{1}{\sigma_d \times \sqrt{2\pi}} \times e^{\frac{-(\ell-\mu_d)^2}{2\sigma_d^2}} \qquad (55)$$
$$\ell = z \times \sigma_d + \mu_d$$

The PDF for the normal distribution of each hour is determined by utilizing the calculated mean and standard deviation derived from the forecasted electrical, heating, and cooling demands.

Techniques for scenario reduction: For a majority of practical issues, the optimization problem that encompasses all conceivable scenarios (known as the deterministic equivalent program) is excessively extensive. In order to address the challenges posed by computational complexity and temporal limitations, algorithms are employed to mitigate the scenarios. The present study employs the SENRED tool, comprising three distinct algorithms (The Fast-Backward method, a mix of Fast-Backward/Forward methods and a mix of Fast Backward/Backward methods), to address the research objective.

III. The mathematical model and solution algorithm

The mathematical model for optimal operation proposed in this study is formulated as a MINLP model. MINLP is a mathematical optimization which encompasses problems that entail both continuous and integer variables, but are nonlinear in nature. The present optimal operation mathematical model is characterized by a combination of binary and continuous variables. The introduction of binary variables serves to prevent the concurrent operation of charging and discharging processes in ESSs. The variables of interest in this study are continuous and include electrical power from CCHP, heating power from ABs, electrical power exchanged between the system and the upstream grid, electrical power exchanged with EES, heating power exchanged with TESS, and cooling power supplied by ISC and EC in each hour of operation. Non-linear terms with the problem include compensation costs resulting from DR programs. The application of the absolute value function results in non-linearity of said variables [35]. The utilization of the SCIP solver has been employed for the resolution of the optimal dispatch model, owing to its exceptional competence in addressing MINLP problems. The Solver is the SCIP (implemented as C callable library and provides C++ wrapper classes for user plugins) as a tool of the GAMS software. The computational procedure was conducted utilizing a PC featuring an Intel Core i7,3.9GHz CPU with 16 GB of RAM. Fig. 3 depicts the implementation flowchart of the proposed model.

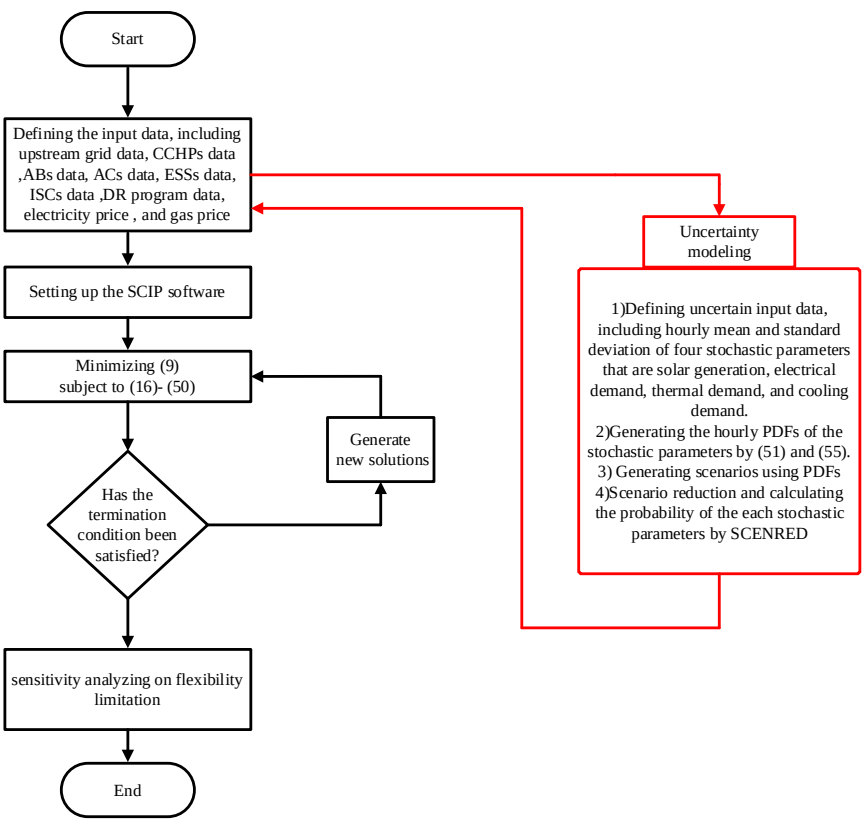

Fig. 3. Flowchart of the proposed model.

IV. Simulation result

The present study utilizes a smart grid system based on EH as a testbed to assess the effectiveness of the proposed mathematical model and it does not belong to any special geographical area. However, it is noteworthy that all three SEHs are frequently used by other researchers. The smart grid under consideration comprises three central hubs, with each hub featuring three sub-hubs, namely the electrical sub-hub, the heating sub-hub, and the cooling sub-hub. The electrical sub-hub imports electrical power from PGU and PV while it exports to ISC, EC, and electrical demand. Besides, it exchanges the electrical power with upstream grid and EES. The heating sub-hub imports heating power from AB, SHE, and HRU while it exports to AC and heating demand. Also, it exchanges the heating power with TESS.

.

TABLE 2 PARAMETERS OF THE SEHS.

	Value				Value				Value		
Parameter	SEH 1	SEH 2	SEH 3	Parameter	SEH 1	SEH 2	SEH 3	Parameter	SEH 1	SEH 2	SEH 3
η_e^{PGU}	0.42	0.4	0.3	$\underline{P}_{PGU}$	140	0	0	$\overline{H}_{AC}$	300	2000	1000
η_h^{AB}	0.88	0.88	0.9	$\overline{P}_{PGU}$	1050	1200	1000	$\overline{H}_{AB}$	2300	2640	800
η_h^{PGU}	0.48	0.5	0.4	$\underline{H}_{HRU}$	155	0	0	$\overline{H}_{HRU}$	1640	1500	1000
η^{HRU}	0.82	1	0.82	K^{EC}	0	0	4	η^{TRA}	0.99	0.95	0.98
K^{AC}	0.9	0.9	1.2	K^{ISC}	0.9	0.85	0.95	$\overline{E}^{EES}$	1000	4200	1800
$\overline{P}_{ESS}^{ch}$	470	450	500	$\overline{P}_{ESS}^{dis}$	180	450	700	η_{ESS}^{ch}	0.9	0.9	0.96
η_{ESS}^{dis}	0.95	0.9	0.96	$\overline{P}^{ELE}$	3500	2850	1470				
S^{pv}	1300	η^{sol}	66.6	S^{sol}	1300	η^{pv}	18.6	$\overline{\Delta P}^{sh,up}$	150	$\overline{\Delta P}^{sh,dn}$	250
θ	0.45	φ_{in}	0.972	φ_g	0.23	ρ^{EDR}	2	ρ^{HairDR}	2	ρ^{HwsDR}	2
ρ^{CDR}	2	$\overline{\phi}^{H}$	0.2	$\overline{\phi}^{ws}$	0.2	$\overline{\phi}^{C}$	0.2				

The cooling sub-hub imports cooling power from AC, EC, and ISC while it exports to cooling demand.

A. Basic data

As specified, the proposed model analyzes three type of loads Fig. 4 illustrates the electrical demand of SEHs collectively. The combined forecast for indoor heating and hot water consumption is illustrated in Fig. 5. 70% of the aforementioned quantity is designated for the purpose of heating water, whilst the remaining portion is allocated towards indoor heating needs. the forecast cooling demand is demonstrated in Fig. 6, Fig. 7 shows the day-ahead forecasted electricity price for the smart grid. Each SEH has a set price for natural gas, with SEH 1 being priced at 3.5 cents, SEH 2 at 5.5 cents, and SEH 3 also at 5 cents. The mean of the forecasted solar generations during day-ahead are shown in Fig. 8 standard deviation of stochastic generations is considered 5%. The characteristics of SEHs and grid are represented in TABLE 2

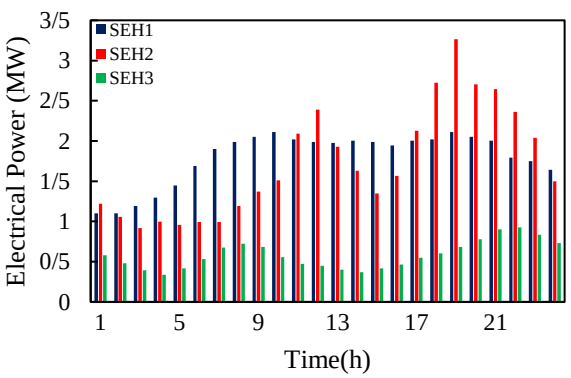

Fig. 4. Electrical demand of SEHs.

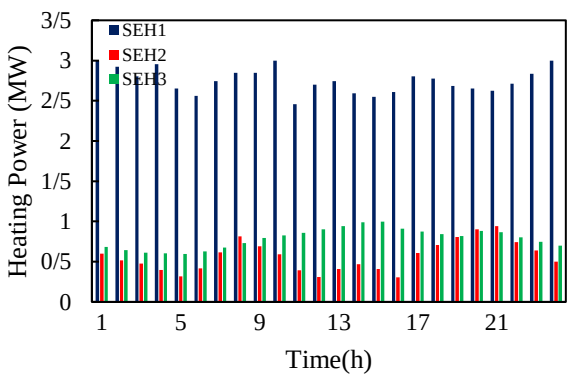

Fig. 5. Forecasted heating demand of SEHs.

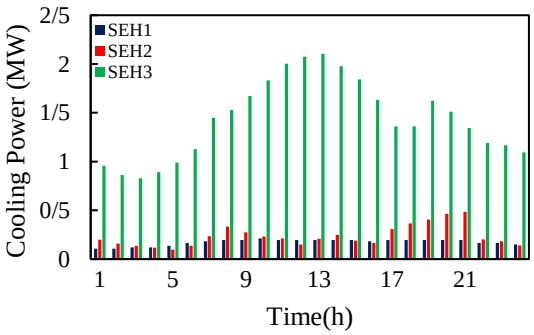

Fig. 6. Forecasted cooling demand.

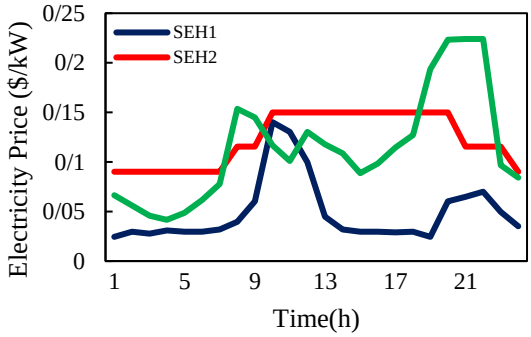

Fig. 7. Electricity price of smart grid.

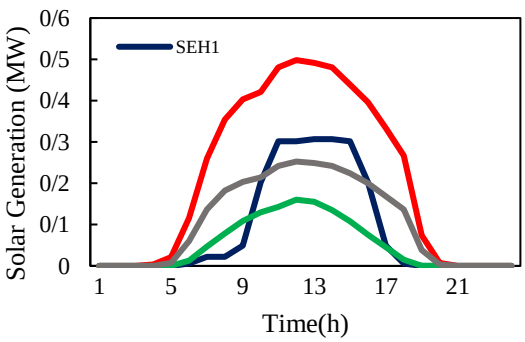

Fig. 8. Solar generations.

B. Results and discussion

The present study endeavors to analyze the effects of P2P transaction and DR programs on costs reduction, as well as the influence of flexibility constraint on enhancing system flexibility. To achieve this objective, three distinct cases have been considered as follows:

Case 1: energy management of SEHs without considering P2P transactions, DR programs, and flexibility constraint

Case 2: energy management of SEHs with considering P2P transactions and DR programs and without considering flexibility constraint

Case 3: energy management of SEHs with considering P2P transactions, DR programs, and flexibility constraint equal to 300KW

The sub-hubs play a crucial role in the collection and allocation of multi-energy. It is necessary for each sub-hub to maintain a balance in energy flow at any given moment. Figures 9-11 show the optimal distribution of energy flows at power, heating and cooling sub-Hubs for different cases. In figures 9-11, the upper and lower sides of the horizontal axis represent the energy flowing into the sub-hub and the energy flowing out of the sub-hub, respectively.

The graphical representation of the optimal dispatch of power flow at the electrical sub-hubs in Case 1 can be observed in the 1st row of Fig. 9 where upstream grid and PV systems supply the electrical demand at the majority of hours. The balance between electrical power generation and electrical consumption is achieved at each hour in electrical sub-hubs. For example, at hour 13, the generation outputs of PV, PGU, and importing from upstream grid in SEH 1 are 306.8 (kW), 140 (kW), and 1528.02 (kW), respectively, while the electrical demand is 1974.8 (kW) at the same hour. On the other hand, in SEH 2, during hours 21-23, when PV generation is zero and the electricity price is low, most of the electrical demand is met by purchases from the upstream grid and less electricity is generated by PGU. In addition, PV generation plays an important role in supplying electrical demand in hours 8-10 and 12-14 in SEH 3. Also, due to the reduction of PV generation at hour 19 in SEH 1, most of the electrical demand is supplied by PGU and upstream grid. the results of power flow in Case 2 are shown in the 2nd row of Fig. 9 While these results are similar to those in Case 1 Since the generation of PGU unit is specifically related to the purchase price of electricity from the upstream grid, during hours 9-13, the role of PGU in providing power demand is more than power traded

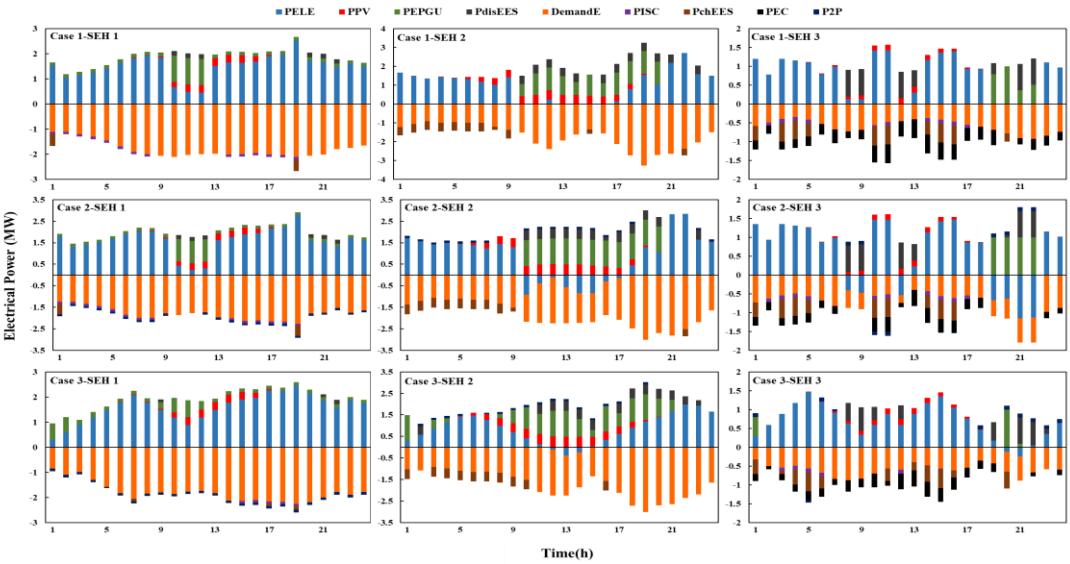

Fig. 9. Electrical power flow at SEHs.

with grid in SEH 1. In SEH 2, there exists evidence showcasing the efficacy of EES. Specifically, EES is charged during the first nine hours of the day that the price of electricity is comparatively lower than the subsequent hours. Consequently, EES unit is discharged during the period of 10 AM - 8 PM when there is a substantial surge observed in the price of electricity. The DR program incorporated in the proposed model operates by curbing the electrical demand in SEH 3 during specified hours of 8, 9, 11, and 12-22, resulting in a drop to 1750 kW, while augmenting the demand during other times of the day to capitalize on the more cost-efficient electricity prices. The implementation of DR strategies has been found to result in a reduction of operational cost through the shiftable electrical loads. Fig. 10 illustrates the energy transfer between interconnected hubs. The utilization of peer-to-peer transaction energy has been found to result in a notable reduction in the production of PGU, as well as a decrease in the need to purchase electricity from the upstream network. This approach also leads to the improvement of energy management within the network. As has been previously indicated, the cost of energy exchange between hubs is not anticipated to have an impact on the total cost.

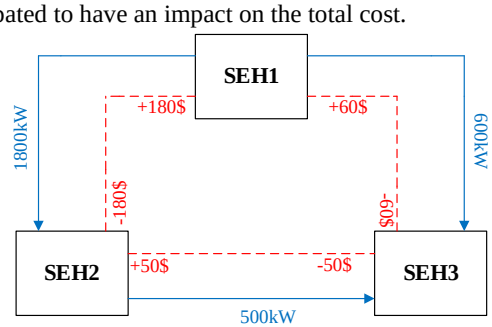

Fig. 10. Energy transfer between SEHs

the results of case 3 shown in the 3rd row of Fig. 9 indicate that the presence of flexibility constraints increases the flexibility of the system and thus the total cost. In the current scenario, the ramp rate at energy is traded with the upstream grid is limited to a maximum of 300. This limitation has resulted in a smoother PELE diagram while increasing the flexibility of the system. As illustrated in the figures, the growth of PELE is limited in the first hours of the day in SEH 1, so PGU production must be increased to meet demand. This increase in production leads to amplified operational costs and carbon emissions. In addition, SEH 2 experiences a significant increase in energy procurement costs during midday hours. This escalation is due to the rigidity constraint that the EH faces, which prevents it from immediately minimizing energy procurement from the upstream grid. Instead, the EH resorts to incremental reductions in energy procurement, resulting in an incremental gradient that inevitably increases system costs.

The 1st row of Fig. 11 shows the optimal dispatch of heat flow at the heating sub-hubs in Case 1. It can be seen that the heating power is balanced in thermal sub-hubs at each hour. For example, at hour 20, the discharge power of TESS and the heat generation of HRU and AB in SEH 1 are 180 (KW), 1640 (kW), and 1346.2 (kW), respectively, while the heat demand and AC consumption are 2653.27 (kW) and 217.75 (kW), respectively at the same hour. It can be seen that the heat demand is mostly covered by HRU. However, during the hours when the electricity price is low and PGU works less to provide the electrical demand, the role of HRU is reduced and AB should supply the heat demand. In addition, for SEH1 and SEH 3, the charging/discharging TESS during favorable hours reduces operating costs at the thermal sub-hub.in SEH 2, the HRU is less active due to the presence of SHE.in Case 2, the 2nd row of Fig. 11 depicts the optimal dispatch of heat flow at the sub-

hubs. Although P2P energy transactions have not yielded so much significant impact on the thermal balance of the system, the DR program has successfully facilitated effective energy management in smart hubs. As an illustration, the implementation of the DR program within SEH 1 has resulted in a decrease in the production of AB, thereby contributing to a corresponding reduction in associated carbon emission costs. the flexibility constraint has resulted in marginal modifications in the heat flow, as illustrated in Fig. 11

The 1st row of Fig. 12 shows the optimal dispatch of cooling flow at cooling sub-hubs in Case 1. It is observed that the AC supplies the cooling demand during all hours. In SEH 3, the assistance of AC alongside EC serves as a substantial contribution to meeting the high demand for cooling and energy supply. The implementation of the discharging process of the ISC during 9-14 within SEH 1 is aimed at mitigating operational costs. In the context of Case 2, the 2nd row of Fig. 12 illustrates the optimized distribution of cooling flow within cooling sub-hubs. Similar to the phenomenon of thermal flow, the utilization of a demand response program within the cooling flow enhances the efficacy of energy management strategies within the system.

TABLE 3 COMPARISON OF TOTAL COST IN THREE CASES

Case Study	Total Cost ($)	Cost of purchasing electricity ($)	Cost of purchasing natural gas ($)	Cost of Emission ($)	compensation cost of EDR ($)	compensation cost of TDR ($)	compensation cost of CDR ($)
Case 1	10400.67	5929.00	4019.8	451.86	0	0	0
Case 2	9231.81	4285.49	3947.08	418.54	109.00	302.42	131.65
Case 3	10142.25	5587.38	3555.16	421.55	87.81	302.42	150.30

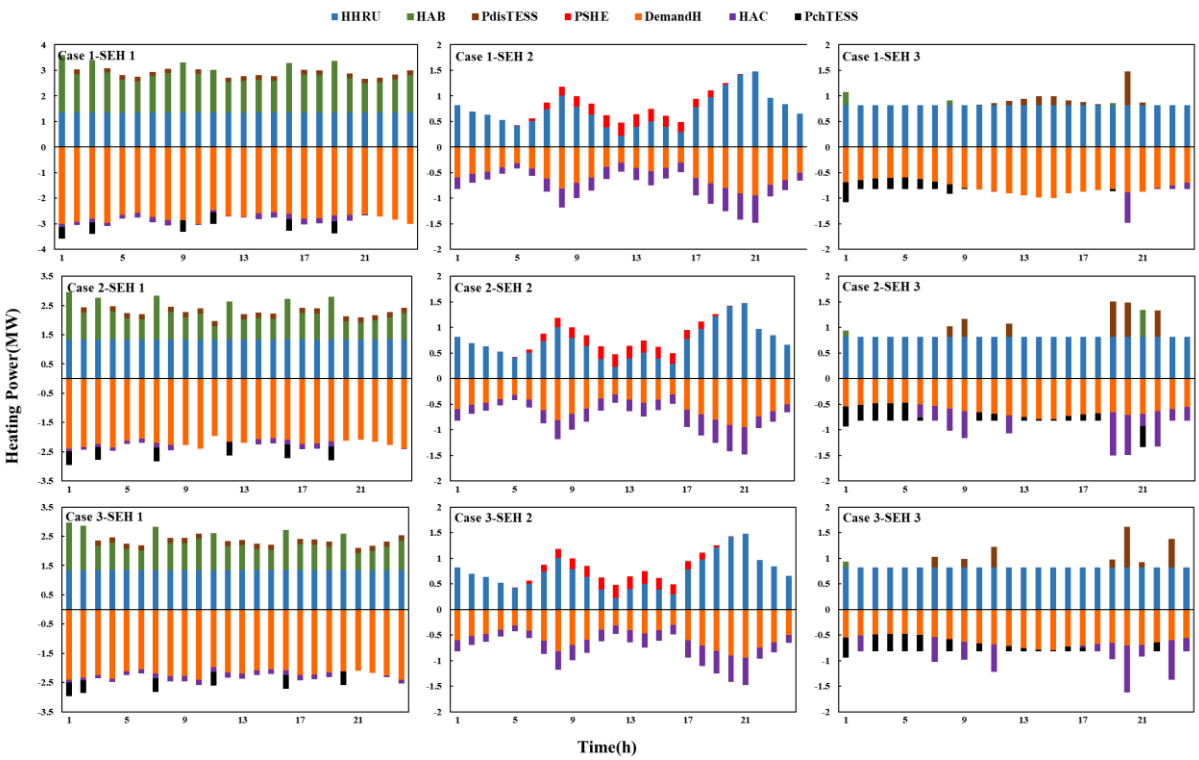

Fig. 11. Heating power flow at SEHs.

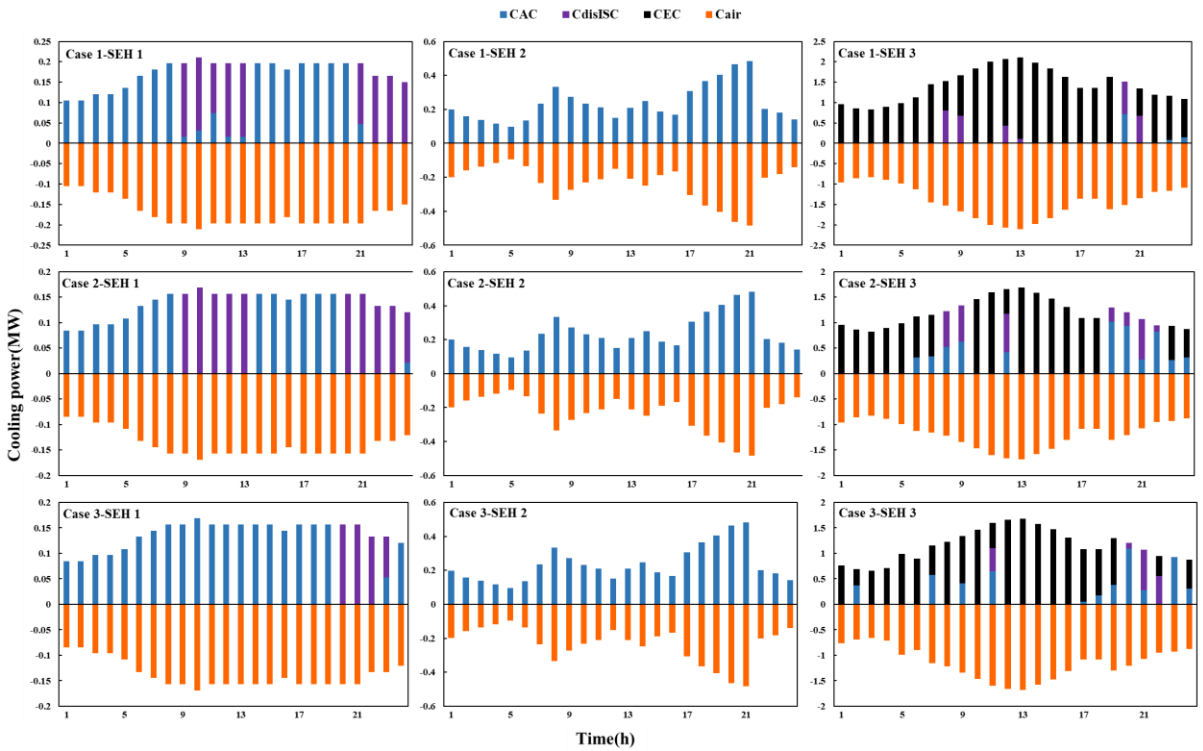

Fig. 12. Cooling power flow at SEHs.

TABLE 3 illustrates the fluctuations in total costs across cases 1 through 3. The utilization of the DR program and the P2P transactive energy has resulted in a reduction of the total cost by 11.2%. In contrast, the implementation of the flexibility constraint with the objective of enhancing the system's flexibility has resulted in a 9.5% rise in operating costs in comparison to Case 2. It is apparent that a decrease in the variable "$P^{Flexibility}$" results in an escalation of the overall system cost. This phenomenon will be thoroughly evaluated through sensitivity analysis in the subsequent section.

C. sensitivity analysis

The flexibility of the interdependence between the upstream grid and SEHs is contingent upon the smooth continuity of the energy exchange graph, which should lack sudden fluctuations. As illustrated in Fig. 13, a decrease in the $P^{Flexibility}$ value corresponds to a reduction in the ramp rate of power exchanged with the upstream grid. This subsequently constrains the ability of energy hubs to meet their energy demands, thereby necessitating a greater reliance on productions from PGUs. Consequently, the cost of system operation and carbon emission experiences an escalated trajectory. Based on the findings depicted in Fig. 13, the selection of $P^{Flexibility}$ by operators should be strategically implemented to ensure the concurrent optimization of the flexibility and total cost of system.

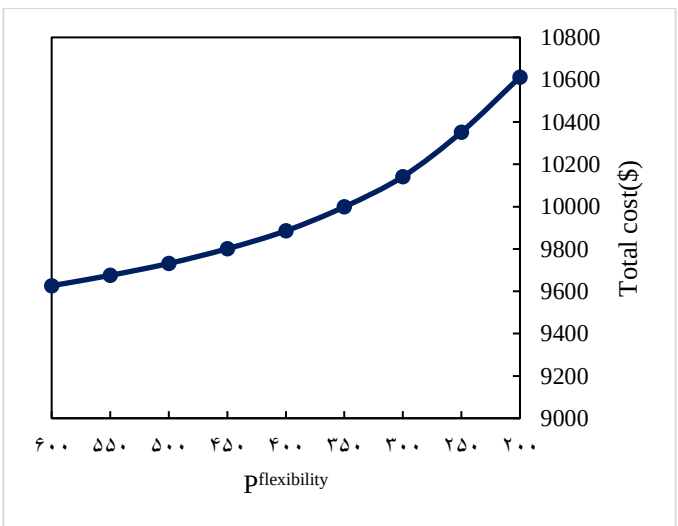

Fig. 13. Sensitivity analysis on Pflexibility

V. Conclusion

In recent years, there has been a surge in need for a variety of energy carriers and a requisite to provide high levels of reliability for fulfilling various energy requirements, with a focus on achieving optimal and economically efficient utilization of energy resources. Consequently, the concept of multi-energy systems has emerged as a solution to these challenges. The concept of energy hub has gained widespread adoption as a potential solution for the utilization of multi-carrier energy systems (MCESs) in various applications. The

SEHs architecture proposed in this study introduces a generic method for reducing the costs of transferring, conversion, and saving energies and optimal dispatch in MG. Furthermore, in this article, special attention has been paid to the flexibility of the system by flexibility constraint. It is noteworthy that the method adopted herein is limited to steady-state energy flow analysis. However, it holds potential for utility in the study of dynamic energy flow as well. In certain instances, wherein the MGO does not possess ownership of specific equipment, such as CCCHP, WT, PV, TESS, SPCAES, and ISC, it is imperative to take into account the investment cost of the said components in relation to the electricity price proffered by the equipment owners to the MGO. The examination of the equipment matter may be analyzed as a prospective area of research.

REFERENCES

[1] K. Zhou, S. Yang, and Z. Shao, "Energy internet: the business perspective," *Applied energy*, vol. 178, pp. 212-222, 2016.

[2] W. Huang, N. Zhang, J. Yang, Y. Wang, and C. Kang, "Optimal configuration planning of multi-energy systems considering distributed renewable energy," *IEEE Transactions on Smart Grid*, vol. 10, no. 2, pp. 1452-1464, 2017.

[3] Y. Chen, W. Wei, F. Liu, Q. Wu, and S. Mei, "Analyzing and validating the economic efficiency of managing a cluster of energy hubs in multi-carrier energy systems," Applied energy, vol. 230, pp. 403-416, 2018.

[4] M. Stratistics, "UAV drones–global market outlook (2016–2022)," Report ID: SMRC16075, 2016.

[5] "CAISO, California Independet System Operator, the net demand trend, 2020." http://www.caiso.com/TodaysOutlook/Pages/default.aspx (accessed 16 July 2020).

[6] S. Bahramara, "Robust optimization of the flexibility-constrained energy management problem for a smart home with rooftop photovoltaic and an energy storage," Journal of Energy Storage, vol. 36, p. 102358, 2021.

[7] A. Mansour-Saatloo, M. Agabalaye-Rahvar, M. A. Mirzaei, B. Mohammadi-Ivatloo, M. Abapour, and K. Zare, "Robust scheduling of hydrogen based smart micro energy hub with integrated demand response," Journal of Cleaner Production, vol. 267, p. 122041, 2020.

[8] F. Jamalzadeh, A. H. Mirzahosseini, F. Faghihi, and M. Panahi, "Optimal operation of energy hub system using hybrid stochastic-interval optimization approach," Sustainable Cities and Society, vol. 54, p. 101998, 2020.

[9] R. Bahmani, H. Karimi, and S. Jadid, "Cooperative energy management of multi-energy hub systems considering demand response programs and ice storage," International Journal of Electrical Power & Energy Systems, vol. 130, p. 106904, 2021.

[10] A. Heidari, S. Mortazavi, and R. Bansal, "Stochastic effects of ice storage on improvement of an energy hub optimal operation including demand response and renewable energies," Applied Energy, vol. 261, p. 114393, 2020.

[11] G. T. Udeh, S. Michailos, D. Ingham, K. J. Hughes, L. Ma, and M. Pourkashanian, "A modified rule-based energy management scheme for optimal operation of a hybrid PV-wind-Stirling engine integrated multi-carrier energy system," Applied Energy, vol. 312, p. 118763, 2022.

[12] A. Najafi, M. Pourakbari-Kasmaei, M. Jasinski, M. Lehtonen, and Z. Leonowicz, "A medium-term hybrid IGDT-Robust optimization model for optimal self scheduling of multi-carrier energy systems," Energy, vol. 238, p. 121661, 2022.

[13] A. Najafi, M. Pourakbari-Kasmaei, M. Jasinski, M. Lehtonen, and Z. Leonowicz, "A max–min–max robust optimization model for multi-carrier energy systems integrated with power to gas storage system," Journal of Energy Storage, vol. 48, p. 103933, 2022/04/01/ 2022, doi: https://doi.org/10.1016/j.est.2021.103933.

[14] X. Lu, Z. Liu, L. Ma, L. Wang, K. Zhou, and N. Feng, "A robust optimization approach for optimal load dispatch of community energy hub," Applied Energy, vol. 259, p. 114195, 2020.

[15] M. M. Sani, H. M. Sani, M. Fowler, A. Elkamel, A. Noorpoor, and A. Ghasemi, "Optimal energy hub development to supply heating, cooling, electricity and freshwater for a coastal urban area taking into account economic and environmental factors," Energy, vol. 238, p. 121743, 2022.

[16] E. Shahrabi, S. M. Hakimi, A. Hasankhani, G. Derakhshan, and B. Abdi, "Developing optimal energy management of energy hub in the presence of stochastic renewable energy resources," Sustainable Energy, Grids and Networks, vol. 26, p. 100428, 2021.

[17] M. Jalili, M. Sedighizadeh, and A. S. Fini, "Stochastic optimal operation of a microgrid based on energy hub including a solar-powered compressed air energy storage system and an ice storage conditioner," Journal of Energy Storage, vol. 33, p. 102089, 2021.

[18] K. Saberi-Beglar, K. Zare, H. Seyedi, M. Marzband, and S. Nojavan, "Risk-embedded scheduling of a CCHP integrated with electric vehicle parking lot in a residential energy hub considering flexible thermal and electrical loads," Applied Energy, vol. 329, p. 120265, 2023/01/01/ 2023, doi: https://doi.org/10.1016/j.apenergy.2022.120265.

[19] S. A. Mansouri, E. Nematbakhsh, A. Ahmarinejad, A. R. Jordehi, M. S. Javadi, and S. A. A. Matin, "A Multi-objective dynamic framework for design of energy hub by considering energy storage system, power-to-gas technology and integrated demand response program," Journal of Energy Storage, vol. 50, p. 104206, 2022/06/01/ 2022, doi: https://doi.org/10.1016/j.est.2022.104206.

[20] W. Gan, M. Yan, W. Yao, and J. Wen, "Peer to peer transactive energy for multiple energy hub with the penetration of high-level renewable energy," *Applied Energy*, vol. 295, p. 117027, 2021.

[21] A. G. Daryan, A. Sheikhi, and A. A. Zadeh, "Peer-to-Peer Energy sharing Among Smart Energy Hubs in an integrated Heat-Electricity Network," Electric Power Systems Research, vol. 206, p. 107726, 2022.

[22] M. S. Javadi, A. E. Nezhad, A. R. Jordehi, M. Gough, S. F. Santos, and J. P. Catalão, "Transactive energy framework in multi-carrier energy hubs: A fully decentralized model," Energy, vol. 238, p. 121717, 2022.

[23] E. Valipour, R. Nourollahi, K. Taghizad-Tavana, S. Nojavan, and A. a. Alizadeh, "Risk assessment of industrial energy hubs and peer-to-peer heat and power transaction in the presence of electric vehicles," Energies, vol. 15, no. 23, p. 8920, 2022.

[24] T. Ha, Y. Zhang, V. Thang, and J. Huang, "Energy hub modeling to minimize residential energy costs considering solar energy and BESS," Journal of Modern Power Systems

and Clean Energy, vol. 5, no. 3, pp. 389-399, 2017.
[25] T. Ma, J. Wu, and L. Hao, "Energy flow modeling and optimal operation analysis of the micro energy grid based on energy hub," Energy conversion and management, vol. 133, pp. 292-306, 2017.
[26] M. Sedighizadeh, M. Esmaili, and N. Mohammadkhani, "Stochastic multi-objective energy management in residential microgrids with combined cooling, heating, and power units considering battery energy storage systems and plug-in hybrid electric vehicles," Journal of Cleaner Production, vol. 195, pp. 301-317, 2018.
[27] W. Gu et al., "Residential CCHP microgrid with load aggregator: Operation mode, pricing strategy, and optimal dispatch," Applied Energy, vol. 205, pp. 173-186, 2017.
[28] N. Mohammadkhani, M. Sedighizadeh, and M. Esmaili, "Energy and emission management of CCHPs with electric and thermal energy storage and electric vehicle," Thermal Science and Engineering Progress, vol. 8, pp. 494-508, 2018.
[29] M. Esmaeili, M. Sedighizadeh, and M. Esmaili, "Multi-objective optimal reconfiguration and DG (Distributed Generation) power allocation in distribution networks using Big Bang-Big Crunch algorithm considering load uncertainty," Energy, vol. 103, pp. 86-99, 2016.
[30] A. Zakariazadeh, S. Jadid, and P. Siano, "Smart microgrid energy and reserve scheduling with demand response using stochastic optimization," International Journal of Electrical Power & Energy Systems, vol. 63, pp. 523-533, 2014.
[31] M. Sedighizadeh, M. Esmaili, A. Jamshidi, and M.-H. Ghaderi, "Stochastic multi-objective economic-environmental energy and reserve scheduling of microgrids considering battery energy storage system," International Journal of Electrical Power & Energy Systems, vol. 106, pp. 1-16, 2019.
[32] S. Talari, M. Yazdaninejad, and M. R. Haghifam, "Stochastic-based scheduling of the microgrid operation including wind turbines, photovoltaic cells, energy storages and responsive loads," IET Generation, Transmission & Distribution, vol. 9, no. 12, pp. 1498-1509, 2015.
[33] Y. Atwa, E. El-Saadany, M. Salama, and R. Seethapathy, "Optimal renewable resources mix for distribution system energy loss minimization," IEEE Transactions on Power Systems, vol. 25, no. 1, pp. 360-370, 2009.
[34] A. Zakariazadeh, S. Jadid, and P. Siano, "Economic-environmental energy and reserve scheduling of smart distribution systems: A multiobjective mathematical programming approach," Energy Conversion and Management, vol. 78, pp. 151-164, 2014.
[35] Z. Li and M. G. Ierapetritou, "A new methodology for the general multiparametric mixed-integer linear programming (MILP) problems," Industrial & engineering chemistry research, vol. 46, no. 15, pp. 5141-5151, 2007.

Ali Riki earned his B.Sc. in Electrical Engineering from Ferdowsi University of Mashhad, Iran, in 2021, followed by an M.Eng. from the Department of Electrical Engineering at Sistan and Balouchistan University, Zahedan, Iran, in 2023. He is currently pursuing a joint Ph.D. at the Department of Electrical Engineering at Bahonar University of Kerman. His research interests focus on power system optimization, energy hubs, and energy management.

Mahmoud Oukati Sadegh was born in 1966 in Zabol, Iran. He received the B.Sc. and M.Sc. degree in electrical power system engineering from Tehran University, Tehran, Iran, in 1989 and 1992 respectively. the Ph.D. degree in electrical engineering from Strathclyde University in Glasgow, UK in2003. Currently, he is an Assistant Professor in the Department of lectrical and Electronic Engineering, University of Sistan and Baluchestan, Zahedan, Iran. His research interests are power system control and operation, Electrical distribution system and Smart grids.

Omid Narouie received the B.Sc. degree in electrical engineering from Shahid Rajaee Teacher Training University, Tehran, Iran, in 2017, and the M.Eng. degree from the Department of Electrical Engineering, Sistan and Balouchistan University, Zahedan, Iran, in 2021. He is currently working toward the joint Ph.D. degree with the Department of Electrical Engineering, Sistan and Balouchistan University. His research interests include power system optimization, power system resilience, restoration and energy management.

International Journal Of
Industrial Electronics Control and Optimization
Print ISSN: 3517-2645
Online ISSN: 3568-2645
Homepage: https://ieco.usb.ac.ir/

Comparison of Dynamic State Estimation Methods in the Time Domain

Saeed Javadi[1] | Ali Hesami Naghshbandy[1] |

Department of Electrical Engineering, University of Kurdistan, Sanandaj, Iran [1]
Corresponding author's email: hesami@uok.ac.ir

Article Info

Article type:
Research Article

Article history:
Received: 5-Mar-2024
Received in revised form: 08-August-2024
Accepted: 09-August-2024
Published online: 21-March-2025

Keywords:
Dynamic state estimation,
Inverter-based resources,
Sample values,
Time domain,.

ABSTRACT

Correct information about a power system's dynamic variables is important and necessary for protection and control issues. Today's power systems, which differ from past systems, face new challenges due to converter-based resources. A solution to these challenges is dynamic state estimation in short time intervals, such as the time domain. This paper simulates a standard 68-bus system in the presence of converter-based resources with a high penetration percentage in DIgSILENT software and compares the performance of four Bayesian filters in estimating the dynamic variables of the synchronous generators of the system using values in the time domain with each other. The four types of filters used include extended Kalman filter, unscented Kalman filter, ensemble Kalman filter, and particle filter. The MATLAB software suite was used for the comparison of the performance of the four filter types in different scenarios, including the presence of measurement and processing noise, extreme noise, network fault, data missing, state estimation time by each filter, and the comparison of time domain method with other methods such as phasor domain. At the end, the advantages and disadvantages of each were identified.

I. Introduction

Today, new power systems, including Converter-Based Resources (CBR) and storage resources, are widespread. With deeper penetration of these sources, the challenges related to the stability, control, and protection of the power system have increased for two crucial reasons: (a) the reduction of system inertia due to the presence of CBRs, and (b) the existence of different time scales from milliseconds or less for CBRs to several minutes or more for synchronous generator boilers. Therefore, it can be mentioned that the high penetration of these sources has caused the new power system to have features such as faster system response, ineffectiveness of common protection logic, and having different power system transients [1, 2]. The following is a review of some works on CBR's presence in power networks.

CBRs in power networks have also affected network distance protection. In [3], adaptive distance protection was used with these CBRs in the condition of fault resistance. As a result, the sensitivity and coordination of distance relays on the transmission lines and the DFIG-based wind farm collector lines were also increased. In [4], the effects of CBRs, such as Double Feed Induction Generators (DFIGs) and Static Series Synchronous Compensator (SSSC), on the stability of power grids were investigated. The system's stability was improved by using a nonlinear controller for these sources.

Today's power systems cannot be properly protected and controlled with these plans due to the random, scattered, and variable nature of renewable energy sources [5].

It has been stated in [1, 6] that in the case without CBR, all network generators are oscillating with respect to a static reference, by using CBRs, the inertia of the whole system is reduced and the reference point also fluctuates, and because other generators also oscillate relative to this (non-static) point, with the presence of CBRs, the fluctuations of waveforms increase. The construction of the phasor by PMUs has a delay due to the use of the DFT algorithm and they cannot follow the fluctuations properly, so we had to use faster units such as

MUs that work in the time domain [7].

On the other hand, despite this new power system, it can be stated that dynamic models are widely used for stability, control, and transient studies of power systems [8]. It can be said that the solution to these new power grid challenges should be searched in Dynamic State Estimation (DSE) [9]. DSE can estimate the state of a power system at different scales, so it can be used as a versatile tool to observe the path of the system state [10]. So far, many research works have been conducted on DSE, some of which are mentioned below.

One of the most important state variables in power systems in terms of stability and control is the rotor speed of the synchronous generator, so measuring the rotor speed has always been a fundamental issue. It can be said that estimating the rotor speed without any mechanical connection is a great improvement in the performance of the power system [11]. Researchers in [12] presented the use of DSE based on the Unscented Kalman Filter (UKF) for a nonlinear system connected to an infinite bus with measurable mechanical torque (Tm) and excitation field (Ef) as inputs and used PMUs. In the following, the dynamic states of a system connected to an infinite bus were estimated by considering the transient model (4th-order model) using the Extended Particle Filter (EPF) [13]. In [14], the state variables were estimated by considering the second-order generator using combined DSE methods. A decentralized method was used in [15] to estimate the dynamic state in the power system based on unscented transformation used to estimate the state of the exact equations of the generator, excitation system, and stabilizer. In [16], a novel centralized controller based on the Kalman filter was presented to control multi-input, multi-output industrial processes with heavy interactions and significant time delays and indicated that the controller performed well in tracking the set point and was robust due to changing the system parameters. In [17], the shortcomings of the EKF method, such as the calculation of the Jacobian matrix and the strong dependence on process and processing noises, were stated, and a PSO-EKF was proposed to make an effective re-adhesion estimator. In [18], state estimation was done with a new method called M-estimation. In this work, the robustness of the proposed algorithm was investigated under different conditions, such as incorrect data in the measurement. In [19], the dynamic states were estimated in the presence of non-Gaussian noises with Iterative Extended Kalman Filter methods of the Generalized Maximum similarity type (GM-IEKF). The method was ineffective in the case of large nonlinearities. Next, DSE was done using the UKF estimation method and H-infinity controller, considering uncertainty in the system and the presence of uncertain measurement noise [20]. In [21, 22], non-Gaussian measurement noises and uncertain inputs were considered in the network, and methods such as GM-UKF and EKF were used. In the works that have already been done, various situations, such as communication channel

TABLE I. STRENCHS, WEAKNESSES, ADVANTAGES, AND DISADVANTAGES OF THE PAST WORKS

Reference	Advantages and strengths	Disadvantages and weaknesses
Ref [1, 2]	- Referring to the power system with CBRs and stating its characteristics - Expressing time domain DSE methods - Expressing time domain equations	- Not doing simulation to prove the claim and just reviewing past works
Ref [3-8]	- Applying and modeling CBR resources in the power network - Examining the effects of these resources on challenges, such as stability, control, and network protection - Improving the above challenges by using new methods	- Not using time domain values and using phasor values - Absence of a comprehensive method that can cover all challenges together - The phasor construction algorithms (DFT) used in these references have delays
Ref [9, 10]	- Expressing the characteristics of the power system - Providing a complete description of basic state estimation	- Not considering CBR resources in the investigated power system - Describing static state estimation, which is not applicable to today's power system.
Ref [11-18]	- Estimating state variables of nonlinear systems with EKF and UKF filters - The robustness and convergence of these filters in different scenarios - Developing a PF method and using the EPF method - Using combined state estimation methods to improve other methods - Applying decentralized and centralized DSE methods and comparing them - Using state estimation methods in other engineering sciences [16] - Combining EKF with PSO to improve the performance of EKF [17]	- Using phasor domain values - Using the old power system without the presence of CBRs - Not checking different scenarios in some references - Effectiveness of algorithms for extreme noises - Divergence of state estimation algorithms in some special states, such as non-Gaussian noise - High calculation time due to the use of phasor construction algorithms such as DFT
Ref [19-25]	- Using the EKF and UKF method based on repetition to estimate the parameter and mode for non-Gaussian noises and their robustness - Combining UKF and H-infinity controller in the presence of system uncertainties and non-Gaussian noises - Improving UKF against cyber attacks, innovation errors, and severe nonlinearities - State estimation with a combination of the above methods for non-Gaussian noises - Estimating CBR modes	- Divergence of the above filters in some simulations - Using simple models of synchronous generators like the classic model - Not considering CBR in the studied power systems - Using phasor values (PMU) - Not checking the robustness of some algorithms in scenarios, such as data missing

interruption, high nonlinearity of the system, innovation errors, and bad and incorrect data, have been considered, and filters, such as UKF based on repetition, developed EKF, have been used to estimate the state variables and the parameters of synchronous generators [23-25].

Table I shows a summary of the strengths and weaknesses, as well as the advantages and disadvantages of the references reviewed in Section I.

By studying past works, it can be stated that various methods have been used to estimate the state of the power system, most of which are methods based on the Kalman filter because Kalman filters cover all linear and nonlinear systems and are the best DSE tools.

By stating the above information about the new power system and DSE, it is concluded that DSE has limitedly been used for networks with CBRs, and it is the best tool for protecting, controlling, and monitoring new systems.

So, the innovation of this paper is the use of DSE in the time domain in a centralized manner with Bayesian methods for networks with CBRs with a high penetration level. The above operations are also implemented for different scenarios, and the advantages and disadvantages of each of the filters are specified.

The general structure of the paper is as follows. Section II describes DSE formulation in the time domain, the estimation model, and the discretization process. Section III describes Bayesian filters and how to implement them. Section IV simulates the system and implements the filters on it. Finally, Section V reports simulation results.

II. DSE Formulation

As already mentioned, a typical power system includes synchronous generators and electromechanical transients with a time period of several seconds. This power system also has electromagnetic transients, which are much faster than electromechanical transients and are ignored [1].

With the increasing penetration of CBRs and the effect of those devices in power systems, the system's dynamic response is highly dependent on the dynamic response of the power electronic devices, their control systems, and dynamic issues related to converters [26].

Also, this equipment distorts the network signals and their deviation from the sinusoidal state. It should be mentioned that the time period studied for CBRs is from microsecond to millisecond due to switching in converters. Hence, the result is that common phasor representation is usually useful for electromechanical studies of synchronous generators. It is unsuitable for electromagnetic problems due to the delay in constructing the phasor (discrete Fourier transform process or DFT), so time domain information (sample values) must be used.

A. Representation of Equations in the Time Domain

According to the previous section, the relationships and measurements required for the dynamic estimation equations should be changed.

Regardless of the time scales of different dynamics, the system can be described with the differential and algebraic equations (1) [1].

$$\begin{cases} \dot{x}(t) = f\big(x(t), y(t), u(t), w(t)\big) \\ 0 = g\big(x(t), y(t), u(t), w(t)\big) \end{cases} \tag{1}$$

in which x(t) is the state vector, y(t) is the algebraic state vector, u(t) is the input vector, and f and g are nonlinear functions.

To go to the time domain, the above equations must be converted from continuous to discrete form, which is fully explained in Subsection C. The important point here is that according to [1], to obtain the equations in the time domain after discretization, they will remain unchanged, and the only difference is that the voltage and current signals will no longer be in the phasor state, but they will be sampled in the time domain and determined by the sampling frequency.

B. The Desired Model for Network Generators

This section explains the synchronous generator model considered for state estimation and then states Euler's method for discretization of state equations. In this paper, a sub transient model generator with IEEE-type I exciter and Power System Stabilizer (PSS) are implemented using Eq. (2) [27, 28].

$$\frac{d\delta}{dt} = \omega_0 \Delta\omega \tag{2a}$$

$$\frac{d\Delta\omega}{dt} = \frac{1}{2H}(T_m - T_e - K_D\Delta\omega) \tag{2b}$$

$$\frac{de'_d}{dt} = \frac{1}{T'_{q0}}\Big(-e'_d - \big(x_q - x'_q\big)\Big\{i_q - \frac{\big(x'_q - x''_q\big)}{\big(x'_q - x_{ls}\big)^2}\big(e'_d + \big(x'_q - x_{ls}\big)i_q + \varphi_{2q}\big)\Big\} \tag{2c}$$

$$\frac{de'_q}{dt} = \frac{1}{T'_{d0}}\Big(-e'_q - (x_d - x'_d)\Big\{i_d - \frac{(x'_d - x''_d)}{(x'_d - x_{ls})^2}\Big\}\big(e'_q + (x'_d - x_{ls})i_d + \varphi_{1d}\big)\Big\} + E_{fd} \tag{2d}$$

$$\frac{d\varphi_{1d}}{dt} = \frac{1}{T''_{d0}}\big(e'_q - \big(x'_d - x_{ls}\big)i_d - \varphi_{1d}\big) \tag{2e}$$

$$\frac{d\varphi_{2q}}{dt} = \frac{1}{T''_{q0}}\big(-e'_d - \big(x'_q - x_{ls}\big)i_q - \varphi_{2q}\big) \tag{2f}$$

$$T_E\frac{dE_{fd}}{dt} = -\Big(K_E + S_E\big(E_{fd}\big)\Big)E_{fd} + V_R \tag{2g}$$

$$T_A\frac{dV_R}{dt} = -V_R + K_A R_F - \frac{K_A K_F}{T_F}E_{fd} + K_A(V_{ref} + V_{PSS} - V_t) \tag{2h}$$

$$T_F\frac{dR_F}{dt} = -R_F + \frac{K_F}{T_F}E_{fd} \tag{2i}$$

$$\frac{dV_{WF}}{dt} = -\frac{1}{T_W}V_{WF} + K_{PSS}\frac{\omega_0}{2H}\times \quad (2j)$$
$$((T_m - T_e - K_D\Delta\omega))$$
$$\frac{dV_{PSS}}{dt} = -\frac{1}{T_2}V_{PSS} + \left(\frac{1}{T_2} - \frac{1}{T_w}\frac{T_1}{T_2}\right)V_{WF} + \quad (2k)$$
$$K_{PSS}\frac{T_1}{T_2}\frac{\omega_0}{2H}((T_m - T_e - K_D\Delta\omega))$$

Equations (2a-2f), (2g-2i) and (2j, 2k) are related to the generator, the excitation system, and the PSS, respectively. In these equations, δ is the angle of the rotor, Δω is the deviation of the rotor speed, $\dot{e'_d}$ and $\dot{e'_q}$ are transient voltages of the stator in the direction of d and q axes, φ_{1d} and φ_{2q} are dampers flux in the direction of d and q, E_{fd} is the excitation field, R_F is the scaled output of the stabilizing transformer, V_R is the scaled output of the amplifier, V_{WF} is the output voltage of steady state eliminator filter, V_{PSS} is the PSS output voltage, and i_d and i_q are the stator currents along d and q axes, respectively. The parameter T_m is the mechanical torque, T_e is the electrical torque of the air gap, ω_0 is the nominal value of the angular frequency, H is the inertia, and K_D is the damping coefficient. The parameters T''_{d0}, T''_{q0}, T'_{d0}, T'_{q0}, T_A, T_E, T_F, T_W, T_1, and T_2 are time constants in seconds, K_E, K_F, and K_A are controller gains, and K_{PSS} is the PSS gain. x_d and x_q are the reactances along the d and q axes, x'_d and x'_q are the transient reactances along the d and q axes, respectively. The above equations should be written as (3-8) in order to be in the framework of state equations.

$$\dot{x} = f_c(x,u) + w_c$$
$$y = h_c(x,u) + v_c \quad (3)$$
$$E[w_c w_c^T] = Q \quad (4)$$
$$E[v_c v_c^T] = R \quad (5)$$
$$x = [\delta\ \Delta\omega\ e'_q\ e'_d\ \varphi_{1d}\ \varphi_{2q} E_{fd}\ V_R\ R_F\ V_{WF}\ V_{PSS}]^T \quad (6)$$
$$u = [T_m\ i_R\ i_I\ V_{ref}]^T \quad (7)$$
$$y = [e_R\ e_I]^T \quad (8)$$

in which x is the state vector, u is the input vector, y is the output vector, the functions f_c and h_c represent the state and output equations, respectively, and the index c indicates the continuous state.

The vectors w_c and v_c represent the process and output noises, respectively, which are modeled as Gaussian (with zero means), and their covariance matrix is defined according to Eq. (4) and (5), respectively, where $E[*]$ is the statistical expectation.

In Eq. (7, 8), e_R are e_I the stator voltages along the R and I axes, and i_R and i_I are the stator currents along the R and I axes, respectively.

To convert Eq. (2) to f_c according to Eq. (3), i_d, i_q, and T_e are written as Eq. (9-11) in terms of *x* and *u*.

$$i_d = i_R sin\delta - i_I cos\delta \quad (9)$$
$$i_q = i_I sin\delta + i_R cos\delta \quad (10)$$
$$T_e \approx P_t = (e'_d + i_q x'_q)i_d + (e'_q - i_d x'_d)i_q \quad (11)$$

Similarly, in order to be able in $h_c[*]$ to write e_R and e_I in terms of relations of *x* and *u*, Eq. (12, 13) should be used.

$$e_R = (e'_d + i_q x'_q)sin\delta + (e'_q - i_d x'_d)cos\delta \quad (12)$$
$$e_I = (e'_q - i_d x'_d)\sin\delta - (e'_d - i_q x'_q)\cos\delta \quad (13)$$

Finally, the state equations are written in terms of state variables and inputs.

C. Discretization of Equations and its Relations

Assuming that the sampling frequency of merging unit (MU) devices, which have the same role in the time domain as the PMU units in the phasor domain, is f_s, and the sampled time interval is equal to $\Delta t_s = \frac{1}{f_s}$, so, as a result, the values of $T_m(j\Delta t)$, $i_R(j\Delta t)$, $i_I(j\Delta t)$, and $V_{ref}(j\Delta t)$ as input and $e_R(j\Delta t)$and $e_I(j\Delta t)$ are output where *j=1,2,...,k*, is applied to the above state equations as the time sample, and the state values of $x = [\delta\ \Delta\omega\ e'_q\ e'_d\ \varphi_{1d}\ \varphi_{2q}\ E_{fd}\ V_R\ R_F\ V_{WF}\ V_{PSS}]^T$ are estimated [1, 27]. For discretization, it should be done as follows, where $j\Delta t_s$ becomes *k*.

In order to make the equations discrete, the definition of the derivative for the variable x is used as described in Eq. (14).

$$\dot{x} = \frac{x(k) - x(k-1)}{\Delta t_s} \rightarrow x(k) = x(k-1) + \dot{x} \times \Delta t_s \quad (14)$$

in which Δt_s is sampling interval and *k* and *k-1* are actually the same as $k\Delta t_s$ and $(k-1)\Delta t_s$.

By placing the above relation in the state matrix relations, Eq. (15) is obtained:

$$x(k) = x(k-1) + \Delta t_s \times (f(x,u) + w_c \quad (15)$$

Finally, by simplifying, Eq. (16) is obtained:

$$x_k = f(x_{k-1}, u_{k-1}) \times \Delta t_s + x_{k-1} + w_{k-1} \quad (16)$$
$$y_k = h(x_k, u_k) + v_k$$

The above equations show those related to the discrete state of a system, which is in the time domain, and phasor values are no longer used, and synchronized sample values are used.

III. An Overview of the Bayesian Filtering Method

Along with many successes in estimating linear systems, Kalman also made achievements for nonlinear systems.

These nonlinear methods include EKF, UKF, EnKF, and PF. The main difference between these methods is how to calculate the mean and covariance of the system states.

In EKF, the state equations of the system are linearized using Taylor expansion to the first approximation, and the mean and covariance are calculated using Jacobian matrices.

In the UKF method, mean and covariance are calculated using sigma points and passing these sigma points from the nonlinear function.

In EnKF, the mean and covariance are extracted using sequential Monte Carlo methods, and the state distribution is created by collecting these particles. In the above methods, it

is assumed that the processing and measurement noise in Gaussian and Bayesian methods are used, but the PF method is not dependent on Gaussian noise, and similar to the EnKF method, particles are used to calculate the possible distribution of state variables [27].

In the Bayesian framework, the above algorithms are implemented similarly. After the initialization, the above filters receive a data sample as input in each stage. Then, two stages of prediction and filtering are performed, and the state variables are estimated. In the prediction stage, the mean and covariance of states at time k are predicted based on the values of time k-1. The predicted values are corrected with the measured values in the filtering stage. The details of the implementation of the filters are fully described below.

A. Extended Kalman Filter (EKF)

The EKF method linearizes the system using Jacobian matrices and includes the following steps [27].

Prediction stage:

In Eq. (17) and (18), the state and covariance matrix of the states are predicted.

$$x_k^- = f(x_{k-1}, u_{k-1}) + w_{k-1} \quad (17)$$

$$P_k^- = F_{k-1} P_{k-1} F_{k-1}^T + Q_d \quad (18)$$

Filtering step:

The updating or filtering stage is defined by Eq. (19-22), respectively.

$$x_k = x_k^- + K_k \tilde{y}_k \quad (19)$$

$$K_k = P_k^- H_k^T (H_k P_k^- H_k^T + R_d)^{-1} \quad (20)$$

$$\tilde{y}_k = z_k - h(x_k^-, u_k) \quad (21)$$

$$P_k = (I - K_k H_k) P_k^- \quad (22)$$

in which x_k^- and P_k^- are the priori values of mean and variance, respectively. They are derived from the values of the previous step, i.e. k-1. The values of x_k and P_k are the posterior values of mean and variance, respectively, which are obtained by adding the measured values of z_k to the previous values. K_k is the gain of the Kalman filter. $\tilde{y}_k$ represents the remainder between $h(x_k^-, u_k)$ and z_k. F_k and H_k are Jacobian matrices expressed by Eq. (23) and (24).

$$F_{k-1} = \left.\frac{\partial f}{\partial x}\right|_{x_k^-, u_{k-1}} \quad (23)$$

$$H_k = \left.\frac{\partial h}{\partial x}\right|_{x_k^-, u_k} \quad (24)$$

B. Unscented Kalman Filter (UKF)

The UKF method is the unscented transformation for taking a set of samples to represent the probability distribution of states and propagating these samples through functions f and g to generate the mean and covariance of states [29]. The UKF method is described as follows:

Prediction stage:

The prediction stage includes Eq. (25-30).

$$x_k^{i-} = f\left(x_{k-1}^i, u_{k-1}\right) + w_{k-1} \quad (25)$$

$$x_{k-1}^0 = x_{k-1} \quad (26)$$

$$x_{k-1}^i = x_{k-1} + \left(\sqrt{(n+\kappa)P_{k-1}}\right)_i \quad i = 1, \dots, n \quad (27)$$

$$x_{k-1}^{i+n} = x_{k-1} - \left(\sqrt{(n+\kappa)P_{k-1}}\right)_i \quad i = 1, \dots, n \quad (28)$$

$$x_k^- = \sum_0^{2n} W_i x_k^{i-} \quad (29)$$

$$P_k^- = \sum_0^{2n} W_i (x_k^{i-} - x_k^-)(x_k^{i-} - x_k^-)^T + Q_d \quad (30)$$

Filtering step:

The filtering stage includes Eq. (31-37).

$$\mathrm{x_k} = \mathrm{x_k^-} + \mathrm{K_k}\tilde{\mathrm{y}}_\mathrm{k} \quad (31)$$

$$\mathrm{K_k} = \mathrm{P_k^-}\mathrm{H_k^T}(\mathrm{H_k}\mathrm{P_k^-}\mathrm{H_k^T} + \mathrm{R_d})^{-1} \quad (32)$$

$$H_k = \sum_0^{2n} W_i \, \tilde{y}_k \tilde{y}_k^T \quad (33)$$

$$\tilde{\mathrm{y}}_\mathrm{k} = \mathrm{z_k} - \mathrm{z_k^-} \quad (34)$$

$$\mathrm{z_k^-} = \sum_0^{2n} W_i \mathrm{z_k^{i-}} \quad (35)$$

$$\mathrm{z_k^{i-}} = \mathrm{h}\left(\mathrm{x_k^{i-}}, \mathrm{u_k}\right) \quad \mathrm{i} = 0, \dots, 2\mathrm{n} \quad (36)$$

$$\mathrm{P_k} = (\mathrm{I} - \mathrm{K_k}\mathrm{H_k})\mathrm{P_k^-} \quad (37)$$

in which x_k^{i-} and W_i represent the values of 2n+1 point and their weights, and κ is the scaling parameter that determines the position of the sigma points.

C. Ensemble Kalman Filter (EnKF)

In the EnKF method, samples are used to extract the probability distribution of the state variables and their covariance, and the algorithm execution steps are as follows [27, 30].

Prediction stage:

The prediction stage includes Eq. (38-41).

$$\mathrm{x_k^{i-}} = \mathrm{f}\left(\mathrm{x_{k-1}^i}, \mathrm{u_{k-1}}\right) + \mathrm{w_{k-1}} \quad (38)$$

$$\mathrm{z_k^{i-}} = \mathrm{h}\left(\mathrm{x_k^{i-}}, \mathrm{u_k}\right) \quad \mathrm{i} = 0, \dots, \mathrm{n_{EnKF}} \quad (39)$$

$$\mathrm{x_k^-} = \frac{1}{\mathrm{n_{EnKF}}} \sum_{\mathrm{i}=1}^{\mathrm{n_{EnKF}}} \mathrm{x_k^{i-}} \quad (40)$$

$$\mathrm{z_k^-} = \frac{1}{\mathrm{n_{EnKF}}} \sum_{i=1}^{\mathrm{n_{EnKF}}} \mathrm{z_k^{i-}} \quad (41)$$

Filtering step:

The filtering stage includes Eq. (42-46).

$$x_k^i = x_k^{i-} + K_k(z_k^i - z_k^{i-}) \quad (42)$$

$$K_k = P_k^- H_k^T (H_k P_k^- H_k^T + R_d)^{-1} \quad (43)$$

$$P_k^- H_k^T = \frac{1}{n_{EnKF}} \sum_{i=1}^{n_{EnKF}} W_i (x_k^{i-} - x_k^-)(z_k^{i-} - z_k^-)^T \quad (44)$$

$$H_k P_k^- H_k^T = \frac{1}{n_{EnKF}} \sum_{i=1}^{n_{EnKF}} W_i \, (z_k^{i-} - z_k^-)(z_k^{i-} - z_k^-)^T \quad (45)$$

$$z_k^i = z_k + v_k^i \quad (46)$$

Here n_{EnKF} is the number of particles. It should be noted that it is no longer necessary to calculate the error covariance

matrix P_K alone.

D. Particle Filter (PF)

The particle filter method, first proposed by Nicholas Metropolis, is suitable for systems with a high degree of nonlinearity. In fact, the particle filter method is resistant to severe nonlinearities while it has a high computational load. This method, also known as sequential Monte Carlo, will be explained further [27, 31].

First, N random state vectors with the initial probability density distribution function P(x0) are generated, which are represented by $x_{0,i}^{+}\,(i=1,..,N)$. Then, for each time step of k, these particles are published from the nonlinear equation of fk, and their value is calculated for the next sample using Eq. (47):

$$x_{k,i}^{-}=f_k(x_{k-1,i}^{+},w_{k-1}^{i}) \quad (i=1,\dots,N) \tag{47}$$

in which w_{k-1}^{i} is the noise of the process and is calculated from the probability distribution of w_k.

After the measurement is received at time k, the relative conditional probability ($P(y_k|x_{k,i}^{-})$) for each particle $x_{k,i}^{-}$ is calculated. This value can be calculated when the noise probability density function (pdf) and the output matrix are known.

For example, if the measurement function is $y_k=h(x_k)+v_k$, then assuming $x_k=x_{k,i}^{-}$ and also the relative probability of q_i is equal to the value of y^*, then q_i is calculated using Eq. (48) as follows:

$$q_i=P\left[(y_k=y^*)\middle|(x_k=x_{k,i}^{-})\right]=P\left[v_k=y^*-h(x_{k,i}^{-})\right] \tag{48}$$

which is equal to:

$$q_i=\frac{1}{(2\pi)^{\frac{m}{2}}|R|^{\frac{1}{2}}}\times exp\left(-\frac{[y^*-h(x_{k,i}^{-})]^T R^{-1}[y^*-h(x_{k,i}^{-})]}{2}\right) \tag{49}$$

For all particles, the relative probability must be calculated and normalized using Eq. (44) so that the sum of probabilities equals one.

$$q_i=\frac{q_i}{\sum_{j=1}^{N}q_j} \tag{50}$$

In the next step, the resampling step is performed to calculate a new set of particles $x_{k,i}^{+}$. This new set of particles is calculated randomly based on q_i. There are different resampling methods. Here, the standard method is used as follows:

i) The random number r is chosen with a uniform distribution between zero and one.

ii) The set of probabilities q_i are calculated such that they are greater than the value of r, i.e., $\sum_{m=1}^{j-1}q_m<r$, but when we reach the data j, the condition $\sum_{m=1}^{j}q_m>r$ is established, the new particles $x_{k,i}^{+}$ will be equal to the set of particles $x_{k,j}^{-}$.

IV. Simulation and State Estimation

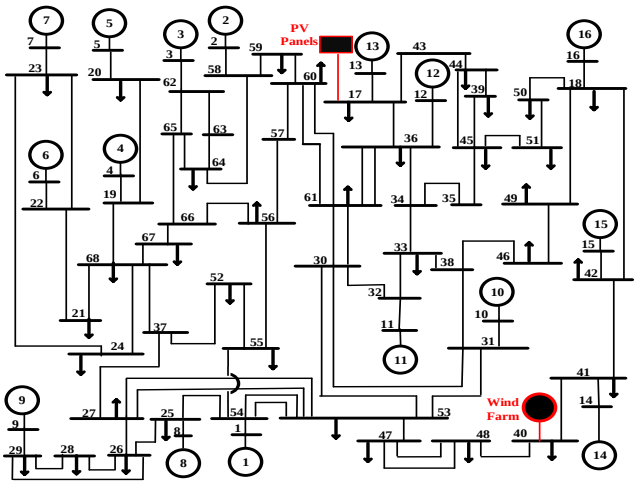

Fig. 1. The 68-bus system simulated in DIGsILENT

This section first describes the simulated system, along with the CBRs. In the following sections, different scenarios are applied in the network, and the above state estimation algorithms are used to estimate the network variables.

A. Simulated System and Results

Fig. 1 is the simulated system in DIgSILNT software, which is the new system of England, New York, and three other geographical regions where the equivalent circuit is available. It has 68 buses, 16 generators, and 83 transmission lines.

It is worth mentioning that the inverter-based resource used in a wind farm includes six two-feed induction generators connected to the 40 bus and a photovoltaic panel connected to the 17 bus. For more information, refer to [31, 32].

The state estimation considered for this article is done centrally and for each generator separately, and the estimated information is sent to the main control center (Fig. 2). Considering that the simulation step must be the same in all generators, the sampling time is also considered to be 1 millisecond.

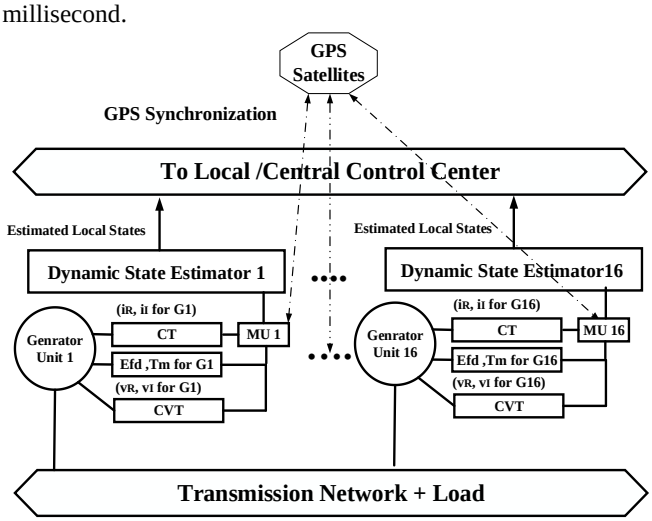

Fig. 2. The estimation of the state of the network in a centralized way

To obtain the initial state of each generator (x_0), the equation $\dot{x} = 0$ in Eq. (2) should be solved for the input values at the initial moment [27].

For all generators, process noise $w_k \sim (0, Q_d)$ with covariance $Q_d = diag([0.0474^2\ 0.0042^2\ 0.0289^2\ 0.0137^2])$ and measurement noise $v_k \sim (0, R_d)$ with covariance $R_d = \text{diag}([0.01^2\ 0.01^2])$ are considered according to [27].

In the following, the simulation results are presented to evaluate the performance of the relationships and the state estimation algorithms of the dynamic variables for the following four scenarios.

B. The First Scenario

In a simple scenario, considering the process and measurement standard noises, the state variables of 16 synchronous generators are estimated.

Figs. 3 to 6 show the state variables estimated by the four filters described in Section III and their actual values related to generator number five (G05). As it is clear from Figs. 3 and 4, in EKF and EnKF filters, after a time of about 2 seconds from the start of state estimation, tend to their real value (black color). The amount of fluctuations and changes for the PF filter (pink color) in the four state variables is less than that of the rest of the filters.

According to Fig. 4, it is clear that the state estimation output for the speed deviation variable tends to its true value, but the amount of changes and the time to reach the true value are more for EKF and EnKF.

It is clear from Figs. 5 and 6 that the amount of changes for UKF and EnKF is more than the others.

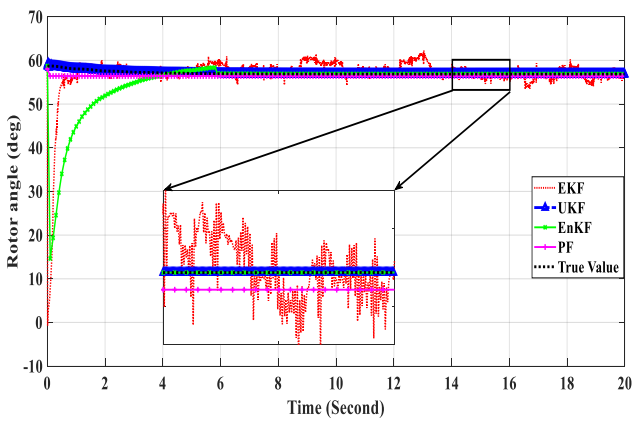

Fig. 3. The dynamic estimation of rotor angle with four studied filters

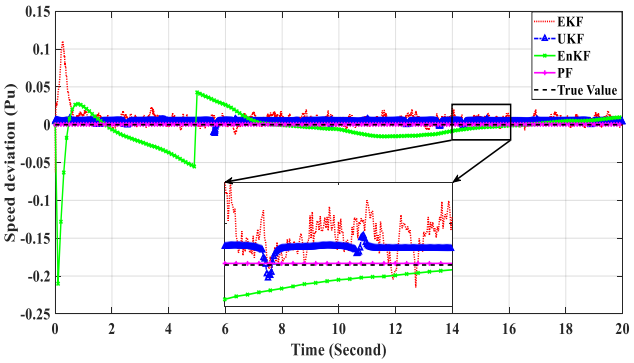

Fig. 4. The dynamic estimation of speed deviation with four studied filters

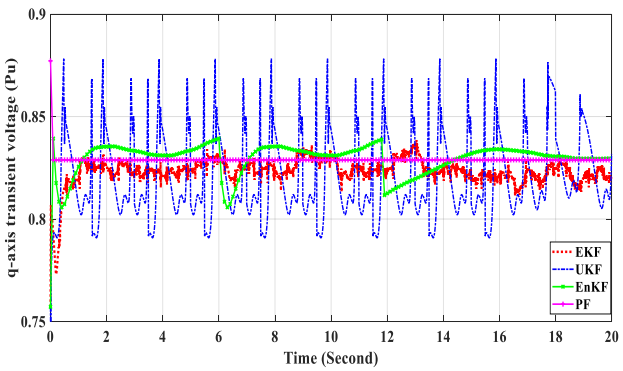

Fig. 5. The dynamic estimation of q-axis transient voltage with four studied filters

In order to show that the state estimation for other synchronous generators works correctly, the maximum deviation index (*MDI*) is defined for some state variables, which is in the form of (51).

$$MDI = max\ |(x_{estimated}(k) - x_{actual}(k)| \quad k = m, m+1, \ldots 20/0.001) \tag{51}$$

in which $x_{estimated}$ is the output state of the estimator, x_{actual} is the actual state of the system, m is the number of samples in that the estimator has reached a stable state, the number 20 is the simulation time, and 0.001 is the sampling interval.

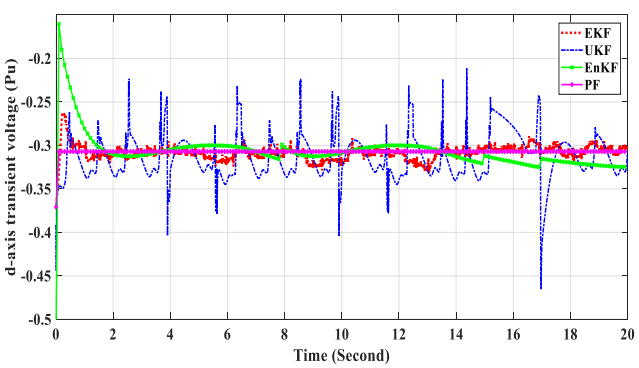

Fig. 6. The dynamic estimation of d-axis transient voltage with four studied filters

TABLE II. COMPARISON OF *MDI* FOR ALL GENERATORS WITH ALL FOUR FILTERS FOR PROCESSING AND MEASUREMENT NOISE

Generator	MDI. EKF	MDI. UKF	MDI. EnKF	MDI. PF
G01	4	5	6.8	2
G02	2.9	4.1	6	1.9
G03	2.8	4.7	5.6	3
G04	4	4.4	6.7	2
G05	3.9	4.1	5.6	2.9
G06	4.1	3.7	6	1.9
G07	4	5.1	5.8	2
G08	3.1	5.2	5.9	2
G09	3.3	5.2	5.1	1.9
G10	3.2	4.1	5	2
G11	3.8	4.2	4.8	2
G12	4	4.3	5	2.7
G13	3.8	4.3	5.3	3.1
G14	3.7	4.1	5.5	3
G15	5.2	3.8	5.8	2.5
G16	4.3	3.4	4.9	2.7

Table II shows the amount of *MDI* for four types of filters after reaching the steady state for the rotor angle variable for 16 synchronous generators. Clearly, the amount of *MDI* for the PF filter is lower than that for other filters.

C. The Second Scenario

In this case, the noise level of the process and measurement is 10 times of the standard noise. In other words, the measuring devices and the system have suffered a severe disturbance, and the first scenario is repeated. Figs. 7 to 10 show the state variables estimated with the four studied filters. It is clear that the noise on the PF filter has almost no effect and causes more changes in other filters for the estimated values compared to the previous states.

It is also clear here that the amount of changes in the estimated values in EKF, EnKF, and UKF is more than the PF filter.

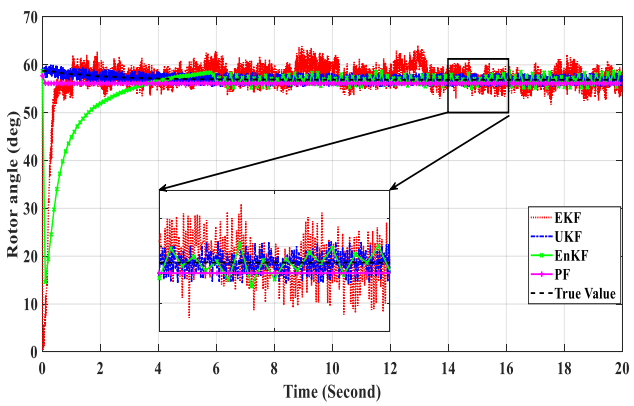

Fig. 7. The dynamic estimation of rotor angle with four studied filters for extreme noise

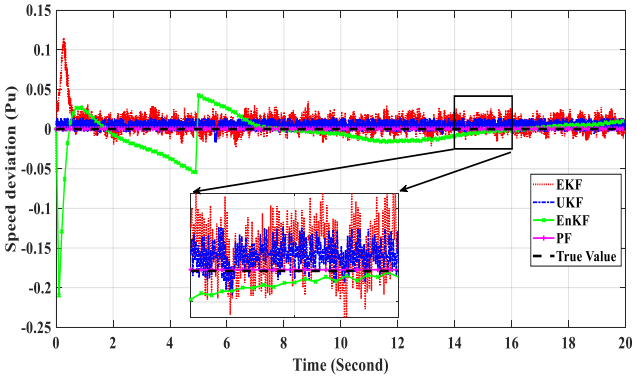

Fig. 8. The dynamic estimation of speed deviation with four studied filters for extreme noise

Figs. 9 and 10 show the transient voltages along the d and q axes for intense noise, respectively.

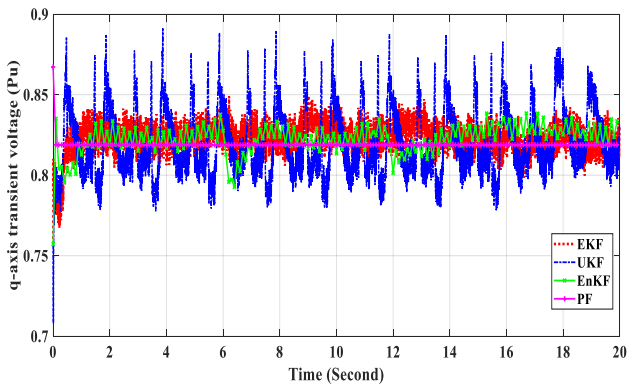

Fig. 9. The dynamic estimation of q-axis transient voltage with four studied filters for extreme noise

Table III shows the amount of *MDI* for all four types of filters after reaching the steady state for the speed deviation variable for 16 synchronous generators. Clearly, the amount of *MDI* for the PF filter is lower than other filters.

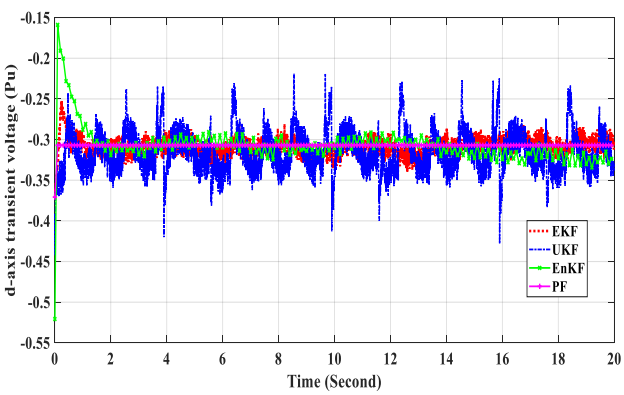

Fig. 10. The dynamic estimation of d-axis transient voltage with four studied filters for extreme noise

TABLE III. COMPARISON OF MDI FOR ALL GENERATORS WITH ALL FOUR FILTERS FOR PROCESSING AND MEASUREMENT EXTREME NOISE

Generator	MDI. EKF	MDI. UKF	MDI. EnKF	MDI. UKF
G01	0.021	0.01	0.02	0.005
G02	0.02	0.011	0.03	0.004
G03	0.019	0.013	0.015	0.008
G04	0.022	0.012	0.018	0.005
G05	0.021	0.011	0.02	0.004
G06	0.023	0.02	0.021	0.004
G07	0.024	0.019	0.021	0.006
G08	0.022	0.02	0.022	0.007
G09	0.022	0.014	0.021	0.006
G10	0.02	0.015	0.02	0.005
G11	0.021	0.02	0.022	0.004
G12	0.018	0.017	0.02	0.005
G13	0.019	0.018	0.019	0.004
G14	0.02	0.021	0.019	0.005
G15	0.025	0.016	0.021	0.005
G16	0.027	0.013	0.02	0.004

D. The Third Scenario

In this scenario, a three-phase fault occurs on line 65-66 in the third second, and after 150 milliseconds, the breakers on both sides of the line open and the fault is cleared. Fig. 11 shows the estimation of the dynamic state of the rotor angle with four types of filters with negligible noise.

As it is clear, changes in the PF filter are less than other filters.

A. The Fourth Scenario with Missing Data

The goal of this scenario is to evaluate all the algorithms when the MU measurements are corrupted by missing data. Missing data may result from temporary communication failures and is often identified via error detection schemes associated with communication protocols.

To model missing data, it is assumed that the amount of measured data has reached zero, the zeroing of this data is detected by telecommunication protocols, and with the detection of missing data, the modified state estimation

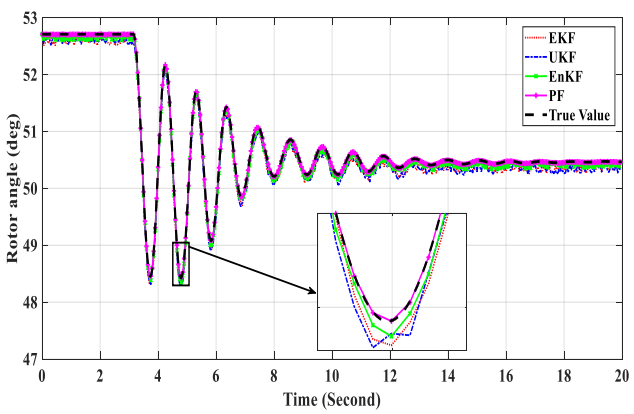

Fig. 11. The dynamic estimation of rotor angle with four studied filters for the three-phase fault on line 13-14

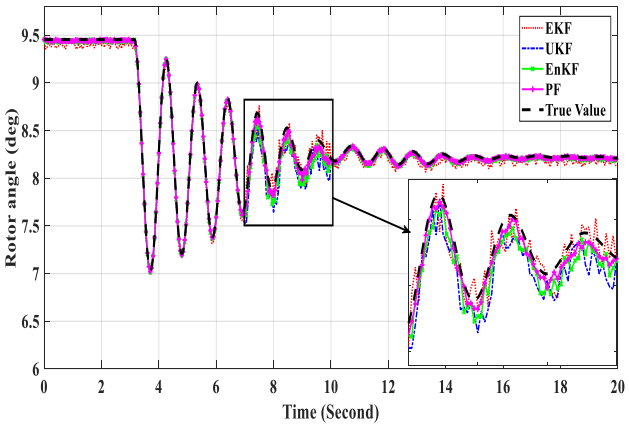

Fig. 12. The dynamic estimation of rotor angle with four studied filters for the data missing in the time of 7 to 8 seconds

algorithm is replaced instead of the original state estimation. As soon as a missing data is detected, the sampling frequency is reduced by about 8 times for higher accuracy, and the pseudo-measurement values obtained by linear interpolation between the samples before and after the event are replaced [27]. In this scenario, the sampling rate is increased from 25 sample/cycle to 200 sample/cycle.

The process noise covariance Q_d is reduced to 1/8 and R_d remains the same as in scenario previous. The. All the other setup remains the same as that in previous scenarios.
The full description of interpolation is given in [27].

To simulate missing data, all measurement data between the 7 to 10 seconds is zeroed.

Fig. 12 shows the estimation of the rotor angle generator one (G01) with the above methods with missing data in 7 to 10 seconds.

As it is clear in Fig.12, with the linear interpolation method, almost all filters are resistant to data missing, and PF filter works better than other filters.

B. The Fifth Scenario

One of the most important issues in DSE is the computation time of each state estimation iteration. For this, the tic command is typed at the beginning of the for loop, and the toc command is typed at the end of the for loop in the MATLAB program. Then, the time obtained is divided by the number of repetitions of the loop, and the execution time of each filter is calculated for one state estimation. Fig. 13 shows the calculation execution time.

As is known, the execution time of the PF and EnKF filters is much longer than that of the EKF and UKF filters, and it is worth mentioning that EKF has the shortest possible time.

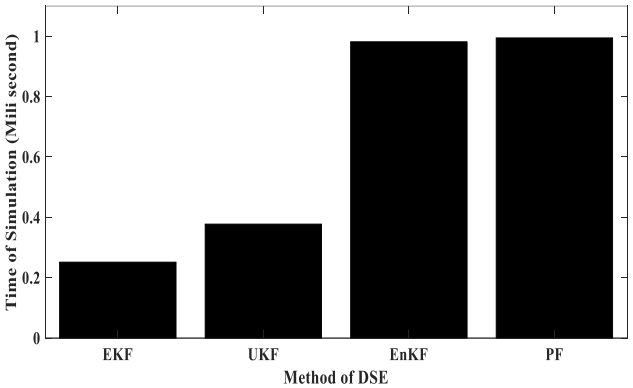

Fig. 13. The computation time of each state estimation iteration

C. The Sixth Scenario

In most previous works, the phasor domain method and PMU have been used for DSE. The purpose of this scenario is to compare the time domain method with the phasor domain method.

In the phasor domain method, the data obtained from the voltage transformer (VT) and current transformer (CT) installed in the generator terminal are first converted into discrete values, and then using the discrete Fourier transform (DFT), the phasor values are extracted from Eq. (52), and these phasor values are used as inputs to state estimation filters.

$$\bar{X} = X_r + jX_i = \frac{\sqrt{2}}{N}\sum_{i=1}^{N}(x_n cos\frac{2n\pi}{N} + jx_n sin\frac{2n\pi}{N}) \quad (52)$$

It should be mentioned that the third scenario (fault on 55-56 line) is repeated in this part.

Fig. 14 shows the performance of four desired filter types with the PMU.

By comparing Figs. 11 and 14 that scenario is the same in both cases, as it is clear, due to the long time of the phasor construction stage by PMU in the phasor method, the accuracy of the phasor method during extreme transients is lower in all filters compared to the time domain method.

By performing this scenario, it is observed that the time domain method performs better in transient states than the previous methods. It should be noted that almost the same results were obtained for other generators.

I. Conclusion

The contribution of this article is the use of DSE algorithms in the time domain with the presence of CBRs, which has not been done in the past. A 68-bus network with CBRs was simulated in the DIgSILNT software. Then, the current and voltage data in the time domain (sample values) related to each generator were extracted with MATLAB software format for six scenarios, including standard noise, extreme noise, network fault, execution time of state estimation, missing data, and comparison with previous methods, and four filters mentioned were implemented on these data. Finally, the related state variables of each generator were estimated. The results are summarized below.

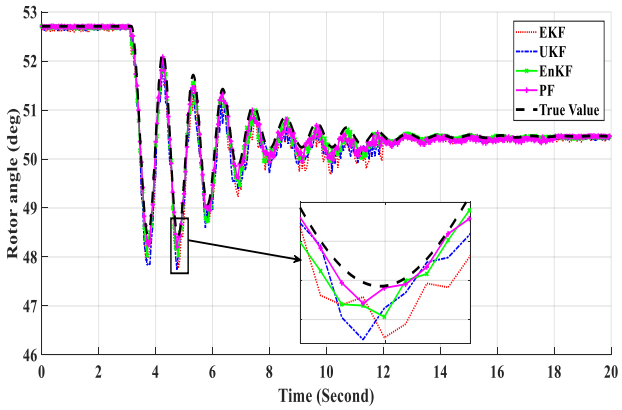

Fig. 14. The performance of four desired filter types with the phasor domain method

Almost all filters detected the state variables correctly, but among them, PF had fewer changes in the steady state of the estimator, and the time to reach the steady state (true state) was shorter. Extreme noise had a lower effect on PF performance. Among the above filters, the duration of PF and EnKF was much longer than that of other filters, which is considered a defect. All filters were resistant to the data-missing scenario, and PF and EnKF performed better than the other filters. The execution time of EKF was shorter than all filters, and it had relatively good performance, which is considered an advantage. Finally, the new DSE was validated by comparing the time domain method and the phasor domain method. The simulations showed that the time domain method performed better in severe transients.

By stating the advantages and disadvantages of each filter and considering the cost required to build each estimator, a balance should be established between these features. For such large networks where CBRs are available, the most favorable filter should be selected by placing MUs in it, so that all state variables related to the generator are properly available.

Future work

What is intended as a new work in the future is the use of state estimation algorithms along with machine learning in distribution and transmission networks.
Another future work is eating is using improved state estimation algorithms.

Another work that can be considered for the continuation of this article is to compare the performance of state estimation methods with control strategies.

REFERENCES

[1] Y. Liu *et al.*, "Dynamic State Estimation for Power System

Control and Protection," *IEEE Transactions on Power Systems*, vol. 36, no. 6, pp. 5909-5921, Nov. 2021.

[2] V. Telukunta, J. Pradhan, A. Agrawal, M. Singh and S. G. Srivani, "Protection challenges under bulk penetration of renewable energy resources in power systems: A review," *CSEE Journal Power Energy Syst.*, vol. 3, no. 4, pp. 365-379, Dec. 2017.

[3] J. Barati, S. Ghodratollah Seifossadat, and M. Joorabian, "Coordination of Adaptive Distance Protection in Transmission and Wind farm Collector Lines under Resistive Fault Conditions," in *International Journal of Industrial Electronics, Control and Optimization*, vol. 3, no. 3, pp. 223-234, July 2020

[4] S. Abazari, "Novel Non-Linear Control of DFIG and SSSC for Stability Increment of Power System," in *International Journal of Industrial Electronics, Control and Optimization*, vol. 7, no. 1, pp. 1-14, March 2024.

[5] N. Hatziargyriou *et al*., "Definition and classification of power system stability revisited & extended,", in *IEEE Transactions on Power Systems*, vol. 36, no. 4, July 2021.

[6] Zhao *et al*., "Power System Dynamic State Estimation: Motivations, Definitions, Methodologies, and Future Work," in *IEEE Transactions on Power Systems*, vol. 34, no. 4, pp. 3188-3198, July 2019.

[7] M. Baechle, V. Knazkins, M. Larsson and P. Korba, "Improved rotor angular speed measurement — A key for proper power grid stabilization," in *2014 IEEE PES General Meeting | Conference & Exposition*, National Harbor, MD, USA, 2014, pp. 1-5.

[8] J. Zhao, *et al*., "Roles of dynamic state estimation in power system modeling, monitoring and operation," in *IEEE Transactions on Power Systems*, 2020.

[9] M. A. Pai, D. P. Sen Gupta, K. R. Padiyar "Small Signal Analysis of Power Systems," in Harrow, U.K: Alpha Science International, 2004.

[10] P. DeRusso, R. Roy, C. Close, A. Desrochers "State Variables for Engineers," 2nd ed. Hoboken, NJ, USA: Wiley, 1998.

[11] C. Wang, Z. Qin, Y. Hou and J. Yan, "Multi-Area Dynamic State Estimation with PMU Measurements by an Equality Constrained Extended Kalman Filter," in *IEEE Transactions on Smart Grid*, vol. 9, no. 2, pp. 900-910, March 2018.

[12] E. Ghahremani, I. Kamwa, "Online state estimation of a synchronous generator using unscented Kalman met phasor measurements units," in *IEEE Transactions on Energy Conversion*, vol. 26, no. 4, pp. 1099-1108, 2011.

[13] N. Zhou, D. Meng and S. Lu, "Estimation of the Dynamic States of Synchronous Machines Using an Extended Particle Filter," in *IEEE Transactions on Power Systems*, vol. 28, no. 4, pp. 4152-4161, Nov. 2013.

[14] L. Lin, Linawati, Lie Jasa and E. Ambikairajah, "A hybrid state estimation scheme for power systems," in *Asia-Pacific Conference on Circuits and Systems*, Denpasar, Indonesia, 2002, pp. 555-558 vol.1.

[15] A. K. Single and B. C. Pal "Decentralized dynamic state estimation in power systems using unscented transformation," in *IEEE Transaction on Power Systems*, vol. 29, no. 2, pp. 794-804, 2014.

[16] H. Fasih, S. Tavakoli, J. Sadeghi and Hamed Torabi, "Kalman Filter-Smoothed Random Walk Based Centralized Controller for Multi-Input Multi-Output Processes," in *International Journal of Industrial Electronics, Control and Optimization*, vol. 2, no. 2, pp. 155-166, April 2019.

[17] R. Havangi, M. Moradi, "PSO-Based EKF Wheel-Rail Adhesion Estimation," in *International Journal of Industrial Electronics, Control and Optimization*, vol. 6, no. 1, pp. 49-62, March 2023.

[18] G. Durgaprasad and S. S. Thakur, "Robust dynamic state estimation of power systems based on M-Estimation and realistic modeling of system dynamics," in *IEEE Transactions on Power Systems*, vol. 13, no. 4, pp. 1331-1336, Nov. 1998.

[19] J. Zhao, M. Netto and L. Mili, "A Robust Iterated Extended Kalman Filter for Power System Dynamic State Estimation," in *IEEE Transactions on Power Systems*, vol. 32, no. 4, pp. 3205-3216, July 2017.

[20] J. Zhao and L. Mili, "A Decentralized H-Infinity Unscented Kalman Filter for Dynamic State Estimation Against Uncertainties," in *IEEE Transactions on Smart Grid*, vol. 10, no. 5, pp. 4870-4880, Sept. 2019.

[21] J. Zhao and L. Mili, "Robust Power System Dynamic State Estimator with Non-Gaussian Measurement Noise: Part II -Theory," arXiv preprint, 1703.04790, 2017.

[22] E. Ghahremani and I. Kamwa, "Dynamic State Estimation in Power System by Applying the Extended Kalman Filter With Unknown Inputs to Phasor Measurements," in *IEEE Transactions on Power Systems*, vol. 26, no. 4, pp. 2556-2566, Nov. 2011.

[23] J. Zhao and L. Mili, "A Framework for Robust Hybrid State Estimation with Unknown Measurement Noise Statistics," in *IEEE Transactions on Industrial Informatics*, vol. 14, no. 5, pp. 1866-1875, May 2018.

[24] A. Rouhani and A. Abur, "Constrained Iterated Unscented Kalman Filter for Dynamic State and Parameter Estimation, " in *IEEE Transactions on Power Systems*, vol. 33, no. 3, pp. 2404-2414, May 2018.

[25] S. A. A. Shahriari, M. Raoofat, M. Dehghani, M. Mohammadi, and M. Saad, "Dynamic state estimation of a permanent magnet synchronous generator-based wind turbine," in *IET Renewable Power Generation*, vol. 10, pp. 1278-1286, 2016.

[26] S. Yu, K. Emami, T. Fernando, H. H. C. Iu and K. P. Wong, "State Estimation of Doubly Fed Induction Generator Wind Turbine in Complex Power Systems," in *IEEE Transactions on Power Systems*, vol. 31, no. 6, pp. 4935-4944, Nov. 2016.

[27] N. Zhou, D. Meng, Z. Huang and G. Welch, "Dynamic State Estimation of a Synchronous Machine Using PMU Data: A Comparative Study, " in *IEEE Transactions on Smart Grid*, vol. 6, no. 1, pp. 450-460, Jan. 2015.

[28] P. Kundur, *Power System Stability and Control* . New York,

NY, USA: McGraw-Hill, 1994.

[29] J. H. Gove, D. Y. Hollinger "Application of a dual unscented Kalman filter for simultaneous state and parameter estimation in problems of surface-atmosphere exchange, " in *JOURNAL OF GEOPHYSICAL RESEARCH*, VOL. 111, D08S07, 2006.

[30] G. Evensen, "Sequential data assimilation with a nonlinear quasigeostrophic model using Monte Carlo methods to forecast error statistics, " in *J. Geophys. Res.*, vol. 99, no. C5, pp. 143–162, May 1994.

[31] G. Anagnostou, L. P. Kunjumuhammed and B. C. Pal, "Dynamic State Estimation for Wind Turbine Models with Unknown Wind Velocity, " in *IEEE Transactions on Power Systems*, vol. 34, no. 5, pp. 3879-3890, Sept. 2019.

[32] S. A. A. Shahriari, M. Raoofat, M. Mohammadi, M. Dehghani, M. Saad, "Dynamic state estimation of a doubly fed induction generator based on a comprehensive nonlinear model," in *Simulation Modelling Practice and Theory*, Volume 69, 2016, Pages 92-112.

Saeed Javadi was born in Kermanshah, Iran. He received his B.E. degree in Electrical Power Engineering from Ilam University, Ilam, Iran, in 2013 and his M.Sc. degree in Electrical Power Engineering from Razi University, Kermanshah, Iran, in 2015. He is currently a Ph.D. student in Electrical Power Engineering at Kurdistan University, Sanandaj, Iran. His current research interests include dynamics, control, and protection of power systems.

Ali Hesami Naghshbandi was born in Sanandaj, Iran. He received his B.S., M.S., and Ph.D. degrees in Electrical Power Engineering from the Iran University of Science & Technology Tehran, Iran, in 1995, 2002, and 2009 respectively. He is currently an Associate Professor at University of Kurdistan, Sanandaj, Iran. His research interests are power system dynamics, stability and control.

International Journal Of
Industrial Electronics Control and Optimization
Print ISSN: 3517-2645
Online ISSN: 3568-2645
Homepage: https://ieco.usb.ac.ir/

Study on a Non-Isolated High Step-Up SEPIC-Based DC-DC Converter with Continuous Input Current for Photovoltaic Applications

Mahdi Elmi | Mohamad Reza Banaei | Hadi Afsharirad

Department of Electrical Engineering, Azarbaijan Shahid Madani University, Tabriz, Iran.[1,2,3]
Corresponding author's email: m.banaei@azaruniv.ac.ir

Article Info

Article type:
Research Article

Article history:
Received: 05-May-2024
Received in revised form: 13-July-2024
Accepted: 29-July-2024
Published online: 21-March-2025

Keywords:
Continuous input current,
High step-up,
Non-isolated DC-DC converter,
Photovoltaic application,
SEPIC-based structure

ABSTRACT

This paper aims to present, study, and analyze a novel non-isolated high step-up SEPIC-based DC-DC converter for photovoltaic applications. The proposed structure is drafted from the SEPIC converter. A two-winding coupled inductor and an improved voltage multiplier cell are utilized to achieve a high voltage conversion ratio. Moreover, a passive voltage clamp is employed to recycle the stored energy in the leakage inductance of the coupled inductor and reduce the voltage stress on the switch. Hence, a switch with low on-resistance could be used. Since all diodes turn off under ZCS conditions, their reverse recovery problems are alleviated. High efficiency, continuous input current, and low cost and size are the other merits of the presented structure, making it a promising solution for photovoltaic systems. At the end, the proposed converter is compared with several DC-DC structures to prove its advantages over the converters presented before. To verify the performance of the designed topology, a 200-W laboratory prototype is implemented and experimental results are depicted. The Results validate the practicability and functionality of the proposed structure for photovoltaic applications.

I. Introduction

Nowadays, a large proportion of electricity used around the world is generated by burning fossil fuels. However, their sources are limited and over-consumption could lead to severe environmental damages such as air pollution and greenhouse emissions. The aforementioned problems along with the capability of renewable energy sources (RESs) to generate clean electricity have led governments and researchers to increase their contribution to electric production [1], [2].

Thanks to energy policies for supporting low or zero-carbon infrastructures, the deployment of photovoltaic (PV) systems has increased significantly in the last decades. High reliability, low maintenance cost, long life span, environmental friendliness, zero or low emissions, and noise are some unique properties of PV systems [3], [4]. However, the voltage provided by PV panels is relatively low in amplitude. Hence, the interfacing DC-DC converters with high voltage gains are utilized to link PV panels to grid-connected inverters [5]- [7]. The other essential requirement in designing DC-DC converters for PV applications is draining continuous current with minimum ripple. Otherwise, the maximum power point tracking (MPPT) algorithm might not operate efficiently [8], [9]. To this end, authors in [10] and [11] have presented a couple of ripple-free non-isolated DC-DC converters for RES applications. In both presented structures, an inductor is in series with an input voltage source to achieve the minimum input current ripple. However, they suffer from low voltage gain which makes them unsuitable for PV applications.

Generally, DC-DC converters which are employed in PV applications could be categorized in two classes including isolated and non-isolated structures. Isolated configurations are mainly based on multi-winding transformers. However,

utilizing the power transformer reduces the efficiency and increases the converter weight and volume [12], [13]. Compared to isolated structures, non-isolated converters share a common ground between the input source and the load. Moreover, they are not isolated electrically. Non-isolated converters are derived from either conventional structures like buck, boost, and buck-boost converters or developed configurations such as Single-ended primary-inductor converter (SEPIC), Ćuk, and Zeta converters [14], [15].

The power circuit of the SEPIC topology is depicted in Fig. 1. Continuous input current and shared common ground between the input source, the load, and the main switch are outstanding characteristics of the SEPIC structure. However, the voltage gain is still low for PV applications.

In literature, a few techniques have been addressed to enhance voltage gains of DC-DC converters. Switched inductors and capacitors, Z-source and quasi Z-source, voltage lift, and voltage multiplier cells are some of the well-known methods [16]- [19]. Another method that researchers use to increase voltage gains of DC-DC converters is utilizing coupled inductors (CIs). In [20], a SEPIC-based DC-DC structure with a CI is studied. Continuous input current and high voltage gain are significant characteristics of the presented topology. Moreover, the energy stored in the leakage inductance of the CI is recycled by a passive voltage clamp. Authors have presented another CI-based converter in [21]. Output voltage level is boosted by using a CI and a voltage multiplier cell. Since a switch is in series with the input voltage source, the input current is not continuous. Hence, it might not be a practical solution to achieve MPPT in PV applications.

In [22], another high step-up DC-DC converter based on CI and switched inductor is presented. The converter benefits from a high voltage conversion ratio. However, regarding the total numbers of components, achieved voltage gain is not suitable. Moreover, the input current ripple is high which makes it unpromising for PV applications.

According to Fig. 1, the main features of a high gain SEPIC-based DC-DC structure could be summarized as: 1) High voltage gain could be obtained by utilization of a CI, 2) Thanks to the presence of two inductors in SEPIC structure, input inductor could be utilized to guarantee that input current is continuous and the inductor L_2 can be converted to a CI, 3) Due to low current ripple in the primary section of the converter, the root mean square (RMS) value of current that is flowing through the switch is significantly reduced, 4) As the average current of second inductor L_2 is low, the average current of the replaced CI will be low and as a result, a small core could be chosen.

This study is devoted to presenting, studying, and analyzing make it a promising solution for PV systems. High voltage gain is attained by utilizing a CI along with an improved

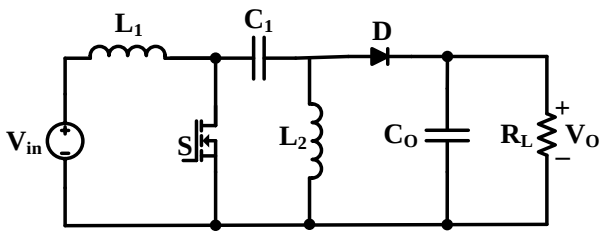

Fig. 1. The Power circuit of the SEPIC structure

voltage multiplier module. Capacitors of the voltage multiplier module are charged by both the primary and secondary sides of CI. Meanwhile, to recycle stored energy in the leakage inductance of the CI, a passive voltage clamp is used. Hence, the voltage across the switch is reduced remarkably, and a low on-resistance (R_{DS-ON}) switch could be utilized. As a result, the structure's cost and conduction power dissipation will be reduced and the efficiency of the proposed converter will be increased. Besides, thanks to the soft switching performance of all diodes at turn-off instant, their reverse recovery problems are eliminated.

II. Operating Principles and Steady State Analysis of the Proposed Converter

Fig. 2 shows the equivalent circuit of the designed high step-up SEPIC-based DC-DC converter. As illustrated in this figure, the presented structure includes a switch S, an input inductor L_{in}, one CI with a turns ratio of n, three capacitors C_1-C_3, an output capacitor C_O, and three diodes D_1-D_3. The capacitor C_2 along with the diode D_1 form the passive voltage clamp. Moreover, an improved voltage multiplier module is employed to enhance the voltage conversion ratio of the presented converter. As depicted in this figure and unlike most conventional DC-DC converters in which the voltage multiplier cell is charged only by the secondary side of the CI, the capacitor C_3 is charged by both primary and secondary windings of the CI.

To simplify the steady-state analysis of the structure, the CI with a turns ratio of $n=N_s/N_p$ is modelled by an ideal transformer that its primary winding is in parallel with magnetizing inductance L_m and in series with the leakage inductance L_k. Moreover, it is assumed that: 1) All capacitors and inductors are large enough without any ripple in their voltages and currents, respectively. 2) All semiconductor components are ideal without parasitic components.

The operating principles of the studied structure in continuous conduction mode (CCM) include five time periods. Current flow paths and main waveforms of operating modes are illustrated in Fig. 3 and Fig. 4, respectively. Operating modes and relative steady-state analysis are explained as follows.

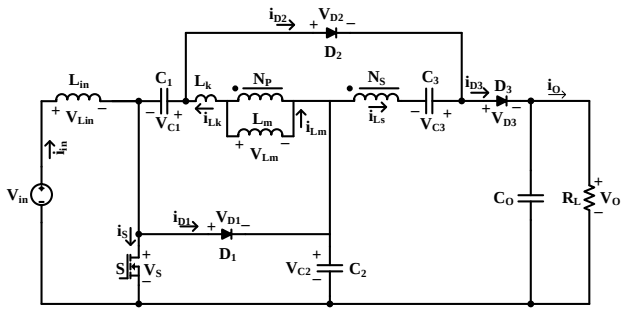

Fig. 2. Equivalent circuit of the presented structure

***Mode I [t_0-t_1]*:** The first mode begins when the switch S is turned on under the ZCS condition at $t=t_0$. Due to the leakage inductance of CI, the diode D_2 is still conducting. While diodes D_1 and D_3 are in off-state. Meanwhile, the input voltage source charges the input inductor L_{in} through the switch S. Since the diode D_3 is biased reversely, the output capacitor C_O supplies energy to the load. Meanwhile, the capacitor C_1 and both sides of the CI charge capacitors C_2 and C_3 through the diode D_2. This mode ends when currents flowing through leakage and magnetizing inductances of CI are equal at $t=t_1$. The following equation could be given for the current flowing through the CI.

$$i_{Lk} = \frac{1}{L_K}\int\left(V_{C2} - V_{C1} + \frac{V_{C3}}{1+n}\right)dt \tag{1}$$

As the voltage across the CI is high and L_k has a low value, the slope of this current is sharp. Hence, the duration of this mode is too short. The relative current-flow path of this mode is depicted in Fig. 3(a).

***Mode II [t_1-t_2]*:** This mode begins when diode D_2 turns off under ZCS condition at $t=t_1$. During this mode, the switch S remains on. Meanwhile, input current increases linearly like mode I. Furthermore, the capacitor C_2 charges both the capacitor C_1 and the CI through the switch S. Energy stored in capacitors C_2 and C_3 along with the CI are transferred to the output capacitor C_O and the load through the diode D_3. This mode ends when the switch S is turned off at $t=t_2$. Fig. 3(b) shows the relative current-flow path. The following equations could be obtained for this mode.

$$v_{Lin} = V_{in} \tag{2}$$

$$v_{Lm} = V_{C1} - V_{C2} \tag{3}$$

$$i_s = i_{in} + i_{Lk} \tag{4}$$

$$n\left(V_{C2} - V_{C1}\right) = V_O - V_{C2} - V_{C3} \tag{5}$$

Mode III [t_2-t_3]: As depicted in Fig. 3(c), the switch S is turned off at the beginning of this mode and the clamp diode D_1 is forward biased simultaneously at $t=t_2$. Consequently, voltage across the switch S is equal with the voltage of capacitor C_2. Moreover, the clamp diode D_1 provides a path to recycle the energy stored in the leakage inductance of the CI. During this mode, the diodes D_2 and D_3 are off and on, respectively. Meanwhile, the energy of input inductor L_{in} is transferred to both the CI and the capacitor C_2. The secondary side of the CI along with the capacitor C_3 supplies energy of the output capacitor C_O and the load. This mode ends when the current which is flowing through secondary side of the CI reaches zero at $t=t_3$. Hence the diode D_3 will turn off under ZCS condition. The following equation could be achieved for the current of the CI.

$$i_{Lk} = \frac{1}{L_K}\int\left(\frac{V_O - V_{C2} - V_{C3}}{n} - V_{C1}\right)dt \tag{6}$$

Since the voltage across the CI is high and L_k has a low value, the slope of this current is sharp. Hence, like mode I, the duration of this mode is too short.

Mode IV [t_3-t_4]: At the beginning of this mode, the diode D_3 is reverse-biased under the ZCS condition. Hence, its reverse recovery problem is eliminated. During this period, diodes D_1 and D_2 are in on-state. Meanwhile, switch S remains off. The energies stored in both input inductor L_{in} and the CI are transferred to capacitors C_2 and C_3. The output capacitor C_O supplies the load. This mode ends when the current which is flowing through the clamp diode D_1 reaches zero at $t=t_4$. Fig. 3(d) shows the relative current-flow path of this mode. The following equations could be formulated for this mode.

$$v_{Lin} = V_{in} - V_{C2} \tag{7}$$

$$v_{Lm} = V_{C1} \tag{8}$$

$$V_{C1} = \frac{V_{C3}}{n+1} \tag{9}$$

Mode V [t_4-t_5]: The last mode begins when clamp diode D_1 is reverse-biased under ZCS condition at $t=t_4$. During this time interval, the switch S and the output diode D_3 are in off-state as well. Meanwhile, the diode D_2 is conducting and energy of both sides of the CI is transferred to the capacitor C_3. Furthermore, the output capacitor C_O supplies the load. The current of input inductor L_{in} declines linearly like in mode IV. Fig. 3(e) shows the relative current-flow path of this mode.

To simplify the steady-state analysis of the proposed structure, short time durations that happen in one complete switching cycle are neglected. Moreover, the voltages of capacitors are presumed to be constant without any ripple.

Employing principle of volt-second balance on inductors in different modes, following equations could be obtained.

$$\langle v_{Lin} \rangle = 0 \Rightarrow V_{C2} = \frac{V_{in}}{1-D} \tag{10}$$

$$\langle v_{Lm} \rangle = 0 \Rightarrow V_{C1} = DV_{C2} \Rightarrow V_{C1} = \frac{DV_{in}}{1-D} \tag{11}$$

Where $\langle v_{Lin} \rangle$ and $\langle v_{Lm} \rangle$ are the average voltage values of input inductor L_{in} and magnetizing inductance of the CI in one complete switching cycle, respectively. Substituting (11) into (9), the voltage of capacitor C_3 could be obtained as:

$$V_{C3} = \frac{(n+1)DV_{in}}{1-D} \tag{12}$$

Substituting (10), (11) and (12) into (5), yields to:

$$M_{CCM} = \frac{V_O}{V_{in}} = \frac{n+1+D}{1-D} \tag{13}$$

It's worth mentioning that since the current that is flowing through the CI is low, influence of leakage inductance of the CI on the voltage conversion ratio is low and ignorable [20].

III. Design of Proposed Converter

Determining voltage and current stresses on semiconductors is crucial in designing the converter. According to Fig. 3, voltage stresses on semiconductors could be formulated as:

$$V_{S,peak} = V_{D1,peak} = V_{C2} = \frac{DV_{in}}{1-D} \tag{14}$$

$$V_{D2,peak} = V_{D3,peak} = V_O - V_{C1} = \frac{(n+D)V_{in}}{1-D} \tag{15}$$

Current which is flowing through the capacitor C_1 could be given by:

$$i_{C1} = \begin{cases} I_{Lm} + ni_{D3} & 0 < t \le DT_S \\ i_{D1} - I_{in} & DT_S < t \le T_S \end{cases} \tag{16}$$

By utilizing the principle of amp-second balance on the capacitor C_1, average current of magnetizing inductance of the CI could be calculated as follows.

$$\begin{aligned} &\langle i_{C1} \rangle = 0 \Rightarrow DI_{Lm} + (n+1)I_O - (1-D)I_{in} = 0 \\ &\Rightarrow I_{Lm} = I_O \end{aligned} \tag{17}$$

It could be proved that the average current values of all diodes are equal to the load current I_O. Thus, by neglecting mode III, the duration of mode IV can be achieved as follows.

$$\langle i_{D1} \rangle = I_O \Rightarrow \frac{I_{in} d_4}{2} = I_O \Rightarrow d_4 = \frac{2}{M_{CCM}} \tag{18}$$

Where d_4 is the time length of mode IV. Maximum current values of diodes D_2 and D_3 could be given by:

$$\langle i_{D2} \rangle = I_O \Rightarrow \frac{i_{D3,peak} D}{2} = I_O \Rightarrow i_{D3,peak} = \frac{2I_O}{D} \tag{19}$$

$$\begin{aligned} &\langle i_{D2} \rangle = I_O \Rightarrow \frac{i_{D2,peak}\left(1-D+(1-D-d_4)\right)}{2} = I_O \\ &\Rightarrow i_{D2,peak} = \frac{2I_O}{2(1-D)-d_4} \end{aligned} \tag{20}$$

According to Fig. 3(b), the following equation could be achieved for the current stresses of switch S and diode D_1.

$$i_{D1,peak} = i_{S,peak} = i_{in,peak} + i_{Lm,peak} + ni_{D3,peak} \tag{21}$$

Substituting (17) and (19) into (21), yields to:

$$i_{D1,peak} = i_{S,peak} = \frac{2n+(2-n)D}{D(1-D)} I_O \tag{22}$$

According to [20], operating a converter in discontinuous conduction mode has major drawbacks including slow dynamic response, high current stress of semiconductors, the dependence of the converter on switching frequency, output power, and inductors. Hence, in order to guarantee the CCM

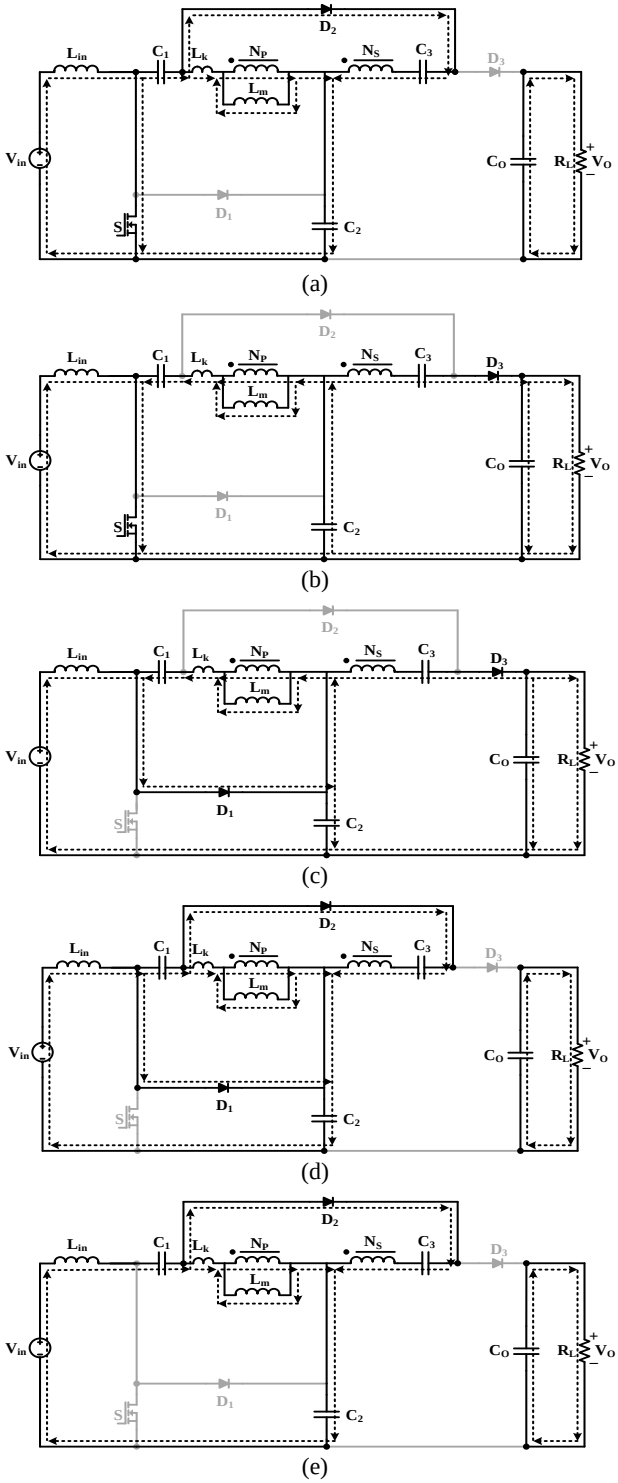

Fig. 3. Current-flow path of operating modes in one switching time interval at CCM operation. (a) Mode I, (b) Mode II, (c) Mode III, (d) Mode IV, (e) Mode V.

operation of the proposed structure, the average current values of inductors L_{in} and L_m have to be more than half of their ripples. Current ripples of inductors could be given by:

$$\Delta i_{in} = \frac{V_{in} D}{L_{in} f_S} \quad (23)$$

$$\Delta i_{Lm} = \frac{(V_{C1} - V_{C2}) D}{L_m f_S} = \frac{V_{in} D}{L_m f_S} \quad (24)$$

To guarantee the CCM operation of the presented structure, the following inequalities have to be satisfied:

$$I_{in} \geq \frac{\Delta i_{in}}{2} \Rightarrow L_{in} \geq \frac{R_L}{2 f_S M_{CCM}} \quad (25)$$

$$I_{Lm} \geq \frac{\Delta i_{Lm}}{2} \Rightarrow L_m \geq \frac{R_L}{2 f_S M_{CCM}} \quad (26)$$

IV. Comparison Study

The proposed converter and some other structures presented before are compared in terms of the type of switching, continuity of input current, number of elements, voltage gain, and voltage stresses on semiconductors in Table 1. Moreover, voltage gains of some structures in Table 1 as a function of duty ratio are depicted in Fig. 5. As shown in this figure, when duty ratio D is less or equal to 0.62, the voltage gain of the designed topology is more than other structures. For duty ratios of more than 0.62, converters presented in [5] and [17] have higher voltage gains. However, hard switching performances of converters in [5] and [17] result in higher switching losses and lower efficiency. Meanwhile, voltage stresses on the switches of both converters are higher than the proposed converter.

In addition to normalized voltage stress on switches and diodes, the other method to evaluate voltage stresses on semiconductors is component stress factor (CSF) analysis. This procedure is similar to component load factor (CLF) analysis. However, they differ in how total and individual component factors are calculated. The CSF method considers the maximum voltage on components of the structure and root mean square (RMS) values of currents flowing through them in a specific set of conditions and output power. Consequently, it gives a quantitative measure of converter performance [23].

To apply CSF analysis, it is assumed that the converters under study have the same resources of silicon, magnetic winding area, and capacitor volume. Hence, CSF analysis consists of three different parts: Semiconductor component stress factor (SCSF), winding component stress factor (WCSF), and capacitor component stress factor (CCSF). These parameters could be formulated as follows [24].

Where N_S, N_W, and N_C symbolize numbers of semiconductors, inductors, and capacitors, respectively. To reduce the complexity of the analysis, it is assumed that: 1) capacitors and inductors are large enough without any ripples in voltages and currents, respectively and 2) there is no power dissipation in components of the converter.

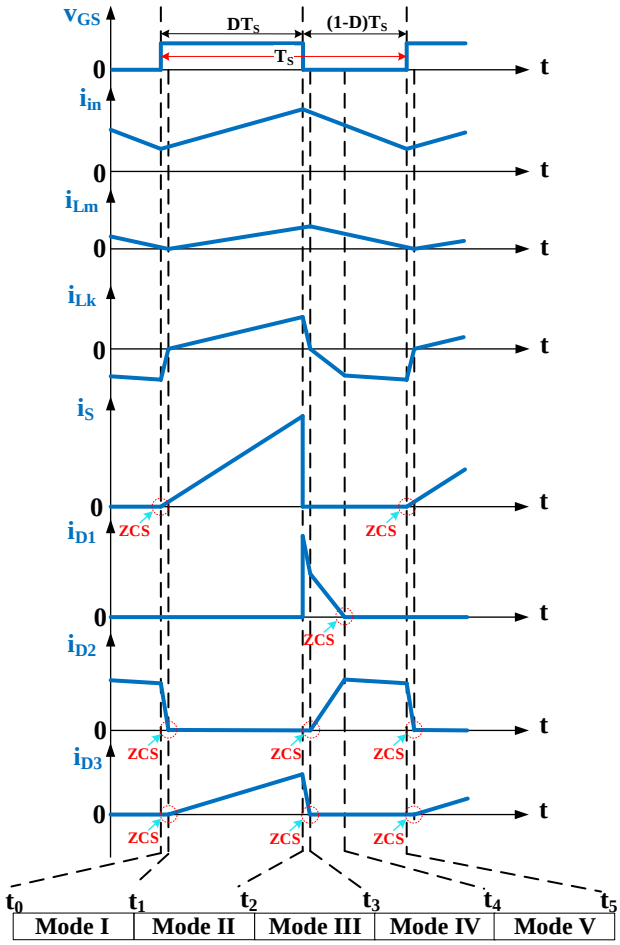

Fig. 4. Typical current waveforms of presented structure at CCM operation

$$SCSF_i = \frac{\sum_j W_j}{W_i} \cdot \frac{V_{\max}^2 . I_{rms}^2}{P_O^2} \quad (27)$$

$$WCSF_i = \frac{\sum_j W_j}{W_i} \cdot \frac{V_{\max}^2 . I_{rms}^2}{P_O^2} \quad (28)$$

$$CCSF_i = \frac{\sum_j W_j}{W_i} \cdot \frac{V_{pk}^2 . I_{rms}^2}{P_O^2} \quad (29)$$

$$SCSF = \sum_{N_s} SCSF_i \quad (30)$$

$$WCSF = \sum_{N_w} WCSF_i \quad (31)$$

$$CCSF = \sum_{N_C} CCSF_i \quad (32)$$

In Fig. 6, the normalized voltage stress on the switch of the presented structure is compared with other structures. As depicted in this figure, voltage stress across the main switch of the presented structure is less than all other topologies. Moreover, only converters presented in [12], [16] and [20] utilize ZCS switching beside the presented structure. Hence, the designed structure will have lower switching losses in

comparison with the converters mentioned in Table 1. In Fig. 7, the total amount of normalized voltage stresses on the diodes of the designed structure and some of the converters in Table 1 are compared. As illustrated in this figure, converters presented in [10], [16] and [17] have lower values than designed topology. However, the converter in [16] utilizes two switches that enhances complexity, cost and volume of the structure. Moreover, converters in [10] and [16] suffer from low voltage conversion ratio using same number of elements.

In Fig. 8, the SCSF of the proposed converter and some of the structures mentioned in Table I are compared. The SCSF of each structure is calculated with the same weighting factor. For simplicity, the weighting coefficient $\Sigma_j W_j$ is assumed to be unit and distributed equally between the semiconductors of each converter. As illustrated in this figure, the designed topology has lower SCSF than the others.

Regarding the comparisons, the presented converter is a promising solution for PV applications. Simple structure, high voltage gain, continuous input current, and soft switching performance of semiconductors are main advantages of the proposed structure. In case higher voltage gains are required, other structures could be utilized. However, higher voltage gains result in an increased number of employed components or higher voltage stresses on semiconductors. Moreover, if the designed converter will operate in duty cycles lower than 0.5, the structure in [19] could be a better solution.

V. Efficiency Analysis

Major parameters in power losses of the converter are related to the switch, diodes, capacitors, and magnetic devices. Supposing that currents of inductors have no ripples, RMS and average values of inductor currents will be equal. In calculating efficiency and power losses of designed structure, short time modes I and III are neglected.

Switch losses include switching and conduction losses. The current of the switch S could be given by:

$$i_S = \frac{i_{S,peak}}{DT_S} \mathrm{t} \quad 0 \le t < DT_S \tag{33}$$

Where T_S is the switching period. Utilizing (33), the RMS value of the switch current could be obtained as:

$$I_{S,rms} = \left(\frac{2n + (2-n)D}{\sqrt{3D}(1-D)} \right) I_O \tag{34}$$

The second element in power loss calculation is the diode. Currents that are flowing through three diodes could be formulated as follows.

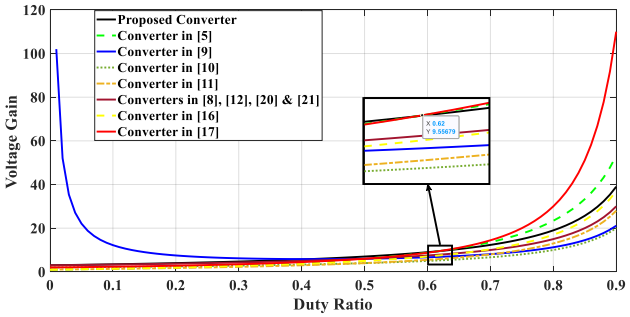

Fig. 5. Voltage conversion ratios of designed converter and topologies in [5], [8-12], [16-17] & [20-21]

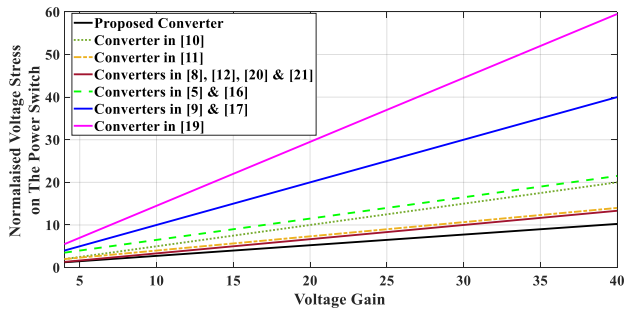

Fig. 6. Voltage stress on the switch of designed converter and topologies in [5], [8-12], [16-17] & [19-21]

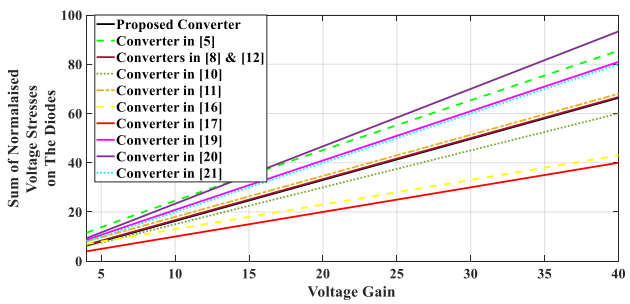

Fig. 7. Total amount of voltage stresses across diodes of the converter and converters in [5], [8-12], [16-17] & [19-21].

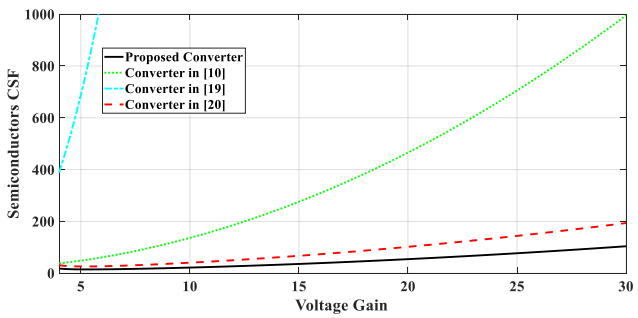

Fig. 8. Semiconductors CSF of proposed converter and structures in [10], [19] & [20]. n=2

TABLE 1 COMPARISON OF PRESENTED STRUCTURE WITH SOME HIGH GAIN DC-DC CONVERTERS PRESENTED BEFORE

Ref.	Number of Components					S.S	Low Input Current Ripple	Voltage Stress on Switch(es)	Voltage Gain	$\sum V_D$
	D	S	C	I/CI	T					
P.C	3	1	4	1/1[2W]	10	YES	YES	$\frac{M+1}{n+2}V_{in}$	$\frac{n+1+D}{1-D}$	$\left(2M-\frac{M+1}{n+1}\right)V_{in}$
[5]	4	1	3	1/1[2W]	10	NO	NO	$\frac{M}{D+1}V_{in}$	$\frac{1+nD}{1-D}(1+D)$	$\frac{4M}{D+1}V_{in}$
[8]	3	1	4	1/1[2W]	10	NO	YES	$\frac{M(n-1)}{2n-1}V_{in}$	$\frac{2n-1}{(n-1)(1-D)}$	$\frac{M(3n-1)}{2n-1}V_{in}$
[9]	3	2	3	2/0	10	NO	NO	MV_{in}	$\frac{1+D}{D(1-D)}$	$\frac{3D+1}{D(1-D)}V_{in}$
[10]	3	1	4	2/0	10	NO	YES	$\frac{M}{2}V_{in}$	$\frac{2}{1-D}$	$1.5MV_{in}$
[11]	2	1	3	1/1[2W]	8	NO	YES	$\frac{n+M}{n+1}V_{in}$	$\frac{nD+1}{1-D}$	$\left(\frac{M+n}{n+1}\right)\left(3+\frac{n(M-1)}{M+n}\right)V_{in}$
[12]	3	1	4	1/1[2W]	10	YES	YES	$\frac{M}{n+1}V_{in}$	$\frac{n+1}{1-D}$	$\frac{M(2n+1)}{n+1}V_I$
[16]	2	2	3	3/0	10	YES	NO	$\frac{M+3}{2}V_{in}$	$\frac{1+3D}{1-D}$	$(M+3)V_{in}$
[17]	3	2	3	2/0	10	NO	YES	$\left(\frac{M(1-D)}{2-D}+M-\frac{1}{1-D}\right)V_{in}$	$\frac{2-D_1}{(1-D_1)(1-D_2)}$	$\left(\frac{2M(1-D)}{2-D}+M-\frac{2}{1-D}\right)V_{in}$
[19]	3	1	3	3/0	10	NO	YES	$\frac{3M-1}{2}V_{in}$	$\frac{1}{1-2D}$	$\left(2M-1+\frac{2M}{M+1}\right)V_{in}$
[20]	3	1	3	0/1[3W]	8	YES	NO	$\frac{M+n_2-n_1}{1+n_2}V_{in}$	$\frac{1+n_1+(n_2-n_1)D}{1-D}$	$\frac{(M+n_2-n_1)(3+n_1+n_2)}{1+n_2}V_{in}$
[21]	3	1	3	0/1[2W]	8	NO	NO	$\frac{M}{n+1}V_{in}$	$\frac{n+1}{1-D}$	$2MV_{in}$

D: Diode, S: Switch, C: Capacitor, I: Inductor, CI: Coupled Inductor, S.S: Soft Switching, P.C: Proposed Converter

$$i_{D1}=i_{D1,peak}\left(1-\frac{t}{d_4T_S}\right)\quad DT_S\le t\le(D+d_4)T_S \tag{35}$$

$$i_{D2}=i_{D2,peak}\begin{cases}\dfrac{t}{d_4T_S} & DT_S\le t<(D+d_4)T_S\\ 1 & (D+d_4)T_S\le t<T_S\end{cases} \tag{36}$$

$$i_{D3}=i_{D3,peak}\left(\frac{t}{DT_S}\right)\quad 0\le t\le DT_S \tag{37}$$

By utilizing (35), (36), and (37), the RMS values of currents flowing through diodes could be achieved as:

$$I_{D1,rms}=\sqrt{\frac{d_4}{3}\left(\frac{2n+(2-n)D}{D(1-D)}\right)}I_O \tag{38}$$

$$I_{D2,rms}=\sqrt{1-D-\frac{4}{3M_{CCM}}\left(\frac{M_{CCM}}{n+D-1}\right)}I_O \tag{39}$$

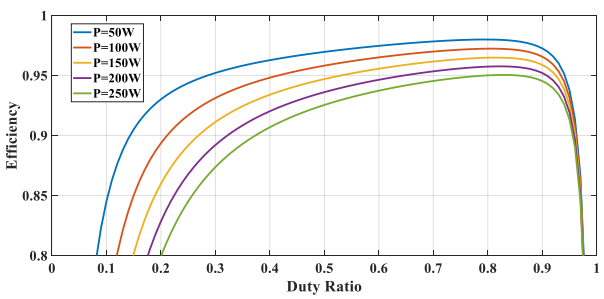

Fig. 9. Efficiency of designed structure versus duty ratio

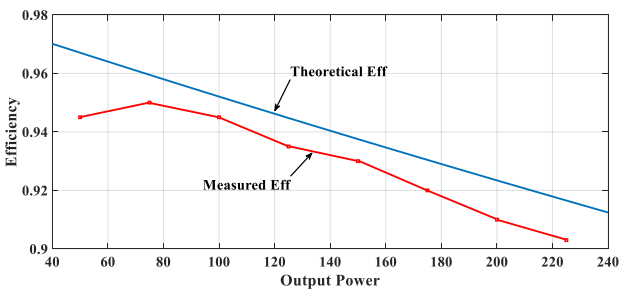

Fig. 10. Theoretical and measured efficiency of presented structure versus output power. n=2, r_C=r_D=10mΩ, r_L=20mΩ, R_{DS_ON}=40mΩ, C_S=600pF, V_F=1V, f_S=30kHz.

$$I_{D3,rms} = \frac{2I_O}{\sqrt{3D}} \tag{40}$$

Assuming that all diodes are similar, power dissipations in diodes could be formulated by:

$$P_D^{loss} = r_D \sum_{k=1}^{3} I_{Dk,rms}^2 + 3V_F I_O \tag{41}$$

Where $I_{Dk,rms}$ represents the RMS value of each diode current, and r_D and V_F are the conduction resistance and voltage drop of each diode, respectively. The RMS values of capacitor and inductor currents could be given by:

$$I_{C1,rms} = I_O \sqrt{\left(\frac{M_{CCM}D+2}{3}\right)\left(\frac{2n+(2-n)D}{D(1-D)}\right)^2 + M_{CCM}^2} \tag{42}$$

$$I_{C2,rms} = I_O \sqrt{\left(\frac{D}{3}\right)\left(\frac{2n+2-nD}{D(1-D)}\right)^2 + M_{CCM}^2} \tag{43}$$

$$I_{C3,rms} = I_O \sqrt{\left(1-D-\frac{4}{3M_{CCM}}\right)\left(\frac{M_{CCM}}{n+D-1}\right)^2 + \frac{4}{3D}} \tag{44}$$

$$I_{CO,rms} = I_O \sqrt{1+\frac{4}{3D}} \tag{45}$$

The RMS values of currents flowing through input inductor L_{in} and CI could be given as follows.

$$I_{Lin,rms} = MI_O \tag{46}$$

$$I_{Lk,rms} = I_O \sqrt{\left(\frac{M_{CCM}D+2}{3}\right)\left(\frac{2n+(2-n)D}{D(1-D)}\right)^2} + I_O \sqrt{\left(1-D-\frac{4}{3M_{CCM}}\right)\left(\frac{M_{CCM}}{n+D-1}\right)^2 + M_{CCM}^2} \tag{47}$$

According to [25], power dissipations in each component and total power losses in the presented converter could be calculated. Regarding [25], the efficiency of the proposed structure could be calculated as follows.

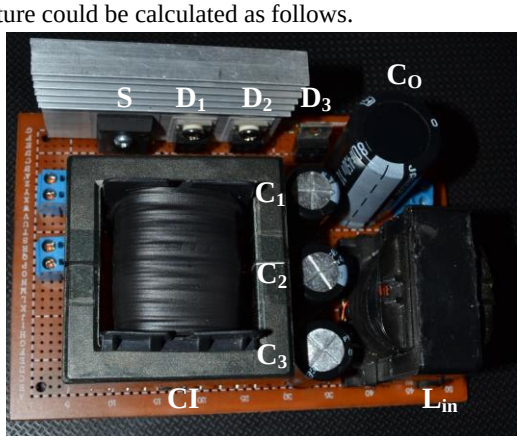

Fig. 11. Experimental prototype of presented structure

$$\eta = \frac{R_L}{2(r_L+r_C)M_{CCM}^2 + \frac{A_1}{3}\left(\frac{2n+(2-n)D}{D(1-D)}\right) + \frac{4}{3D}(r_D+3r_C)} + \frac{R_L}{A_2(r_C+r_L+r_D) + \left(1+\frac{3V_F}{V_O}\right)R_L + f_S C_S \left(\frac{DR_L}{n+1+D}\right)^2 + r_C} \tag{48}$$

Where r_L, r_C, and R_L represent the resistance of each inductor, the ESR of each capacitor, and the output load, respectively. Moreover, A_1 and A_2 are coefficients given by the following.

$$A_1 = D\left(R_{DS\_ON} + 2r_C + r_L\right) + \frac{2}{M_{CCM}}\left(r_D + r_C + r_L\right) \tag{49}$$

$$A_2 = \left(1-D-\frac{4}{3M_{CCM}}\right)\left(\frac{M_{CCM}}{n+D-1}\right)^2 \tag{50}$$

The theoretical efficiency of the designed topology versus duty ratio for some output power is shown in Fig. 9. As shown in this figure, the efficiency of the presented structure is more than 93% for duty ratios of more than 0.5 and output power up to 250 W. As the duty ratio increases, the efficiency of the structure gets higher as well. This trend continues for duty ratios less than 0.84.

In Fig. 10, the measured and calculated efficiency of the presented topology has been depicted. According to this figure, the converter has a maximum efficiency of 95% at the output power of 75 W.

VI. Experimental Results

To confirm the practicability of the proposed converter and theoretical analysis of the presented configuration, a 200-W converter operating at a switching frequency of 30 kHz is implemented. Fig. 11 shows the laboratory prototype of the presented structure. Different components of the converter are illustrated in this figure. Meanwhile, the specifications of the proposed prototype are listed in Table 2. As mentioned in this table, the winding turns ratio of CI is 2. Meanwhile, the duty cycle of the main switch is chosen to be 0.65. Thanks to the low voltage across switch S, a low $R_{DS\text{-}ON}$ MOSFET switch IRFP260 is selected. Furthermore, voltage and current waveforms of components are obtained and illustrated in Fig. 12. Comparing waveforms in Fig. 4 and Fig. 12 proves that the analytical and experimental results are the same. Fig. 12(a)

TABLE 2 CIRCUIT PARAMETERS OF THE PROTOTYPE

Specifications	Values
Input voltage (V_{in})	20 V
Output voltage (V_O)	200 V
Output Power (P_{out})	200 W
Capacitors (C_1-C_3)	47 µF
Output capacitor (C_O)	180 µF
Input inductor (L_{in})	320 µH
Magnetizing inductor of CI (L_m)	100 µH
Turns ratio of CI (n)	2
Switching frequency (f_S)	30 kHz
Power switch (S)	IRFP260
Diodes (D_1-D_3)	MUR1560

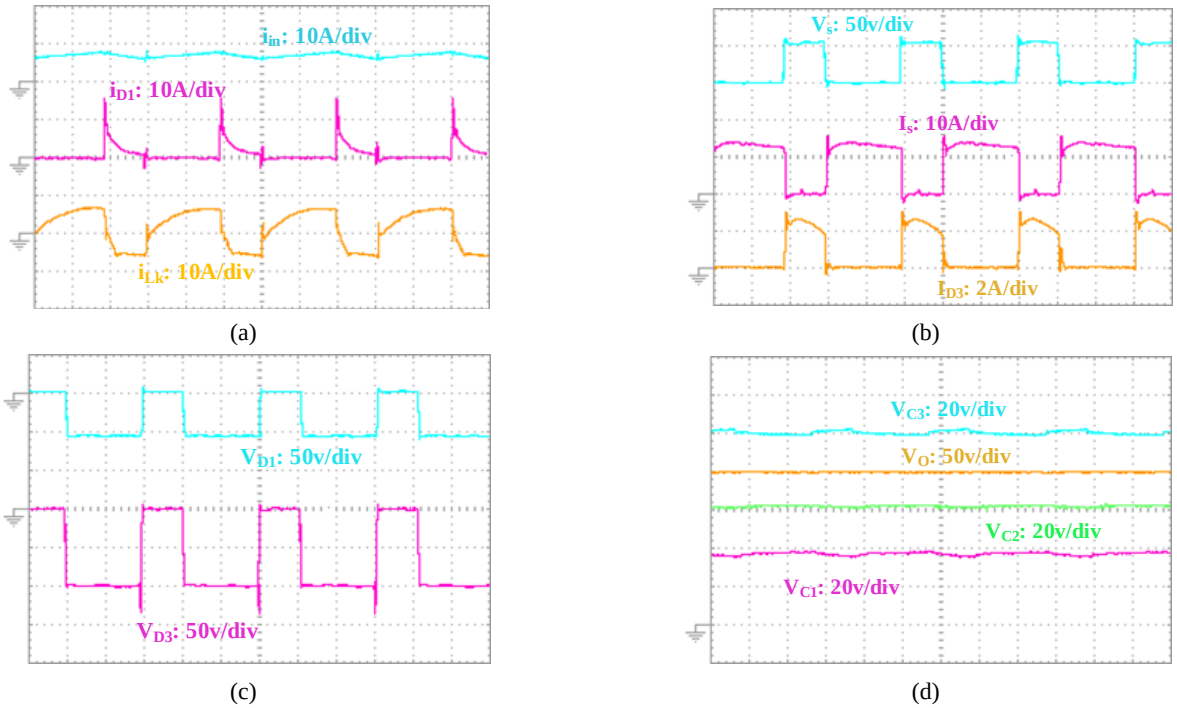

Fig. 12. Experimental result of prototype structure. (a) input current i_{in}, currents of diode D_1 and the primary side of CI, (b) voltage and currents of switch S and diode D_3, (c) voltage of diodes D_1 and D_3, and (d) voltage of capacitors and output voltage V_O.

represents input current and currents flowing through diode D_1 and CI. As depicted in this figure, the input current ripple is relatively low. Hence, the presented converter is a promising solution for PV systems. According to this figure, diode D_1 is turned off under ZCS conditions. Fig. 12(b) shows the voltage across switch S along with switch S and diode D3 currents. According to this figure, the voltage stress of switch S is clamped to the voltage of capacitor C_2. Moreover, it is shown that diode D_3 is turned on and off under ZCS conditions. Fig. 12(c) illustrates voltage stresses on diodes D_1 and D_3. Meanwhile, voltages of capacitors C_1, C_2, C_3 along with output voltage is depicted in Fig. 12(d).

VII. Conclusions

In this paper, a non-isolated high step-up SEPIC-based DC-DC converter has been presented and studied. The proposed converter has outstanding merits such as continuous input current and high voltage conversion ratio that make the structure a promising and functional solution for PV applications. Meanwhile, the stored energy of the leakage inductance of the CI has been recycled by a passive voltage clamp. Hence, power losses of the presented topology and voltage stress on the switch have been reduced. As a result, a switch with low on-resistance ($R_{DS\text{-}ON}$) has been employed. Since all diodes of the presented converter are biased reversely under ZCS conditions, their reverse recovery problems have been eliminated. Moreover, Thanks to the low voltage across switch S, the steady-state analysis of the proposed converter has been discussed and the design procedures of different components have been carried out. Specifications of the presented converter and some other structures presented before have been compared through various methods. The comparison has proved the advantages of the proposed converter over them. Furthermore, the efficiency analysis of the converter has been studied thoroughly and results have been depicted. In the end, experimental results have been added to validate the feasibility of the proposed structure. The results have confirmed the practicability of the proposed converter for PV applications.

References

[1] M. R. Banaei and S. G. Sani, "Analysis and Implementation of a New SEPIC-Based Single-Switch Buck-Boost DC-DC Converter With Continuous Input Current," in IEEE Transactions on Power Electronics, vol. 33, no. 12, pp. 10317-10325, Dec. 2018.

[2] J A. Mahmood et al., "A Non-Inverting High Gain DC-DC Converter With Continuous Input Current," in IEEE Access, vol. 9, pp. 54710-54721, 2021.

[3] S.G. Sani, M. R. Banaei and S. H. Hosseini, "Investigation and implementation of a common ground DC-DC buck converter with a novel control method for loss reduction in the converter," in IET Power Electron, pp. 1-12, June 2024.

[4] F. Kardan, R. Alizadeh and M. R. Banaei, "A New Three Input DC/DC Converter for Hybrid PV/FC/Battery Applications," in IEEE Journal of Emerging and Selected Topics in Power Electronics, vol. 5, no. 4, pp. 1771-1778, Dec. 2017.

[5] Yang, L-S. "Implementation of high step-up DC-DC converter using voltage-lift and coupled inductor techniques. IntJ Circ Theor,Appl. 2018; 46: 2079– 2097.
[6] O. Abdel-Rahim and H. Wang, "A new high gain DC-DC converter with model-predictive-control based MPPT technique for photovoltaic systems," in CPSS Transactions on Power Electronics and Applications, vol. 5, no. 2, pp. 191-200, June 2020.
[7] M. E. Azizkandi, F. Sedaghati, H. Shayeghi, and F. Blaabjerg, "A High Voltage Gain DC-DC Converter Based on Three Winding Coupled Inductor and Voltage Multiplier Cell," in IEEE Transactions on Power Electronics, vol. 35, no. 5, pp. 4558-4567, May 2020.
[8] F. Sadaghati, H. Shayeghi, S. Pourjafar and S. Hashemzadeh, "A High Step-up Transformer-Less DC-DC Converter with Continuous Input Current," 2020 11th Power Electronics, Drive Systems, and Technologies Conference (PEDSTC), 2020, pp. 1-6.
[9] A. Rajabi, A. Rajaei, V. M. Tehrani, P. Dehghanian, J. M. Guerrero and B. Khan, "A Non-Isolated High Step-Up DC-DC Converter Using Voltage Lift Technique: Analysis, Design, and Implementation," in IEEE Access, vol. 10, pp. 6338-6347, 2022.
[10] Al-Saffar, Mustafa & Ismail, Esam. "A high voltage ratio and low stress DC-DC converter with reduced input current ripple for fuel cell source" Renewable Energy., vol. 82, 2014.
[11] Z. Chen and J. Xu, "High boost ratio DC-DC converter with ripple-free input current", Electron. Lett., vol. 50, no. 5, p.p. 353-355, 2014.
[12] R. Gules, W. M. dos Santos, F. A. dos Reis, E. F. R. Romaneli and A. A. Badin, "A Modified SEPIC Converter With High Static Gain for Renewable Applications," in IEEE Transactions on Power Electronics, vol. 29, no. 11, pp. 5860-5871, Nov. 2014.
[13] Yavuz Koç, Yaşar Birbir, Hacı Bodur, "Non-isolated high step-up DC/DC converters–An overview", Alexandria Engineering Journal, Vol. 61, no. 2, 2022, pp. 1091-1132.
[14] M. R. Banaei and H. A. F. Bonab, "A High Efficiency Nonisolated Buck-Boost Converter Based on ZETA Converter," in IEEE Transactions on Industrial Electronics, vol. 67, no. 3, pp. 1991-1998, March 2020.
[15] S. G. Sani, M. R. Banaei, and S. H. Hosseini, "Research and implementation of an innovative modular non-isolated step-down DC-DC structure with continuous input current based on the Ćuk converter," in Int J Circ Theor Appl, vol. 52 no.5, pp. 2421-2434, 2024.
[16] M. A. Salvador, T. B. Lazzarin and R. F. Coelho, "High Step-Up DC-DC Converter With Active Switched-Inductor and Passive Switched-Capacitor Networks," in IEEE Transactions on Industrial Electronics, vol. 65, no. 7, pp. 5644-5654, July 2018.
[17] V. Karthikeyan, S. Kumaravel and G. Gurukumar, "High Step-Up Gain DC-DC Converter With Switched Capacitor and Regenerative Boost Configuration for Solar PV Applications," in IEEE Transactions on Circuits and Systems II: Express Briefs, vol. 66, no. 12, pp. 2022-2026, Dec. 2019.
[18] M. R. Banaei, S. G. Sani and H. Afsharirad, "A bidirectional high voltage ratio DC-DC topology for energy storage systems in microgrid," in IET Power Electron, vol. 17, no. 2, pp. 281-294, 2024.
[19] K. Patidar, and A.C. Umarikar, "High step-up pulse-width modulation DC-DC converter based on quasi-Z-source topology," in IET Power Electronics, vol. 8, no. 4, pp. 477-488, April 2015.
[20] H. Ardi, A. Ajami and M. Sabahi, "A Sepic based high step-up DC-DC converter integrating coupled inductor for renewable energy applications," 2017 8th Power Electronics, Drive Systems & Technologies Conference (PEDSTC), 2017, pp. 206-211.
[21] S. -M. Chen, T. -J. Liang, L. -S. Yang and J. -F. Chen, "A Boost Converter With Capacitor Multiplier and Coupled Inductor for AC Module Applications," in IEEE Transactions on Industrial Electronics, vol. 60, no. 4, pp. 1503-1511, April 2013.
[22] M. Eskandarpour Azizkandi, F. Sedaghati and H. Shayeghi,, "A New Boost DC-DC Converter Based on a Coupled Inductor and Voltage Multiplier Cells, " International Journal of Industrial Electronics, Control and Optimization (IECO), Vol. 2, No. 4, pp. 265-278, Feb. 2019.
[23] Ernie Wittenbreder, "Topology Selection by the Numbers," Technical Witts Inc., pp. 32-43, March 2006.
[24] M. C. Mira, A. Knott, and M. A. E. Andersen, "A three-port topology comparison for a low power stand-alone photovoltaic system," 2014 International Power Electronics Conference (IPEC-Hiroshima 2014 - ECCE ASIA), Hiroshima, Japan, 2014, pp. 506-513.
[25] T. Jin, X. Yan, H. Li, J. Lin, Y. Weng, and Y. Zhang, "A New Three-Winding Coupled Inductor High Step-Up DC-DC Converter Integrating With Switched-Capacitor Technique," in IEEE Transactions on Power Electronics, vol. 38, no. 11, pp. 14236-14248, Nov. 2023.

Mahdi Elmi was born in Tabriz, Iran, in 1990. He received the B.Sc. and the M.Sc. degrees in power electronics from Azarbaijan Shahid Madani University, Trabriz, Iran, in 2012 and 2014, respectively, where he is currently working toward the Ph.D. degree in electrical engineering. His research interests include power electronic converters, power quality, battery rectifier chargers, photovoltaic systems and wind turbines. He is currently working on high step-up converters for photovoltaic applications.

Mohamad Reza Banaei was born in Tabriz, Iran. He received the M.Sc. degree in control engineering from the Polytechnic University of Tehran, Tehran, Iran, in 1999, and the Ph.D. degree in power engineering from the Faculty of Electrical Engineering, Tabriz University, Tabriz, in 2005. He is currently a Professor with the Department of Electrical Engineering, Azarbaijan Shahid Madani University, Tabriz, where he joined in 2005. His main research interests include the designing and controlling of power electronic converters, renewable energy systems, modeling and controlling of FACTS and custom power devices, and power systems dynamics.

Hadi Afsharirad was born in Abhar, Iran, in 1985. He received the B.Sc. degree from the Zanjan University, Iran and M.Sc. and Ph.D. degrees, from the University of Tabriz, Tabriz, Iran, in 2008, 2010, and 2018, respectively, all in electrical engineering. He is an Assistant Professor with the Department of Electrical Engineering, Azarbaijan Shahid Madani University, Tabriz, which he joined in 2020. His main research interests include the electric and hybrid electric vehicles, renewable energy, linear electric machines and electrical drives.